THE FABRICATION AND ANALYSIS OF HARD, Si_3N_4-BASED, DISPERSED PHASE COMPOSITES

Olwen J. Pullum

Thesis submitted for the degree of Doctor of Philosophy (PhD)

University of Warwick

Department of Physics

April 1993

ABSTRACT

This thesis describes experiments which were carried out to fabricate new silicon nitride-based ceramic composites and to analyse their microstructural and physical characteristics. Possible applications considered were those involving high hardness or wear-resistant properties.

Two composite systems were investigated which had either silicon carbide platelets or cubic boron nitride particles, dispersed in a silicon nitride matrix (or binder) phase. The composites were fabricated using unconventional techniques, involving the hot-pressing of hybrid, laminated composites and ultra-high pressure sintering (at pressures exceeding 4 GPa). Each of these techniques was considered to offer a means of improving the fracture toughness of the ceramics, in addition to the high hardness.

Hybrid, laminated SiC-Si_3N_4 composites were succesfully fabricated by hot-pressing composites consisting of structurally arranged tape cast laminae with different proportions of SiC platelets. These composites showed promising indications of enhanced fracture toughness through delamination along laminar interfaces in addition to microstructural toughening mechanisms within the laminae.

Fabrication by ultra-high pressure sintering was found to be detrimental to the mechanical properties of the SiC-Si_3N_4 composites and it is suggested that the microstructural toughening effects due to the SiC platelets were rendered ineffective by residual stresses believed to arise from the ultra-high pressure process. Particularly low fracture toughnesses of 2.0 to 3.4 $MPam^{1/2}$ were determined for these composites and the Vickers hardness values were close to 20 GPa.

Additional studies were made on these composites to examine a polytypic phase transformation (to 3C SiC) that was induced in the platelets by the extreme fabrication conditions. This was attributed to the co-operative motion of partial dislocations on the basal planes.

The cBN-Si_3N_4 composites exhibited considerable plastic deformation of the cBN grains, in common with other superabrasive compacts. High Vickers hardness values above 35 GPa were achieved in these composites. However, the Knoop hardness values were lower than expected and the composites were found to have low strength and moderate fracture toughness, which was attributed to crack deflection and microcracking processes. The best fracture toughness value achieved was 5.81 ± 0.25 $MPam^{1/2}$, obtained for a 60 wt% cBN composition which also exhibited the highest strength, 316 ± 12 MPa.

TABLE OF CONTENTS

Chapter Five

ULTRA-HIGH PRESSURE FABRICATION AND MICROSTRUCTURE OF CUBIC BORON NITRIDE / SILICON NITRIDE COMPOSITES

LIST OF FIGURES

LIST OF TABLES

ACKNOWLEDGEMENTS

I would like to thank Prof. M. H. Lewis for his encouragement, guidance and supervision of this research project. I would also like to thank Dr. R. J. Caveney and the De Beers Industrial Diamond Laboratory for their generous funding of the research and for my visit to their laboratories. In particular, I would like to express gratitude to Dr. R. A. Chapman and Lucas for their assistance with the experiments at these laboratories and also, for their general encouragement.

Some supplementary high pressure experiments were carried out at the SERC High Pressure Laboratory (based in the former STC laboratories, Essex) for which I would like to thank Dr. J. Lees for permission to use the facility and Mr. G. Bolton for his proficient technical assistance.

The majority of the research was carried out at Warwick where many people have offered me much valued support and encouragement. I would especially like to thank Steve York and Gerald Smith for their initial tuition and assistance in electron microscopy, Dan Lee for helping me to cut, grind and polish numerous ceramic specimens, Dave Hammond for his assistance with the hot press, Simon Kohn and Andy Howes for their assistance in acquiring the MAS-NMR spectra and for useful discussions about the technique and John Lumby for some very helpful conversations concerning the mechanical testing of materials.

I am grateful to my office colleagues and to other friends and staff in the department for their part in creating a pleasant working environment. The encouragement of friends outside the department has also been very welcome. In particular, I am appreciative of encouragement from Alan Taylor, Stuart Sutherland and Nick Davies.

Finally, I would like to thank my parents for their continual support and interest.

DECLARATION

This thesis contains an account of my own independent research work, carried out between November 1988 and January 1993. Any contributions from outside research have been specifically acknowledged in the text. No part of this work has been submitted to this or any other institution in respect of a degree or other qualification. However, some aspects of the research have been presented as follows:

(i) O. J. Pullum and M. H. Lewis, *Microstructure of Cubic Boron Nitride Ceramics*, Proc. Diamond Conference, Reading, July 1990

(ii) O. J. Pullum and M. H. Lewis, *Tape-Cast Laminates of Dispersoid (cBN, SiC) - Containing Ceramics*, Proc. Diamond Conference, Oxford, July 1991

(ii) O. J. Pullum and M. H. Lewis, *A High Pressure Phase Transition in Silicon Carbide*, Proc. Diamond Conference, Cambridge 1992.

The results of some preliminary investigations conducted at the beginning of the research (bound at the back of the thesis) have been published as

O. J. Pullum and M. H. Lewis, Mater. Lett. 9 [2,3] (1990), *Microstructural Analysis of a Cubic Boron Nitride Ceramic*

LIST OF ABBREVIATIONS

α	phase identifier for α-Si_3N_4, on XRD spectra
β	phase identifier for β-Si_3N_4, on XRD spectra
EDAX	Energy Dispersive Analysis of X-rays
EELS	Electron Energy Loss Spectroscopy
HIP	Hot Isostatic Pressure
JCPDS	Joint Committee for Powder Diffraction Standards
MAS-NMR	Magic Angle Spinning Nuclear Magnetic Resonance
ppm	parts per million
r.f.	radio frequency
SEM	Scanning Electron Microscopy
SiC_p	Silicon carbide Platelet
SERR	Strain energy release rate
TEM	Transmission Electron Microscopy
TGA	Thermogravimetric Analysis
UHP	Ultra-High Pressure
wt%	percentage by weight
XRD	X-ray Diffraction

Chapter One

INTRODUCTION

1.0 DEVELOPMENTS IN ADVANCED CERAMICS

'Advanced' ceramic materials are normally polycrystalline masses of inorganic, non-metallic compounds with unique combinations of physical and chemical properties that are the result of strong, mixed ionic-covalent bonding. Typical ceramic properties include high melting (or dissociation) points, low densities and good chemical stability, all desirable attributes for engineering purposes. Advanced ceramics are to be found in electronic devices (capacitors, packaging, semiconductors, superconductors), optical devices (nonlinear and laser optics), thermal and magnetic devices. As structural components, ceramics are able to withstand extreme environmental conditions and ceramic coatings are often used to protect other materials from corrosion. Structural applications range from dental implants and bone replacements (for which alumina and porcelain have become recognised as good 'bioinert' materials) to wear-resistant applications and components for gas turbine engines, where the more covalent ceramics can survive at elevated temperatures (above 1000°C) and, being lightweight, can operate at faster speeds than are possible using metallic components. Therefore, the use of ceramic components can lead to dramatic increases in engine efficiency.

The single most important factor in determining whether or not ceramic materials reach their full capabilities for particular applications is their microstructure. For example, strictly controlled porosity levels are required for molecular sieves, an even distribution of different ceramic phases (and no porosity) is necessary to minimise inherent flaws in structural ceramics while interconnecting networks of conducting phases are needed in some thermal and electrical devices. Successful manipulation of ceramic microstructures to exploit the full potential of these materials relies on precise control of the ceramic processing conditions, from the purity and initial handling of the starting materials (many of which must be synthetically produced) to the conditions under which the ceramic is consolidated.

Ceramic materials are fabricated by sintering together a porous mass of very pure, fine powders. This process requires temperatures of 1000-2000°C to promote material diffusion as the mass densifies with elimination of the pores. For the more strongly covalent ceramics with low self-diffusion rates, successful powder consolidation often requires the simultaneous application of external pressures during sintering, which proceeds by a 'liquid phase sintering' process described in chapter two. These fabrication pressures vary from a few hundred atmospheres for most conventional processes, to tens of thousands of atmospheres in the highly specialised processes associated with ultrahard, diamond-like materials.

Processing methods that prove most beneficial for particular ceramic properties are usually evaluated by detailed investigations of the post-fabrication microstructure in conjunction with studies made on the physical properties. The microstructural observations can then be used to gain an understanding of mechanical behaviour and also to guide modifications that may be made to the fabrication techniques. Whilst the sintering temperatures and external fabrication pressures determine the final phase compositions and residual porosity levels, the powder treatment prior to sintering also has a significant influence on the microstructure. Despite there being fairly well established techniques for powder processing, these cannot be applied universally to all ceramic powders without some experimentation. As most powder preparation is carried out in a liquid medium, processing techniques must often be adapted to accommodate variations in particle size, surface chemistry and interaction with the liquid medium.

The research described in the ensuing chapters concerns hard, structural ceramics relevant to applications for wear resistance or high hardness and cutting tool materials. Since engineering materials are continually being developed to meet the needs of specific applications (for example, new aerospace alloys, ceramics for gas turbines) there is an increasing demand for cutting tools specially suited for rapid mass production, having a long tool life and high impact resistance whilst causing little machining damage. In recent decades progress has been made towards enabling ceramics to overcome well recognised limitations imposed by their characteristic brittle behaviour. Through more refined processing control and a detailed understanding of ceramic fracture behaviour, ceramic 'composites' have evolved which have a

microstructurally engineered tolerance of impact damage, rendering them suitable for an ever widening range of applications.

The remaining sections of this chapter introduce those ceramics used for cutting tool tips, the concept of ceramic 'fracture toughness' and finally, the objectives of this research project. Chapter two presents a detailed review of the fabrication and properties of the types of materials involved in this research and of the microstructural toughening behaviour of ceramic matrix composites. The fabrication and analytical techniques that have been used in this work are described in chapter three and the remaining chapters contain the findings of this research.

1.1 CERAMICS FOR HIGH-HARDNESS APPLICATIONS

The structural ceramics are attractive materials for use in cutting tools due to their high hardness, good physical and chemical wear resistance and thermal stability. Ceramics rival metal tools, particularly the hard steels used in the cutting of high melting point materials (iron, steel) where temperatures generated at the cutting edge may be as high as 900°C [1] and also compete with the 'cermets' (metal-ceramic alloys) such as tungsten carbide/cobalt alloys. At such temperatures ceramics are less susceptible to the problems suffered by metals which restrict the operational cutting speeds. As ceramic tools require lower cutting forces and have greater compressive strengths than metals, ceramic tool tips are less likely to deteriorate at high machining speeds. In addition, metal tools may undergo temperature-induced structural changes that can affect their hardness and wear resistance, so limiting their efficiency.

The oxide ceramics (alumina, zirconia) have a very high oxidation resistance and are used mostly for refractory purposes. Alumina is also used as a component phase in cutting tool tips, but has poor thermal shock resistance compared with the strongly covalent, non-oxide ceramics. Silicon nitride, silicon carbide and the 'sialons' (derived from Si_3N_4) have high hardness, low thermal expansion and good high temperature strength retention. All are now established in cutting and wear resistant operations. Some physical properties of selected structural ceramics are given in table 1.

Table 1: Physical properties of selected wear-resistant ceramics

Ceramic	†Hardness	Fracture Toughness	Young's Modulus	Linear Thermal Expansion	Source
silicon nitride	14.1 GPa 18.5 GPa	4.9 $MPam^{1/2}$ 4.0 $MPam^{1/2}$	300 GPa	3.0 - 3.2 x $10^{-6}K^{-1}$	[2] [3] [4]
silicon carbide	19.3 GPa 24.0 GPa	4.0 $MPam^{1/2}$ 4.0 $MPam^{1/2}$	436 GPa	4.4 - 4.8 x $10^{-6}K^{-1}$	[2] [3] [4]
Lucas Syalon™ (101)	13.25 GPa	7.7 $MPam^{1/2}$	288 GPa	3.04 x 10^{-6} K^{-1}	[5,6]
alumina	13.1 GPa 20.1 GPa	2.9 $MPam^{1/2}$ 3.9 $MPam^{1/2}$	390 GPa 406 GPa	8.3 x $10^{-6}K^{-1}$	[3] [3] [7]
‡zirconia	10.0 GPa	7.6 $MPam^{1/2}$	210 GPa		[3]

†*Vickers hardness scale* ‡*calcium-stabilised*

The property variations exhibited by individual ceramics of the same compound are explained by the different available fabrication methods and their influence on ceramic microstructure. For instance, pressureless sintering is favoured to consolidate powder preforms that have been moulded into specific component shapes, reducing the need for expensive diamond machining, but producing more porous materials than pressure-assisted sintering processes.

Fabrication techniques for the non-oxide, strongly covalent ceramics usually produce a diphasic microstructure since the powders are virtually non-sinterable without the addition of 'densification aids' (section 2.1.2) which form a residual, intergranular phase. Although only a small percentage of the overall ceramic composition, the secondary phase (the matrix phase is taken to be the primary phase) has a significant influence on the ceramic behaviour and is generally responsible for some deterioration in physical properties. The softening of this phase at high temperatures gives rise to grain boundary sliding and creep deformation processes, stimulating research to identify more refractory intergranular phases.

The hardest ceramics currently in existence are diamond and the cubic form of boron nitride, classed together as the 'superabrasives'. However, there is some speculation about the possibilities of synthesising new hard materials, based on theoretical predictions of bulk moduli and one suggested new compound [8] is a carbon

nitride (C_3N_4) structure similar to Si_3N_4 which may be created using the techniques involved in diamond synthesis. In 1989, the results of some very unusual research [9] reported the fabrication of a boron suboxide ($B_{22}O$) with a hardness approaching that of diamond, but with no further information on chemical stability or other properties important to cutting tool materials.

The superabrasives are commonly used as loose, abrasive grit or are sintered to form materials for cutting tools, rock drills, wire drawing dies or thermal heat sinks, since both diamond and cubic boron nitride have high thermal conductivity. Although the superabrasives are more expensive to fabricate than conventional ceramics, they are considerably harder and more durable, produce superior machining finishes and maintain lower cutting surface temperatures. The main distinction made between them is in their areas of application. Polycrystalline diamond is used for machining non-ferrous materials while polycrystalline cubic boron nitride is able to machine ferrous metals (steel, cast iron) that would chemically react with diamond. One advantage demonstrated for cubic boron nitride tools over conventional ceramics is a lesser susceptibility to thermal fracture induced by variations in cutting speed and coolant delivery [10]. Additional claims made for cubic boron nitride tools [11] are (i) tool lifetimes that are between three and five times greater than for titanium carbide-ceramic alloys (ii) a wear resistance of up to three times that for ceramic tools in cast iron machining and (iii) operational cutting speeds up to five times more than those used for hard alloy tools.

Polycrystalline diamond or cubic boron nitride materials are generally diphasic as the conditions that would be required to fabricate single phase superabrasive ceramics are extreme (section 2.3.2). The properties of the additional binder phase(s) present in polycrystalline superabrasives (see section 2.3.3, with reference to cubic BN) strongly influence the overall material characteristics and can either limit or optimise the material's capabilities for a specific purpose. The fabrication of superabrasive ceramics with new binder phases is undergoing continual research with some emphasis on materials in which refractory ceramics form the binder phase. In general, such research is beset with problems peculiar to the complexities of the ultra-high pressure apparatus involved. The stability of this apparatus is extremely sensitive to any changes

made in the interior construction of the high pressure chamber and to variations from standard operating conditions. It interesting to note that a diamond-alumina ceramic has been fabricated [12] under conventional hot-pressing conditions of 32 MPa and 1250°C, contrary to the usual methods involving pressure at least a hundred times greater than this.

1.2 CERAMIC FRACTURE BEHAVIOUR AND 'FRACTURE TOUGHNESS'

1.2.2 *Ceramic Fracture Behaviour*

The inability of brittle materials to realise their theoretically predicted strengths was first studied by Inglis [13] and later by Griffith [14] who established a relationship between the actual strength and the existence of microstructural defects that initiate cracking. Inglis carried out a mathematical treatment which described microstructural flaws as acting as 'stress concentrators' and showed that the local stress at the tip of a narrow crack is inversely proportional to the radius of curvature of the crack. In contrast, Griffith considered the condition required for fracture in terms of energy criteria. He proposed that the stored elastic energy (from strained bonds) is dissipated from the cracked body on formation of new fracture surfaces during the crack extension [14]. The 'Griffith' relationship which describes the condition for fracture is as follows:

$$\sigma_f = \left(\frac{2 E \gamma}{\pi a}\right)^{\frac{1}{2}} \qquad (1.1)$$

where σ_f = the failure stress (modulus of rupture), E = Young's modulus, γ = the energy of a free surface and a = the crack length (of the dominant flaw).

The understanding of fracture mechanics, which underlies the basis for ceramic engineering, has been advanced further from the early work of Griffith and a detailed review explaining each development can be found in reference [15]. A particularly significant contribution was made by Irwin [16] who defined a 'stress intensity factor' ('fracture toughness') for the crack opening mode (see figure 1.1), related to the magnitude of the stress field in a plastic zone around the crack tip.

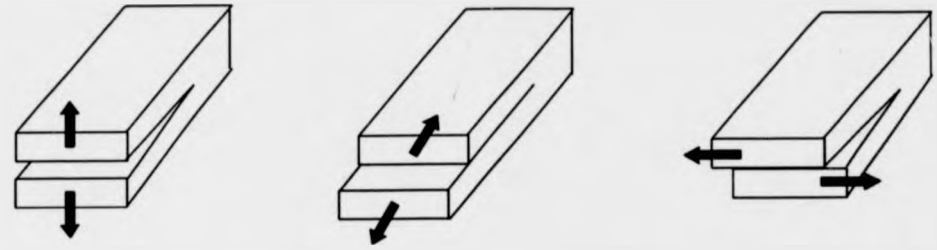

Mode I: Opening | Mode II: Sliding | Mode III: Tearing

Figure 1.1: Modes of crack propagation

The relation between fracture stress and crack length, derived from Irwin's work [16] is

$$K_{Ic} = \sigma_f Y a^{1/2} \qquad (1.2)$$

where K_{Ic} is the critical stress intensity factor (experimentally determined), σ_f is the stress driving fracture and Y is a geometrical factor (dimensionless constant) relating to the flaw shape and loading configuration. Fracture occurs when the critical value of K_{Ic} is exceeded as this determines the local fracture driving forces.

Irwin [16] considered an alternative way of evaluating the release of stored elastic energy during crack extension and related the fracture toughness to the strain energy release rate (crack extension force) by

$$K_{Ic}^2 = EG \qquad (1.3)$$

where G = the strain energy release rate.

(ii) Ceramic Toughening

The toughness and strength of ceramics can be improved by microstructural manipulation, such as by

(i) finer processing control to reduce the occurrence of flaws in monolithic ceramics (improving the strength);

(ii) use of anisotropic grains in the fabrication (improving the fracture toughness);

(iii) 'transformation' toughening in the case of zirconia ceramics [17] whereby crack propagation energy is absorbed during the volume expansion that occurs during a diffusionless phase transition of zirconia, induced by fracture stress. (This toughening method is limited to low temperatures where the tetragonal zirconia phase is metastable and can be induced to transform to the monoclinic form);

(iv) increasing the ceramic resistance to crack growth through the fabrication of 'ceramic composites' in which a secondary, reinforcing phase is combined with a fine-grained ceramic matrix. (The toughening mechanisms that operate in 'dispersed phase ceramic composites' are discussed further in section 2.2.1.)

1.3 RESEARCH OBJECTIVES

The overall objective of this research programme was to fabricate novel hard ceramic composites and to examine the effects of the fabrication procedures on the resulting ceramic microstructures and physical properties. Potential applications are for new, hard and wear-resistant materials such as cutting tools, for which the improved fracture toughness combined with high hardness offered by composite ceramic systems is also beneficial.

A silicon nitride-based matrix phase was selected for all the ceramic composites on account of the excellent physical and chemical properties of silicon nitride ceramics (described more fully in section 2.1). Silicon carbide platelets and cubic boron nitride particulates were dispersed into the matrix phase to fabricate a range of composites for two ceramic systems, the aims being:

(i) the fabrication of novel silicon carbide / silicon nitride composites under both conventional and ultra-high pressures;

(ii) the fabrication of cubic boron nitride/silicon nitride composites under ultra-high pressures.

The various fabrication experiments involved both conventional pressure-assisted sintering methods (at about 20 MPa) to fabricate hybrid composites (see section

2.2.4) and sintering under ultra-high pressures (above 4 GPa) to create unique materials which cannot be fabricated under more conventional conditions. Laminated silicon carbide-silicon nitride composites were prepared using the 'tape casting' technique (section 2.24) and fabricated under conventional pressures, to produce hybrid composites with compositional variations within the bulk material. Silicon carbide-silicon nitride composites were also fabricated using ultra-high pressures to assist the densification of composites containing an unusually high volume fraction of silicon carbide platelets and to investigate the apparent trends of increasing fracture toughness with increasing dispersed phase content. Application of the ultra-high pressures offered a means of overcoming difficulties in composite densification which impede the attainment of theoretically dense composites with dispersed phase volume fractions above about 30 wt% (see section 2.2.3).

Experiments were carried out to fabricate cubic boron nitride/silicon nitride ceramics and hence, produce a refractory cubic BN ceramic having higher hardness and greater chemical inertness than cubic BN materials consolidated with conventional binder phases. In these experiments, the ultra-high pressures were necessary for maintaining the thermodynamic stability of the cubic BN phase at the high sintering temperatures (1700°C) which were required to sinter the silicon nitride-based matrix phase.

Chapter Two

FABRICATION, PROPERTIES AND MICROSTRUCTURE OF CERAMICS BASED ON SILICON NITRIDE, SILICON CARBIDE AND CUBIC BORON NITRIDE

2.0 INTRODUCTION

This chapter contains a review of previous research concerned with the development of composites based on the ceramic phases involved in this project. Firstly, the typical characteristics and fabrication of Si_3N_4-based ceramics are discussed, as Si_3N_4 was the common 'element' in all the composites fabricated during this research. The reasons are explained for the presence of an additional phase in polycrystalline Si_3N_4 and for the selection of an Y_2O_3-SiO_2 mixture as a 'sintering additive'. The mechanisms by which the dispersed phases (of SiC platelets and cBN particulates) might be expected to induce toughening in the Si_3N_4-based ceramics are described in a detailed discussion of microstructural toughening behaviour. The more recent concept of hybrid composites is also introduced and the background to the laminated composites is explained.

Towards the end of the chapter the use of ultra-high fabrication pressures is reviewed with emphasis on the development of cBN ceramics (from the synthesis of cubic BN to its combination with a Si_3N_4 ceramic phase) and the potential effects of extreme pressure on the SiC crystal structures.

2.1 SILICON NITRIDE CERAMICS

2.1.1 *Silicon Nitride Crystal Structures*

Silicon nitride is a synthetically-fabricated material of which there are two crystal forms [18]. Both are hexagonal structures where silicon atoms are centred in irregular tetrahedra of nitrogen atoms. The layers of β-Si_3N_4 (figure 2.1) are repeated in an 'AB' stacking sequence (the labelling associated with different distinctive layers

normal to the c-axis) whilst α-Si_3N_4 layers follow an 'ABCD' stacking sequence in which layers C and D correspond to a rotation of layers A and B through 180° about the crystallographic c-axis. The additional layers describing the stacking sequence of α-Si_3N_4 account for its c-axis lattice parameter (c = 5.617Å) being twice that of β-Si_3N_4 (c = 2.909Å).

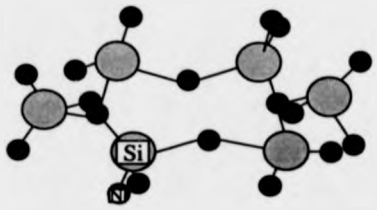

Figure 2.1: Crystal structure of β-Si_3N_4

α-Si_3N_4 is believed to be the less thermodynamically stable crystal form and a phase transformation to the β-phase can be induced at temperatures above about 1400°C. A reverse β to α transformation has only once been reported [19].

The typical commercial manufacture of Si_3N_4 is by a vapour phase reaction in which loose silicon powder is heated in a nitrogen atmosphere ('nitrided') to produce an initially amorphous powder [20]. This powder is crystallised on further heating which usually results in a mixture of both the α and β phases, with a passive surface layer of silica on grain surfaces.

2.1.2 *Fabrication of Polycrystalline Silicon Nitride*

There are two common routes for the fabrication of polycrystalline silicon nitride. These are either by the nitridation of a silicon powder compact ('reaction bonding') to produce a porous Si_3N_4 ceramic or by consolidation of Si_3N_4 grains during a sintering process driven by the reduction in free surface energy as particles become bonded together. However, the sintering of Si_3N_4 is impeded by its very low diffusion coefficient arising from the small vacancy concentration of a covalent lattice. Hence, sintering Si_3N_4 requires temperatures above about 1700°C and the addition of 'densification aids' (usually oxides) to provide liquid phase-assisted material transport

(see the following section). Additionally, grain consolidation is often assisted by external pressure application. In the absence of any additional pressure, an increased ambient nitrogen pressure is essential to avoid thermal decomposition of Si_3N_4 at sintering temperatures approaching the decomposition temperature of 1900°C under 0.1 MPa [21].

(i) Liquid Phase Sintering

The liquid phase sintering mechanism has been well-studied and found to proceed through the following stages: particle rearrangement, solution of grains into the liquid phase, diffusion of the dissolved species, reprecipitation and coalescence (or grain coarsening), as described by Kingery [22] and illustrated in figure 2.2.

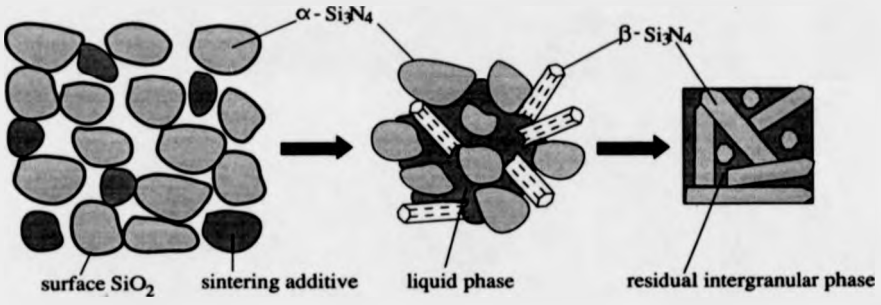

Figure 2.2: Densification of Si_3N_4 by liquid phase sintering

The sintering additives and surface silica on the Si_3N_4 grains melt and react above a eutectic temperature to form a liquid phase that fills pores as it infiltrates between the grains. Particle rearrangement is promoted by capillary pressure and this is followed by dissolution of complete α-Si_3N_4 grains into the liquid phase. Although Kingery proposed that solid particles have a greater solubility at grain contact points than elsewhere, the dissolution of α-Si_3N_4 is more likely driven by its thermodynamic instability with respect to the β phase, as suggested by [23]. The dissolved species diffuse through the liquid and as the solution reaches supersaturation, Si_3N_4 reprecipitates as rod-like, elongated β-Si_3N_4 grains. Densification occurs simultaneously with the α to β transformation, although full densification is not

necessarily accompanied by complete α to β conversion [24]. Both these processes are controlled by atomic diffusion [23,25] at a rate found to be linearly dependent on the sintering temperature and the quantity of the liquid phase. If β-Si_3N_4 is present in the initial powder composition, particles precipitate on the coarser β-Si_3N_4 grains and continuous grain growth to large, spherical grains ensues. A predominantly α-Si_3N_4 phase content is desirable in the starting powder in order to realise the optimal mechanical properties that arise from the fibrous microstructure of newly-formed β-Si_3N_4 grains [26-28].

On cooling, the liquid phase is converted to a glassy or crystalline intergranular phase. Although the liquid phase is advantageous for sintering purposes, the properties of the residual phase (melting point, viscosity) strongly influence those of the final Si_3N_4 ceramic and lead to a degradation in high temperature strength and creep resistance. The glassy phase also tends to trap impurity ions present in the starting powders which may further reduce its viscosity.

(ii) Pressure-Assisted Sintering

Application of external pressure during sintering produces a marked increase in the densification rate [24,25] and results in generally stronger materials through a decrease in final porosity and use of lower sintering additive levels, hence a reduced intergranular phase content.

In the **hot pressing** process, sintering is carried out inside a graphite die with uniaxial pressure application, of typically 20-30 MPa, limited by the strength of the die. The uniaxial nature of the applied pressure causes some orientational alignment of elongated grains [29,30] and is responsible for differences in physical properties measured parallel and perpendicular to the hot-pressing axis.

Greater pressures and hence, higher final densities are attained by **hot isostatic pressing** (**HIP**ing): sintering under tri-axial pressure application of 100-200 MPa through the medium of an inert gas (usually argon). Using this process, it has been possible to densify Si_3N_4 to 95% theoretical density in the absence of any densification aids [31].

2.1.3 *Silicon Nitride Sintering Additive Systems*

The conflicting roles of silicon nitride sintering additives, in providing a liquid phase sintering medium to the detriment of final material properties, has motivated much research to find sintering additives that form a more refractory intergranular phase. Sintering additives can be divided into two classes, depending on whether or not they form a 'solid solution' in the Si_3N_4 lattice.

(i) SiAlON Ceramics

The fabrication of SiAlON (or 'sialon') ceramics developed from the discovery that Al_2O_3 sintering aids become absorbed into the β-Si_3N_4 crystal lattice during the sintering process [32, 33]. This takes place by substitution of Al^{3+} ions onto Si^{4+} sites, made possible by their similar ionic radii and is accompanied by substitution of O^{2-} for N^{3-} ions to maintain charge neutrality and a constant cation:anion ratio of 3:4. The solid solution of Al_2O_3 expands the β-Si_3N_4 crystal lattice into what is termed the β'-Si_3N_4 lattice and reduces problems of degraded mechanical properties associated with a residual intergranular phase. An α' sialon is also formed by the incorporation of interstitial metallic ions into the α-Si_3N_4 lattice. A full review of the different sialon crystal structures can be found in reference [34].

The advantages of sialons are that they can be sintered to high density at normal atmospheric pressure and therefore, can be produced in the final component shape, reducing the need for mechanical machining. The sialon sintering mechanism is by solution and reprecipitation (as described for sintering Si_3N_4) and the densification rate can be similarly increased by addition of another oxide additive to lower the eutectic temperature and reduce the liquid phase viscosity.

(ii) Non-Sialon-forming additives

Early fabrication of hot-pressed Si_3N_4 used MgO as a sintering additive [35], but Gazza [36] produced a material of higher density and greater mechanical strength by

hot pressing with an Y_2O_3 additive. However, since the Y_2O_3 additive forms a more viscous liquid phase than that formed by MgO, increased sintering temperatures (above 1700°C) are required to reduce the viscosity so as not to inhibit particle rearrangement during sintering. External pressure application (by hot-pressing or HIPing) is also necessary for full densification of Si_3N_4 with an Y_2O_3 additive.

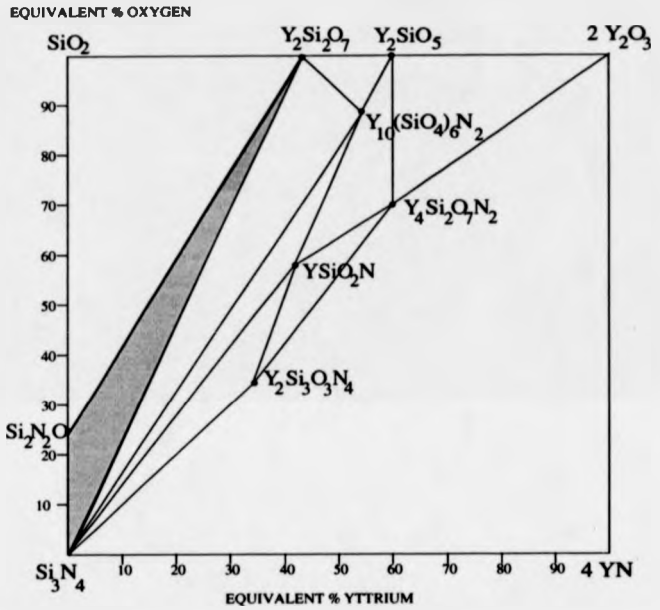

Figure 2.3: Phase relationships in the Si_3N_4-SiO_2-Y_2O_3-YN system, after [39].

There are several possible yttrium silicate phases that may be formed on reaction with the surface SiO_2 on Si_3N_4 grains and these have been studied in relation to their properties as an intergranular residual phase [37-39]. Many Si-Y-O-N phases are unstable on oxidation, undergoing a volume expansion that is high relative to silicon nitride. When these phases are present in Si_3N_4 ceramics their oxidation behaviour induces internal stresses sufficient to catastrophically degrade the ceramic. However, Lange *et al.* [38] found that materials fabricated within the Si_3N_4-Si_2N_2O-$Y_2Si_2O_7$ triangle of the phase-relation diagram (shaded in figure 2.3) have excellent oxidation resistance compared with other Si_3N_4 ceramics, explained by the compatible existence of $Y_2Si_2O_7$ and SiO_2, the oxidation product of both Si_3N_4 and Si_2N_2O.

Despite the good mechanical properties of ceramics formed from the Si-Y-O-N

system, secondary phase oxide additives are often added to lower the eutectic temperature of the liquid phase and enhance the densification kinetics so that full densification may be achieved with lower sintering temperatures. Typical additive systems are Y_2O_3-Al_2O_3 [40] in which some Al_2O_3 dissolves into the Si_3N_4 grains, forming a sialon, Y_2O_3-MgO [41] and Y_2O_3-NdO_3 [42]. Hirosaki *et al.* [43] studied the effect of the addition of Al_2O_3, MgO, La_2O_3 and Nd_2O_3 secondary additives on the Y_2O_3 additive system and found that whilst all these additional additives facilitated the densification process, the addition of Al_2O_3 and MgO degraded the final mechanical properties whereas the other systems showed comparable refractory behaviour to the single additive system.

2.2 DISPERSED-PHASE CERAMIC COMPOSITES

The microstructure of ceramic composites provides a means of absorbing crack propagation energy by interaction of the crack front with a secondary phase. This interaction leads to a reduction in the stress intensities around the crack tip and allows the material to tolerate a larger critical flaw size. As a result, the resistance to fracture is increased as the crack extends (known as 'R-curve' behaviour), enhancing the fracture toughness and strength. The secondary phase may be a random dispersion of particulates, platelets (flat discs), whiskers (short, needle-shaped filaments) or uniaxially-aligned fibres.

Composite fabrication procedures are crucially important to the attainment of theoretically-predicted toughening increases and in some instances, the complexities involved may offset advantages in mechanical behaviour. Fibre-containing composites are the most difficult to fabricate (the procedures are described in ref. [44]), encountering typical problems of non-uniform fibre alignment, incomplete matrix densification and degradation of the fibres (grain growth, oxidation) during sintering. Hence, the fabrication of dispersed-phase composites, where the main difficulties involved are in attainment of a homogeneous dispersion, is favoured for many applications. Ceramic fabrication techniques also provide a means to exploit further the potential to produce novel materials through the modification of conventional methods.

The creation of composites with macroscopic compositional variations is discussed in section 2.2.4.

Silicon nitride composites were developed from the need for the structural improvement of polycrystalline Si_3N_4 to expand the already excellent physical and chemical properties that make Si_3N_4 an important engineering material. Silicon carbide, a traditional abrasive, possesses similarly attractive properties to those of Si_3N_4 and so can effectively toughen silicon nitride ceramics without adversely affecting the desirable characteristics. Both Si_3N_4 and SiC are strongly covalent, refractory materials and typically exhibit the following properties: (i) high hardness (ii) good wear resistance (iii) strength retention over a wide range of temperatures (iv) low thermal expansion and (v) good chemical stability in corrosive environments. Lange [45] fabricated a SiC particulate-reinforced Si_3N_4 composite with twice the strength of monolithic Si_3N_4 at 1400°C. Continued research indicating the substantially improved mechanical behaviour of SiC-Si_3N_4 ceramics over monolithic Si_3N_4 has consistently been reported [46, 47]. Much research is currently in progress to evaluate relative advantages of the different morphological forms of dispersed SiC phases.

2.2.1 *Dispersed-Phase Composite Toughening Mechanisms*

The toughening mechanisms exhibited by dispersed-phase composites are governed by the characteristics of the interface between the matrix and reinforcing particle, in the same way as for fibre-reinforced composites [48], which leads to enhanced toughness by providing relatively weak fracture paths that absorb energy without catastrophic failure. The strength of the interfacial bonding is not easy to control during processing and this accounts for some deviations between predicted and observed toughening behaviour. Debonding of the matrix-dispersoid interface occurs when the interfacial fracture energy is exceeded by the propagating crack energy and is determined by (i) the relative orientation of the dispersoid to the crack and (ii) the ratio of interfacial fracture energy to dispersoid fracture energy [49]. Toughening mechanisms that arise from interfacial debonding are crack deflection, crack bridging and pullout, as described in the following sections.

(i) Crack Interaction with Dispersed Inclusions

The presence of secondary phase inclusions may promote toughening provided that they do not act as stress concentrators. Lange [50] described a 'crack bowing' toughening mechanism where the crack front becomes momentarily pinned between dispersed inclusions and bows out with a curved path that increases the crack length. Toughening is effected by absorption of the crack propagation energy as the new fracture surfaces are formed. However, the crack is able to move away from its pinning positions when the fracture stress of the dispersed phase is reached and failure occurs. Lange derived an expression [50] for the composite fracture energy and found that the resistance to fracture should increase with a decrease in the distance between inclusions (and hence, with a greater volume fraction of the inclusions).

(ii) Crack Deflection

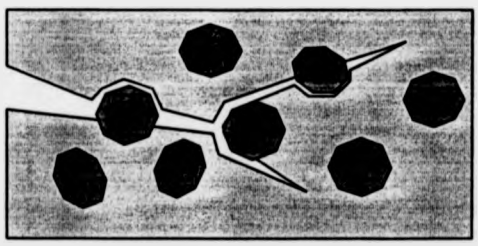

Figure 2.4: Crack deflection by a dispersed phase (regular platelets)

Crack deflection takes place where weakened interfaces or residual stresses provide preferential, non-planar fracture paths around secondary phase inclusions in the matrix. As the crack plane changes its orientation relative to the applied stress, the crack driving force is reduced and so further energy is required for continued propagation. Faber and Evans [51] examined the separate contributions of crack tilting and twisting to the crack deflection toughening mechanism and they calculated the crack driving force associated with a random, three dimensional distribution of different particle morphologies in a matrix phase. On interception of an inclusion particle, the crack plane is initially tilted about an axis parallel to the crack front, involving opening

(I) and sliding (II) crack propagation modes. The degree of tilting depends on the position and orientation of the inclusion in the crack path. When adjacent inclusions are orientated such that the crack is required to tilt in opposite directions, the crack plane becomes twisted about an axis perpendicular to the crack front, propagating in opening (I) and tearing (III) modes. Faber and Evans assessed the angularly-dependent, local stress intensity factors at tilted and twisted sections of the crack front and predicted the toughening increments using the relationship

$$G_c = \left(\frac{G_m}{\langle G \rangle}\right) G_{c,m} \tag{2.1}$$

where G_c is the effective critical strain energy release rate (SERR) for the deflected crack, G_m is the SERR for an undeflected crack, <G> is the average SERR (considered to represent the average crack driving force) and $G_{c,m}$ is the critical SERR for an undeflected matrix crack. Their predictions suggested that toughening by crack deflection is dependent on the aspect ratio (length (radius) to width (thickness)) and volume fraction of dispersed-phase particles, but is not influenced by the particle size.

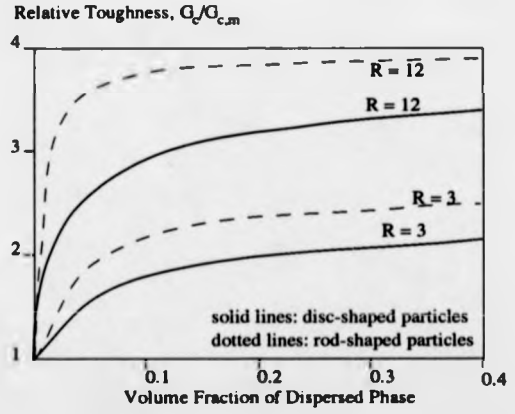

Figure 2.5 : Predicted toughening increases from crack deflection around discs or rod-shaped inclusions as a function of volume fraction and aspect ratio, R (adapted from [51])

Rods of high aspect ratio were expected to provide the greatest toughening, mainly by crack twisting whilst high aspect ratio discs can considerably improve toughness by initial crack tilting in addition to crack twisting. Spherical particles were expected to be the least effective in toughening by crack deflection on account of their low aspect ratio. At dispersed phase volume fractions much above 20% the effects of overlapping

particles were expected to inhibit further toughening increases as is shown by the asymptotic behaviour of the graphs in figure 2.5.

Liu *et al.* [52] adopted a similar approach to Faber and Evans to calculate the crack deflection toughening due to rod-shaped whiskers. However, Liu *et al.* considered that the densification of dispersed phase composites requires pressure-assisted sintering, typically hot-pressing for which uniaxial pressure application causes whisker alignment perpendicular to the pressing direction. Hence, Liu *et al.* treated the reinforcing phase as being randomly orientated in a two dimensional plane only and showed that the orientation of the whiskers (rods) to the advancing cracks also influences the toughening increment. From these calculations, borne out by experiment, the degree of crack deflection and hence, fracture toughness is significantly higher for a crack travelling perpendicular to the plane of aligned whiskers than for crack propagation within this plane.

(iii) Crack Bridging

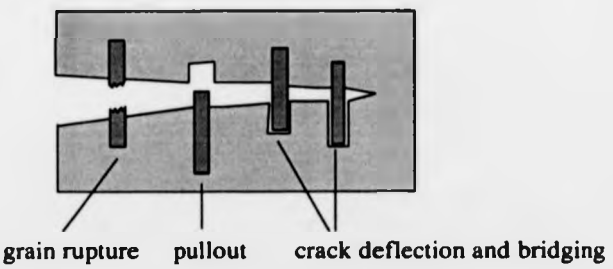

Figure 2.6: Crack bridging processes giving rise to toughening

Crack bridging is a prominent toughening mechanism in fibre-reinforced composites [48] and is also important in whisker and platelet-containing materials. Observations in whisker-reinforced ceramics [53] suggest that crack bridging may additionally inhibit grain boundary sliding at high temperatures. The bridging action, where separating crack surfaces are joined by particles of the reinforcing phase, is induced by partial debonding of the matrix-reinforcement interface in a 'bridging zone' created behind the crack tip [54]. As the applied stress is transferred from the matrix to

the reinforcing grain, crack propagation energy may be absorbed by rupture of the grain itself or by frictional dissipation during grain 'pullout', when continued interfacial debonding leads to extraction of the grain from the matrix. Crack bridges remain behind the crack tip, exerting frictional closure forces across the interface and cumulatively increase the resistance of the material to crack propagation [55,56]. Becher *et al.* [57] found that toughness in whisker-composites increased with whisker strength and radius, dispersed phase volume fraction, an increasing ratio of composite:whisker Young's modulus and with an increasing ratio of matrix:interface fracture energy. The contribution of dispersed-phase toughening by pullout mechanisms is restricted by the shorter available length compared with fibre-toughening.

(iv) Microcrack Toughening

Microcracks may already exist in a ceramic from the spontaneous relief of local stresses by subcritical crack propagation. The internal stresses typically arise on cooling after fabrication, due to (i) thermal expansion differences between the constituent phases of a ceramic composite, (ii) volume increasing phase transformations [58,59] or (iii) anisotropic thermal expansion in single phase material [60]. Davidge and Green [61] found that spontaneous stress relief occurs only around particles above a minimum size, but can be induced around smaller particles by applied stresses.

When microcracking occurs in response to crack propagation, material is degraded ahead of the microcrack, creating a permanently deformed 'process zone' due to non-linear fracture behaviour and stress-strain hysteresis. This has a toughening effect if the strain energy released on microcracking is greater than that which would be expended on the formation of new fracture surfaces during continued crack extension. The greatest degree of toughening can be obtained by optimising the grain size of the material. If the grains are too small, the microcracks induced around them are insufficient for adequate stress relief and will only serve to weaken the material, whereas if the grains are too large, the associated microcracks may be comparable to the critical flaw size and initiate fracture.

2.2.2 *Silicon Carbide Platelet Reinforcement*

Although particulates of SiC have been successfully used [45] to improve the toughness of Si_3N_4 ceramics, more promising improvements were made following the development of SiC whiskers, reviewed in ref. [62], which are synthesised by the pyrolysis of SiO_2 contained in rice husks. SiC whiskers are single, needle-shaped crystals that are less prone to processing damage than SiC fibres, more easily incorporated into ceramic matrices and can effect toughening by similar mechanisms of crack bridging and crack deflection. There has been extensive research on SiC whisker-reinforced matrices of Al_2O_3 (a cutting tool material) and Si_3N_4, indicating a promising trend of increasing fracture toughness with increasing whisker content [46,47,62]. However, a major disadvantage of SiC whiskers is in having a morphology that is also potentially highly toxic [63,64] and this has lead to the development of SiC platelets as an environmentally safer alternative.

SiC platelets are mostly hexagonal polytypes and are characterised by a flat, disc-shaped morphology, predicted to toughen materials by crack deflection [51]. The platelets are formed by a carbothermic reduction process (similar to whisker synthesis) where SiO_2 is reacted with carbonaceous materials at high temperatures [65].

Toughening mechanisms of crack deflection, crack branching and crack bridging have been observed in platelet-reinforced materials and an increase of fracture toughness with platelet volume fraction has also been found [66-69], as for whisker-reinforced materials. Sakai *et al.* [68] suggested that SiC platelets are particularly effective in Si_3N_4 matrices (compared with Al_2O_3, mullite and sialon) perhaps as a result of relatively weaker platelet-matrix interfacial bonding. Sakai *et al.* fabricated a Si_3N_4 matrix containing 30 wt% SiC platelets with a fracture toughness of 14.3 $MPam^{1/2}$ an increase of 6.3$MPam^{1/2}$ over the unreinforced matrix. However, despite achieving good toughness increases, SiC platelets have been found to reduce composite strength and actually weaken the matrix materials [67-69], behaviour not associated with SiC whiskers. The reduction in strength has been related to the platelet size as composites with smaller sized platelets exhibit higher strengths [67] and this suggests that SiC platelets also act as fracture-initiating defects.

2.2.3 *Fabrication of Dispersed-Phase Composites*

Ceramic composite fabrication entails two separate processing stages: firstly, 'green state' preparation in which the component phases are mixed and secondly, sintering and densification.

(i) *Green State Preparation*

The initial green state fabrication bears an important influence on the final microstructural homogeneity. Relatively complicated techniques, such as chemical vapour infiltration, are required to introduce a matrix phase to woven fibre or filament-based composites, but for dispersed phase composites, the secondary phase can be randomly introduced by mechanical mixing of the starting powders, usually performed in a fluid suspension.

A typical method used for preparing green state composites is **slip casting**. This involves mixing the powdered composite components in an aqueous slurry (or 'slip') and casting the slip into a porous mould (made from plaster of Paris) that allows the liquid to drain away leaving the slip to dry and solidify. (It is assumed that there is no contamination of the ceramic powders by the plaster of Paris.) Some alignment of anisotropic particles may result from the viscous flow of the water and may be beneficial for composite toughening behaviour in the final ceramic. The homogeneity of the final composite is determined by the effectiveness of the wet mixing stage as any inhomogeneities introduced at this point may not be removed by subsequent processing. During the wet mixing, the component phases can be evenly dispersed and agglomerates in fine powders can be broken down by deflocculating the suspension. In aqueous suspensions, powder deflocculation can be induced by modifying the particle surface charge to counteract strong electrostatic attractions between fine powders. This is achieved by a change in the slip pH value to reach an experimentally established condition for the best simultaneous deflocculation of all the phases present. The optimum pH value can either be determined from electrokinetic measurements of the zeta potential (the potential between the bulk suspension and the charged solvation layer attracted to particle surfaces) which provides a measure of the particle surface charges

or more simply, is the pH value which results in the lowest slip viscosity [70].

(ii) *Sintering and Densification*

The densification of green state composites is inhibited by the presence of non-sintering inclusions of the secondary phase and thus is more difficult than for monolithic ceramics. Composite densification necessitates the addition of externally-applied pressures to increase the driving forces that operate during sintering. The main reason for pressure-assisted sintering is to overcome the 'hydrostatic backstresses' which arise on account of differential sintering rates in localised regions of the composite.

Differential rates of sintering in the composites may arise from non-sintering areas in the matrix or from local variations in the matrix density due to the presence of inclusions or to the existence of crack-like defects from residual stresses in the green state material [71] (perhaps from initial cold compaction). This results in the creation of tensile stresses in the matrix which may be sufficient to degrade the ceramic by macroscopic cracking. Weiser and De Jonghe [72] found, from their studies on densification rate, that there is a nearly invariant 'shell' of the matrix material adjacent to inclusions and they suggested a strong dependence of the matrix densification rate on the ratio of the sizes of the inclusion and matrix particles; there being a greater decrease in densification rate with larger relative inclusion sizes.

The difficulties involved in the densification of ceramic composites lead to failure in achieving the predicted increases in fracture toughness associated with higher dispersed phase content. Decreases in the densification rates of SiC whisker composites have been found to correspond with increases in whisker volume fraction and attributed to an effective reduction in the quantity of sintering additive and formation of rigid whisker clusters that inhibit grain rearrangement [73]. SiC platelets do not impede densification processes as greatly as SiC whiskers and platelet-reinforced composites have even been fabricated by sintering at atmospheric pressure [66]. However, Baril and Jain [67] found that under hot-pressing conditions of 55 MPa and 1500°C, it was not possible to densify fully a SiC-Al_2O_3 matrix with SiC platelet volume fractions above 30 wt%. Possibly as a result of this, the observed trend of increasing fracture toughness with increasing platelet content suffered an abrupt reversal for a SiC content of 40 wt%.

2.2.4 *Fabrication of Hybrid Composites*

An alternative method of toughening is provided in laminated ceramics which have different bulk and surface compositions in a structural arrangement designed to optimise the fracture toughness and strength. Another advantage offered by a laminated construction is that more economical use can be made of the hard, expensive phases in cutting tools. In one example, a laminate was fabricated by alternately slip casting slurries with different particulate sizes to build up a laminated structure of alternating bands with different porosity levels [74]. This led to improvements in the strength of monolithic Al_2O_3 ceramics. The contribution made by the laminated structures to fracture toughness arises from delamination of the interfaces between adjoining laminae, as observed by Clegg *et al.* [75, 76]. In their experiments, individual (tape-cast) laminae were coated with graphite to prevent strong interlaminar bonding and this resulted in a fourfold increase in toughness (as compared to non-laminated material).

The fracture toughness of ceramics can be enhanced by combining the microstructural toughening mechanisms in composites with toughening due to a laminated construction, for which the stress profile variations can be controlled by the arrangement of laminae with different thermal expansions and relative thicknesses. For example, Kragness *et al.* found that SiC whisker/Al_2O_3 laminated composites (fabricated by tape casting) showed an increased strength for composites with a higher volume fraction of SiC (of lower thermal expansion than Al_2O_3) in the surface layers than in the bulk material [77], as this introduced beneficial compressive stresses in the surface layers. The tape casting technique is a well-established process in the fabrication of fibre-reinforced composites [44], but has more recently been applied to expanding the structural possibilites for dispersed-phase composites. An additional advantage offered by this technique is the alignment of anisotropic particles with the direction of casting (as well as in the plane of the tape, as is obtained from slip casting).

An interesting alternative has been suggested for fabricating SiC-Si_3N_4 ceramics with a compositional gradient. Dongliang *et al.* [78] HIPed a pre-sintered SiC ceramic in a nitrogen atmosphere to cause transformation of the surface SiC to Si_3N_4. The induced surface stresses led to improved strength and fracture toughness.

2.3 CERAMIC FABRICATION AT ULTRA-HIGH PRESSURES

2.3.1 *Introduction to Ultra-High Pressure Fabrication*

The materials that are usually fabricated under extremes of ultra-high pressure (UHP) are sintered masses of diamond and cubic boron nitride (cBN) for the production of superhard, industrial cutting tool materials. Pressures of a similar magnitude to those used in diamond or cBN synthesis are necessary to maintain their thermodynamic stability at high sintering temperatures, so preventing reversion to soft, graphitic phases.

In most commercial UHP apparatus the diamond or cubic BN powders used to prepare the superhard composites are encapsulated in a deformable, high melting point material (usually tantalum). This is immediately surrounded by a solid 'pressure-transmitting' medium inside a high pressure capsule that is uniaxially compressed during the fabrication process. Materials which are typically used as 'pressure-transmitting' media are sodium chloride [79], boron nitride (hexagonal phase), and pyrophyllite [80-82] (an alumina silicate), selected according to the criteria discussed in reference [83]. However, the use of solid 'pressure-transmitting' media prevents the attainment of truly hydrostatic pressures inside the high pressure capsule and also provides a major source of difficulties in the calibration of effective fabrication pressures. Pressure calibration is additionally complicated by any structural changes in the 'pressure-transmitting' media, such as volume expansion or phase transitions which may occur at the extreme pressure and temperature conditions.

Temperature measurement inside the capsule is inhibited by the practical difficulties of passing thermocouples into the high pressure region and then protecting them against mechanical failure. Another problem encountered in temperature measurement is defining the influence of UHP on the thermocouple e.m.f. [84].

In general, progress in the determination of exact processing conditions has been constrained by the many factors involved. High pressure equipment is usually calibrated using the pressure-induced electrical phase transitions of bismuth to provide reference points [85], sample capsule temperatures being estimated from the input heating power.

2.3.2 *Cubic Boron Nitride*

Cubic BN (cBN) was first synthesised from hexagonal BN (hBN) in 1957 [86] following speculation concerning an analogy between the structural forms of carbon and boron nitride. Hexagonal BN (hBN), a soft refractory and lubricant, has a similar crystal structure to graphite while cubic BN has a diamond-like structure. The analogy between carbon and boron nitride was carried further in 1963 [87] by the discovery of a hexagonal BN phase with the 'wurtzite' crystal structure common to meteoritic diamonds [88]. In the cubic BN crystal lattice, boron and nitrogen atoms are tetrahedrally co-ordinated from the intersection of two separate, face-centred-cubic sublattices for boron and nitrogen atoms. This crystal arrangement is also shared by zincblende (β-zinc sulphide). The relationship between the crystal structures of BN is illustrated in figure 2.7 (below).

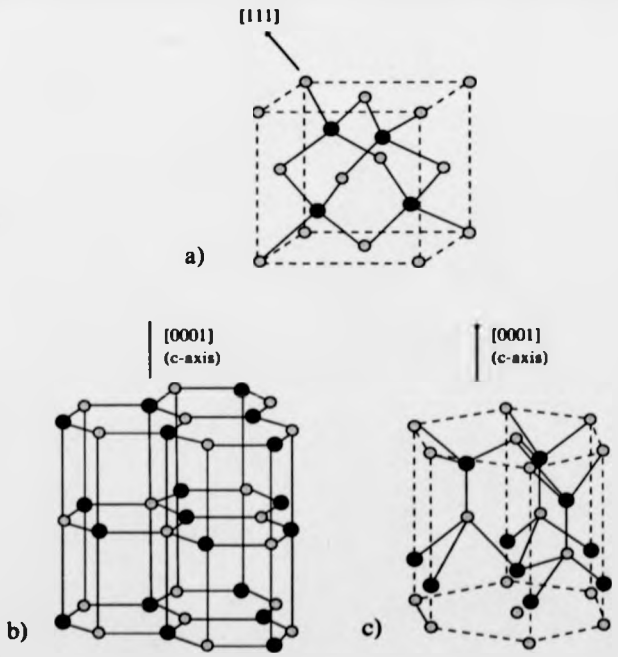

Figure 2.7 : Crystal structures of boron nitride:
(a) cubic BN, (b) hexagonal BN, (c) wurtzitic BN

(i) Properties of Cubic BN

The cubic phase of BN, second only to diamond in hardness, has an excellent combination of physical and chemical properties that make it eminently suitable as a 'superabrasive' or cutting tool material. In such applications, cBN has advantages over diamond, being more resistant to chemical reaction in ferritic environments. The early experiments [86] showed that cBN is a good electrical insulator, is not attacked by the more common acids, scratches and is scratched by diamond and is only slowly oxidised in air, at about 2000°C. Other properties are given in the following table.

Table 2.1: Physical Properties of Cubic Boron Nitride

PROPERTY	CUBIC BN	DIAMOND	REFERENCE
Lattice Parameter	3.6157 ± 0.001 Å		[89]
Crystal Space Group	$F\bar{4}3m$	Fd3m	[86]
Density	3.487 ± 0.003 g/cm^3	3.515 ± g/cm^3	[89,86]
Microhardness (Vickers)	60 - 75 GPa	120 GPa	[90]
Linear Thermal Expansion x 10^{-6} K^{-1}	200 K: 0.50 400 K: 1.80 600 K: 3.23 800 K: 4.70 1000 K: 5.96 1200 K: 6.45	200 K: 0.45 400 K: 1.79 600 K: 3.17 800 K: 3.81 1000 K: 4.38 1200 K: 4.93	[91]
Thermal Conductivity	1300 W/m K (theoretical) 200 - 900 W/m K	2000 W/m K	[92] [93, 94]
Young's Modulus	890 GPa		[95]
Poisson's Ratio	0.138		[95]
Compressive Strength	450 MPa		[96]
Stability in Air	oxidation begins in air at 2.1 x 10 Pa and 950 K 6.67 Pa and 1000 K		[97]
	apart from surface oxidation, stable in air at 1300 K for 30 mins.		[96]

(ii) The Boron Nitride Phase Diagram

The boron nitride phase diagram was first determined by Bundy and Wentorf [87] from their studies of direct, non-catalysed transitions of hBN to denser phases under ultra-high pressures. A direct phase transition to the cubic BN phase involves thermal disruption of the hBN atomic lattice and the reformation of bonds under cBN-stable conditions. Wakatsuki *et al.* [96] showed that less extreme conditions are needed for this phase transition if the starting powder has a poorly defined crystal structure which lowers the high transformation energy barrier.

The boron nitride phase relationships can be determined in studies of 'direct' transitions since the presence of catalysts causes a displacement of the phase equilibrium boundary line. In a patent describing the uncatalysed conversion of hBN to cBN, Sirota and Mazurenko [98] claimed that the phase boundary between hBN and cBN as given by Bundy and Wentorf should be shifted towards higher temperatures. This finding met agreement with investigations of BN phase transitions by Corrigan and Bundy [99] who used both static pressures and shock-compression methods and also the results of Corrigan [93] in the conversion of pyrolytic BN to cBN. The phase diagram determined by Corrigan and Bundy is given in fig.2.8. In this diagram, the hBN-cBN equilibrium line is parallel to the graphite-diamond equilibrium boundary, a feature that is disputed by Solozhenko [100, 101]. Taking experimental data on the thermodynamic characteristics of cBN, Solozhenko calculated the position of the hBN-cBN equilibrium line and concluded that it should intersect the temperature axis at 1570 K rather than the pressure axis at 1.3 GPa. Solozhenko suggests that cubic BN is the stable phase under low pressures and is wrongly represented as a metastable state.

The determination of a thermodynamically stable region for the wurtzitic BN phase is still unclear. Wurtzitic BN has been obtained under both static pressures [102] and by shock compression [99] in a diffusionless ('martensitic') transformation from hBN, but it has been concluded that this phase is probably thermodynamically unstable [100,102]. Tani *et al.* [102] reported that wBN transforms to hBN between 1200 and 2200 K in pressure regions where cBN is the stable phase.

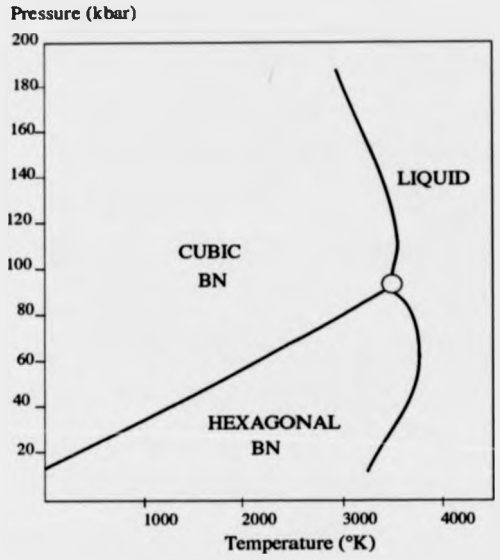

Figure 2.8 :Boron Nitride Phase Diagram

(iii) Catalytic Synthesis of Cubic BN

The initial synthesis of cBN was by direct conversion from hBN under simultaneous conditions of 85000 atmospheres and 1800°C [86]. However, it was later discovered that the high activation energy barrier for the phase transformation could be reduced with the aid of a catalyst such as the alkali, alkaline earth metals and their nitrides [103,104]. The phase transformation then occurs by chemical dissolution of the hBN followed by precipitation of BN in the cubic form. Commercial cBN production takes place by catalytic synthesis and has stimulated wide-ranging research to determine a lower pressure limit for cBN synthesis. The main considerations involved are the minimum temperature at which a solvent can dissolve hBN and the cubic-hexagonal phase boundary. Some of the more unusual catalysts that have been effective in cBN synthesis include water, urea, ammonium nitrate and boric acid [105,106].

2.3.3 *Fabrication of Cubic Boron Nitride Composites*

The fabrication processes for cBN aggregates can be divided into two groups: (i) spontaneous sintering of cBN formed during synthesis from hBN and (ii) sintering powdered cBN (starting phase), usually with a binder phase.

Polycrystalline cBN fabricated from direct, uncatalysed conversion of hBN has been reported to have extremely high wear resistance [98], very high Vickers' microhardnesses (60-70 GPa) [90] and thermal conductivities as high as 9 W/cm°C [93] that approach the theoretical prediction of 13 W/cm°C for a single crystal [92]. The excellent physical properties are attributed to the absence of any other phases that may degrade the material. However, this fabrication process generally requires pressures above 60 kbar and temperatures exceeding 1800°C whereas less extreme conditions can be used to produce a cBN material which has secondary, binder phases. Such materials can be fabricated by spontaneous sintering during the catalysed conversion of hBN or by embedding cBN in a metal or resin matrix.

Polycrystalline cBN can be fabricated with properties that can be modified for specific applications by the judicious choice of catalysts for cBN synthesis. Examples include the fabrication of a light-transparent material [107], also of high hardness (57-64 GPa) obtained using catalysts formed from lithium or alkaline earth metals that were reported to achieve this result by uniformly diffusing into the initial hBN powder. A cBN material of fairly high thermal conductivity (6.5 W/cm°C) and extreme hardness (60-65 GPa) resulted from hBN conversion catalysed by an alkaline earth metal hydroxide [108]. Aluminium nitride is also reported to be a good catalyst, allowing the synthesis of cBN together with formation of a strongly bonded material [109]. Another cBN material of high hardness (51 GPa) has been produced using an ammonium nitrate catalyst, to promote hBN transformation with seed crystals of cBN (to promote direct bonding between cBN grains) [110].

The physical properties of these composites and the conditions required for their fabrication are summarised in table 2.2.

Table 2.2: Fabrication conditions and properties of catalytically-synthesised cBN composites

Fabrication Conditions	Catalyst	Properties	Reference
6.5 GPa, 1800 - 2000°C,	none	thermal conductivity, 9 W/cm°C	[93]
5 - 7 GPa, 1550°C, 30 mins.	lithium or alkaline earth metal nitrides or their compounds with BN	Vickers microhardness, 57 - 64 GPa Light-transparent.	[107]
5.5 GPa, 1500°C, 30 mins.	alkaline earth hydroxide	microhardness, 60 - 65 GPa	[108]
5 -7 GPa, 800 - 1700°C, non-oxidising atmosphere, 15 mins.	aluminium nitride	thermal conductivity, 6.5 W/cm°C	[109]
7 GPa, 1700°C, 30 - 60 mins.	ammonium nitrate	Vickers microhardness 51 GPa (average)	[110]

Industrial cBN tool materials are usually produced under slightly less extreme conditions (3-5 GPa, about 1300°C) by sintering a layer of cBN powder with a metallic binder and supported by a Co-bonded substrate of tungsten carbide that can easily be welded onto cutting tool equipment. Fukunaga *et al.* [111] investigated the phases formed when cBN was sintered with a cobalt-aluminium alloy on a cobalt-tungsten carbide substrate. Coarse grains of cobalt were found to have penetrated the pores, helping to prevent the cBN from reverting to hBN and a $Co_{23}B_6$ compound was identified at cBN grain boundaries. A typical binder phase for cBN tool materials is formed from aluminium. As the aluminium melts during the fabrication process it penetrates intergranular pore space and partially reacts with the cBN grains. Walmsley [112] identified the resultant intergranular phase in such a material as a mixture of AlN and AlB_2 that isolates each cBN grain and so prevent direct cBN-cBN bonding.

2.3.4 *Cubic boron nitride / Silicon nitride composites*

The use of silicon nitride as a catalyst for conversion of hBN to cBN is described in a patent of 1976 [113]. Claimed advantages are in the greater ease of handling such a catalyst which is more environmentally stable compared with the alkaline and alkaline earth metals typically used. Silicon nitride can also provide a hard, refractory binder phase for cBN, but the direct sintering of these two covalent

materials requires higher temperatures than those normally used in industrial cBN processes. A refractory, abrasive cBN composite has been patented [114] for which the matrix phase formed from reaction of α-Si_3N_4 powder with residual aluminium, present as a solvent material to aid bonding by partial dissolution of the cBN grains. Silicon nitride has also been consolidated with cBN by shock compaction [115] of a mixture of Si_3N_4 whiskers and cubic BN powder. The resulting material, of high microhardness (50 GPa), was reported to be bonded by a network of highly deformed whiskers.

Further investigations on the cBN-Si_3N_4 composite system have been made to examine the influence of different starting materials and fabrication conditions on the properties of the composite produced. The phases of BN and Si_3N_4 that have been used as the initial precursors for cBN-Si_3N_4 composites are wurtzitic BN, sintered with α or β Si_3N_4 [116] and 'turbostratic BN' (a randomly orientated hexagonal layer structure), sintered with either amorphous Si_3N_4 or β-Si_3N_4 [117]. In the research discussed in chapter five of this thesis, the initial ceramic phases used in the composite fabrication were cBN and an α-Si_3N_4-based matrix.

Gromyko *et al.* [116] converted powder mixtures of wBN, α and β-Si_3N_4 to cBN and β-Si_3N_4 (under 7.7 GPa and 1750°C) to investigate the possibility of Si_3N_4 forming a 'solid solution' with cBN. Evidence of a small amount of silicon dissolution into the cBN lattice was detected via a slight increase in the crystal lattice constant (as measured by X-ray diffraction), reported to be comparable with results they obtained from the interaction of cBN with powdered silicon under similar conditions.

Experimental cBN-Si_3N_4 composites (of mm dimensions) have been fabricated under 8-10 GPa and 1600-2200°C from starting mixtures of (i) amorphous Si_3N_4 and (ii) β-Si_3N_4, incorporated into the turbostratic BN structure (expanding the interlayer distance) by means of a chemical vapour deposition process [117]. These experiments revealed that the presence of Si_3N_4 in turbostratic BN increased the temperature necessary for cBN formation and identified 1400°C as the lowest possible temperature for crystallisation of β-Si_3N_4 and cBN phases. It should be noted that this conflicts with the catalytic behaviour of Si_3N_4 that was suggested by Kabayama [113].

Table 2.3 summarises the properties of the cBN-Si_3N_4 composites reviewed.

Table 2.3: Fabrication conditions and properties of cBN-Si_3N_4 composites

Final Phase Composition	Sintering Conditions	Hardness (Vickers)	Other Properties	Reference
cBN and β-Si_3N_4(10.6 wt%)	10 GPa, 1600°C, 10 mins.	49 - 60 GPa		[117]
	8 GPa, 1700°C, 10 mins.	46 - 57 GPa		[117]
	8 GPa, 1600°C, 10 mins.	45 - 56 GPa	Fracture toughness above 5.5 $MPam^{1/2}$ Young's modulus, 570 GPa	[117]
85 wt% cBN, 15 wt% Si N	Dynamic shock compaction	50 ± 13 GPa		[115]
80 wt% cBN 20 wt% SiC	Dynamic shock compaction	34 ± 14 GPa		[115]

2.3.5 *Consolidation Mechanisms of Polycrystalline Cubic Boron Nitride*

The sintering of polycrystalline cBN materials requires the application of ultra-high pressures in order to maintain the thermodynamic stability of the cubic phase. Under particularly high sintering temperatures and less extreme pressures, the cubic phase would be converted into hBN, degrading the physical properties of the final product. The extreme hardness of the cubic BN phase prevents the externally-applied pressures from being evenly supported by the grains and results in voids of localised low pressure inbetween the grains. In the fabrication of many cBN materials, suppression of a cubic to hexagonal BN phase transformation in these voids is achieved by the infiltration of a secondary, liquid phase. However, in the absence of sufficient liquid phase to fulfil this role, BN phase transformations play an important part in promoting full densification with pore elimination. Gargin [118] established that the cubic to hexagonal phase transformation becomes reversed above a certain critical temperature because increasing amounts of hBN fill up the pores and lead to localised pressure increases. Unfortunately, this critical temperature was not identified since the experiments related to the input heating power rather than directly to the sintering temperatures. At higher temperatures, the particle consolidation surfaces are increased by plastic grain deformation which has been found to begin at about 1400 K and 8 GPa [119] in regions of grain contact. Shipilo *et al.* [119] found the dislocation density and extent of crystal lattice deformation to increase with sintering temperature and correlated these processes with observed increases in density, microhardness (reporting

values up to 100 GPa) and thermal conductivity. Deformed cBN grains have been described as exhibiting similar behaviour to that of face-centred cubic metals with low stacking fault energy [120], being characterised by a high density of interacting dislocations and bands of microtwin lamellae [112,121]. The plastic deformation is believed to arise from the high-pressure compaction process.

2.3.6 *Application of Ultra-High Pressures to Ceramic Sintering*

In addition to providing phase stabilisation during the fabrication of cBN or diamond-based composites, other possible benefits of UHP application have been investigated for the densification of polycrystalline, covalent ceramics. Conventionally, covalent ceramics can be fully densified only in the presence of a sintering additive which promotes liquid phase sintering and this can be assisted by pressure application. However, the quantity of the sintering additive required can be reduced when higher fabrication pressures are used. Since the presence of sintering additive residue is detrimental to the mechanical properties of the final material, densification using higher than usual fabrication pressures is of interest. UHP fabrication is believed to provide a means for fully densifying covalent ceramics without compromising their excellent intrinsic properties. Yeheskel *et al.* [122] estimated that full densification of Si_3N_4 could be achieved without additive phases at 1800°C and 250 MPa or 1600°C and 700 MPa from their studies of Si_3N_4 densification by HIPing. However, these conditions are too extreme for most HIP equipment.

Yeh and Sikora [31] achieved the fabrication of additive-free Si_3N_4 of greater than 95% theoretical density at HIPing conditions of 1760°C and 275 MPa, observing that the degree of densification in different specimens had some correspondence with the degree of α to β phase transformation of the Si_3N_4. The mechanism proposed for densification in the absence of a liquid phase was by the plastic deformation of the starting α-Si_3N_4 grains and the subsequent phase transformation to unstrained β-Si_3N_4 grains by the release of stored strain energy in the plastically deformed regions. Pejryd found the α to β Si_3N_4 transformation in HIPed, additive-free Si_3N_4 to be principally governed by temperature, requiring at least 1600°C to take place [123]. The β-Si_3N_4

grains formed did not have an acicular morphology and Pejryd suggested this to be due to the absence of a liquid phase which would allow preferentially-directed grain growth.

Shimada *et al.* [124] obtained theoretically dense Si_3N_4 under conditions of 1.5 GPa and 1600°C. Similar observations were made concerning the dependence of the degree of α to β-Si_3N_4 phase transformation on the densification as for HIPed, additive-free materials [123], lending support to the phase transformation mechanism proposed by Yeh and Sikora [31]. Shimada *et al.* [124] observed the fragmentation and agglomeration of the starting α-Si_3N_4 grains in ceramics fabricated at 3 GPa and 1400°C and also, evidence for the recrystallisation of plastically deformed α-Si_3N_4 grains in ceramics sintered at 1500°C (and 3 GPa). At higher temperatures (1550°C), the β-Si_3N_4 phase was observed to be predominant and a reduction in porosity was also noted. The values of fracture toughness, determined by indentation techniques, for additive-free Si_3N_4 ceramics fabricated under 1.5 - 3.0 GPa and 1500-1800°C ranged from 3.29 to 4.30 $MPam^{1/2}$ [125] with microhardness values of 15 to 21.5 GPa and the β-Si_3N_4 grains formed during fabrication were of an irregular, elongated morphology.

2.4 THE STRUCTURAL RELATIONSHIP BETWEEN POLYTYPES OF SILICON CARBIDE

2.4.1 *Silicon Carbide Crystal Structures*

Silicon carbide exists in numerous polytypes that have similar close-packed structures to the polymorphs of diamond and cubic boron nitride [126]. The main crystal phases are cubic (the 'β' form, with the zincblende structure) and numerous structural arrangements (over a hundred variations have been reported) with hexagonal or rhombohedral structures (collectively known as the 'α' polytypes) which differ from one another by the repeat sequence of silicon and carbon 'double layers' stacked along the crystallographic c-axis and hence, by the length of the c-axis lattice parameter.

The silicon and carbon atoms have a mutual tetrahedral co-ordination, common to all the polytypic structures. The 'double layer' comprises the (Si or C) atoms in the triangular bases of the tetrahedra (in the basal planes) and the planes of (C or Si) atoms

in the centres of the tetrahedra. The atomic distance between these two layers is shorter than that between the planes of the central atoms and the atoms at the height of the tetrahedra. Hence, slip on the basal planes can occur either between the more closely spaced planes of the double layer ('glide' planes) or between the widely spaced planes ('shuffle' planes) [127].

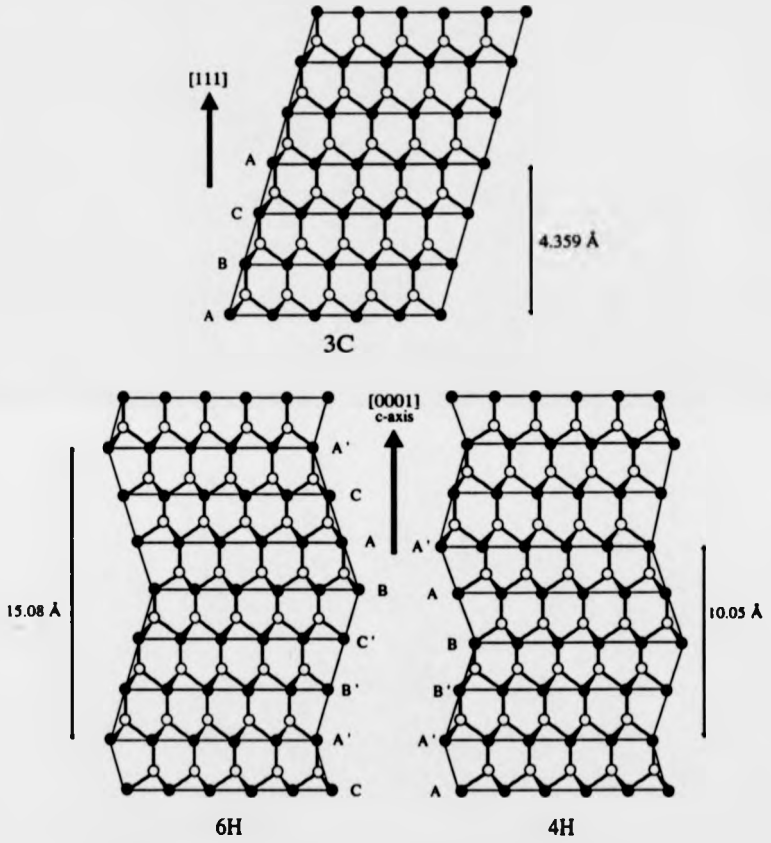

Figure 2.9: Crystal structures of the cubic (3C) polytype and the 4H and 6H hexagonal polytypes of SiC, viewed normal to the c-axis.

2.4.2 *Relative Polytypic Phase Stabilities*

The cubic phase of SiC has become well known as being thermodynamically less stable than the other polytypes and was found by Baumann [128] to transform to the 'alpha' polytypes at temperatures above 2000°C and atmospheric pressure. Sokhor *et al.* [129] investigated a possible analogy between the phases of SiC, BN and carbon

and established that the reverse hexagonal to cubic transformation could be obtained in SiC at 3-7 GPa, similar to the phase transitions which occur in hBN and graphite at ultra-high pressures. Cubic SiC has also been identified as the phase which formed from reaction between silicon and diamond during the commercial UHP sintering of a diamond compact [130], providing further evidence for cubic SiC being the 'high pressure phase'. One explanation for the origin of the numerous hexagonal polytypes is demonstrated by the apparent ease of stacking fault formation in SiC, as the higher-order polytypes can be regarded as a regular arrangement of stacking faults in a parent structure. For the 6H polytypes, the energy of stacking fault formation has been evaluated to be 2.5 ± 0.9 mJ/m^2 [131]. The compatible existence of several different polytypes is demonstrated by the intermixing of the 4H, 6H, 15R and 21R polytypes, bounded by planar interfaces, within individual SiC platelets (Alcan International Ltd.) [132].

2.4.3 *Plastic Deformation in Silicon Carbide*

Maeda *et al.* [131] observed that the main defects introduced by the plastic deformation of 6H SiC crystals were dislocations on the basal planes with a Burgers vector of $^a/_3$ $[11\bar{2}0]$. The dislocations were dissociated into Shockley partial dislocations, separated by wide bands of stacking faults, for which the dissociation reaction is described by the equation

$$^a/_3\,[11\bar{2}0] \rightarrow {}^a/_3\,[01\bar{1}0] + {}^a/_3\,[\bar{1}010]. \qquad (2.2)$$

Maeda *et al.* observed crystal slip which arose from dislocation glide on the basal planes and led to the formation of stacking faults with widths determined by the mobility of the partial dislocations. The primary slip system above 1000°C was identified as being (0001) $<11\bar{2}0>$ [131]. Suematsu *et al.* [133] made observations that were consistent with this from their experiments in which hexagonal single crystals were compressed parallel to the basal plane at varying temperatures. As a result, dislocation-induced 'kink' boundaries and cracking were obtained at temperatures above 1000°C, in addition to slip deformation on the basal planes.

2.5 THE SPECIFIC RESEARCH OBJECTIVES

The overall objective of this research programme was to create novel composites with high hardness and enhanced fracture toughness. Two parallel composite systems were investigated, with dispersed phases of SiC platelets and cBN particulates. In these composites, the Si_3N_4 phase was to be considered both as a matrix phase (where the dispersed phase concentrations were below 50 wt%) and as a binder phase (where the dispersed phase concentrations exceeded 50 wt%).

One aim of this project was to identify a means of overcoming the limitations imposed on the mechanical properties of SiC_p-Si_3N_4 composites by current processing methods. To this end, two new approaches were considered. The first approach was to combine the microstructural composite toughening mechanisms (discussed in this chapter) with toughening due to the construction of a laminated composite structure. This could be achieved using the green state 'tape casting' technique and conventional hot-pressing. The second approach was to explore the potential benefits offered by ultra-high pressure sintering, possibly providing a means to counteract the detrimental stresses opposing the sintering of composites with large SiC volume fractions (section 2.2.3). The phase stability of the SiC platelets at extreme processing conditions was also to be investigated, as an additional part of these experiments.

The objectives in fabricating cBN-Si_3N_4 composites were to investigate the promising microhardness values reported in the research reviewed in section 2.3.4 and to establish whether the combination of cBN and Si_3N_4 would indeed result in a composite with superior mechanical properties to those of cBN composites which are commercially available. The fabrication experiments were mainly to involve larger-scale, commercially-based apparatus rather than the more exploratory apparatus of the other research reviewed in this chapter. A second difference between this research and that reviewed is in the selection of the precursor ceramic phases for the fabrication experiments. The cubic BN phase was used as a starting material, to be sintered with the Si_3N_4-based matrix as a dispersed, inclusion phase. Hence, the ultra-high fabrication pressures were principally required to maintain the thermodynamic stability of the precursor cBN and not to effect any BN phase transformation.

Chapter Three

EXPERIMENTAL MATERIALS AND TECHNIQUES

This chapter presents details of the experimental procedures involved in this research, ranging from the different fabrication methods explored to the techniques used for the physical and microstructural analysis of the fabricated materials.

3.1 POWDER PROCESSING

The starting materials for ceramic fabrication carried out during this research were commercially obtained powders of high chemical purity. The powder specifications are given in table 3.1.

Table 3.1: Data for the ceramic starting powders (as provided by the manufacturers).

Powder	Manufacturer	Grade	Impurities	Average size	Other information
Si_3N_4	UBE, Japan	SN-E10	O: 1.55 wt% Cl: <100 ppm Fe: <100 ppm Ca: <50 ppm Al: <50 ppm	0.2 μm	Crystallinity above 99.5 wt% Proportion of β-phase: <5 wt% α-phase: >95 wt%
SiC	C-Axis Technology (Canada) Ltd.	F [medium]	O: 0.14 % Fe: 0.01 % Ti: 0.003 % Ca: 0.004 % Al: 0.43 % Mg: 0.001 %	17 μm	4H and 6H polytypes
cBN	De Beers, Ireland	PCABN Grades 3 and 9	Ca: <500 ppm	3 μm 9 μm	
Y_2O_3	London & Scandinavian		Ca: <20 ppm Other rare earth oxides:<20 ppm		>99.99 % pure
SiO_2	Pilkington	Limoge Quartz	K_2O: 40 ppm Na_2O: 60 ppm Li_2O: 2 ppm Al_2O_3: 160 ppm Fe_2O_3: 10 ppm		

3.1.1 *Preparation of the Silicon Nitride-based Ceramic Matrix Phase*

A Si_3N_4-based composition was used as the 'matrix' phase for all the composites fabricated although the volume fraction of this phase was varied considerably for different ceramic composites. The matrix phase was prepared from a mixture of Si_3N_4 with sintering additives of Y_2O_3 and SiO_2. The precise quantity of each sintering additive present was determined after examining the Si-Y-O-N phase diagram (figure 2.3). The starting composition of the matrix phase was arranged to lie in the region where formation of the most refractory yttrium silicate phases was expected. An enlarged corner of this phase diagram is given in figure 3.1, where different phase compositions are represented as a function of two variables. From these, the atomic percentages of each element can be calculated. Composition 'M', the matrix phase selected for this research, was prepared from a mixture of 94 wt% Si_3N_4 (UBE) powder, 5 wt% Y_2O_3 and 1 wt% SiO_2 after taking account of the surface SiO_2 already present on Si_3N_4 grain surfaces (Appendix A).

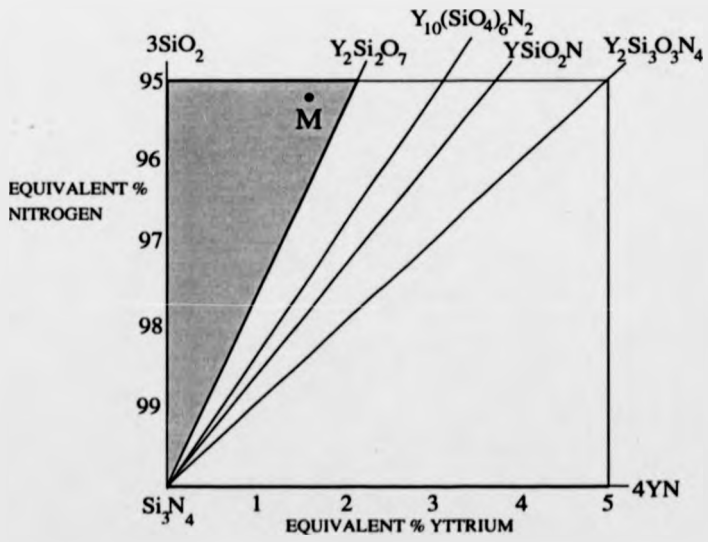

Figure 3.1: Enlarged corner of the Si-Y-O-N phase diagram, taken from figure 2.3.

The constituent powders for the matrix phase were ball milled together to crush powder agglomerates and ensure an even distribution of the sintering additives. Milling

media of a composition 95 wt% Si_3N_4, 5 wt% Y_2O_3 (fabricated by HIPing to a high density at ABB, Sweden) were used in order to minimise powder contamination from media 'pick-up'. The matrix powder was milled in batches of 100 g, with 100 g milling media and about 250 ml propan-2-ol inside polythene jars that were continuously rotated for 24 hours. After this time, the powder suspension was dried in an oven at 100°C and subsequently sieved (through a 50 μm sieve) to crush any soft agglomerates formed on drying. The starting matrix powder was then ready for combination with other phases (SiC platelets or cubic BN powder).

3.1.2 *Preparation of Green State Composites and Slip Casting*

Various powder mixing processes have been tried during the course of this research. The reasons for this were to optimise the final ceramic homogeneity by improving the mixing of component phases and limiting agglomeration of the submicron particles. Early attempts to introduce dispersed phases to the matrix powder included dry-mixing (vigorously agitating the powders in a polythene jar) and the powders were then compacted into pellets under 0.5 MPa (using a hand-operated press). However, the dry-mixing method was proved inadequate by the observation of large agglomerated regions (several hundreds of microns across) on polished surfaces of finally consolidated material. Wet-mixing methods were then employed for all remaining composite fabrication. The green state composites to be sintered at ultra-high pressures were prepared using the 'slip casting' technique which is described in the following.

A slip was formed by dispersing the ceramic powders in distilled water (75 % powder, 25 % water, by weight) and a few drops of aqueous ammonia were added to increase the slip pH to effect a marked reduction in the slip viscosity (associated with optimum particle deflocculation). The pH values required to lower the slip viscosity were determined experimentally. For dispersions containing the Si_3N_4-based matrix powder alone, ammonia was added until the slip reached pH 9, but when either cBN powders or SiC platelets were added to the matrix phase, this value was raised to a value between 11 and 12. Although a further reduction in slip viscosity could be

obtained with still higher pH values, the coarser phases (SiC platelets, cBN particles) then became distinctly separated from the submicron matrix powders which tended to settle at the bottom of the suspension. A 'shear blender' (designed to crush particle agglomerates in suspensions) was used to mix the ceramic powders evenly and then the slip was 'outgassed' in a vacuum desiccator. Finally, the slip was cast into a mould with a porous base (plaster of Paris), covered and left to dry at room temperature (a slow drying procedure was necessary to prevent severe cracking).

3.1.3 *Tape Casting*

Tape casting is a wet-forming technique which produces organically-bonded sheets of ceramic powders, flexible enough for easy handling. Particular advantages of this technique are good powder homogeneity, the ability to fabricate tapes of controlled and uniform thickness, and some degree of alignment of anisotropic particles (which takes place as they are dragged beneath the 'doctor blade'). In contrast, a disadvantage of tape casting is the difficulty in complete removal of the organic tape components prior to ceramic sintering. This is essential because any residual carbon presence may inhibit the powder sintering [134].

The tape casting procedure involved the suspension of ceramic powders in an organic medium to form a tape slurry which was passed under a knife (or 'doctor') blade and onto a moving (at 5 cm/s), non-porous carrier sheet ('mylar'™ film). As the solvents evaporated, thin layers of flexible tape remained and these were peeled from the carrier sheet and cut into the shapes desired. The drying was not assisted by heating. Figure 3.2 illustrates the experimental arrangement.

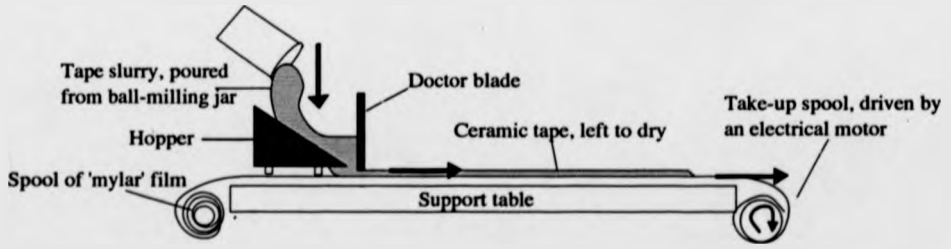

Figure 3.2: Apparatus used for the tape casting of ball-milled, ceramic powder suspensions.

The organic tape components are described separately in the following section.

(i) *Polymeric Binder*

This was the main component with which all the other slurry constituents were required to be compatible. The role of the binder (usually an organic polymer) was to coat the surfaces of the ceramic particles and bond them into an organic tape. Two important properties of the binder were its decomposition into non-toxic gases, with no residual ash, on heat treatment and the ability to form a tape with reasonable tensile strength (for ease of handling). An acrylic resin was selected as a suitable binder. The resin chosen was one made by Du Pont (5200 MLC binder†, developed to form dielectric ceramic tapes) with the composition 62.3% ethyl methacrylate, 37.1% methyl acrylate and 0.6% methyl methacrylate. This had been dissolved to form 30% of a solution in methyl ethyl ketone (butanone) [135].

(ii) *Plasticiser*

The role of the plasticiser (lower molecular weight than the binder) was to impart flexibility to the dry, ceramic tape by reducing intermolecular forces between the polymer chains of the binder [136] so as to lower the glass transition temperature of the binder and increase the molecular mobility. A compatible plasticiser with the binder selected was Monsanto Santisiser 160 (butyl benzyl phthalate, Central Solvents, USA) .

(iii) *Powder Dispersant*

A powder dispersant was required in the slurry to maintain a stable powder suspension. This could be achieved by steric stabilisation, where dispersant macromolecules with long polymeric chains become physically attached to the powder surfaces, by Coulombic repulsion or by a combination of these mechanisms. The dispersants used in these experiments were 'Hypermer'™ (ICI) compounds 'KD1' and 'KD2' (which are weakly cationic polyoxyalkylene amine derivatives). A claimed advantage of these compounds over the commonly used fatty acid dispersants is a thicker (steric) stabilisation barrier due to their relatively high molecular weights [137].

(iv) *Solvents*

A mixture of two solvents, with relatively low boiling points, were used to optimise the solubility of the binder in the slurry and easily dissolve all the other components. The solvents selected were 1,1,1 trichloroethane and ethanol.

† No longer commercially available. A suggested replacement product is B7 Acryloid, Chemacryl.

3.1.4 *Thermogravimetric Analysis*

The heating cycle for burning out the organic components of tape-cast ceramic sheets was devised with the aid of thermogravimetric analysis (TGA), using a Stanton Redcroft TG-750 unit equipped with a microfurnace, electronic microbalance and temperature programmer. Small pieces of the ceramic tape (usually of a few mg) were positioned inside a platinum crucible lined with alumina (to prevent reaction between the platinum and nitrides in the specimen) and suspended on a hanging platinum stirrup. The weight of the specimen was balanced against counterweights in order to cause maximum deflection on the electronic microbalance. The microfurnace was drawn up around the specimen and the heating rate was set at 1°C/min. Changes in temperature (measured by a 20%:40% rhodium-platinum thermocouple inside the furnace) and specimen weight with time were recorded on a pen chart recorder.

3.2 HOT PRESSING

Green state ceramic composites were consolidated under pressures of about 20 MPa using a conventional hot pressing technique where the ceramic powders were heated and compressed inside a graphite die (figure 3.3).

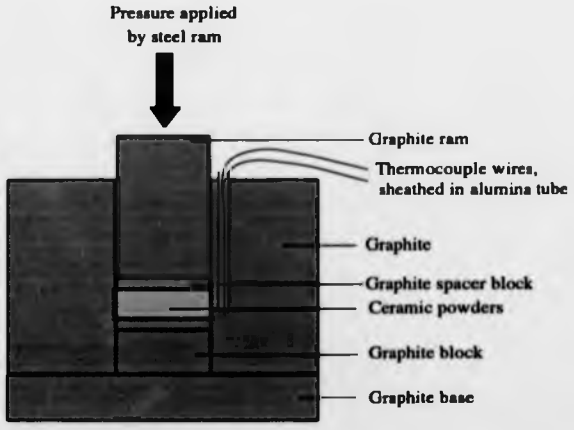

Figure 3.3: Construction of the graphite die in which ceramic powders were sintered.

The die interior was lightly coated with fine boron nitride (hexagonal) powder to provide an inert layer between the graphite and the specimen powders and also to facilitate specimen removal after the hot pressing. When the die had been assembled, it was centrally positioned inside a water-cooled copper coil and inductively heated by a radio frequency (r.f.) field supplied by an r.f generator (Radyne, UK, 30 kW) that was coupled to the copper coil. Insulation was provided by coarse alumina powder ('bubble' alumina) used to cover both the copper coil and the graphite die. A 20%:40% rhodium-platinum thermocouple was used for the temperature measurement. The rate of heating was usually 25 °C/minute. The final temperature reached during sintering could be altered by varying the power from the r.f. generator.

Pressure was applied to the ceramic powders by means of a steel ram operated by a hydraulic pump (Enerpac BPE 3000-173) and in alignment with the graphite ram in the die. The pressure was first applied when the specimen temperature reached 1000°C and then gradually increased with temperature until the full hot pressing conditions were reached. The actual pressure applied to the specimen was calculated from a gauge reading of the pressure applied to the steel ram and the cross-sectional area of the graphite ram, under the assumption that negligible pressure losses were caused by friction between the graphite ram and die walls. A linear displacement transducer connected to a pen chart recorder was used to monitor the movement of the steel ram and hence, the initial thermal expansion and subsequent densification of the ceramic powders being compressed. The full hot pressing conditions were maintained until the powder densification was complete (usually 1-2 hours). This was indicated by no further steel ram movement. However, one possible source of error was attributed to thermal expansion of the steel ram which inevitably became hot after a few hours in close proximity to the graphite die. On completion of the hot pressing cycle, the r.f. power was immediately switched off and the graphite die was allowed to cool naturally.

3.3 ULTRA-HIGH PRESSURE FABRICATION

Ceramic fabrication under pressures above 3 GPa was undertaken in two systems that operate on similar mechanical principles: (i) 'belt' apparatus and (ii) a

tetrahedral anvil system. The belt apparatus, used for the commercial synthesis of diamond and cubic BN, was able to accommodate the larger sample volumes, but lacked a means of temperature measurement. Conversely, despite the limited specimen sizes fabricated (a few mm in height and diameter), in the tetrahedral system the sintering temperatures could be monitored more accurately using a thermocouple.

3.3.1 *Ceramic Fabrication using the Belt Apparatus*

Green state composites to be densified in the 'belt' apparatus were encapsulated in tantalum and embedded in the solid 'pressure-transmitting' medium of a high pressure sintering capsule. This capsule was positioned in the pressure chamber between two cylindrical, tungsten carbide (high compressive strength) anvils.

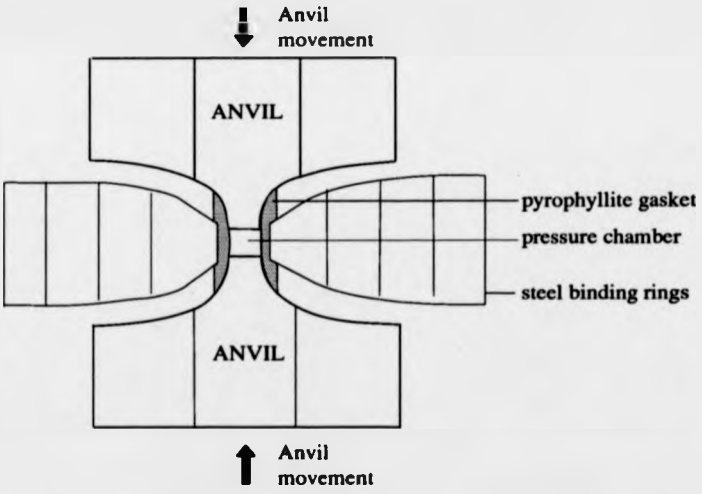

Figure 3.4: Cross-section of the ultra-high pressure 'belt' apparatus, after [138]

Mechanical support for the (highly stressed) anvils was provided by the 'belt' of hardened steel rings that encircled the anvils and the pressure chamber. The chamber was sealed on compression of the surrounding pyrophyllite gasket as the anvils moved inwards and this led to the generation of ultra-high pressures.

Figure 3.5 shows the components of a typical (salt-based) sintering capsule. The role of the pressure-transmitting medium (salt) was to convert the uniaxial

compressive stresses applied to the capsule into a stress acting uniformly on the specimen. However, in practice, non-uniform stresses and hence, pressure gradients often existed in this medium. (Modifications made to the construction of the high pressure capsule are discussed in chapter five.)

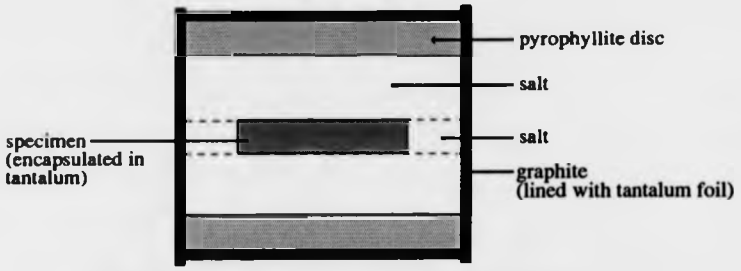

Figure 3.5: Cross-section of a typical sintering capsule with salt as the 'pressure-transmitting medium'.

In all fabrication experiments, the specimens were pressurised to the desired pressure level before the temperature was raised to promote sintering. The specimens were heated by passing a large electrical current (few thousand amps) through a graphite heater sleeve around the high pressure capsule to heat the interior. The temperature was controlled by the power input and largely uncalibrated. Full pressure and power levels were maintained for dwell times ranging from 10 to 70 minutes, such times being occasionally restricted by the necessity to prevent the anvils from becoming too close together (during ceramic densification or contraction of the specimen capsule on cooling) as this would make the apparatus unstable. On completion of the experiment, the crushed capsule was retrieved and broken apart to release the specimen inside.

3.3.2 *Ceramic Fabrication in the Tetrahedral Anvil System*

The tetrahedral anvil system, fully described in reference [139] comprises (i) four tungsten carbide anvils with triangular end faces (fig. 3.6 a) that fit together to define a central, tetrahedral pressure chamber and (ii) a tetrahedral pyrophyllite block, slightly larger than the pressure chamber. Ultra-high pressures are generated on compression of a pyrophyllite gasket, formed by the extrusion of the excess pyrophyllite

into gaps between the anvils, which seals the pressure chamber. A boron nitride (hexagonal) sample capsule, into which the ceramic powders were packed, is located in the pyrophyllite tetrahedron (figure 3.6 b) along with a surrounding graphite heater.

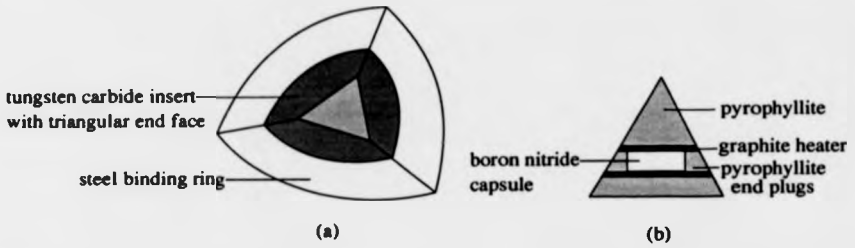

Figure 3.6: (a) single anvil from the tetrahedral system (b) cross section of the pyrophyllite tetrahedron

The specimens were heated in the same way as in the belt apparatus, by passing an electrical current (few hundred amps) through two of the anvils and the graphite heater. The temperature was measured by inserting a thermocouple through the pyrophyllite to the heater.

3.4 X-RAY DIFFRACTION

X-ray diffraction was used to identify the crystalline phases present in fabricated ceramics. The crystal lattice spacings were calculated from the angles where X-ray peaks were obtained as a result of Bragg diffraction and the phases were then identified with reference to the JCPDS (1984) data files containing crystallographic data for most known compounds. Copper K_α radiation (wavelength 1.5405 Å) was used in two X-ray instruments: (i) a moving goniometer unit (Philips) with a pen chart recorder and (ii) a curved position sensitive detector (Inel) connected to a computer (Dell) via a multichannel analyser (Varro), using the 'Diffractinel' (Inel) software programme for analysis.

Powdered specimens were attached to a glass slide with silica grease while ceramic specimens were ground so as to present a flat surface to the X-ray beam and minimise errors due to surface roughness.

3.5 ELECTRON MICROSCOPY

3.5.1 *Scanning Electron Microscopy (SEM)*

Scanning electron microscopy was undertaken with a Cambridge Stereoscan 250 and a Jeol 6100 microscope. These were used to investigate the phase distributions within ceramic composites and for the observation of topographical features. Some chemical analysis was carried out using the X-ray detection facilities housed within the Cambridge microscope.

(i) SEM Specimen Preparation

Ceramic specimens were prepared for SEM examination by grinding one surface flat, using a coarse (70 μm) diamond-impregnated pad, then carefully polishing it to remove all scratches and evidence of grinding damage which might detract from observations of the features under investigation. The specimens were often first embedded in a conducting bakelite mould to ease handling. Since the materials fabricated during this research were of particularly high wear resistance, the usual silicon carbide grinding pads were not used for any stage of the grinding or polishing operations, but successively finer grades of diamond-containing slurries (oil or water based) were used with a cast iron lapping plate that was covered with a nylon cloth for use with the finer grades (from 3 to $^1/_4$ μm). Particulate specimens, such as loose silicon carbide platelets, were cemented onto an aluminium stub with a conducting, carbon paste. Finally, the specimens were cleaned in acetone and then coated with a thin film of either carbon or gold (by evaporative deposition) to provide a conducting path on the specimen surface.

(ii) *SEM Operational Procedures*

Topographical features were imaged by the detection of secondary electrons ejected from the specimen surface, whilst compositional information was obtained from

3.5 ELECTRON MICROSCOPY

3.5.1 *Scanning Electron Microscopy (SEM)*

Scanning electron microscopy was undertaken with a Cambridge Stereoscan 250 and a Jeol 6100 microscope. These were used to investigate the phase distributions within ceramic composites and for the observation of topographical features. Some chemical analysis was carried out using the X-ray detection facilities housed within the Cambridge microscope.

(i) SEM Specimen Preparation

Ceramic specimens were prepared for SEM examination by grinding one surface flat, using a coarse (70 μm) diamond-impregnated pad, then carefully polishing it to remove all scratches and evidence of grinding damage which might detract from observations of the features under investigation. The specimens were often first embedded in a conducting bakelite mould to ease handling. Since the materials fabricated during this research were of particularly high wear resistance, the usual silicon carbide grinding pads were not used for any stage of the grinding or polishing operations, but successively finer grades of diamond-containing slurries (oil or water based) were used with a cast iron lapping plate that was covered with a nylon cloth for use with the finer grades (from 3 to $^1/_4$ μm). Particulate specimens, such as loose silicon carbide platelets, were cemented onto an aluminium stub with a conducting, carbon paste. Finally, the specimens were cleaned in acetone and then coated with a thin film of either carbon or gold (by evaporative deposition) to provide a conducting path on the specimen surface.

(ii) *SEM Operational Procedures*

Topographical features were imaged by the detection of secondary electrons ejected from the specimen surface, whilst compositional information was obtained from

electrons back-scattered from the specimen, which depend strongly on the atomic density, allowing different ceramic phases to be distinguished by different contrast levels in the resulting image. However, the images obtained from back-scattered electrons are more limited in resolution than those due to secondary electrons which are associated with a smaller interaction volume. To differentiate between the Si_3N_4 and SiC phases (similar atomic number contrast), it was necessary to reduce the distance between the specimen and back-scattered detector to about 12 mm (for increased detection efficiency) and use an electron accelerating voltage of at least 12 kV (to increase the strength of the back-scattered signal). The back-scattered detector was a solid state device and was divided into four quadrants, each receiving independent signals which were combined for maximum atomic contrast. Topographical information could also be obtained by reversing the polarities of signals received from opposite sides of the detector. This had the advantage of suppressing other sources of contrast and was found to be a useful way of imaging surface impressions, revealing more clearly defined impression boundaries than the secondary electron image.

Energy-dispersive X-ray analysis (EDAX) was performed on the X-rays ejected from the specimen by the electron beam. The specimens were brought within a 'working distance' of 15 mm (from the lens aperture) in order to allow efficient X-ray detection. Incoming X-rays produced a current in the detector that was amplified and stored in a multichannel analyser for rapid analysis using 'LINK' analytical software that stored the values of characteristic X-ray energies for the elements. Detection of the 'light' elements (those with atomic numbers below 11) required the removal of the beryllium window protecting the detector from contamination. This was necessary to prevent the absorption of the softer X-rays emitted from the 'light' elements.

A digital X-ray mapping programme was also used, in order to acquire X-rays from selected elements simultaneously. As the beam was slowly scanned over the specimen, the data acquired was displayed on a grey level scale. However, the images obtained by this technique had lower resolution than the electron images.

3.5.2 *Transmission Electron Microscopy (TEM)*

A 200 kV, JEOL 2000FX microscope was used for higher resolution electron microscopy studies, enabling investigation of the individual ceramic grains and interfaces together with electron diffraction and elemental analysis, taking advantage of the better spatial resolution over that obtained in the SEM.

(i) TEM Specimen Preparation

Preparation of TEM specimens was more complicated than for SEM specimen preparation. A thin ceramic slice (a few hundred μm) was diamond-cut from the bulk material and ground to a thickness of about 100 μm with a coarse (70 μm) diamond-impregnated wheel and then polished on one side (using diamond slurries with successively finer diamond particles, down to $^1/_4$ μm) to a much finer surface finish. The ceramic slice was mounted for 'dimpling' (using a South Bay Technology 'dimpler'), to further reduce the thickness of a small, central area to about 40 μm, using a brass wheel covered in a diamond impregnated (6 μm grains) paste. The dimpled area was finally polished with a $^1/_4$ μm diamond paste and finally, a brass supporting ring (3mm diameter) was affixed around this area with araldite resin. The specimen was eventually reduced to electron transparency by bombardment with argon ions (accelerated at 5 kV) whilst being rotated to ensure uniform thinning. The 'ion beam thinning' continued until a visible hole had developed in the specimen centre, around which could be found a region (< 1 μm in thickness) of electron transparency.

(ii) *TEM Operational Procedures*

High resolution images of the ceramic grains were obtained using the 'bright field' imaging mode, in which the image is formed from transmission of the direct electron beam (strongly scattered electrons are obstructed by the objective aperture) and consists of diffraction, phase and thickness contrast.

The selected area diffraction (SAD) method was used to determine crystalline

orientations within a selected area which was defined by inserting an aperture in the electron beam. To minimise diffraction contributions from regions outside that selected, the objective lens was focussed as accurately as possible on the image. The specimen could be tilted, in two perpendicular planes, to vary its orientation relative to the electron beam. Crystal lattice spacings were measured from the negatives for the diffraction patterns, using the relationship:

$$d = \lambda L/r \qquad (3.1)$$

where d = the crystal lattice spacing, (λL) = the 'camera constant' (λ = the electron wavelength), and r = the radial distance of a diffraction spot from the directly transmitted beam (measured). The camera constant was determined (at preset camera length (L) conditions) from the objective lens current, to accommodate fine adjustments in the focussing position.

The dark field imaging technique (in which the image is formed solely from a selected diffraction beam) was carried out by tilting the (directly transmitted) electron beam to allow the selected beam to travel along the optic (microscope) axis. The smallest objective aperture was then centred around the optic axis, preventing the transmision of all off-axis diffraction beams.

Some elemental analysis was also undertaken in the TEM. For this, the electron beam was focussed into a fine probe positioned on the area of interest and the presence of particular elements was identified using an EDAX spectrometer and associated software, already described in connection with the SEM. One disadvantage of analysis in the TEM was the proximity of the specimen holder and microscope column, both of which are metallic, to the specimen. Hence, metallic elements (such as Cu and Ni) were able to contribute to the X-ray spectrum. Electron energy loss spectroscopy (EELS) was also carried out and used to identify the cubic BN phase from the fine structure of the spectra obtained. This was carried out using a spectrometer (located beneath the viewing screen) that scanned across the energy spectrum arising from the inelastic scattering of electrons by the specimen.

3.6 MAGIC ANGLE SPINNING NUCLEAR MAGNETIC RESONANCE

Magic angle spinning nuclear magnetic resonance (MAS-NMR) is complementary to other methods of solid-state structural characterisation and has an advantage over phase identification by X-ray diffraction (XRD) regarding its ability to distinguish between different atomic environments. This is of particular interest for complex structures, such as silicon carbide, where the XRD data may be confused by the overlapping of diffraction peaks shared by different polytypes. MAS-NMR can assist in distinguishing between the different polytypic structures by revealing the local atomic co-ordination of the nuclei. The technique is described in more detail in reference [140].

A Bruker MSL 360 spectrometer was used to perform MAS-NMR (using the pulsed Fourier Transform method) on ceramic specimens at ambient temperature. The specimens were crushed into a fine powder and compacted into a cylindrical, alumina 'spinner' which was then placed inside the coil of the Bruker NMR probe. The coil was electrically tuned to the resonant frequency of ^{29}Si nuclei, being 71.5 MHz under the conditions used. To reduce spectral broadening from anisotropic atomic interactions and to allow fine resolution within the spectral dispersion obtained, the sample was spun at 3-4 kHz inside the coil which was orientated at the magic angle (54.7°) to the magnetic field (8.45 T). Short (1 μs, so as to irradiate all spectral frequencies uniformly), intense pulses of an r.f. magnetic field were applied to the sample by the coil at three minute intervals (the relaxation delay time) in order to produce a resultant field at 30° to the static magnetic field. (Ideally, the resultant field would have been perpendicular to the static magnetic field, but a shorter relaxation time is required when using a 30° resultant field, making possible the collection of a larger number of measurements in a given time period.)

The data was collected during relaxation of the nuclei inbetween these pulses and the 'data acquisition' cycle was repeated about 300 times for each experiment. The data was then Fourier transformed to produce chemical shift spectra which were expressed in parts per million (ppm) with reference to the chemical shift of the tetramethylsilane standard (most commonly used). As tetramethylsilane ($(CH_3)_4Si$) has

a single resonance peak at the high frequency end of the ^{29}Si spectrum (most other chemical shifts are on the low frequency side of this peak and so have negative values), all the Si sites are crystallographically indistinguishable; with four methyl (CH_3) groups being symmetrically arranged around a central Si atom. The ceramic phases were identified by comparison with published chemical shift data and the spectra obtained were consistently accurate within 0.5 ppm.

3.7 DENSITY MEASUREMENT

Measurements of specimen density were made with a digital balance (Precisa 125A), using Archimedes' principle. The specimens were weighed (i) in air and (ii) immersed in a fluid (water). Any evidence of encapsulant materials or other contamination adhering to the surface layers was removed by surface grinding, followed by ultrasonic cleaning in acetone. After being weighed in air, the specimens were placed in a weighing pan that was permanently suspended in water inside an enclosed compartment below the main balance. Evidence for open porosity in the specimens was indicated by a steady rise in weight whilst they were immersed in water.

The measured densities were compared with theoretical density values calculated (Appendix B) using the rule of mixtures and assuming complete reaction of the sintering additives with no residual phases, according to

$$2Si_3N_4 + Y_2O_3 + 3SiO_2 \rightarrow Si_3N_4 + Y_2Si_2O_7 + 2Si_2N_2O \qquad (3.2)$$

The composition of the post-sintered matrix phase was expected to be 88.20 wt% Si_3N_4, 7.66 wt% $Y_2Si_2O_7$ and 4.14 wt% Si_2N_2O, having a theoretical density of 3.235 g/cm^3.

3.8 INDENTATION EXPERIMENTS

An indentation technique was used measure the microhardness of fabricated ceramics and also to provide an indication of their fracture toughness, taking advantage of the small sample volume that this method requires. A Vickers diamond indenter

(pyramidal with apex angles of 136°) was used with a high enough load to generate cracking around the indentation and additional experiments were performed using a Knoop indenter (with apex angles of 172.5° and 130°). The ceramic surfaces were polished to a good optical finish (with 1 μm diamond paste) in preparation for the experiments. These were carried out using an Instron 1122 universal testing instrument (5 kN capacity) with a 0-50 kg loadcell (calibrated using a 1 kg weight) and the experimental arrangement is shown in figure 3.7.

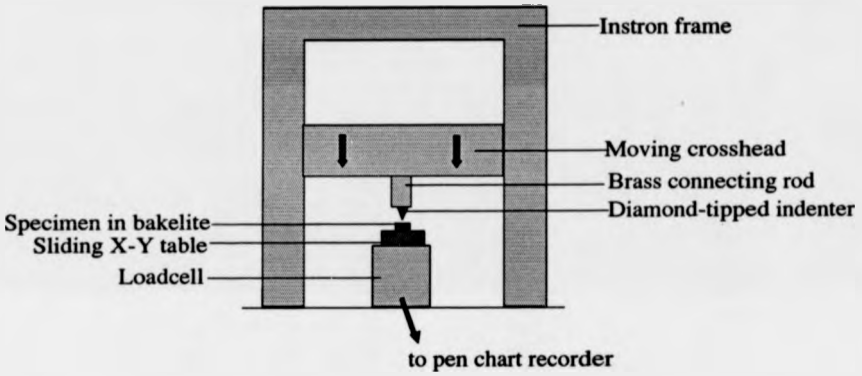

Figure 3.7: Experimental arrangement for indentation

To perform the indentation, the crosshead was lowered towards the specimen, at a speed of 8 μm/sec and as the diamond indenter contacted the specimen surface, load was applied until a preset value (2 kg) was measured by the loadcell. The load was then maintained for a dwell time of 15 seconds to form each indentation and the variation of load over time was monitored using a pen chart recorder. The specimens to be indented were supported in a bakelite mould which was positioned on a sliding X-Y table and the indentations were made at regular intervals (to facilitate their location in a microscope). Measurements were made on a series of indentations either using an Olympus (BH-2) optical microscope (with maximum magnification of x500) or using the SEM, for which (in both cases) the scale markers were calibrated against a copper graticule of 10 μm spacing. The hardness values were calculated using the relationship:

$$H = \text{applied load, } P \text{ (in N)} / \text{indentation area, } A \qquad (3.3)$$

For the Vickers indenter, the indentation area is taken as being the (pyramidal) area of the surface in contact with the indenter, given by

$$A = d^2 / 2 \sin(136°/2) \qquad (3.4)$$

where d = diagonal length of the indentation (in μm). The equation used to obtain Vickers microhardness values (in GPa) is,

$$H_v = 1854.4 \times (P / d^2). \qquad (3.5)$$

For the Knoop indenter, the projected indentation area (in the plane of the surface) is used in calculating the hardness:

$$H_K = 14230 \times (P / d_l^2) \qquad (3.6)$$

where d_l = the length of the **long** indentation diagonal (in μm).

The indentation fracture toughness was determined from measurements of the lengths of radial cracks emanating from the corners of the Vickers impressions (see figure 3.8), using the equation derived by Evans and Charles [2, 141]

$$K_{Ic} = 0.16 H_V a^{1/2} (c / a)^{-3/2} \qquad (3.7)$$

where K_{Ic} = the fracture toughness ($MPam^{1/2}$), a = the half-diagonal length (μm) and c = the surface crack length (μm).

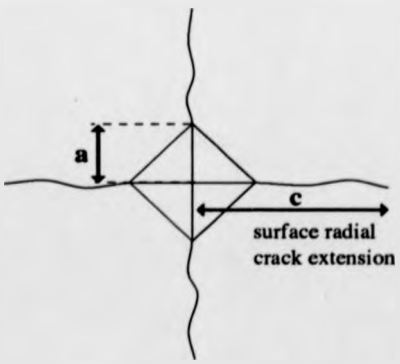

Figure 3.8 (right):
A typical surface impression made by a Vickers diamond indenter.

3.9 CERAMIC STRENGTH MEASUREMENT

The strength of ceramic composites was measured using four-point bending, in which it is assumed that a constant stress is exerted on the the surface of the bend test bar between the inner steel rollers (see the inner span, figure 3.7). In preparation for these tests, ceramic bars were machined from the bulk with lengths exceeding 10 mm (the outer span) and cross-sections of 3 mm x 5 mm. The bending surfaces were polished to a finish of 1 μm to eliminate fracture-initiating, surface flaws.

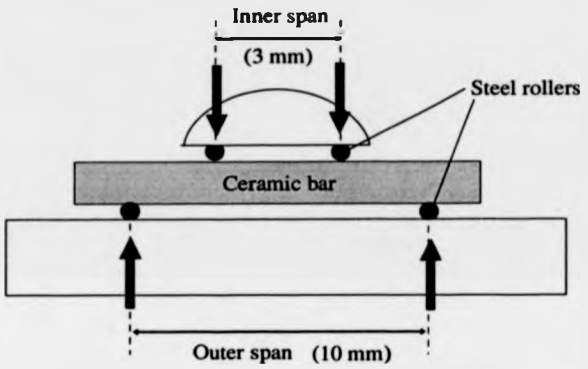

Figure 3.9: Cross-section of (brass) four-point bend apparatus. The arrows indicate the action of applied stress on the ceramic.

The bend testing apparatus (figure 3.9) was mounted on a 0 - 500 kg loadcell (calibrated with a 5 kg weight) connected to the Instron (1122) testing machine in a similar arrangement to that shown in figure 3.7. The crosshead was lowered onto the upper brass support (in which the inner steel rollers were mounted) at a rate of 0.5 mm/s and the stress applied to the ceramic specimen was measured by the loadcell (connected to a pen chart recorder). The fracture stress was evaluated for each specimen according to the well-known relationship:

$$\sigma_f = \frac{3\,P\,(L - l)}{2\,w\,h^2} \qquad (3.8)$$

where σ_f = the fracture stress (in Pa), P = the fracture load (in N), L = the outer span (in mm), l = the inner span, w = the specimen width and h = the specimen height.

3.10 SINGLE-EDGE NOTCHED BEAM FRACTURE TOUGHNESS

Fracture toughness is one of the most contentious parameters to be experimentally determined. Several techniques have been developed for its evaluation and these are compared in reference [142]. Whilst indentation techniques can easily be applied in cases where only a limited quantity of specimen material is available, their accuracy is restricted by errors made in the physical measurements of surface cracking and by uncertainties in the parameters used in the semi-empirical equations; particularly in the constants which are generally obtained from 'calibrations' against comparative data for a limited range of materials.

The single edge notched beam (SENB) technique is now well established in the evaluation of fracture toughness and involves the machining of a large, artificial flaw (a narrow notch) in the polished, tensile surface of a test bar which (usually) is broken in four-point bending (see figure 3.10). Although any microcracking which arises from residual stresses at the notch tip is very small in relation to the size of the notch, it should be noted that the SENB technique has been found to be sensitive to both the width and the depth of the notch [143] and so results obtained from specimens with different geometries can not easily be compared.

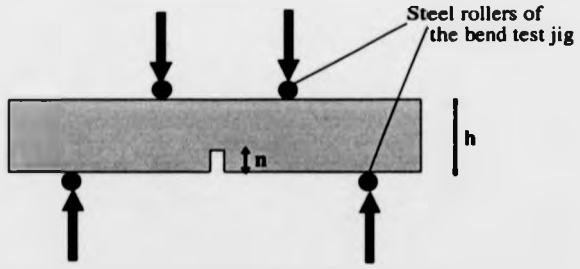

Figure 3.10: SENB test configuration (cross-section).
The (larger) arrows indicate the action of applied stress on the ceramic.

Notches were machined into the ceramic bars to an accurately-measured depth of 0.3 x the specimen height and the fracture toughness values were calculated from the maximum applied load before failure using the following equation [144].

$$K_{Ic} = \frac{3\,P\,(L - l)\,n^{\frac{1}{2}}}{2\,w\,h^2}\;F\left(\frac{n}{h}\right) \qquad (3.9)$$

where K_{Ic} = the fracture toughness (MPa $m^{1/2}$), P, L, l, w and h are as defined for equation 3.6, n = the depth of the notch and the function F ($^n/_h$) is given by

$$F\left(\frac{n}{h}\right) = 1.99 - 2.47\left(\frac{n}{h}\right) + 12.97\left(\frac{n}{h}\right)^2 - 23.17\left(\frac{n}{h}\right)^3 + 24.8\left(\frac{n}{h}\right)^4 \quad (3.10)$$

3.11 LINEAR THERMAL EXPANSION

Linear thermal expansion experiments were carried out using a quartz dilatometer, calibrated with a platinum standard to allow for expansion of the quartz. The experimental arrangement inside the furnace is shown in figure 3.11.

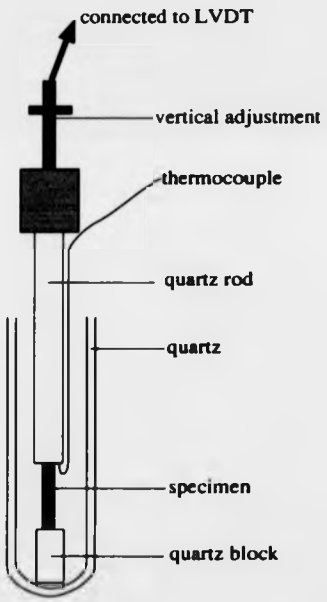

Figure 3.11: Cross-section of the quartz dilatometer used for thermal expansion experiments.

During the experiments, the specimen was heated to 1000°C at a constant rate of 3°C per minute. The temperature was measured using a thermocouple in contact with the specimen and connected to a pen chart recorder (x-axis). On expansion of the specimen, the quartz rod was pushed upwards and its displacement was measured using a linear variable displacement transducer (LVDT) for which the output (in mV) was

connected to the pen chart recorder (y-axis). The linear thermal expansion coefficient, α, was calculated from the relationship:

$$\alpha \Delta T = \left(\frac{\Delta l}{l}\right) \tag{3.11}$$

where Δd = the change in temperature and $(\Delta l / l)$ = the fractional increase in length, found from

$$\left(\frac{\Delta l}{l}\right) = C \Delta V \tag{3.12}$$

where ΔV = the change in output voltage due to the displacement of the quartz rod and C = the calibration constant (obtained from a preliminary experiment with a Pt sample).

Chapter Four

FABRICATION AND MICROSTRUCTURE OF SILICON NITRIDE CERAMICS TOUGHENED WITH SILICON CARBIDE

4.0 INTRODUCTION

In this chapter, the investigations made during this research project are presented and discussed. The successful combination of silicon nitride with silicon carbide as a reinforcement phase in hard, toughened ceramics has already been reviewed (section 2.2). Against this background, silicon carbide platelet-reinforced silicon nitride ceramics have been fabricated by two unusual and quite different approaches, to explore the possibilities for creating novel wear-resistant ceramics with improved fracture toughness.

The first approach considered is the fabrication of hybrid, laminated composites (section 2.6) using a conventional hot pressing process preceded by the green state preparation of ceramic laminae. Specific objectives were to fabricate ceramics with a particularly high concentration of the harder, SiC phase at the ceramic surfaces and also, to tailor the ceramic macrostructure to provide a weakly-bonded interface between adjacent laminae, thus giving rise to an additional potential fracture path. The fabrication of SiC-Si_3N_4 ceramic tapes (with different compositions), laminate fabrication procedure and microstructural evaluation of the fabricated ceramics, are recorded in this chapter. Some physical properties of these materials are presented in chapter six.

In the second approach, described in the second half of this chapter, SiC-Si_3N_4 ceramic composites were fabricated by sintering at ultra-high pressures. This was to investigate whether the extreme pressures could enable full densification of a wide ceramic compositional range, even reversing the normal ratio of ceramic matrix to dispersed phase content. This also meant sintering the ceramics in the presence of very little liquid phase. An investigation was also carried out into the apparent trend of increasing fracture toughness with the volume fraction of the SiC platelets (see chapter

six). One possible benefit perceived for the UHP fabrication was a reduction in the residual porosity associated with high SiC_p concentrations, as usually exists following more conventional processing. The survival (resistance to fragmentation or deformation) of the SiC platelets at these pressures was also investigated and evidence is presented for a structural phase change induced in the SiC platelets by the extreme sintering conditions.

4.1 THE FABRICATION OF HYBRID, LAMINATED CERAMICS

4.1.1 *Macrostructural designs*

Macrostructural arrangements were devised for enhanced fracture resistance, taking account of the effects of interfacial stresses in providing preferential fracture paths. Where neighbouring laminae have a very different SiC content, residual microstresses, arising from the thermal expansion mismatch between the laminae, would be expected to develop as cooling takes place after sintering. As the thermal expansion of Si_3N_4 (3.0 - 3.2 x 10^{-6}) [4] is less than that of SiC (4.4 - 4.8 x 10^{-6}) [4], predominantly SiC layers would be restrained on contraction and held in tension by the surrounding Si_3N_4 layers. If sufficiently high microstresses were concentrated along the interlamina boundaries, this would promote fracture stress relief by delamination at the weakened interface.

Two basic designs were used to fabricate hybrid ceramic composites. The first laminated design comprised layers of the unreinforced, Si_3N_4-based matrix phase alternating with SiC platelet-containing laminae (figure 4.1a). It was considered that the incompatible thermal expansion of adjacent laminae might give rise to microstresses concentrated along their compositional boundary. The weak interface so created would add to the composite toughening mechanisms operating in the ceramic, providing an additional possible fracture path to prevent ceramic fracture. An additional investigation was carried out to discover if it might also be possible to consolidate composites with localised regions of higher SiC content than can be fully densified at conventional fabrication pressures.

The second laminate design (figure 4.1b) is an arrangement with a surface SiC content higher than that of the bulk material. Such a design would permit a more economical use of the SiC platelets. For this, it was considered necessary to minimise any residual sintering stresses from the thermal expansion mismatch of neighbouring laminae by constructing a gradual compositional gradient within the bulk material.

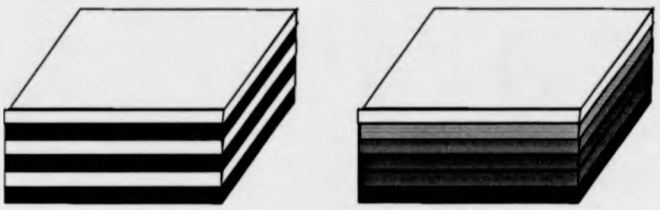

Figure 4.1: Macrostructural designs for laminated ceramic composites

4.1.2 *Experimental Procedure for Laminate Fabrication*

Laminated ceramics were fabricated by a sequence of processing steps: (i) tape casting, (ii) removal of the organic tape component and (iii) conventional hot pressing. Each of these steps required some experimentation, but of most critical importance was the refinement of a tape casting technique to form defect-free, homogeneous SiC-Si_3N_4 tapes with different ceramic compositions. An organic, rather than aqueous, tape slurry was used on account of the greater tolerance of organic slurries to variations in the concentration of the constituents. (Typical problems that have been associated with aqueous systems are unstable tape viscosities, more severe powder dispersion problems (controlled by pH), foaming and brittle tapes [145].)

Following successful tape fabrication, layers of the tapes were stacked according to the macrostructural designs described previously. The organic component was removed before the laminated arrangements were hot-pressed as any residual carbon in the laminates would have been detrimental to the sintering process [134]. This was done using controlled heat treatment (in air), being guided by the results of thermogravimetric analysis (TGA) experiments. The laminated arrangements were

finally hot-pressed, using externally-applied pressures of 10 - 30 MPa, to achieve maximum densification and to overcome difficulties in sintering stemming from the engineered density gradients.

4.2 TAPE CASTING EXPERIMENTS

The relative concentrations of the tape slurry constituents were determined experimentally for several different ceramic powder compositions and were classified according to the quality of the tapes, measured in terms of the absence of agglomerates, lack of cracking and tape flexibility. The tape porosity and shrinkage that followed the solvent evaporation were not primary concerns of these experiments.

Although the Si_3N_4 particle agglomerates (present in the 'as received' powder) were crushed by ball milling, they tended to reform on drying. Once formed, further crushing and sieving proved ineffective so far as their removal was concerned and they could not be broken apart by high speed 'shear blending' in suspension. In the initial tape casting experiments, difficulties were encountered in dispersing the fine, Si_3N_4 powders in the solvent-dispersant solutions, on account of the strong electrostatic attractions between the submicron-sized particles. This problem led to the production of poor quality tape which was typically lumpy and cracked from differential shrinkage around the agglomerates during solvent evaporation. However, it was found that these difficulties could be overcome when the ball-milled slurry of the fine, ceramic powders was directly used as a basis for making the tape slurry. In this way, agglomerates were prevented from reforming at any intermediate stage during powder drying.

Where SiC platelets were to be mixed into the tape slurry, the platelets were added after the milling of the matrix powders, but before adding the binder. The platelets were mixed inside the ball milling jars for the minimum time needed (one hour) to ensure homogeneous mixing whilst avoiding a significant reduction in platelet size and aspect ratio that might adversely affect their toughening behaviour.

The procedure adopted for tape fabrication is shown in figure 4.2. However, some practical difficulties in implementing this procedure arose from a conflict between

the requirement for a low slurry viscosity during ball milling (to allow effective agglomerate crushing by shear action) and that for a relatively high viscosity to permit controllable tape casting. The problem was particularly pronounced when fabricating tapes with a high (above 75% solid content) proportion of ultra-fine ceramic powders, as is discussed in the following sections.

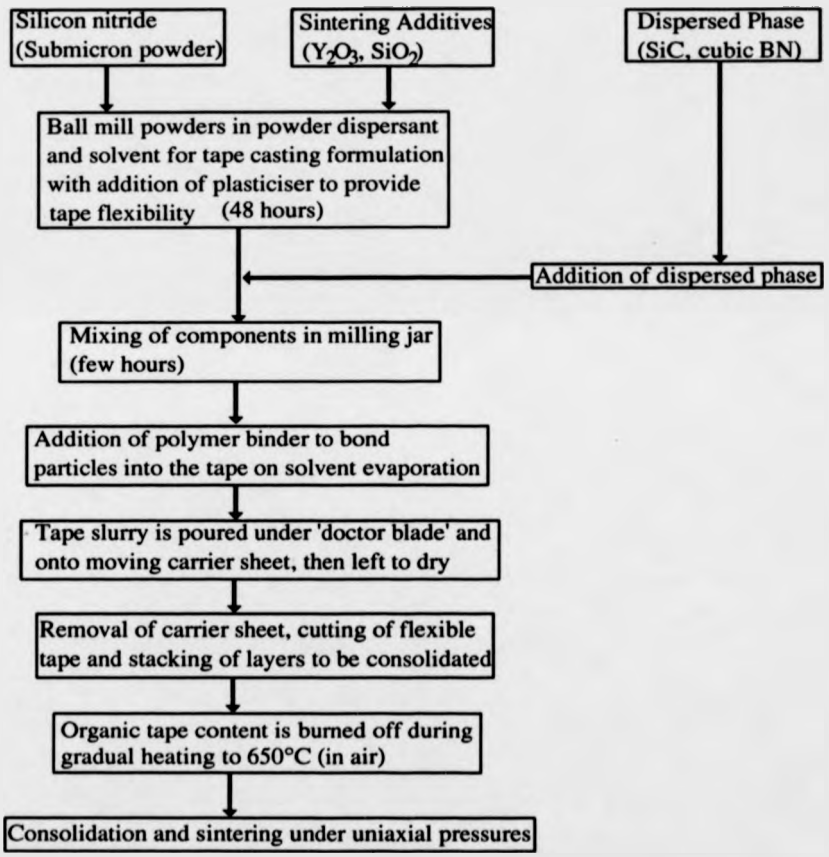

Figure 4.2: Flow diagram summarising the procedure for ceramic tape fabrication

4.2.1 *The Influence of Organic Components on Ceramic Powder Suspensions*

The behaviour of the ceramic suspensions on adding the various organic components (which were discussed in chapter 3) was recorded in order to learn how to achieve a minimal viscosity of about 0.01 Pas during the ball milling stage (necessary for a homogeneous, defect-free tape), but a higher relative viscosity of about 2 Pas once all the organic components had been added.

Two solvent-dispersant systems were initially used to examine the influence of solvent choice on the viscosity of the ball milling and the tape slurries after the other organic components were added. The two systems, which exhibited very different rheological behaviour, were:

(i) propan-2-ol (the usual ball milling medium) with dispersant 'KD2' and ethanol;

(ii) 1,1,1 trichloroethane with dispersant 'KD1' and ethanol.

Addition of the binder to the propanol-based slurries resulted in complete dissolution of the binder into the slurry with a dramatic reduction in relative viscosity. By contrast, the relative viscosity of the trichloroethane-based slurries was increased on adding the binder. This was most likely due to particle 'bridging' by the binder molecules.

Following these investigations, all further ball milling was carried out in a mixture of ethanol with a solution of the dispersant (6 wt% KD1) in trichloroethane. The presence of the dispersant was critical to the stability of the ball milling suspension. However, higher dispersant concentrations (above 6 wt%) were found to increase the slurry viscosity detrimentally.

The plasticiser (butyl benzyl pthalate) was found to effect a reduction in the viscosity of ceramic-dispersant suspensions, consistent with the observations of Braun *et al.* [146], who suggested that this plasticiser either behaves similarly to the dispersant, becoming adsorbed onto particle surfaces, or acts as a particle lubricant. On account of this beneficial action, the plasticiser was added during the ball milling stage, but in concentrations below 2 wt% (of the total slurry). It was found that higher plasticiser concentrations led to difficulties in removing fabricated tapes from the mylar carrier sheet.

Typical viscosities of the tape slurries prior to casting were 2 Pas (at a constant

shear rate of 6.6 s^{-1}). However, the slurries exhibited thixotropic behaviour during viscosity measurements, which suggested the formation of flocculated structures arising from inadequate powder dispersion. It is believed that this was unavoidable to some extent, particularly with a high concentration of very fine, colliding particles in suspension.

4.2.2 *The Effect of Ceramic Composition on Tape Fabrication*

It was found that for the fabrication of monolithic Si_3N_4-based tapes, the precursor tape slurries required a much higher solvent concentration to achieve effective ball milling. This was due to the viscosity increase associated with the high, ultra-fine powder content and was attributed to the very large surface area of 10-12 m^2/g [147] associated with the Si_3N_4 particles. Hence in the fabrication of tapes with very low SiC platelet content, an additional solvent of methyl ethyl ketone (MEK), which rapidly evaporated during tape casting, was added to increase the slurry fluidity during ball milling. Although only a slight increase in binder content is indicated for the monolithic tapes in table 4.1, these tapes tended to be more brittle and prone to cracking than the other compositions, suggesting that higher binder and plasticiser concentrations also were required to coat the excess particle surfaces and improve the tape quality, as has been shown in other research [148]. However, a homogeneous distribution of the sintering additives in the Si_3N_4 was obtained (as indicated in figure 4.3) and the formation of distinct, agglomerated regions of Si_3N_4 was avoided.

Despite the brittleness of the monolithic tapes, they could be cut into defect-free laminae for stacking into a laminated arrangement. The highest attainable powder content in monolithic tapes was 38 wt%.

Considerable platelet alignment was observed in the tapes, such that the SiC basal plane (also the plane of the platelets, see figure 4.4) lay within the plane of the tape. Although a homogeneous SiC distribution was found over the plane of the tape, it was found that some particle rearrangement had taken place during the tape drying process (solvent evaporation), resulting in sedimentation of the SiC platelets. This is clearly

Figure 4.3: X-ray map showing the dispersion of the Y_2O_3 sintering additive in the Si_3N_4-based ceramic matrix powder after ball milling.

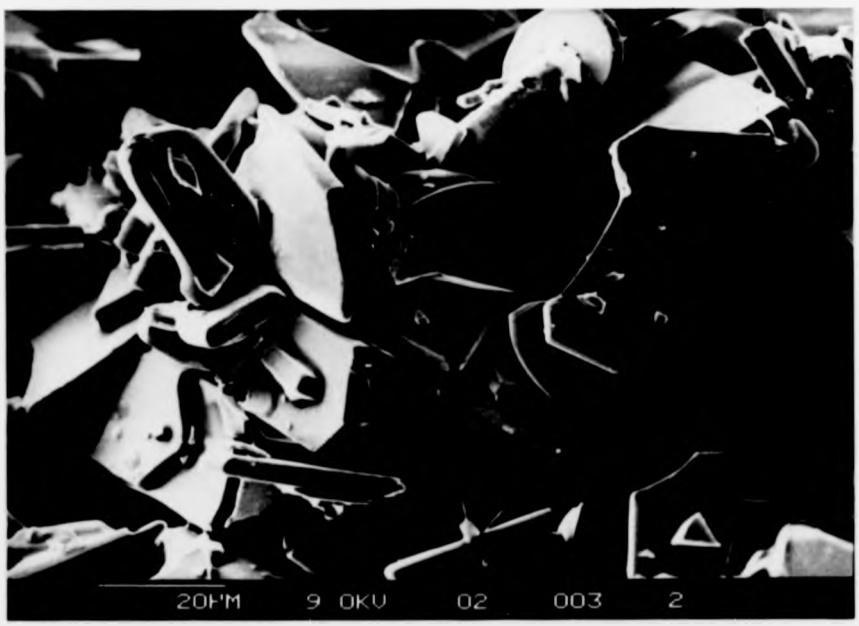

Figure 4.4: Secondary SEM image of the 'as received' SiC platelets. The SiC basal plane lies in the plane of the platelets.

illustrated in figures 4.5 and 4.6, in which the SiC platelets can be seen to be submerged below the finer ceramic powders at the tape surfaces whilst a higher platelet concentration is apparent at the bottom of the tape, giving rise to a density gradient within individual tape layers. Such behaviour was more restricted in tapes with relatively viscous slurries, since the higher viscosities inhibited particle movement whilst the tapes were drying. It may have been possible to reduce the platelet sedimentation still further by reducing the height of the doctor blade and hence, the thickness of the tapes produced. However, the height was limited to a minimum of about 0.5 mm because after tape shrinkage (to about 0.25 mm) it was impossible to peel thinner tapes away from the carrier sheet without damage.

The bottom tape surfaces which had been attached to the carrier sheet were much smoother than the upper surfaces (also seen in figures 4.5 and 4.6) and also revealed some entrapped porosity. (The tape slurries had not been outgassed before casting, but had been left to stand for half an hour instead.) The densities of the ceramic tapes (approximately 2 g/cm^3, showing little difference between monolithic and platelet-containing tapes) suggested tape porosity levels of at least 40% and so considerable laminate shrinkage was expected during sintering.

Table 4.1: Tape formulations for typical ceramic tapes, with component concentrations expressed as a percentage (by weight) of the final slurry.

Powder Composition	Powder Content	Solvents			Dispersant (KD1)	Plasticiser	Binder
		trichloroethane	ethanol	MEK			
Monolithic, Si_3N_4-based ceramic matrix	38.0	16.0	9.0	13.8	1.2	2.0	20.0
20 wt% SiC platelets in ceramic matrix	51.5	16.5	9.0	---	1.2	2.0	19.8
30 wt% SiC platelets in ceramic matrix	52.8	16.0	8.8	---	1.1	1.9	19.4
40 wt% SiC platelets in ceramic matrix	55.3	15.8	7.0	---	1.1	1.8	19.0
60 wt% SiC platelets in ceramic matrix	58.7	15.5	6.5	---	1.0	1.7	17.0

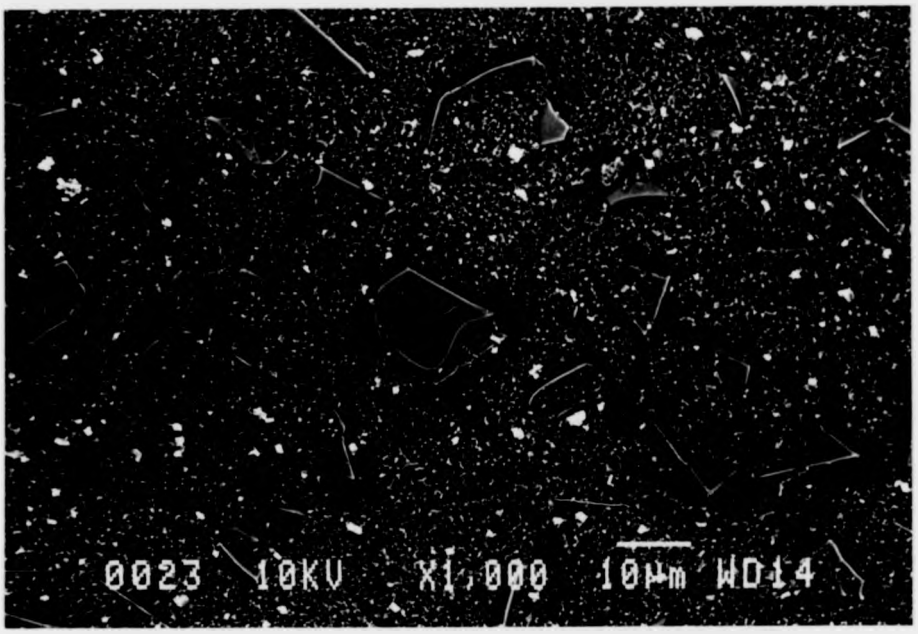

Figure 4.5: Secondary SEM image of the **upper** tape-cast surface of a (green state) SiC-Si_3N_4 lamina.

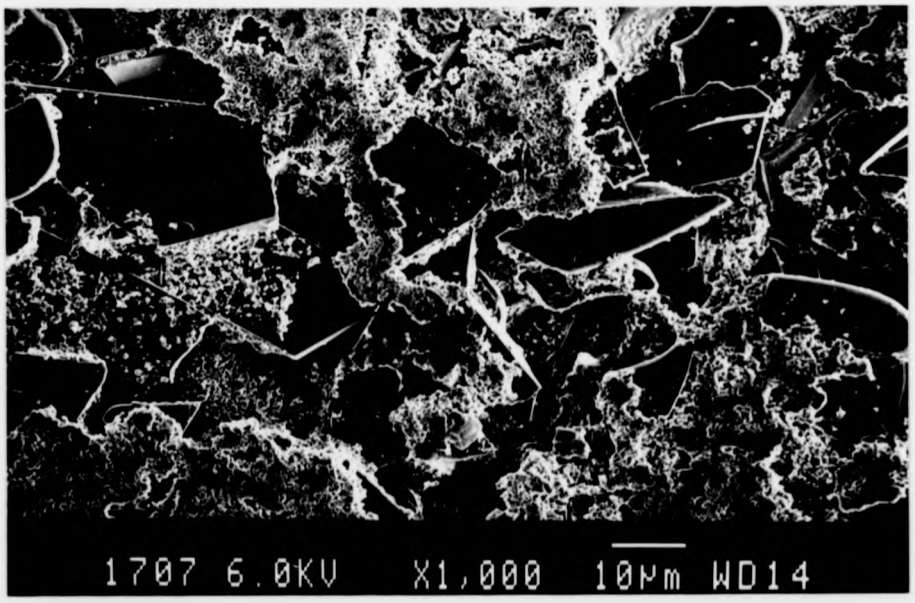

Figure 4.6: Secondary SEM image of the **lower** tape-cast surface of a SiC-Si_3N_4 lamina, after its removal from the carrier sheet.

4.2.3 *Laminate Construction*

After the fabrication of ceramic tape laminae the tapes were cut to fit the interior dimensions of the hot pressing die and arranged in compliance with the two structural designs described earlier (section 4.2.1). Typically, 20 - 30 layers of ceramic tape, each of 0.3 mm average thickness, were consolidated by hot pressing. Tape laminae of composition 60 wt% SiC were alternated with laminae of the monolithic, Si_3N_4-based composition to fabricate the first design. For the second structure, the difference in ceramic composition between consecutive tape laminae was a 5 wt% or 10 wt% change in SiC volume fraction.

It was found advantageous to pre-compress the stacked laminae under 0.15 MPa before removing the organic components and then hot pressing. This increased the green density of the laminates, reducing the possible occurrence of defects from uneven shrinkage. This also rendered the compressed arrangements less fragile (after binder removal) than the loosely stacked, individual laminae and so the green state laminates were less likely to become damaged during transfer to the hot pressing die.

4.3 REMOVAL OF ORGANIC TAPE COMPONENTS

The organic components (binder, plasticiser) in the laminate arrangements were burned out in air before consolidation by hot pressing. Thermogravimetric analysis experiments (TGA) were carried out at constant heating rates of 1°C and 3°C/minute using single-layer fragments (few mg) of monolithic tape (selected due to its slightly higher organic content than the other tape compositions). From these experiments (figure 4.7), it was found that no organic components were released at any temperature below 200°C. The greatest rate of weight loss was recorded on reaching temperatures above 400°C and there was a negligible change in specimen weight above 650°C.

The recommended cycle for removing the binder is by very gradual heating (over 60 hours) to 300°C, with no need for any heating at a higher temperature [149]. However, from consideration of the TGA data, the heating cycle used to remove the organic tape content was as shown in figure 4.8.

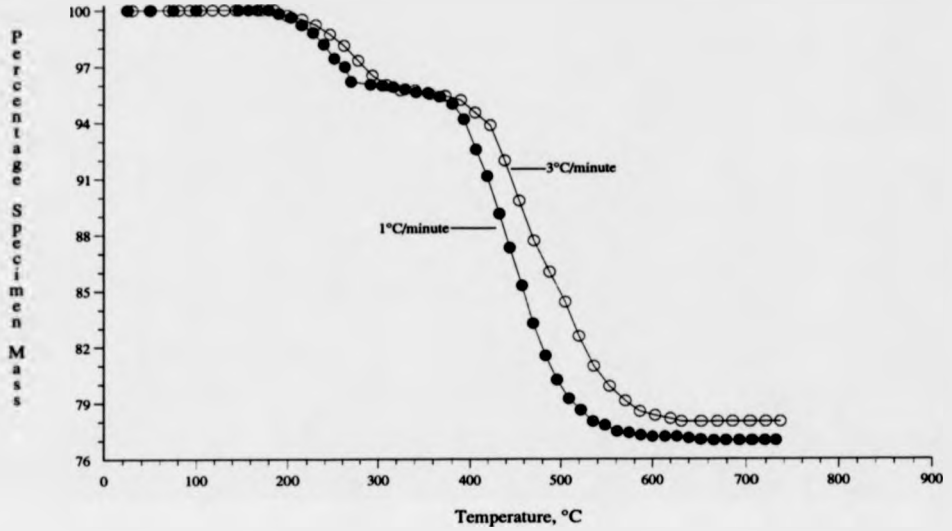

Figure 4.7: Constant heating rate thermogravimetric analysis experiments for a single, monolithic tape.

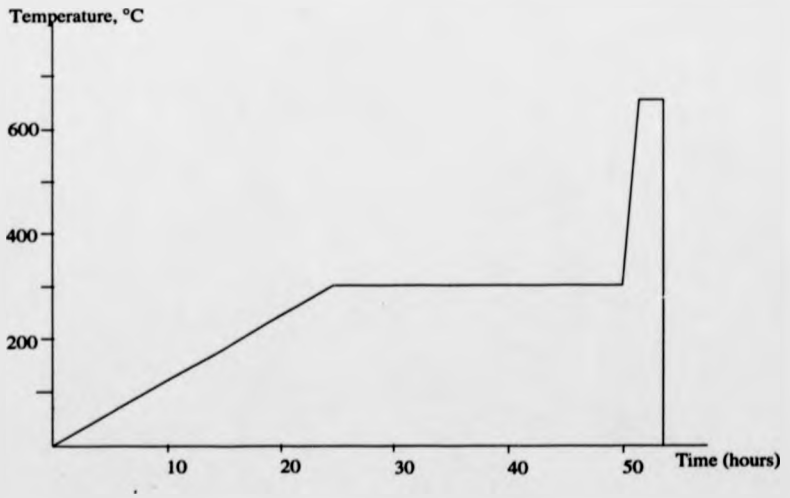

Figure 4.8: Heating cycle for removal of the organic component in fabricated tapes.

4.5 HOT PRESSING

The laminated arrangements were sintered at temperatures above 1700°C (1700-1750°C) and pressures of 10, 20 and 30 MPa. The hot-pressing cycle used in the laminate fabrication is illustrated in figure 4.9.

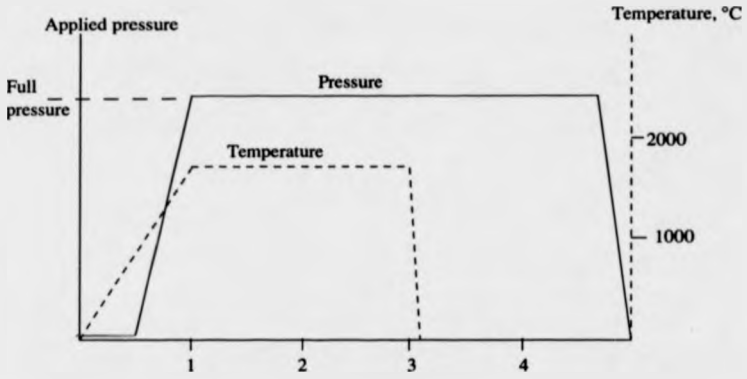

Figure 4.9: Hot pressing cycle used in the laminate fabrication

Similar densification behaviour was observed for all the laminates fabricated. The onset of the densification was indicated by the continued displacement of the graphite ram under a steady pressure. (Ram movement was also observed as the laminates were compressed under increased external pressures, which sometimes confused identification of the start of densification.) Little variation in behaviour was found for the different laminate specimens. In each case, the densification began at temperatures approaching 1500°C, which was associated with some liquid phase formation and a significant acceleration was observed above 1700°C (found to be independent of the applied pressure), which continued for about 30 minutes. The full hot-pressing conditions were held until a negligible change was registered in the ram displacement, suggesting that the densification process was complete.

The results presented in table 4.2 show that pressures of at least 30 MPa were required to attain high levels of densification. The lower density of specimen 11 is attributed to difficulties in densifying the laminae with a particularly high (60 wt%) SiC volume fraction and this is confirmed by microstructural observations (section 4.6).

Table 4.2: Fabrication conditions and resulting densities of laminated ceramics

Specimen	Composition		Pressure (MPa)	Temperature (°C)	Time (full conditions)	Density (g/cm^3)	% T. D.†
	No. of layers	% SiC					
1	2 5 5 5	0 30 40 80	10	1700	60 mins.	2.32	73
2	12 12 2	60 40 0	22	1740	60 mins.	2.69	84
3	10 14	40 60	20	1750	80 mins.	2.90	90.6
4	15	0	22	1710	60 mins.	2.98	93.4
5	8 8 8	20 30 40	20	1750	90 mins.	2.94	91.0
6	8 8 8	20 30 40	20	1750	90 mins.	2.95	91.3
7	* 20	0 5-50% (5% steps)	20	1710	110 mins.	3.14	97.5
8	* 20	0 5-50% (5% steps)	20	1710	180 mins.	3.19	99.0
9	15 5	0 60	30	1710	180 mins.	3.13	97.2
10	33	0-50% (5%steps)	30	1715	180 mins.	3.21	99.7

* Slip cast block (5 mm height) † Theoretical Density

Comparison of the densities of specimens fabricated at 20 MPa shows that increased sintering times led to an increase in the level of densification, accounting for the reduction in porosity. Evidence for the α to β-Si_3N_4 transformation was identified using XRD (see figure 4.10). The XRD spectra results taken from surfaces cut parallel and perpendicular to the hot-pressing direction, revealed some preferential orientation of the β-Si_3N_4 grains, most likely to have arisen from the uniaxial nature of the hot-pressing. Full Si_3N_4 transformation was not achieved in any of these hot-pressing experiments, even after sintering times of 180 minutes which may either be indicative

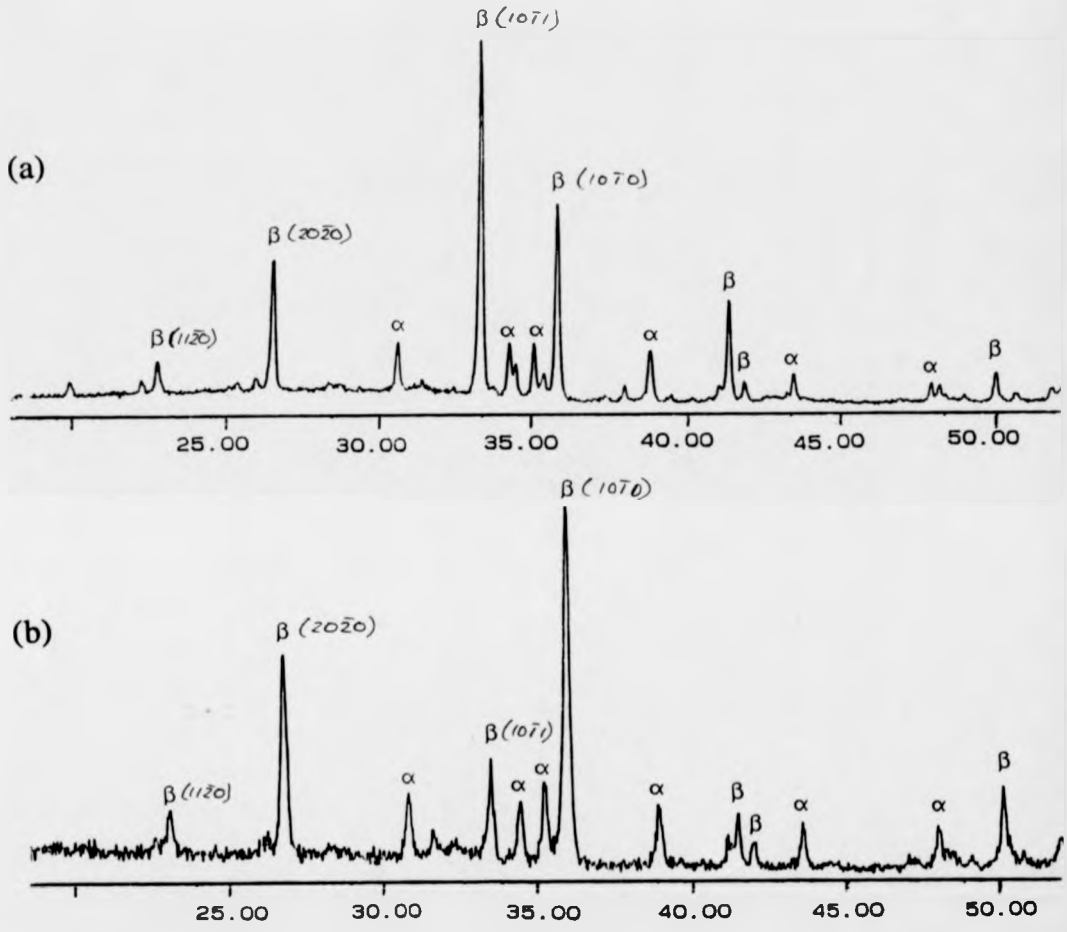

Figure 4.10: XRD spectra taken from a laminate constructed with alternating layers of monolithic Si_3N_4 and SiC (60 wt%)-Si_3N_4, that was hot-pressed at 30 MPa and 1710°C for 180 minutes. Spectrum (a) was acquired from a surface orientated parallel to the hot-pressing direction whereas spectrum (b) was acquired from a monolithic surface orientated perpendicular to the hot-pressing direction. The additional, unlabelled peaks in the spectra arise from the SiC platelets in the ceramic.

of inadequate sintering temperatures being reached or the presence of residual organic material from the tape fabrication. Some contamination in the surface layers was found to arise from either the graphite (hot-pressing) die itself or from the boron nitride powder used to coat its interior.

It was not possible to fabricate layers of the monolithic matrix phase alternating with layers of high SiC content unless the matrix layers were of much greater thickness than the SiC layers. In experiments where alternating layers of equal thickness were sintered, the resulting composites exhibited severe delamination and fragmentation which might be explained by the very high interfacial shear stresses arising from the difference in thermal contraction between Si_3N_4 and SiC-containing laminae.

4.5 THE MICROSTRUCTURE OF HYBRID, LAMINATED COMPOSITES

4.5.1 *Scanning Electron Microscope Observations*

Figure 4.11 shows a polished, cross-sectional surface of the laminate fabricated at 30 MPa with alternating layers of monolithic Si_3N_4 (from three stacked sheets of tape) and layers of 60 wt% SiC composition (from single tape laminae). Considerable shrinkage, of 60 - 70 %, is indicated by the final thicknesses of these laminae (0.4 and 0.1 mm average thickness, repectively). This observation is consistent with the overall reduction in height of the green state composite that was recorded after sintering. Evidence for the differential sintering behaviour of the composite and monolithic laminae is apparent from observations of residual porosity in the SiC-containing laminae and indicates the existence of regular density gradients throughout the bulk material as the surrounding, monolithic layers appear well densified. The residual porosity is particularly evident in one of the SiC bands which is twice the thickness of the others.

Figure 4.12 shows a polished cross-section of a surface cut perpendicular to the direction of hot-pressing, the platelets are mainly viewed perpendicular to the platelet plane (i.e. 'edge-on') on account of the preferential alignment which was induced during the tape fabrication and enhanced by hot-pressing. The platelets are bonded in a

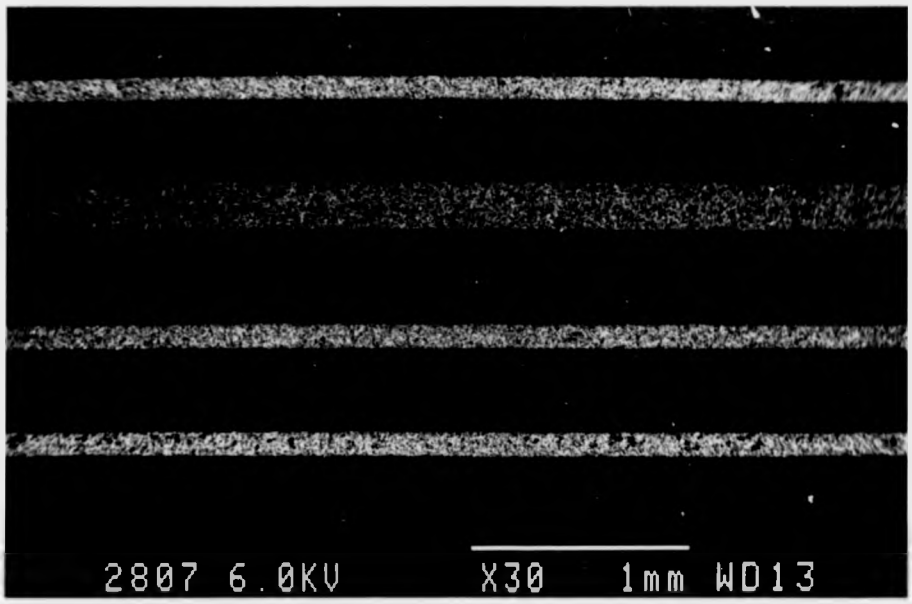

Figure 4.11: Back-scattered SEM image of the polished cross-section of a laminate fabricated (at 30 MPa) with alternating compositional layers of the monolithic Si_3N_4 phase and SiC (60 wt%)-Si_3N_4 laminae.

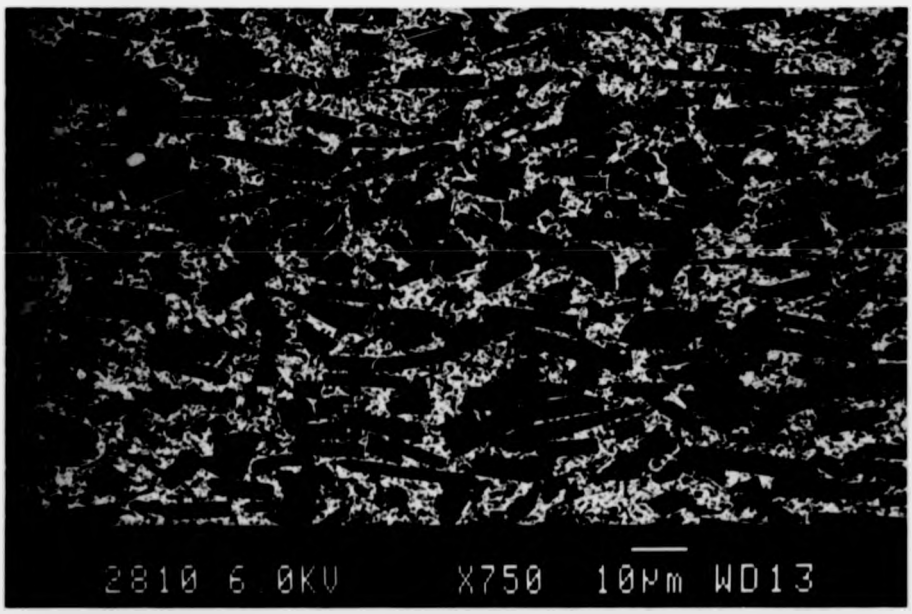

Figure 4.12: Back-scattered SEM image of the polished cross-section of a SiC (60 wt%)-Si_3N_4 layer from the composite shown in figure 4.11.

relatively fine-grained network of the matrix phase and the regions of porosity frequently occur at the boundaries between the matrix phase and the platelets; interfaces at which high, post-sintering shear stresses would be expected.

The polished, cross-section of a laminate constructed with a gradual compositional variation through the bulk (after figure 4.1 b) is shown in figure 4.13. Distinct boundaries can be observed between the laminae of different compositions, which vary from the monolithic Si_3N_4-based matrix (bottom of the figure) to 60 wt% SiC in the upper layers. The greater difficulties in densifying the 60 wt% SiC laminae is apparent from the visible porosity in the upper layers. However, the regions which contain a much lower concentration of platelets (figure 4.14) appear to be well consolidated and there is no evidence of microcracking at the platelet-matrix interfaces. The preferential alignment of the platelets in the plane of the laminae is also visible.

4.5.2 *Transmission Electron Microscope Observations*

The fine-grained structure of the matrix phase, with overlapping elongated crystals characteristic of the β-Si_3N_4 phase, is shown in figure 4.15. The dark, glassy phase which surrounds the Si_3N_4 grains derives from the liquid phase sintering additives and can be observed to have infiltrated the interface between two of the SiC platelets (top right). Whilst inclined stacking faults are visible in one of the platelets (bottom left), the platelets were found to be largely defect-free, exhibiting contrast arising only from thickness contours.

A higher resolution image of the fine, hexagonal grains in the matrix phase is given in figure 4.16, in which Moiré fringes from overlapping crystals are visible in the bottom corners. The intergranular, glassy phase (black) was finely dispersed in the matrix phase and was frequently found to have infiltrated Si_3N_4 grain boundaries such as that in the centre of figure 4.16 (triangular, black region). X-ray analysis of the composition of this phase suggested that it was an yttrium silicate and the detection of nitrogen in the EDAX spectrum was due to difficulty in focusing the probe electron beam on the intergranular region without it overlapping with the surrounding, Si_3N_4 grains.

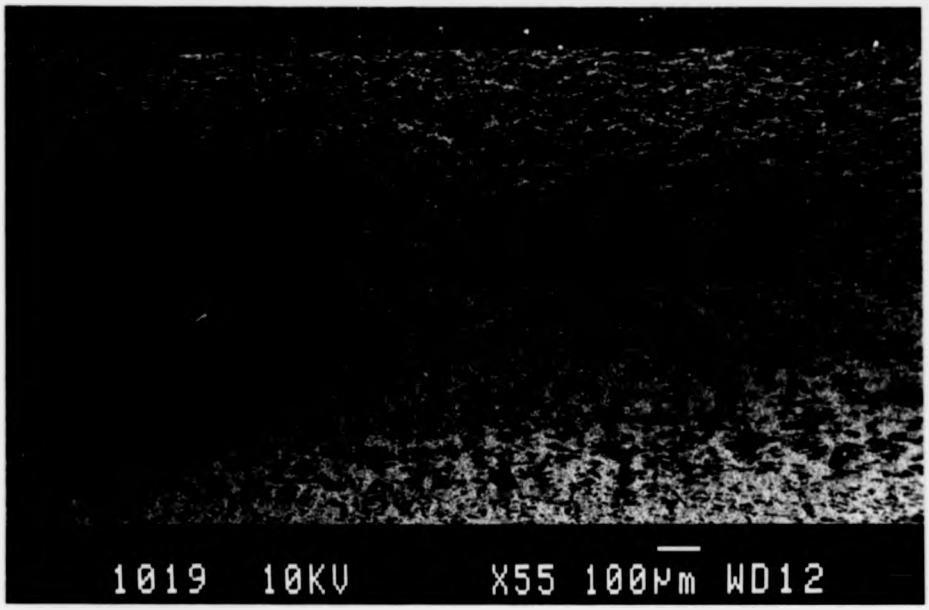

Figure 4.13: Back-scattered SEM image of the cross-section of a hybrid composite fabricated at 20 MPa, showing an increasing concentration of SiC platelets from the bottom to the top of the figure.

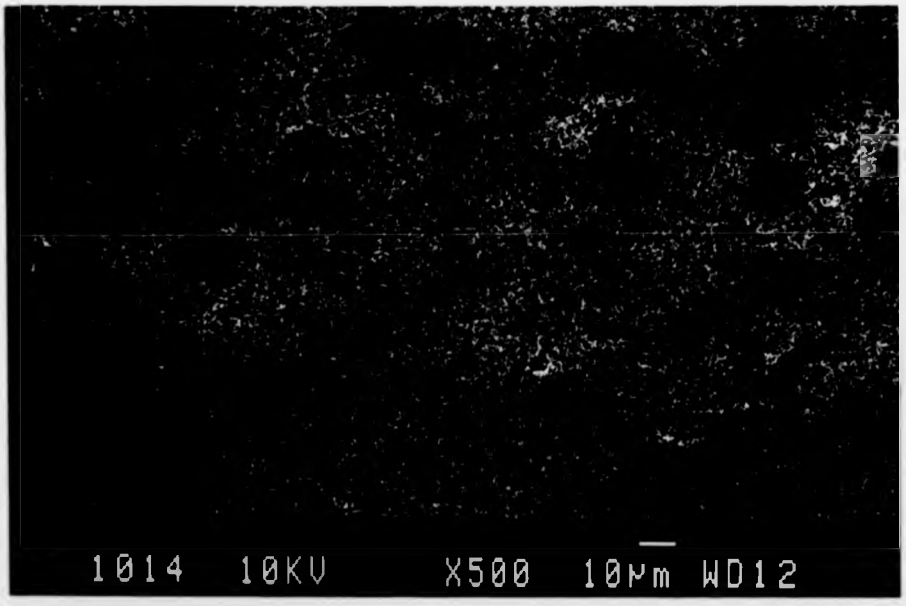

Figure 4.14: Back-scattered SEM image showing a cross-sectional view of the laminae with the lowest SiC volume fraction dispersed in the matrix phase.

Figure 4.15: Bright-field TEM image showing a region of the Si_3N_4-based matrix phase in a hot-pressed (at 30 MPa) laminate, surrounded by the relatively large SiC platelets.

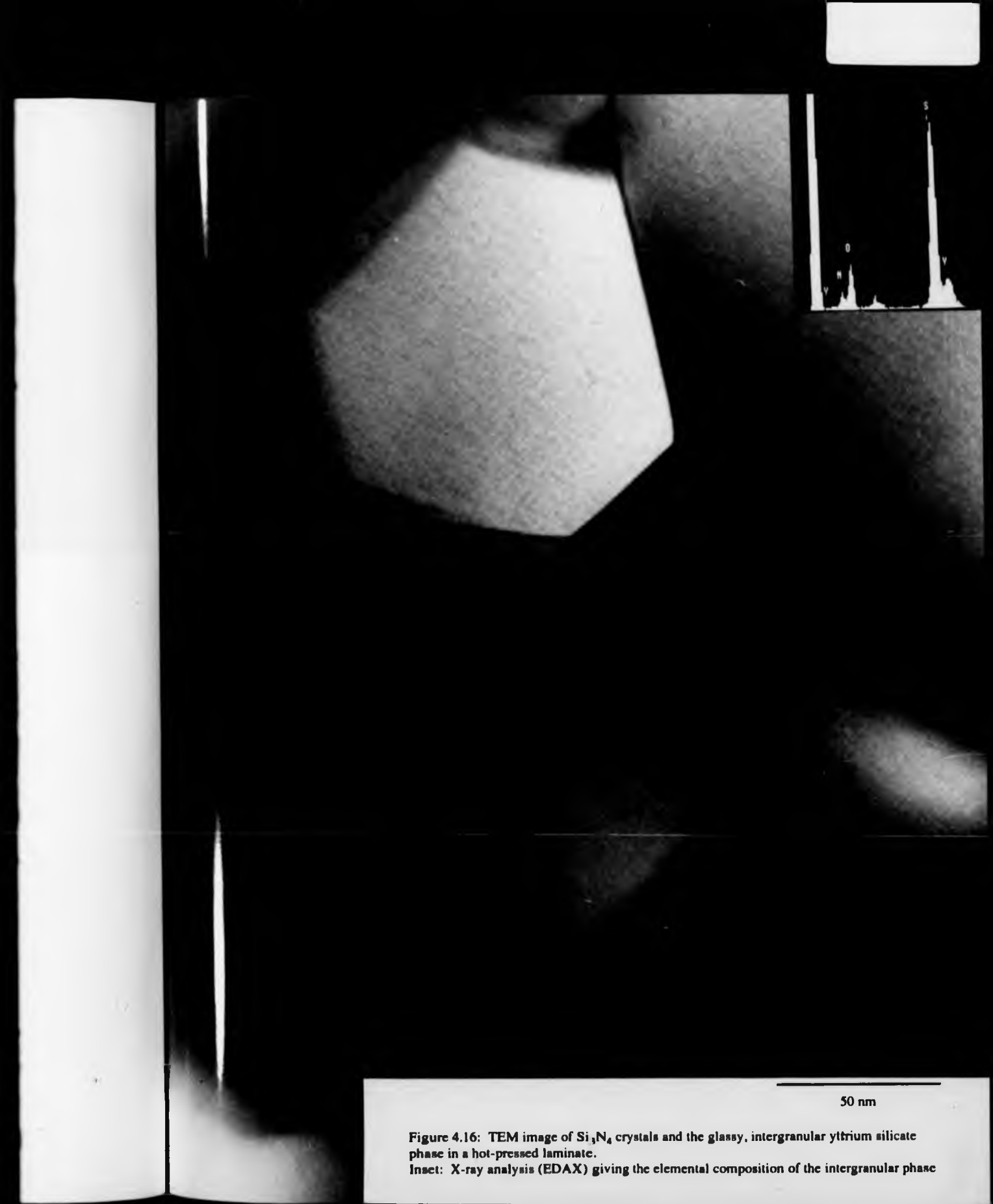

Figure 4.16: TEM image of Si_3N_4 crystals and the glassy, intergranular yttrium silicate phase in a hot-pressed laminate.
Inset: X-ray analysis (EDAX) giving the elemental composition of the intergranular phase

4.6 SILICON CARBIDE / SILICON NITRIDE CERAMIC FABRICATION AT ULTRA-HIGH PRESSURES

Ultra-high fabrication pressures, of about 4 GPa, were used to assist the sintering of SiC-Si_3N_4 composites with widely differing SiC concentrations. The effects of these pressures on the ceramic phases were investigated using several analytical techniques, during the course of which striking evidence was revealed for a polytypic phase transition in the SiC platelets.

4.6.1 *Experimental Procedure for Ultra-High Pressure Ceramic Fabrication*

The green state composites were prepared by slip casting the constituent ceramic powders into porous moulds and the compositions prepared were 20 wt% SiC, 40 wt% SiC, 60 wt% SiC and above 80 wt% SiC. (Although the initial platelet volume fractions were accurately measured before slip casting, it is believed that some phase separation occurred during the mixing process, removing some components from the slip and rendering the values for platelet volume fraction somewhat inaccurate.) The green state composites were sintered at UHP conditions, for which the processing details are discussed more fully in chapter five. For these composites, a boron nitride 'pressure-transmitting' medium (see section 5.4) was used to allow high enough operating power to be applied to promote liquid phase sintering.

The actual temperatures reached during sintering were unknown. However, the effectiveness of the sintering process was evaluated according to post-fabrication observations made on the α to β-Si_3N_4 phase transformation since this is known to procede concurrently with liquid phase sintering, being mostly dependent on temperature [123]. The estimated fabrication pressures can be taken only as approximate (for reasons discussed in chapter five) and may be slightly higher than the actual fabrication pressures. The full pressure and temperature conditions were maintained simultaneously for ten minutes.

4.7 PHASE IDENTIFICATION BY X-RAY DIFFRACTION

The phases present in the final ceramics were identified using X-ray diffraction which was performed on sections cut to expose surfaces orientated parallel and perpendicular to the anvil motion in the high pressure belt apparatus during fabrication. This permitted the identification of any preferential orientation of the ceramic phases arising either from the UHP fabrication process itself or from the initial slip casting of the ceramic powders.

In the unreinforced, monolithic Si_3N_4 ceramic the Si_3N_4 XRD peaks indicated that complete transformation of the α to β-Si_3N_4 phase had taken place (figure 4.17). This would suggest that the temperatures reached during sintering were sufficient to promote liquid phase sintering and also, that the extreme pressures may have accelerated this process since the Si_3N_4 phase transformation was accomplished in a much shorter sintering time than would be required by sintering at much lower pressures (for example, HIPing, hot-pressing). There was no difference in the relative peak intensities for spectra obtained from the two surface orientations and the β-Si_3N_4 diffraction peak (at 26.9°) was the most intense in both cases, giving no evidence for any strong preferential orientation.

A striking difference was observed between the XRD spectra for unprocessed (i.e. 'as received') SiC platelets and those subjected to UHP processing conditions. This is clearly illustrated in figure 4.18, which shows the result of an experiment in which SiC platelets were loosely packed into tantalum cups and treated under the same conditions as those used for the UHP ceramic fabrication. The initial SiC platelets were mainly a mixture of 4H and 6H SiC polytypes, apparently present in the ratio 57:43 [65] and the most intense peak in the X-ray spectrum at 35.7° (Cu Kα radiation) corresponds with the third most intense peak of the 4H spectrum (from (0004) planes) enhanced by the superposition of the most intense peak of the 6H spectrum (from ($10\bar{1}2$, 0006) planes). After UHP processing, all the original diffraction peaks were broadened (indicative of crystalline disorder or a reduction in grain size) with a corresponding reduction in intensity to the extent that many original peaks totally disappeared amongst the background radiation. Comparison of this spectrum with figure 4.19 implies that the

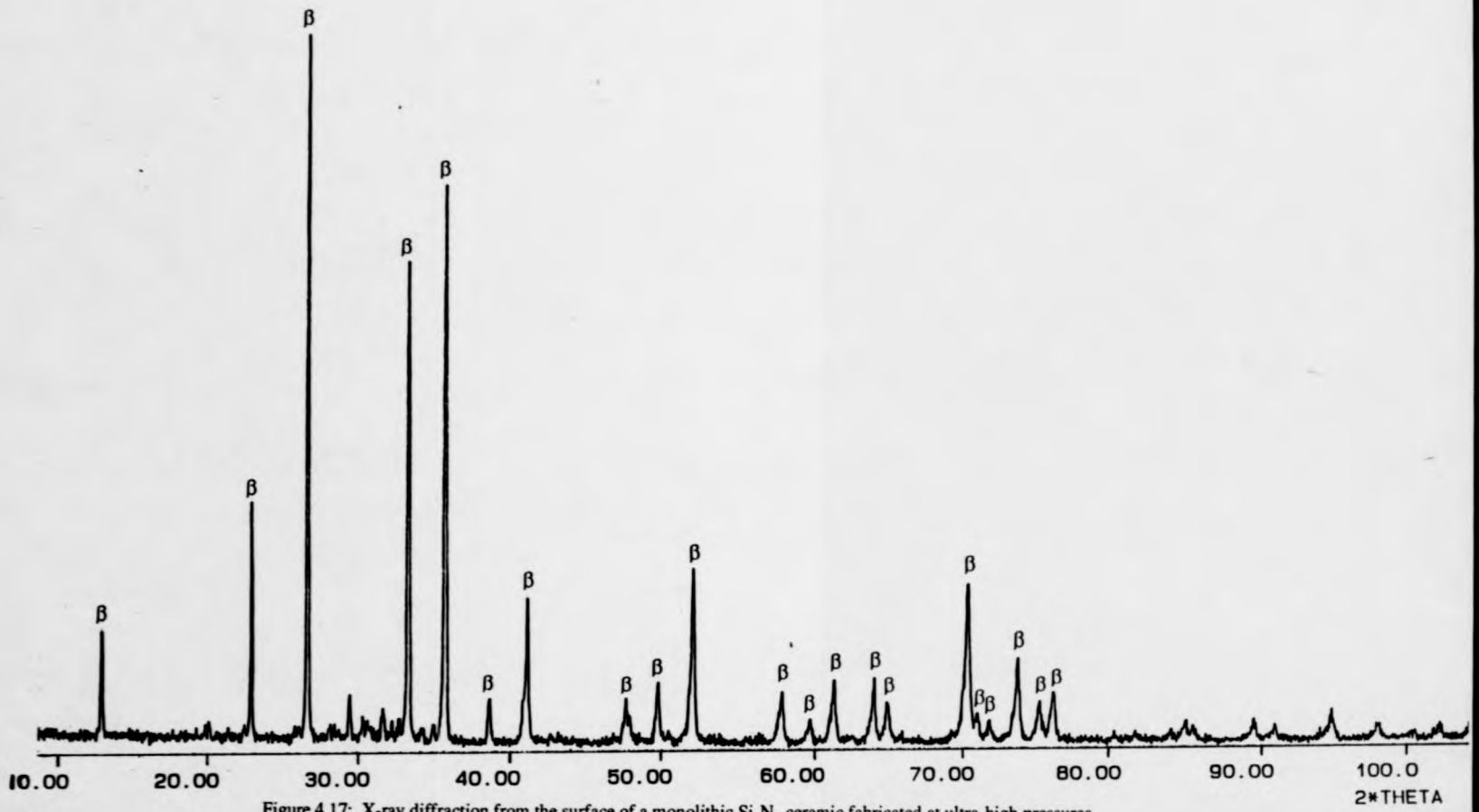

Figure 4.17: X-ray diffraction from the surface of a monolithic Si_3N_4 ceramic fabricated at ultra-high pressures.

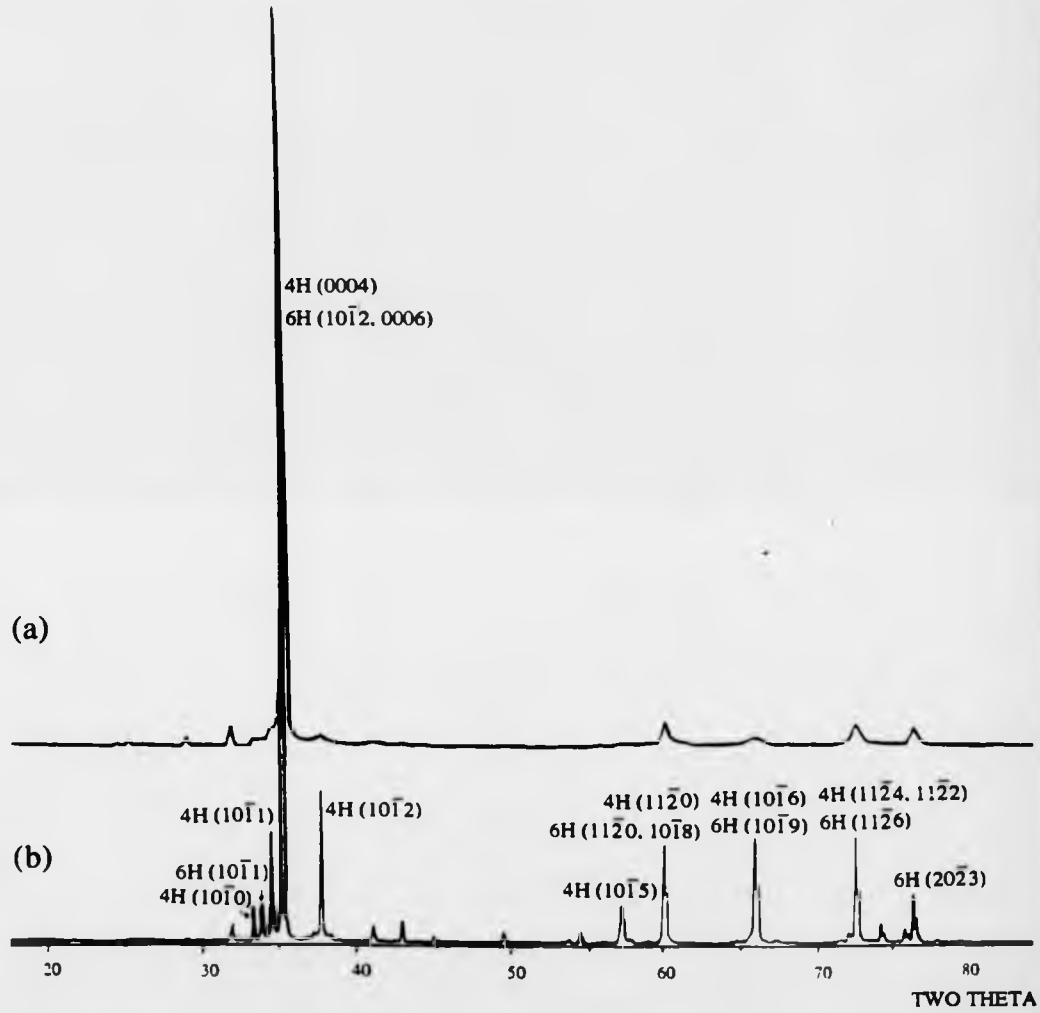

Figure 4.18: X-ray diffraction from (a) SiC platelets that were subjected to the ultra-high pressure conditions used in composite fabrication and (b) the 'as received' SiC platelets.

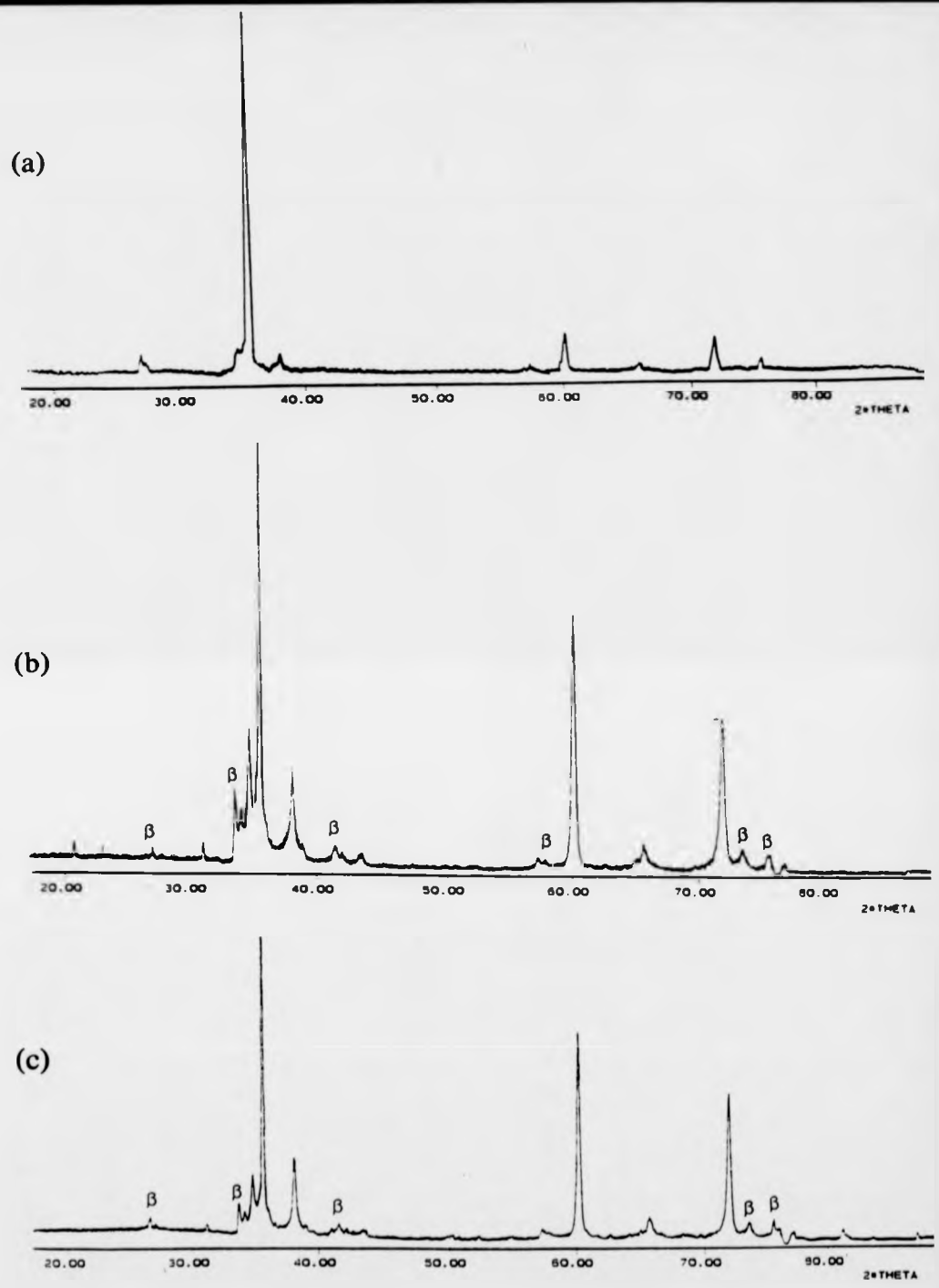

Figure 4.19: X-ray diffraction from different orientations of a SiC-Si_3N_4 composite fabricated at ultra-high pressure: (a) from a surface cut perpendicular to the direction of anvil motion; (b) from a surface cut parallel to the direction of anvil motion; (c) the powder diffraction spectrum.
The peaks labelled 'β' are from the β-Si_3N_4 phase.

differences between the spectra in figure 4.18 may in part be due to some platelet alignment caused by the UHP processing. Figures 4.19 (a) and (b) were obtained from a SiC-Si_3N_4 ceramic with SiC volume fraction above 80 wt%. Some very weak XRD peaks are present from the β-Si_3N_4 phase, but the spectra can be easily compared with those of figure 4.18. The particularly strong intensity of the SiC 4H (0004)/6H ($10\bar{1}2$, 0006) diffraction peak in figure 4.19 (a), arising from a surface cut perpendicular to the direction of anvil motion, is explained by a predominant alignment of the platelet plane (also the SiC basal plane) with the surface. Figure 4.19 (b), taken from a surface cut parallel to direction of anvil motion, shows a much stronger intensity for the 4H ($11\bar{2}0$) / 6H ($11\bar{2}0$, $10\bar{1}8$) peak at 60.2° and the 4H ($11\bar{2}4$, $11\bar{2}2$) / 6H ($11\bar{2}6$) peak at 71.7°, indicating some orientation of the platelet plane normal to the surface. Figure 4.19 (c) shows the powder XRD spectrum for this specimen and this differs from figure 4.19 (b) only in the relative intensities of the peaks present, explained by the preferential orientation in the ceramic.

Another notable feature of these XRD spectra is the close correspondence of the most intense diffraction peaks with those of the cubic SiC phase. For instance, the most intense peak in these spectra could equally well be ascribed to the 3C (111) diffraction peak (the maximum peak for this phase). On account of the additional confusion engendered by the overlap of diffraction peaks from the different SiC polytypes and the broadening of the peaks in UHP-fabricated ceramics, it was not possible to identify the SiC phases conclusively using X-ray diffraction. Therefore, additional analysis of the SiC phases was carried out using a combination of MAS-NMR and TEM.

4.8 STRUCTURAL ANALYSIS USING SILICON-29 MAGIC ANGLE SPINNING NUCLEAR MAGNETIC RESONANCE

4.8.1 *Determination of Post-Processing Structural Changes in Silicon Carbide Platelets*

To investigate further the apparent structural change induced in the SiC platelets by UHP processing, ^{29}Si magic angle spinning nuclear magnetic resonance (MAS-NMR) was employed. This technique provided ^{29}Si chemical shift spectra associated

with the different distinctive SiC lattice sites and which could be interpreted to give information about the Si atomic environments. The influence of the atomic arrangements on chemical shift is believed [150, 151] to extend to 5 Å from a central Si atom whilst more distant neighbours are considered to have little effect.

The ^{29}Si chemical shift spectra that have so far been obtained in the other research on SiC have been correlated with the known structures of SiC polytypes. In references [150-154], a lattice site designation system has been devised, on the assumption that there are no more than four basic, crystallographically inequivalent lattice sites in all the possible SiC structures. The slight discrepancies which are found between ^{29}Si chemical shifts, associated with the same type of lattice site in different polytypes, reflect variations in the polytypic lattice parameters and the bond symmetry. Although some interpretation of ^{29}Si chemical shift spectra can be made to identify characteristic lattice sites by reference to the published research, it is not possible to identify a mixture of SiC polytypes unambiguously using this technique alone [150]. Identification of the peaks is also restricted by the limited range of polytypes that have been examined using MAS-NMR on account of the difficulties in obtaining pure crystals of a single SiC polytype. To date, the published research has been concerned mainly with the 3C, 6H, 4H and 15R polytypes.

All the MAS-NMR experiments were conducted under, as near as possible, identical conditions to enable accurate comparisons to be made between the spectra obtained from different specimens. (These conditions are described in more detail in chapter three.) The results of the MAS-NMR experiments, presented in this chapter, have been normalised with respect to the most intense peak of a given spectrum and so it is important to consider only the relative intensity differences between any two spectra.

Figure 4.20 shows the MAS-NMR spectra obtained† with a three minute relaxation delay from three different SiC-Si_3N_4 ceramics fabricated at UHP. Spectra (a) and (b) were obtained from ceramics fabricated concurrently in the same high pressure sintering capsule and are assumed to have, therefore, experienced identical processing conditions. The difference between these specimens is in the proportion of the SiC platelets; present at above 80 wt% for (a) and at approximately 40 wt% for (b). For

†: Very little (5 Hz) exponential line broadening has been applied to 'smooth' the spectra.

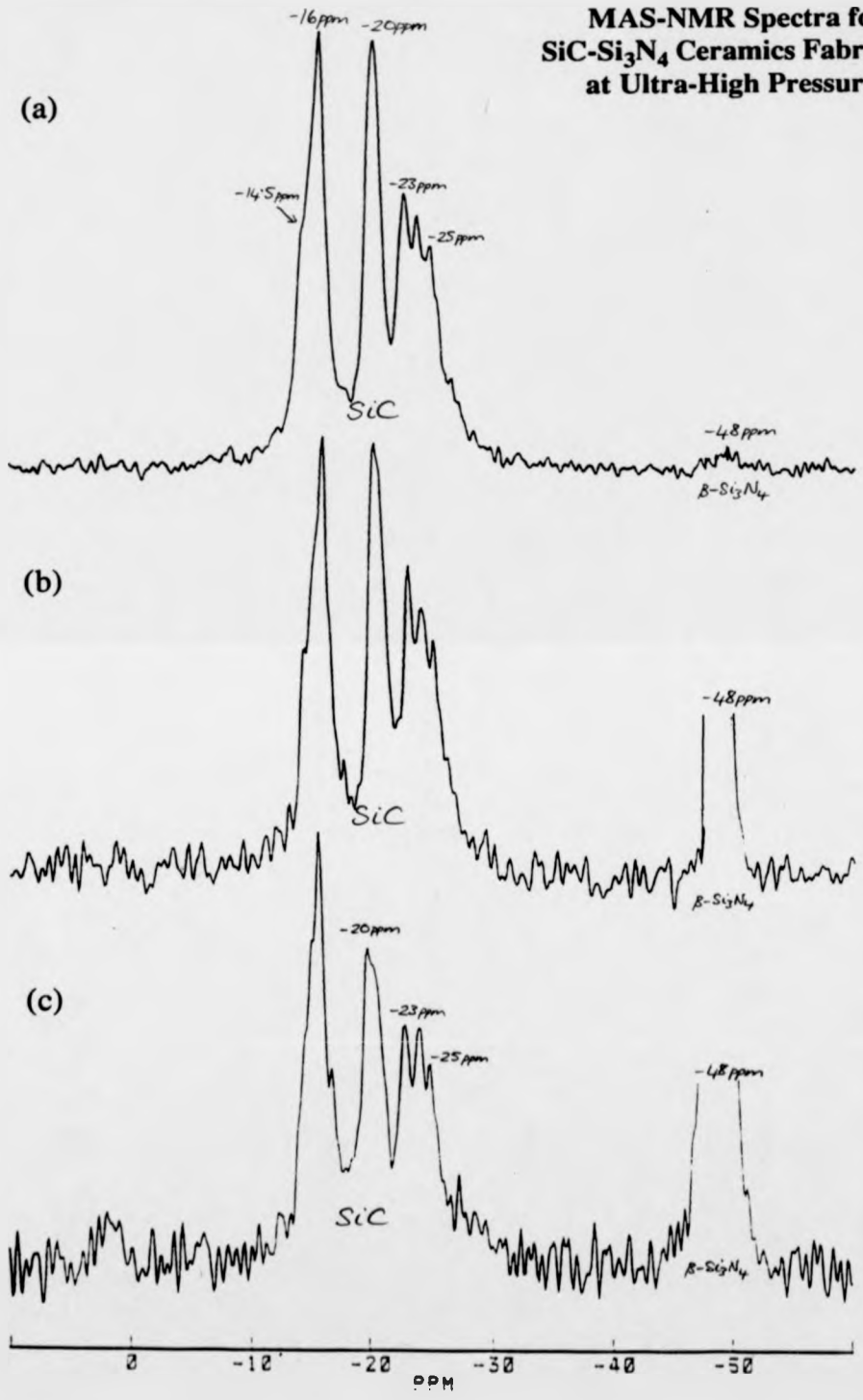

Figure 4.20: ^{29}Si chemical shifts (from the tetramethylsilane reference peak) for three SiC-Si_3N_4 composites fabricated at ultra-high pressures, using a three minute relaxation delay time.

spectrum (a), there is very little evidence of the β-Si_3N_4-based matrix phase (represented by the small peak at -48 ppm [155]) from which it is believed that the SiC concentration is in fact much higher than the stated 80 wt%. However, there is little difference between the SiC peaks of figures 4.20 (a) and (b), which is contrary to what would be expected if any SiC structural changes had been influenced by the presence of the (sintering additive) liquid phase which would assist a diffusion-based mechanism. The specimen giving rise to spectrum (c) was fabricated under UHP conditions that differed from those for (a) and (b) on account of changes made to the construction of the high pressure sintering capsule which were expected to slightly reduce the applied pressure, but have little effect on the sintering temperature and the increased sintering time of one hour for this particular fabrication experiment. The different UHP fabrication conditions are believed to explain the much greater relative intensity of the peak at -15.8 ppm and the different relative peak intensities between -22 and -25 ppm in figure 4.20 (c), as compared with figures (a) and (b). In all three spectra, the peaks appear superposed on a diffuse background resonance; a feature that is indicative of some crystalline disorder. Another similarity is in the pronounced asymmetry of the peak at -16 ppm which appears to be overlapping another peak between -14 and -15 ppm. The presence of another unresolved peak may also explain the asymmetry in the more central peak at -20.3 ppm.

To ascertain whether these spectra were truly representative of the ceramic specimens and had not been saturated by too frequent signal pulsing, an additional experiment was carried out using a longer relaxation delay time of 30 minutes. The specimen with the highest SiC content was used for this experiment and the spectrum given in figure 4.21 (a) should be compared with that of figure 4.20 (a) to identify the changes due to different relaxation delay times. (The small peak due to β-Si_3N_4 has now become hidden by signal noise.) Although it is tempting to conclude that the peak at -14.5 ppm may be attributable to background noise, this peak occurs at the same position as the shoulder on the peaks at -16 ppm in figure 4.20 and this gives credibility to the peak now resolved at -14.5 ppm. In addition, the longer relaxation delay led to improved resolution of peaks between -22 and -25 ppm, suggesting that these peaks had been saturated during the experiments with a three minute relaxation delay. This can be

Comparison of MAS-NMR Spectra for UHP-processed SiC platelets and the 'as received' platelets.

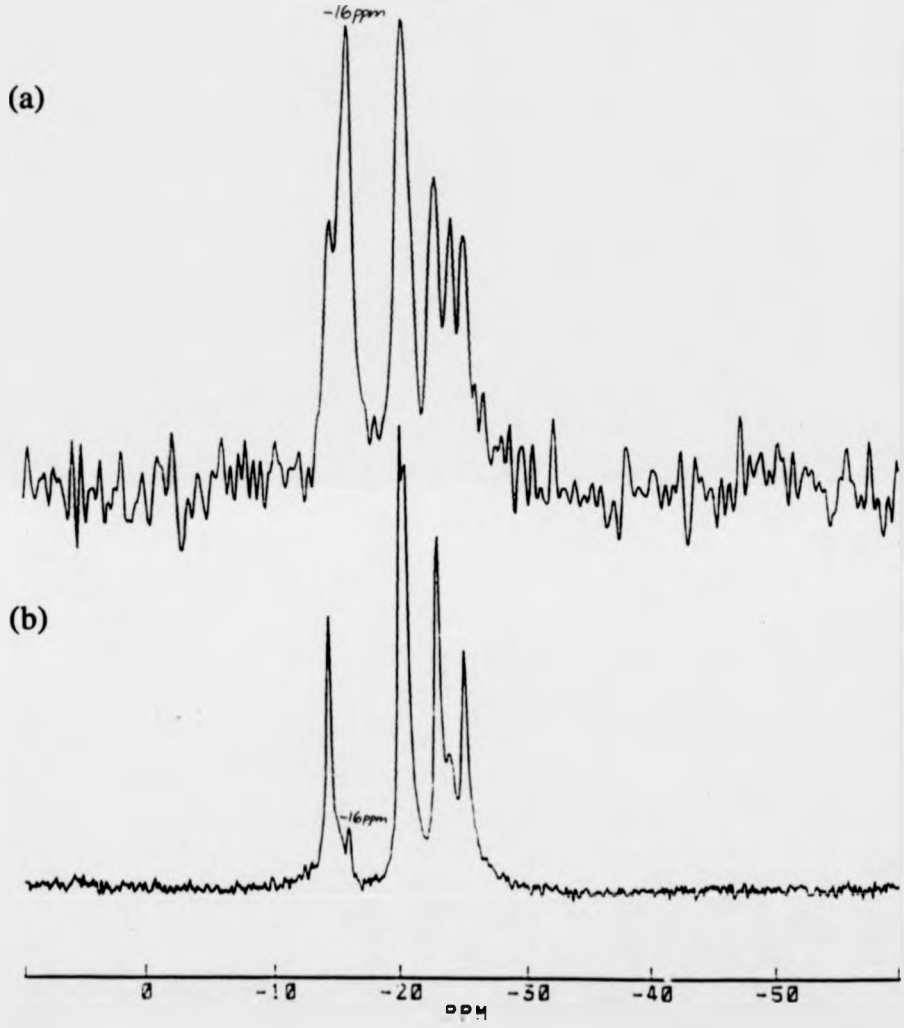

Figure 4.21: ^{29}Si chemical shifts (from the tetramethylsilane reference peak) for (a) a SiC-Si_3N_4 composite (with >80 wt% SiC) fabricated at ultra-high pressures and (b) the 'as received' SiC platelets. Both spectra were acquired using a 30 minute relaxation delay time.

explained by the corresponding SiC lattice sites having particularly long spin-lattice relaxation times, as is discussed by Hartman *et al.* [151].

Comparison of the post-UHP spectrum for the platelets with that for the original (i.e. 'as received') platelets, in figure 4.21 (b), reveals that the individual peaks in the ^{29}Si chemical shift spectrum have been markedly broadened as a result of the UHP processing, suggesting an increase in crystalline disorder, consistent with the observations made from the XRD spectra (section 4.7). The broadening of the spectrum after UHP treatment partially obscures the original peak at -14.5 ppm and also, may be preventing resolution of the two closely spaced peaks at -20.1 and -20.4 ppm in the original spectrum. A particularly striking difference between these spectra is the apparent growth of the peak at -16 ppm, in figure 4.21 (a), relative to the very small peak at this position in the original spectrum (figure 4.21 b). Other differences between figures (a) and (b) can be seen in the relative intensities of the peaks between -22 ppm and -25 ppm.

4.8.2 *SiC Polytype Identification Using ^{29}Si Chemical Shift Data*

Using the SiC phase identification obtained by XRD and the results of the published research which examined the characteristic chemical shifts in the more common SiC phases (summarised in appendix C), it was possible to identify the various chemical shift positions of the unprocessed platelets with those of the different SiC polytypes. In table 4.3, the chemical shifts have been analysed for the spectrum shown in figure 4.21 (b), in which the best peak resolution was obtained.

Table 4.3: Analysis of chemical shifts for the 'as received' SiC platelets.

Si chemical shift (in ppm)	Relative peak intensity	SiC Polytype
-20.1 -22.9	very strong strong	4H
-14.5 -20.5 -25.0	medium very strong medium	6H
shoulder, between -14.5 and -15.5 -23.9	weak weak	15R
-15.9	very weak	3C

The particularly strong intensity of the peaks between -20.1 and -20.5 ppm is believed to arise from some overlapping of peaks for the 4H and 6H phases and probably also from the 15R peak expected to lie in this region. The remaining two peaks ascribed to the 6H phase are of fairly similar intensity, in accordance with the 6H lattice sites being equally populated and the greater intensity of the 4H peak at -22.9 ppm is consistent with there being a greater proportion of the 4H phase [65]. Having identified the most intense peaks with the 4H and 6H phases, the presence of other polytypes, such as 15R SiC and trace amounts of 3C SiC is suggested by the weaker peaks. An analysis of the phases present in the post-UHP processed platelets is presented in table 4.4, for data taken from the spectrum in figure 4.21 (a).

Table 4.4: Analysis of chemical shifts for SiC platelets processed at ultra-high pressures.

Si chemical shift (in ppm)	Relative peak intensity	SiC Polytype
-15.9	very strong	3C
-20.2	very strong	4H/ 6H/ 15R
-22.8	strong	4H
-14.5	medium	6H
-24.1	medium	15R
-25.0	medium	6H

4.8.3 *The Structural Stability of Silicon Carbide Platelets During Ceramic Fabrication*

Additional MAS-NMR experiments were conducted to establish whether these observed structural changes were caused by the extreme pressures or the high sintering temperatures. Such experiments involved SiC platelet-Si_3N_4 ceramics that had been fabricated by hot pressing at 20 MPa and 1700°C and by hot isostatic pressing (HIP) at 160 MPa and 1725°C. (The HIPed ceramic was prepared by Dr. S. M. Ketchion, University of Warwick, using a separate batch of SiC platelets.) In figure 4.22, the spectrum for the UHP-processed SiC is reproduced from figure 4.20 for ease of comparison. The ^{29}Si chemical shift peaks at -47 and -48 ppm in figure 4.22 (b) arise from a mixture of the α and β-Si_3N_4 phases [155] which were also present in the hot-pressed ceramic. The peaks associated with the SiC lattice sites in the hot-pressed ceramic show little difference from those in the spectrum for the unprocessed platelets.

The Effect of Different Sintering Conditions on the MAS-NMR Spectra for SiC platelets.

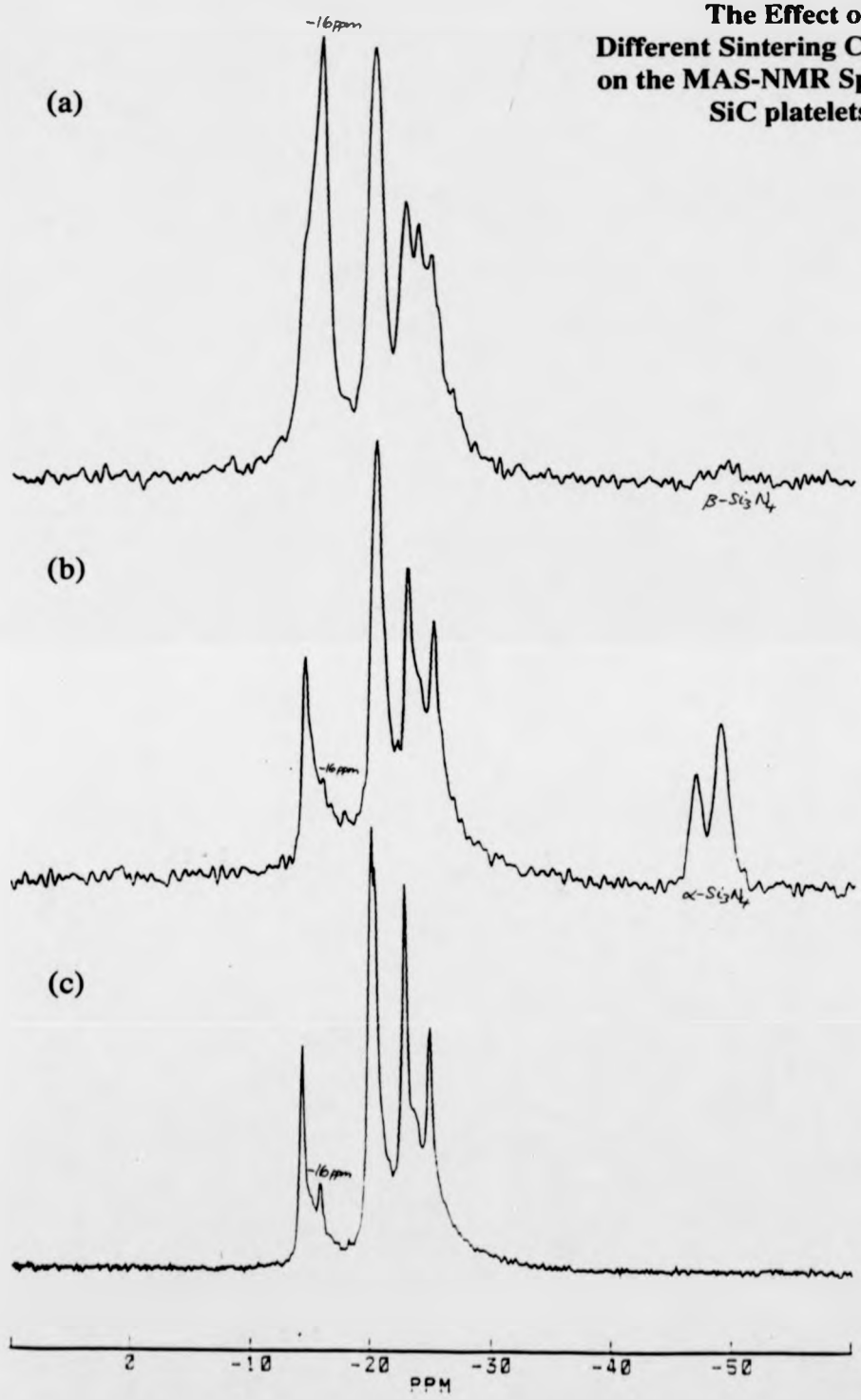

Figure 4.22: Comparison of the ^{29}Si chemical shifts (from the tetramethylsilane reference peak) for SiC platelets subjected to different processing conditions: (a) from a UHP-sintered ceramic (reproduced from figure 4.20 a); (b) from a SiC-Si_3N_4 composite fabricated by hot-pressing at 20 MPa; (c) from the 'as received' SiC platelets.

In figure 4.23 (a) the peak at -48 ppm is associated with the β-Si_3N_4 phase and the remaining peaks, associated with SiC lattice sites, show a strong resemblance to the spectrum for the unprocessed platelets. Figure 4.23 (b) was obtained with a shorter relaxation delay of one minute and this may explain the more prominent diffuse background, as the structurally disordered features would be expected to have much shorter relaxation times [150].

Both the hot-pressed and HIPed ceramics were fabricated at temperatures believed to be comparable with those attained during the UHP ceramic fabrication and yet no significant SiC structural changes were revealed by the MAS-NMR spectra taken from these ceramics. Therefore, the experiments infer that the observed differences between the ^{29}Si chemical shifts for the SiC platelets before and after UHP processing were not caused solely by the high sintering temperatures, but by the application of extreme pressures.

However, it was found that the structural changes could not be effected by the extreme pressures alone. A final experiment was carried out to subject SiC platelets to the same UHP conditions as were used in ceramic fabrication, but at ambient temperature. No change in atomic structure was indicated by the MAS-NMR spectrum obtained from the platelets after this experiment (figure 4.24), from which it was inferred that the combination of both high temperature and extreme pressure was necessary to induce structural changes in the platelets.

Another observation, revealed by comparison of figures 4.22 and 4.23, is a variation between the different SiC batches. In particular, for the HIPed ceramic (fabricated from an 'earlier' batch of SiC platelets), the peak at -16 ppm is of a much greater intensity than that for the hot-pressed material. A chemical shift of -16 ppm (from tetramethylsilane) has been identified as being the characteristic, single resonance peak for the 3C polytype [151-153]. Therefore, the stronger intensity of this peak in figure 4.23 suggests there to be a higher proportion of 3C SiC (also known as β-SiC) in the platelet component of the HIPed ceramic.

The dramatic growth of a peak at -16 ppm in the chemical shift spectra for all the SiC-Si_3N_4 composites sintered at UHP conditions is indicative of a systematic mechanism for the polytypic phase transformation in the SiC platelets. As the presence

The Effect of HIPing on the MAS-NMR Spectrum for SiC platelets

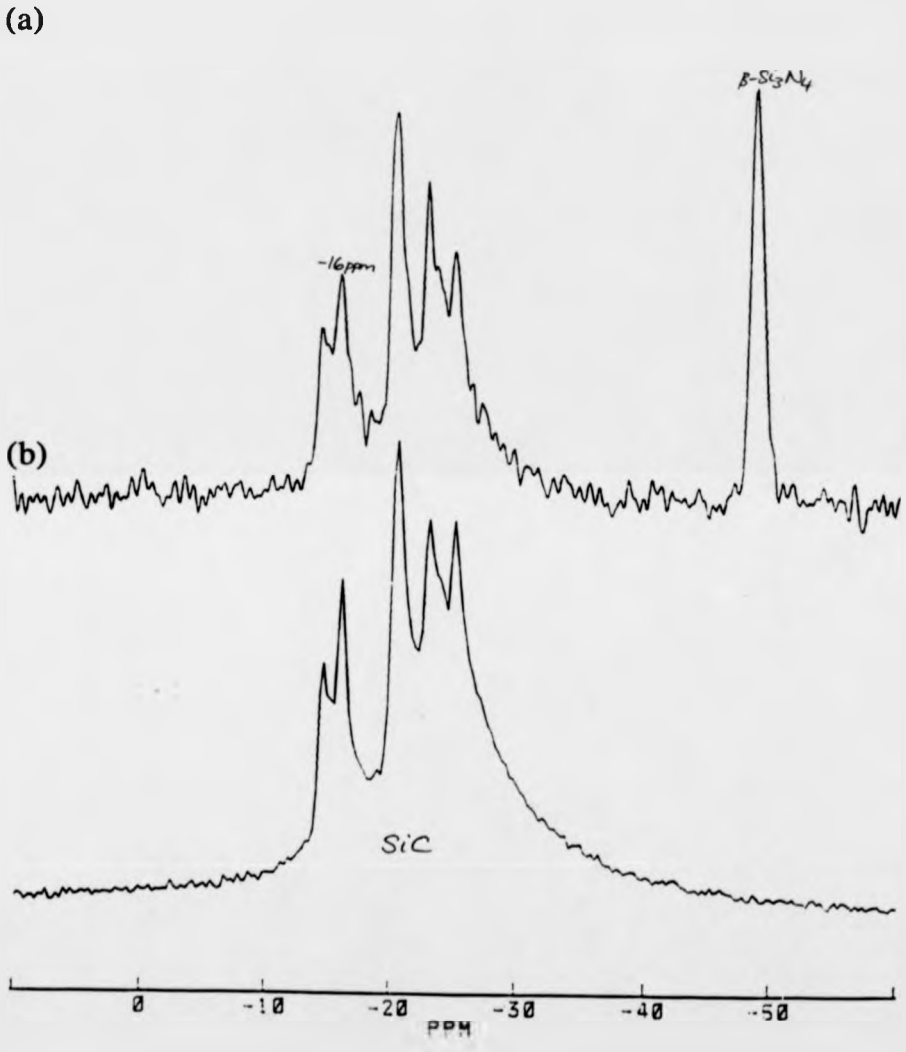

Figure 4.23: ^{29}Si chemical shifts (from the tetramethylsilane reference peak) for (a) a SiC-Si_3N_4 composite that had been fabricated by HIPing at 160 MPa and 1725°C and (b) the unprocessed SiC platelets used for the composite fabrication.

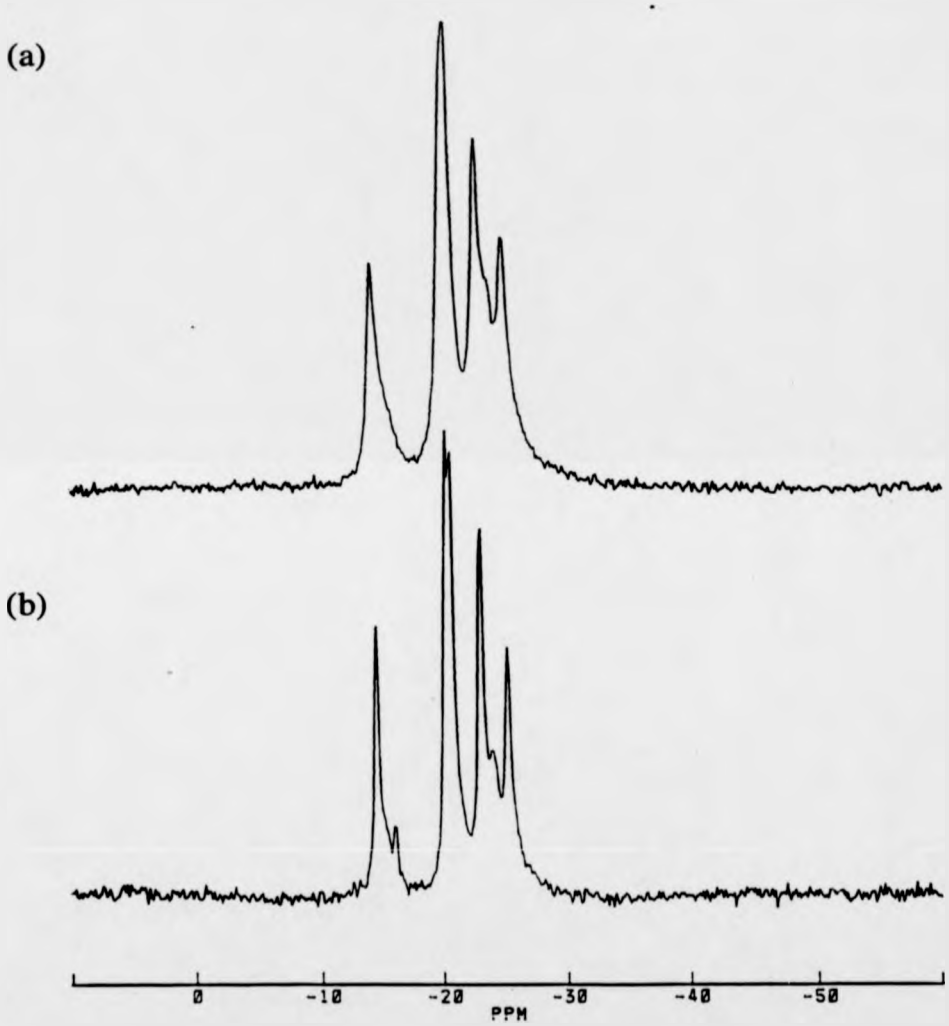

Figure 4.24: ^{29}Si chemical shifts (from the tetramethylsilane reference) for (a) SiC platelets subjected to ultra-high pressures at ambient temperature and (b) the 'as received' SiC platelets.

of the sintering additive liquid phase appeared to have no influence on this mechanism, it is proposed that the structural changes were caused by a diffusionless ('martensitic') phase transformation.

4.9 TRANSMISSION ELECTRON MICROSCOPE INVESTIGATION OF THE PHASE TRANSFORMATION IN SILICON CARBIDE PLATELETS

The microstructure of the SiC-Si_3N_4 composites fabricated at UHP appeared to be similar to that of the composites fabricated by hot-pressing when examined by SEM (figure 4.25). However, TEM observations made on the SiC platelets have revealed significant structural changes within the platelets themselves. Figure 4.26 shows the extensive plastic deformation induced in the SiC platelets by the UHP processing conditions and this includes stacking faults and 'kink' boundaries within the individual platelets. Severe stacking fault and twinning deformation is visible in figure 4.27, on multiple platelet planes. A platelet microcrack can also be observed in this figure (bottom right). The diffraction pattern (inset) consists of two superposed [$10\bar{1}0$] diffraction patterns, rotated in relation to each other by 66°; with streaking arising from the fine stacking faults and in a direction perpendicular to the fault planes. The diffraction pattern strongly resembles a [110] cubic pattern, but evidence for the superposition of two [$10\bar{1}0$] patterns is revealed by the higher order reflections, which are not coincident.

A survey of [$10\bar{1}0$] SiC diffraction patterns, from which the different polytypic structures can be distinguished is presented in figure 4.28. In these examples, streaking is visible along the c-axis direction and this arises from stacking fault deformation. The first two diffraction patterns (a and b) are typical examples of those found in the SiC platelets in hot-pressed composites and indicate the presence of the 4H polytype and also, the 15R polytype, which lends credence to the tentative identification of this phase from the MAS-NMR spectra (see table 4.3). The next three patterns (c, d and e) were taken from platelets in the UHP-fabricated composites and are representative of the 4H, 15R and 6H polytypes respectively, indicating the retention of these phases following the UHP sintering. The last pattern (f) is the [110] pattern from the 3C SiC phase, in

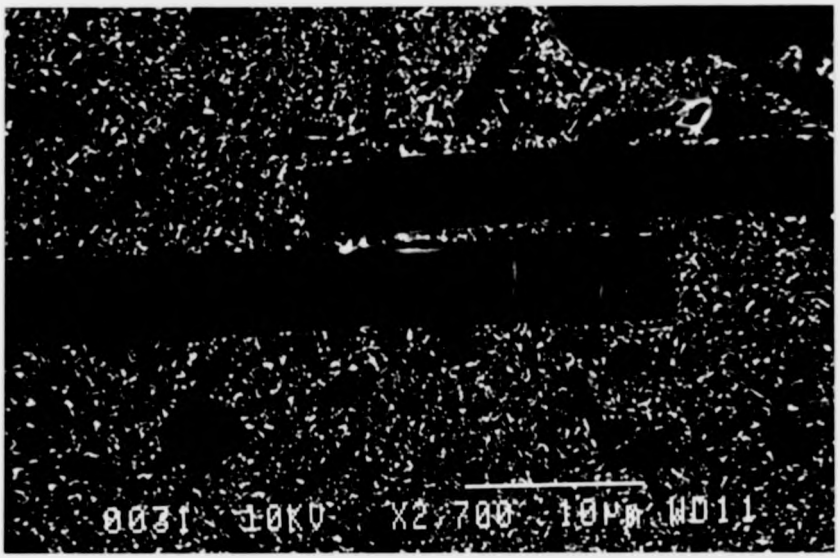

Figure 4.25: Back-scattered SEM image taken from a SiC-Si_3N_4 composite fabricated at UHP, showing (relatively large) SiC platelets, viewed perpendicular to the platelet plane, dispersed in a β-Si_3N_4-based matrix phase.

Figure 4.26: Bright field TEM image demonstrating extensive plastic deformation of the SiC platelets, including stacking faults and 'kink' boundaries within individual platelets.

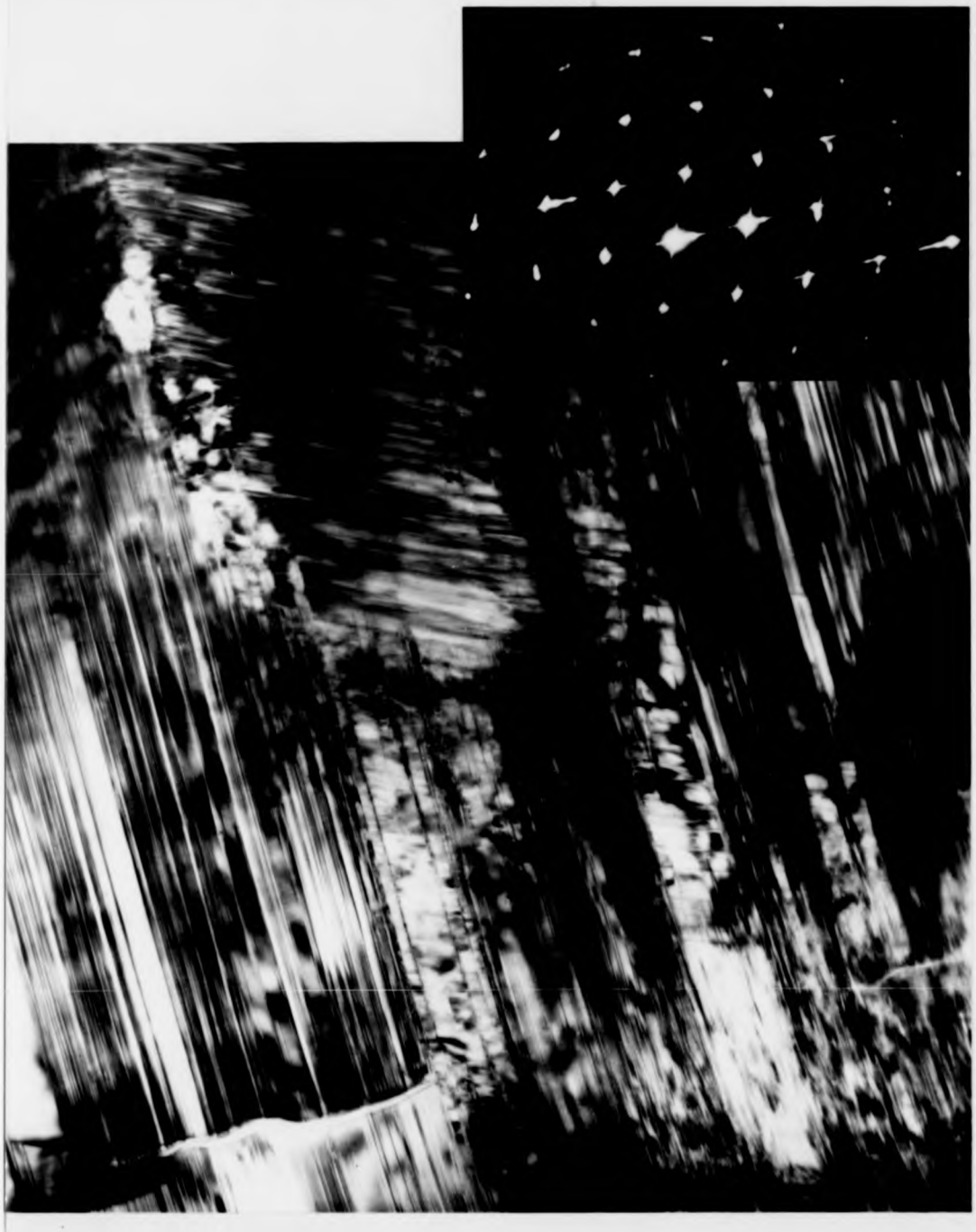

Figure 4.27: Bright field TEM image of severe stacking fault deformation on multiple platelet planes. Inset: Superposition of two [10$\bar{1}$0] diffraction patterns, with streaking arising from the fine stacking fault deformation.

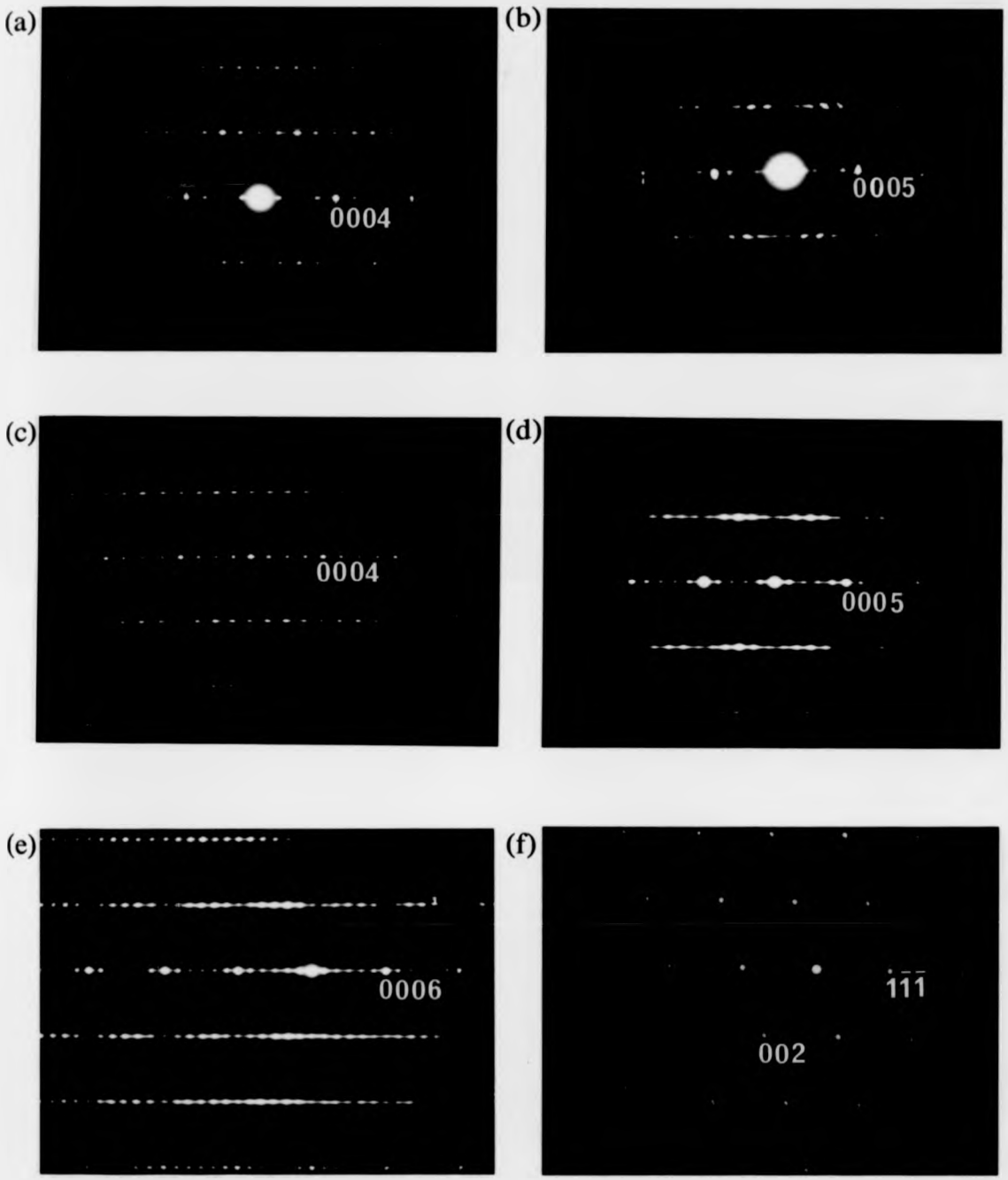

Figure 4.28: Selected area electron diffraction patterns used to identify the presence of different SiC polytypes in SiC-Si_3N_4 composites. Patterns (a) and (b) were obtained from SiC platelets in a hot-pressed composite whereas patterns (c), (d), (e) and (f) were obtained from platelets in UHP-fabricated composites. The identity of the patterns is as follows:
(a) $[10\bar{1}0]$ zone axis, 4H polytype; (b) $[10\bar{1}0]$ zone axis, 15R polytype; (c) $[10\bar{1}0]$ zone axis, 4H polytype; (d) $[10\bar{1}0]$ zone axis, 15R polytype; (e) $[10\bar{1}0]$ zone axis, 6H polytype; (f) [110] zone axis, 3C polytype.

which the [111] direction corresponds with the c-axis direction in the hexagonal polytypes (see figure 2.9). This diffraction pattern was found only in the UHP-fabricated composites, suggesting that the 3C phase was formed at the extreme conditions during UHP-processing.

An example of the partial transformation of a 6H SiC platelet to the 3C phase is given in figure 4.29. The spacing between the fine striations was identified with lattice fringes from the (0001) basal planes and the irregularities in their periodicity were attributed to stacking fault deformation. No lattice fringes could be resolved in the region inbetween bands exhibiting the striped contrast and of about 80 nm in width. It is most likely that this is due to a shorter-range atomic order in this region rather than to a variation in thickness, which would not be expected to show such sharply defined boundaries. The corresponding diffraction pattern was identified as a superposition of the $[10\bar{1}0]$ 6H diffraction pattern (with streaking characteristic of the stacking fault deformation) from the region with striped contrast and the [110] 3C pattern which was associated with the band of shorter-range order. The orientational relationship between the 6H and 3C polytypes is such that the {0001} 6H planes lie parallel with the {111} 3C planes. This is the relationship that would be expected if the 6H phase had transformed into the 3C phase via a change in stacking sequence along the c-axis. A higher resolution image of the basal plane periodicity in a 6H platelet is given in figure 4.30, in which the distance between the most closely spaced lines corresponds with the 6H c-axis lattice parameter. Very wide stacking fault discontinuities are evident in this image and it is possible that some of the wider bands, in which no finer structure is discernable, may be thin lamellae of the 3C phase.

Extensive dislocation networks were also observed at orientations near to the [0001] zone axis in UHP-processed platelets whereas similar observations were not made on platelets in hot-pressed composites. Figure 4.31 is a typical image of inclined dislocations, viewed along the [0001] axis.

Although no examples of 4H transformation to the 3C phase have been presented, further investigations are required, on account of the selective nature of the TEM technique, to establish conclusively if this transformation had also occurred.

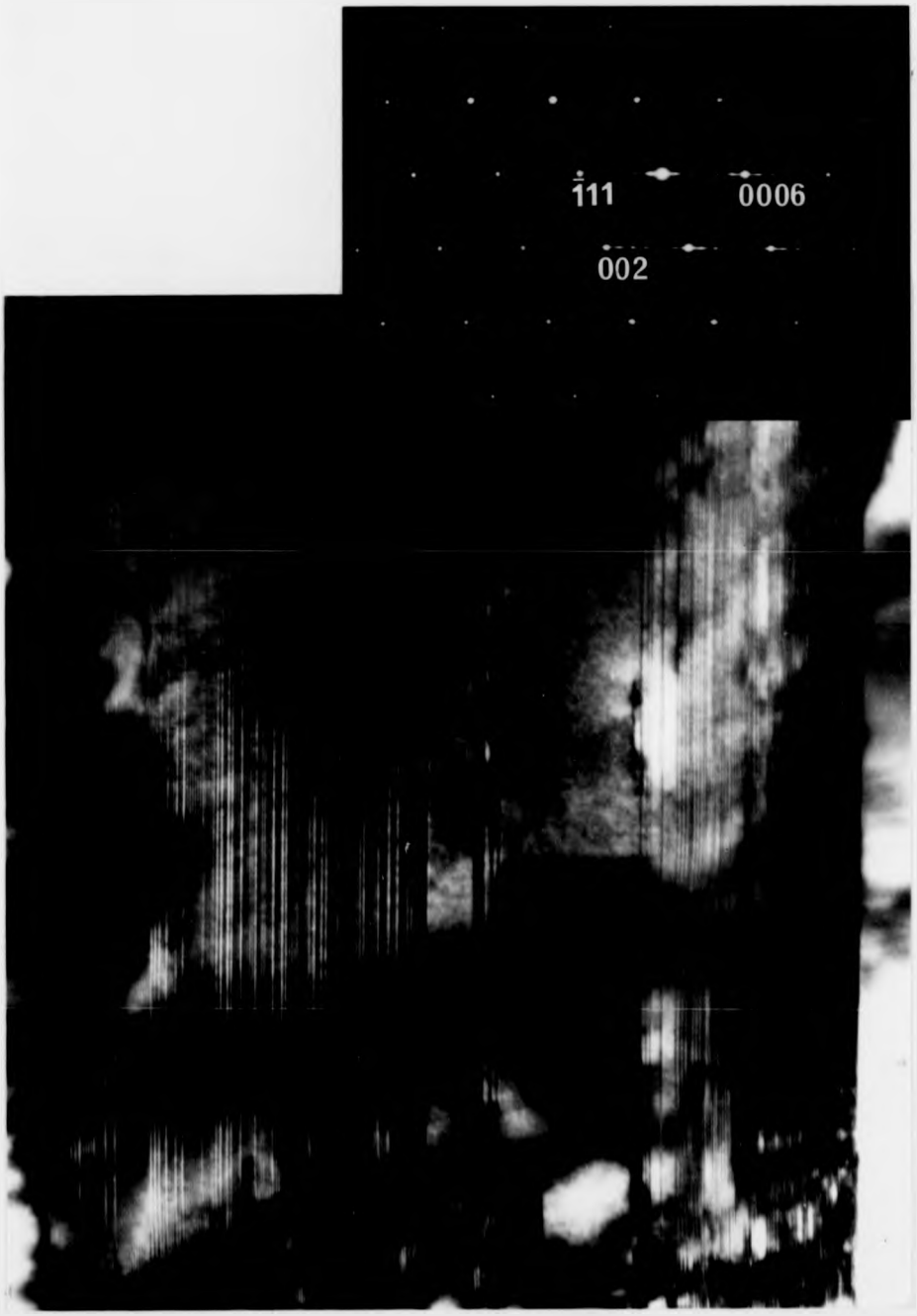

Figure 4.29: Bright field TEM image of a 6H SiC platelet, viewed perpendicular to the basal planes to reveal the structural periodicity along the c-axis. Inset: overlapping diffraction patterns from regions of the 6H and 3C SiC phases.

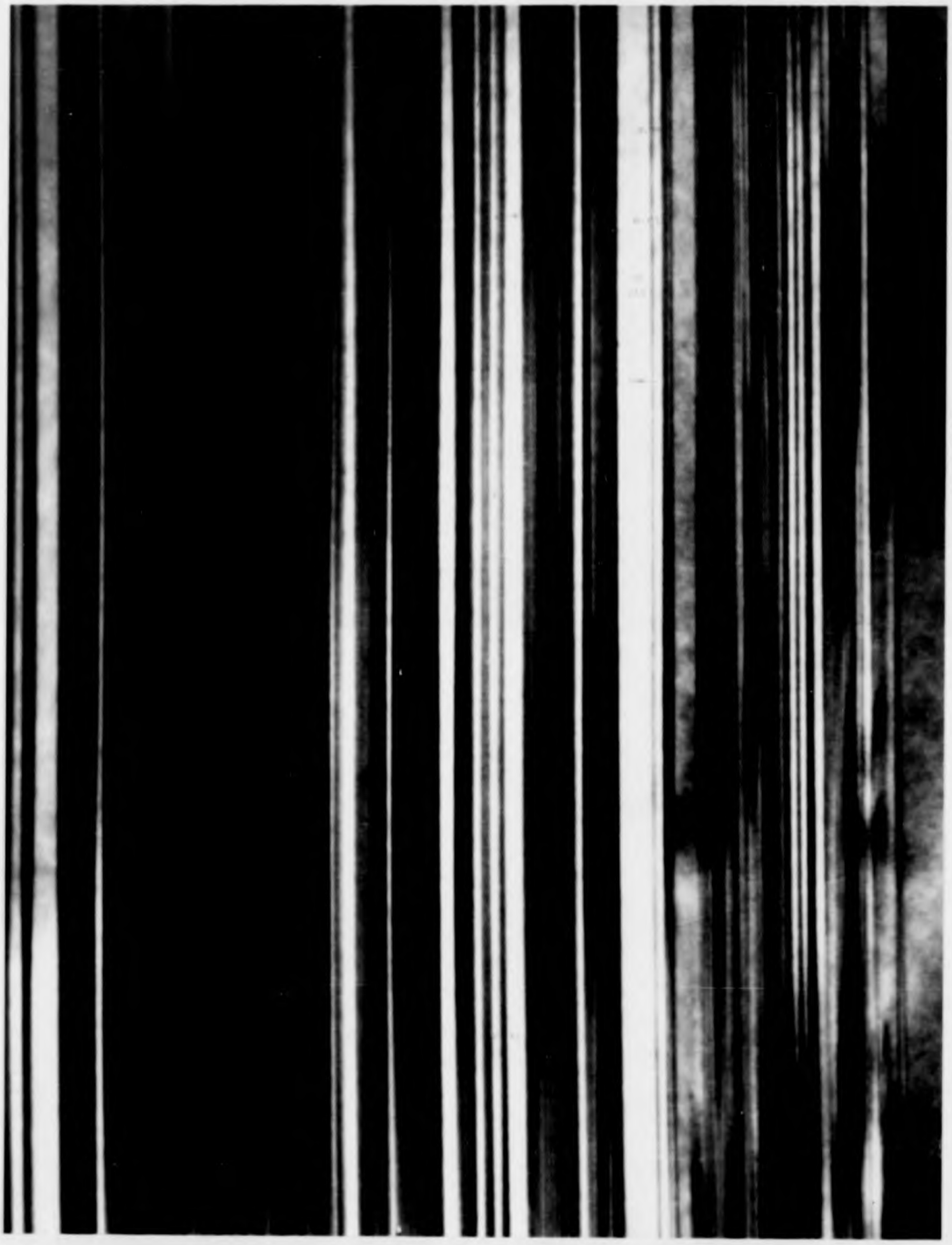

Figure 4.30: Bright field TEM image of a SiC platelet, viewed perpendicular to the basal planes. The distance between the most closely spaced lines corresponds with the 6H c-axis parameter.

Figure 4.31: Bright field TEM image of inclined dislocations viewed along the [0001] zone axis.

4.10 DISCUSSION OF THE HIGH-PRESSURE PHASE TRANSFORMATION IN SILICON CARBIDE PLATELETS

The results discussed in this chapter provide clear evidence for a hexagonal to cubic SiC phase transformation having been induced in the SiC platelets by the ultra-high pressure sintering conditions. Very similar evidence has also been observed recently by Yang *et al.* who identified a partial transformation of the 6H polytype to the cubic phase following compression tests on single crystals at 1100°C and shear stresses of about 50 MPa [156]. Yang and Pirouz [157] have found further evidence for this being a stress-induced transformation from the observation of narrow bands of 3C SiC (with some deformation twinning) within a 6H single crystal in the vicinity of indentations made in a vacuum at 1170°C, using an indenter load of 300 g. Other investigations into the SiC polytypic transformations (including a 2H to 3C transformation) have also been discussed by Pirouz and Yang [158]. Their conclusions that such phase transformations are both time and temperature dependent are in agreement with the results of this research. A possible mechanism for the phase transformation is discussed below, being suggested by the results presented in this chapter.

4.10.1 *Mechanism for the Hexagonal to Cubic Silicon Carbide Phase Transformation*

The results of the MAS-NMR and TEM experiments revealed that the UHP sintering conditions caused considerable plastic deformation within the SiC platelets, but that this occurred by a systematic mechanism, leading to a diffusionless ('martensitic') phase transformation to the cubic phase. The co-operative motion of partial dislocations is considered to provide the transformation mechanism. Dislocation glide has been observed to play an important role in the 'martensitic' phase transformations in wurtzite (hexagonal ZnS) crystal structures [159] and in silicon [160] and similarly could explain a transformation in hexagonal SiC.

In figure 4.29, the orientation relationship between the newly-formed 3C phase and the parent 6H phase indicates that the transformation mechanism may have been

accomplished by alteration of the stacking of SiC double layers along the 6H c-axis. This could be achieved by shearing atoms in the basal planes by exactly the amount required to translate the atoms to the next atomic site positions. This could occur from the glide of partial dislocations having the Burgers vectors identified from the dissociation of perfect screw dislocations on the basal planes of SiC [131]. Shearing the atoms above the glide plane by these vectors ($^a/_3$ [01$\bar{1}$0] and $^a/_3$ [$\bar{1}$010]) would transform A planes into B planes, B into C and C into A. In addition, the atoms at the bases of those tetrahedra containing the glide planes would remain invariant during this process, causing the tetrahedra to transform into twinned variants (related to the untransformed tetrahedra by a rotation of 180° about the c-axis). It is considered that the dislocation glide could be repeated on consecutive basal planes via the 'flipping' of the parent screw dislocation onto planes parallel to the c-axis, eventually leading to the formation of the 3C stacking sequence. This is illustrated in figure 4.32, where the transformed tetrahedra are shown in boxes, dislocation glide is represented by horizontal arrows and the vertical arrows represent 'cross-slip' of the dislocation onto planes parallel to the c-axis.

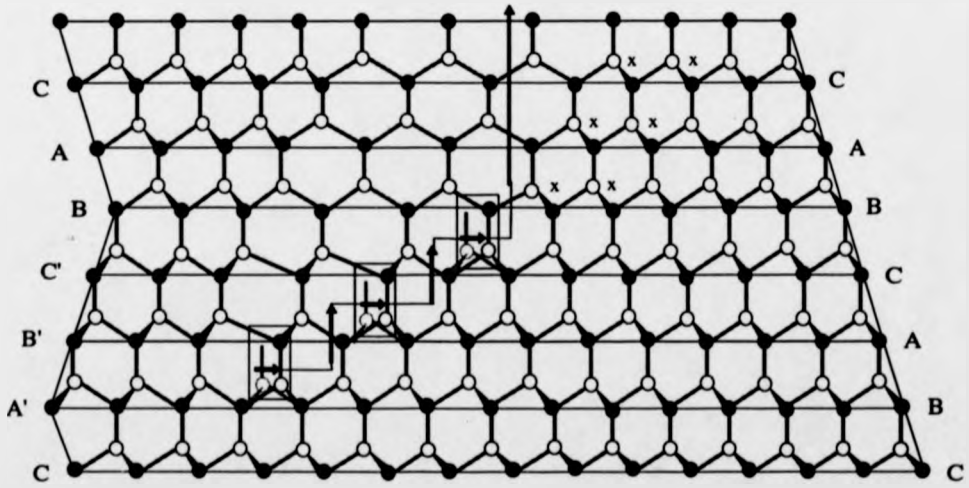

Figure 4.32: The sequential change in stacking sequence from that for 6H SiC (left) to that of the cubic, 3C phase (right) via repeated dislocation glide on consecutive basal planes. The vertical direction is parallel to the c-axis.

It should be noted that the partial dislocations are unable to shear atoms above the glide planes of the B, A and C layers to the positions marked 'x' on the figure. This would not

result in an energetically favourable stacking configuration and would violate the 'stacking rule' whereby the layers of Si and C atoms are arranged such that they share tetrahedral interstices. Therefore, the parent dislocation is unable to dissociate on the B, A and C planes and so cross-slips to the next A' plane, from which the process can be repeated.

Recently, Pirouz has proposed a similar mechanism which can explain the polytypic phase transformations in SiC [161] in greater detail. The main requirement of the mechanism is a pinned screw dislocation segment on the (0001) glide plane which dissociates into two partial dislocations with the Burgers vectors $^1/_3$ <10$\bar{1}$0> and $^1/_3$ <01$\bar{1}$0>. The different mobilities of these partial dislocations (arising from the different energies involved in the breakage and reformation of C-C and Si-Si bonds along the dislocation cores) forms the basis for this mechanism. Under the action of a sufficiently large resolved shear stress on the (0001) glide plane, Pirouz proposes that the partial dislocation with the greatest mobility becomes detached from the 'trailing' partial and forms a faulted loop (changing the stacking sequence of the enclosed crystal planes) on the glide plane, after which the relative mobilities of the partial dislocations become reversed. The screw dislocation is then able to 'cross-slip' onto a prism plane (parallel to the c-axis) and then is driven to cross-slip back to the next available (0001) glide plane (as discussed by Pirouz) on which a repeat of the dissociation and faulted loop formation is possible. A more detailed discussion of this mechanism can be found in references [162] and [158].

4.11 SUMMARY AND CONCLUSIONS

Hybrid, laminated composites were fabricated using two different structural arrangements of tape-cast laminae. Preferential alignment was observed in the SiC platelets, such that the platelet planes were normal to the hot-pressing axis. This was attributed to both the tape casting and hot-pressing. The onset of densification was observed to commence as temperatures above 1500°C were reached and post-sintering XRD observations indicated that the α to β-Si_3N_4 phase transformation had taken place during the densification, although no complete phase transformation was achieved, even

after full sintering conditions of 1710° and 30 MPa were maintained for 180 minutes. This may be due to the presence of contaminants, such as residual organics from the tape-casting process.

The microstructure of the hybrid composites exhibited distinct lamina boundaries and local density variations related to the compositions of the different laminae. Those with high volume fractions of the SiC platelets were found to contain the highest porosity levels and this was independent of the compositions of neighbouring laminae. The SiC platelets were bonded in a fine-grained matrix structure, in which evidence of the residual sintering additives was found as a glassy, yttrium silicate phase at Si_3N_4 grain boundaries.

In the UHP-fabricated composites, the α to β-Si_3N_4 phase transformation was achieved by sintering for only ten minutes at the extreme pressure conditions. Additionally, XRD observations made on these composites suggested that a structural change had taken place in the SiC platelets and this was confirmed using MAS-NMR and TEM. The broadening of the XRD and NMR spectra in the UHP-processed platelets indicated an increase in crystalline disorder which was observed as extensive stacking fault deformation and grain 'kinking' by TEM. The appearance of the 3C SiC phase, present only as a trace amount in the 'as recieved' platelets was identified from interpretation of the NMR spectra and supported by observations of the partial transformation of 6H SiC into the cubic phase.

The MAS-NMR experiments indicated that this phase transition took place only under the extreme conditions of UHP sintering and no similar observations were made on SiC platelets that had been hot-pressed or HIPed. A mechanism for thc 6H to 3C transformation is described which requires the mobility of partial dislocations. Hence, this is only possible with the simultaneous application of stress and temperature.

Chapter Five

ULTRA-HIGH PRESSURE FABRICATION AND MICROSTRUCTURE OF CUBIC BORON NITRIDE / SILICON NITRIDE COMPOSITES

5.0 INTRODUCTION

This chapter presents the results of the research concerned with the superabrasive, cBN-containing composites. Polycrystalline cubic boron nitride ceramics are now fairly well established for wear-resistant applications and are mass-produced using specialised ultra-high pressure (UHP) equipment. However, promisingly high microhardness values have been reported from the so far limited research on cBN-Si_3N_4 ceramics, reviewed in section 2.3.4. This work differed from the research previously reviewed [116, 117] in two important respects. Firstly, phase transformation of boron nitride to the cubic phase did not take place, as cubic BN powder was used as a starting material. This choice was based on the assumption that greater pressures are required to effect a phase transformation to synthesise cubic BN than to maintain the thermodynamic stability of this phase [96]. With this in mind, fabrication experiments were begun using lower pressures (4-5 GPa) than those reported elsewhere. Secondly, 'belt'-type UHP apparatus (section 3.3.1), widely used for commercial mass-production, was used and this meant that several additional factors in the fabrication process had to be taken into account.

This chapter begins with the fabrication part of the work. As there were difficulties in determining the actual pressures and temperatures achieved in the 'belt' apparatus, it was impossible to determine accurately the minimum pressure and temperature conditions required for sintering. Therefore, supplementary fabrication experiments were conducted using the tetrahedral anvil system (section 3.3.2), in which these parameters can be more easily measured.

The composite densities, phase analysis (by X-ray diffraction) and electron microscope observations are discussed in the second half of this chapter. The results of further mechanical tests on the cBN-Si_3N_4 composites are discussed in chapter six.

5.1 FABRICATION OF THE cBN-Si_3N_4 CERAMIC COMPOSITES

5.1.1 *Fabrication Objectives and Composition Selection*

The objective of the UHP sintering experiments was to fabricate, under reproducible conditions, crack-free and homogeneous cBN-Si_3N_4 composites from which specimens could be machined for mechanical testing, as well as for microstructural examination. One additional aim of this work was to fabricate large enough specimens to enable the determination of fracture toughness by mechanical bend testing without being confined to the use of less satisfactory indentation techniques by specimen size-related restrictions.

Two different cBN grain sizes were used and the compositions varied in cBN content, from 40 wt% cBN to 80 wt% cBN. However, the quantity of the sintering additives in the precursor powders was kept as a constant proportion of the matrix phase (by wt%). Although the sintering additive quantity was therefore substantially reduced in those compositions with particularly high cBN content, it was expected that the extreme pressures might enhance the sintering (following trends observed in hot-pressing and HIPing [24, 25, 31]), rendering the necessity for sintering aids less significant to the ceramic consolidation. However, it was intended that sintering should take place via the liquid phase sintering mechanism and that sufficiently high fabrication temperatures must be reached to enable this to occur.

Although most of the cBN-Si_3N_4 ceramics fabricated were of a homogeneous composition, a hybrid composite with different compositions was also fabricated from stacked, tape cast laminae. The preservation of the compositional arrangement during the UHP processing was assessed from microstructural observations.

5.1.2 *Experimental Procedures for cBN-Si_3N_4 Composite Fabrication*

Both the powder processing and sintering stages were of vital importance to the physical characteristics of the resulting ceramics. In particular, several preliminary ultra-high pressure sintering experiments were necessary to determine the operating

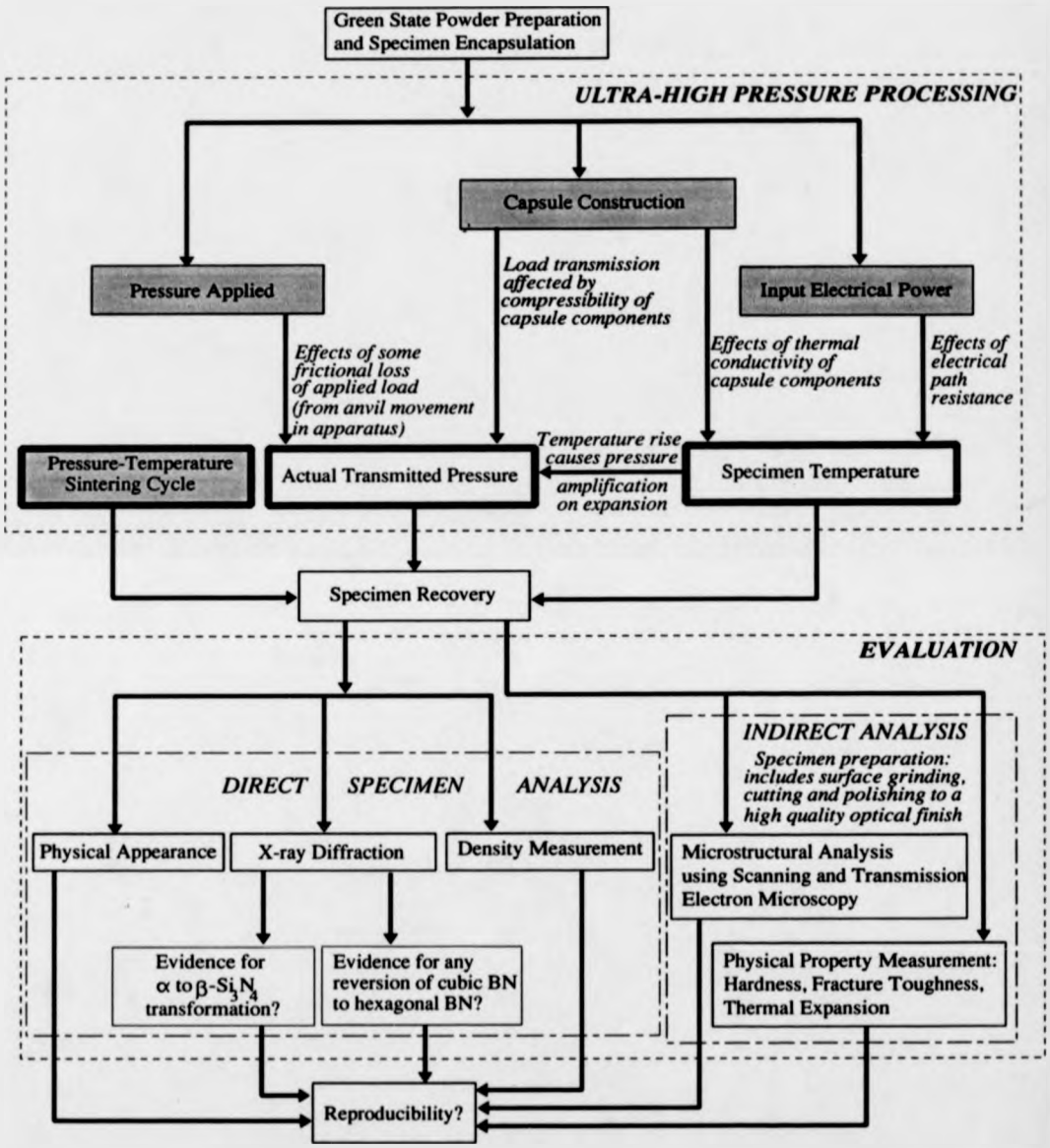

Figure 5.1: Flowchart illustrating the procedure followed for the high pressure fabrication and evaluation of cBN-Si_3N_4 ceramics. The shaded boxes in the '**ultra-high pressure processing**' section represent parameters that were varied in order to change the conditions directly experienced by specimens during the fabrication process (heavily outlined boxes). The ways in which the fabricated composites were evaluated are summarised in the '**evaluation**' section and the results are presented later in this chapter and in chapter six.

conditions at which the ceramics could be successfully consolidated. A summary of the entire procedure of fabrication and subsequent evaluation is given in the flowchart (figure 5.1). This shows the sequence of steps involved, the different factors that had to be considered during the experiments and the links between them.

5.2 GREEN STATE COMPOSITE PREPARATION

The homogeneity of the composites was largely determined by the green state mixing of the constituent starting powders. Following the failure of dry, mechanical mixing methods to provide uniform particle distribution, the starting powders were mixed in aqueous slurries, using the 'slip casting' method described in section 3.1.2. It was discovered that the slurries could be successfully cast directly into tantalum capsules (rather than porous molds) with little cracking if the fluid content was allowed to evaporate at room temperature. The slurry-filled capsules were covered and allowed to dry for about 24 hours before being placed in an oven at 100°C.

cBN-Si_3N_4 ceramic tapes were also fabricated, using the same organic chemical system as for the fabrication of SiC-Si_3N_4 tapes, discussed in section 4.2. Tape casting of the cBN-Si_3N_4 mixtures was investigated both as a means of improving the final homogeneity (as was observed in tape-cast SiC-Si_3N_4 composites) and as a first step towards extending the fabrication of hybrid composites to the fabrication of superabrasive ceramics. The observations made on the rheological behaviour of cBN-Si_3N_4 tape slurries with different compositions were consistent with those described in detail in chapter four: a higher solvent concentration being required for compositions with relatively high fine-grained Si_3N_4 concentrations. The organic mixtures that produced well dispersed cBN-Si_3N_4 tapes (using 3 μm cBN powder) were determined experimentally and are given in table 5.1.

All the green state composites were encapsulated in tantalum prior to the ultra-high pressure processing. The encapsulation was carried out by placing the composites inside a tantalum cup which was then sealed by a second tantalum cup forming a tightly-fitting lid. For some experiments, an additional pair of steel cups was used as a secondary encapsulant and these could be welded together, making the specimens 'air

tight' after vacuum treatment to remove entrapped gases. However, this practice was discontinued after it was discovered that components of the steel cups became molten and infiltrated the sintering powders during the high temperature experiments, contaminating the final ceramic.

Table 5.1: Tape formulations for cBN-Si_3N_4 tapes, with the separate component concentrations expressed as a percentage (by weight) of the tape slurry mixture.

Powder Composition	Powder Content	Solvents		Dispersant (KD1)	Plasticiser	Binder
		trichloroethane	ethanol			
20 wt% cBN in Si_3N_4-based ceramic matrix	51.4	17.5	7.2	1.2	2.2	20.5
40 wt% cBN in ceramic matrix	53.2	16.8	6.8	1.1	2.1	20.0
60 wt% cBN in ceramic matrix	54.4	16.3	6.5	1.1	2.0	19.7
80 wt% cBN in ceramic matrix	56.0	16.0	6.2	1.1	1.9	18.8

5.3 ULTRA-HIGH PRESSURE SINTERING

The most severe fabrication difficulties in this research arose on account of the interdependence and uncontrollable variability of factors arising from the operation of the high pressure apparatus. As it was found impossible to prevent deviations from truly hydrostatic conditions inside the sintering capsule, the consolidated ceramics exhibited differing degrees of cracking and lamination. The factors which most strongly influenced the pressure and temperature gradients in the sintering capsule were the capsule arrangement and the component materials themselves. To meet the technical requirements for high temperature (1700°C) sintering of the cBN-Si_3N_4 composites, a critical reassessment of some of the intricacies of the 'belt' apparatus was unavoidable. Therefore, some experiments were carried out to investigate different structural arrangements of the capsule and these are described in section 5.3.2. However, owing to the constraints imposed by the other research objectives, this was not considered in as much depth as would have been ideal.

5.3.1 *The Sintering Cycle*

The pressure-temperature cycle for the ceramic sintering is shown in figure 5.2. This was arrived at after the initial experiments had led to explosive pressure release whilst the sintering capsule was allowed to cool (over a period of ten minutes) under full pressure. The explosive situation was found to be preventable when removal of the applied pressure commenced simultaneously with the specimen cooling.

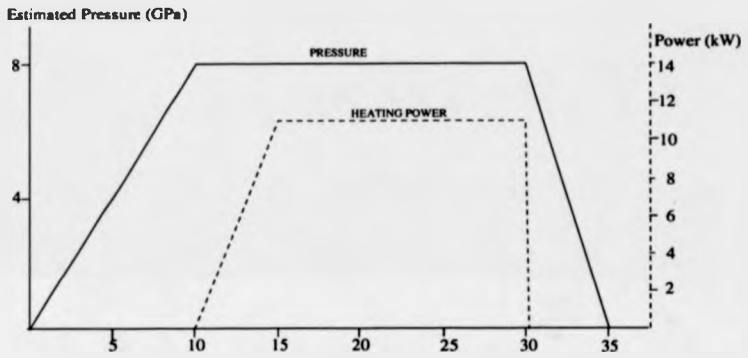

Figure 5.2: Ultra-high pressure sintering cycle for cBN-Si_3N_4 ceramics fabricated at 8 GPa. The experiments carried out at other pressures and heating powers followed the same pattern as is shown here.

5.3.2 *Capsule Modification in the High-Pressure 'Belt' Apparatus*

To begin with, the tantalum-encapsulated specimens were embedded in a standard NaCl-based sintering capsule (see section 3.3.1). However, as is apparent from the results described in section 5.7, it would seem that higher sintering temperatures were required than those reached in the production of conventional cBN ceramics. To accommodate this requirement, the commonly-used NaCl 'pressure-transmitting' medium was replaced by (granulated) boron nitride (hexagonal) powder. Whilst NaCl is known to 'transmit' the applied pressures more efficiently than hBN [83], the NaCl might become molten at higher temperatures, enabling it to corrosively attack the graphite heater sleeve. This would increase the risk of explosive pressure release whereas the higher melting point of the BN permitted the attainment of higher sintering temperatures with no phase change within the capsule components.

The replacement of NaCl by BN relieved the restrictions on the maximum operating power, but it also led to an increase in the pressure gradients within the sintering capsule, as was indicated by the severity of the cracking and lamination (in a plane perpendicular to the anvil motion) within the specimens retrieved from these experiments. Further capsule modifications were carried out to improve the pressure distribution. These involved the addition of (dehydrated) pyrophyllite and (cobalt-bonded) tungsten carbide discs to reduce the overall capsule compressibility. Additional molybdenum discs acted as a physical barrier to molten cobalt, limiting any specimen contamination from the tungsten carbide discs in the capsule.

The most promising BN-based sintering capsule that was developed is shown in figure 5.3. Further work would be needed to reduce the residual specimen cracking and lamination to comparable levels with those from NaCl-based capsules.

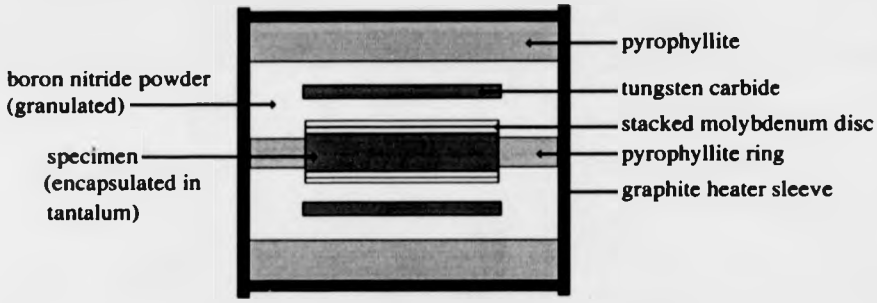

Figure 5.3: Cross section of the high temperature sintering capsule.

5.3.3 *Sources of Difficulty in Repeating The Fabrication Experiments*

A persistent problem throughout the fabrication experiments was the inability to measure the specimen temperature. One possible method for overcoming this problem in any future work might be to subject a diamond-based material to the conditions to be determined and then to make use of the well known correlations between photoluminescence spectra (from the diamond-based material) and the thermal history of the diamond compact [163]. However, during the research discussed here, the temperatures reached could only be estimated from the input electrical power and from XRD evidence for the α to β-Si_3N_4 transformation.

Further inaccuracies in estimating the fabrication conditions were due to an unknown degree of pressure amplification on heating. As a result of difficulties in determining and monitoring the actual pressure and temperature during the ceramic sintering, it was impossible to guarantee any repeat of a particular experiment, even when the operating conditions apparently remained unchanged.

Additional problems concerning apparatus stability arose during attempts to quench the ceramic phases after sintering (allowing the specimen to cool under pressure). For experiments which involved large degrees of ceramic shrinkage, further restrictions were imposed as a result of the consequent reduction of the central high pressure chamber to a critical size (beyond which the apparatus would not withstand the extreme pressures).

5.4 PHYSICAL APPEARANCE OF THE cBN-Si_3N_4 COMPOSITES

The difficulties in reproducibly fabricating the cBN-Si_3N_4 composites were clearly indicated by the variation in colour obtained from different experiments. Whilst all the ceramics fabricated at pressures above 8 GPa were processed at, as near as possible, identical conditions, the resulting composites ranged in colour from black to pale grey. In some of these, the uneven pressure and temperature distribution was manifest as a well defined boundary between a central grey zone and outer black ring around the specimen edge. In addition, ceramic inhomogeneity could be discerned as a slightly mottled appearance in many of those composites that initially had been prepared by slip casting, although this was less obvious than in the ceramics which were prepared by dry mixing.

5.5 DENSITY MEASUREMENTS

The densities of the most successfully consolidated composites are given in table 5.2. Each value is the average of measurements made on ceramic bars machined from each composite. The errors quoted are the population standard deviation (σ_{n-1}) values and the number of measurements made for each specimen ranged from six to ten.

As can be seen from the table, the composites of greatest density were correspondingly darker in colour. Apart from the first two entries in the table, the composites were fabricated at pressures above 8 GPa. Specimens 3 and 4 show an increase in density over specimen 2, as would be expected from the greater fabrication pressure, but no similar increase is apparent for the 80% cBN specimens of larger cBN grain size (specimens 10 and 11). The particularly low density of specimen 1 arises from reversion of cBN to hBN, discussed in section 5.7.

Table 5.2: The densities of cBN-Si_3N_4 composites.

Specimen	Composition	Density	% Theoretical Density	Colour	Fabrication Conditions
1	80% cBN	2.41 ± 0.01	70.2	Off-white	† 4.5 GPa, 1700°C
2	80% cBN	3.31 ± 0.02	96.5	Grey	4.5-5.0 GPa
3	80% cBN	3.39 ± 0.05	98.8	Black	8.0 GPa
4	80% cBN	3.35 ± 0.05	97.7	Black	8.0 GPa
5	60% cBN	3.36 ± 0.01	99.4	Black	8.0 GPa
6	40% cBN	3.32 ± 0.02	99.6	Black	8.0 GPa
7	40% cBN	3.20 ± 0.02	96.0	Grey	8.0 GPa
8	40% cBN	3.19 ± 0.03	95.7	Grey	8.0 GPa
9	40% cBN	3.17 ± 0.02	95.1	Grey	8.0 GPa
10	80% cBN	3.32 ± 0.02	96.8	Grey	8.0 GPa
11	80% cBN	3.28 ± 0.04	95.6	Grey	8.0 GPa

† This specimen was fabricated in the tetrahedral anvil apparatus, allowing temperature measurement.

Specimens 1 to 7 were fabricated from grade 3 cBN, whilst specimens 8 to 10 were fabricated from grade 9 cBN powder.

Despite specimens 3 to 11 being fabricated under apparently identical operating conditions, it is interesting to note that the specimens with an average cBN grain size of 9 μm (7 to 10) are of much lower density than those with average cBN grain size of 3 μm. However, there is insufficient evidence to suggest that these differences in density are due to difficulties in compacting the larger cBN grains. A more likely explanation concerns the limited control over the actual fabrication conditions and this is supported by the low density of specimen 6, for which the density measurements were for ceramic sections machined from within a central grey zone in the specimen.

All the specimens with particularly high cBN content (1, 2, 3, 9, and 10) exhibited severe macrocracking, which is a possible reason for the larger standard deviations that have been recorded for these results.

5.6 PHASE ANALYSIS USING X-RAY DIFFRACTION

X-ray diffraction (XRD) provided a means of evaluating the 'success' of the cBN-Si_3N_4 fabrication by identifying evidence for liquid phase sintering (from the formation of β-Si_3N_4) and enabling the retention of the cubic BN phase to be examined. Whilst the density results in section 5.5 might indicate some residual porosity in the composites, the lower than theoretically-predicted measurements might also be explained by the formation of the low density hBN phase (density 2.27 g/cm^3 [7]). Although this possibility was investigated using XRD, there was some unambiguous phase identification due to the superposition of the α and β-Si_3N_4 XRD spectra onto that for hBN. The hBN spectrum contains a single peak of relatively strong intensity at 26.8° (2 theta angle, arising from the (0002) planes) and this may be obscured by the third most intense peak (from the $(20\bar{2}0)$ planes) of the β-Si_3N_4 spectrum at 26.9° and partially obscured by that (from the $(20\bar{2}0)$ planes, with 50% maximum intensity) of the α-Si_3N_4 spectrum at 26.5°.

5.6.1 *XRD Results for Ceramics Fabricated at 4.0 - 5.0 GPa*

Initially, the ceramic powders were processed at 4 - 5 GPa and about 1400°C for between ten and thirty minutes, which are comparable conditions to those at which polycrystalline superabrasives are conventionally sintered. However, as figure 5.4 shows, whilst these conditions allowed good retention of the cubic BN phase, limited α to β-Si_3N_4 (below 15 wt%) conversion had occurred, suggesting that the necessary temperatures to effect liquid phase sintering had not been reached.

Figure 5.5 gives a comparison of the XRD results from three sintering experiments carried out in the tetrahedral anvil apparatus at temperatures of 1600°C-1750°C and pressures of 4.5-5.0 GPa. In all cases, the sintering time at these conditions

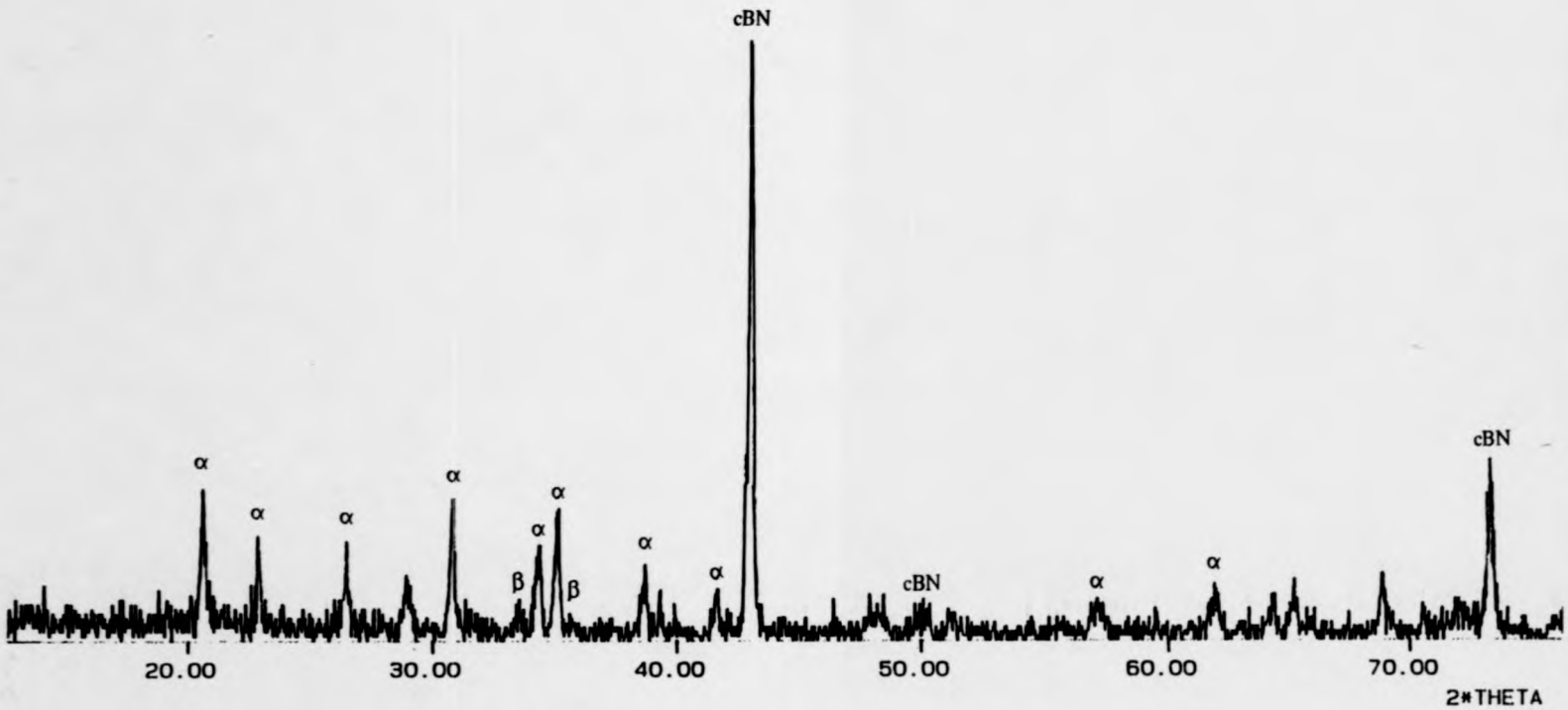

Figure 5.4 XRD spectrum acquired from a cBN (80 wt%)-Si_3N_4 composite fabricated at 4.5 GPa (in the 'belt' apparatus).

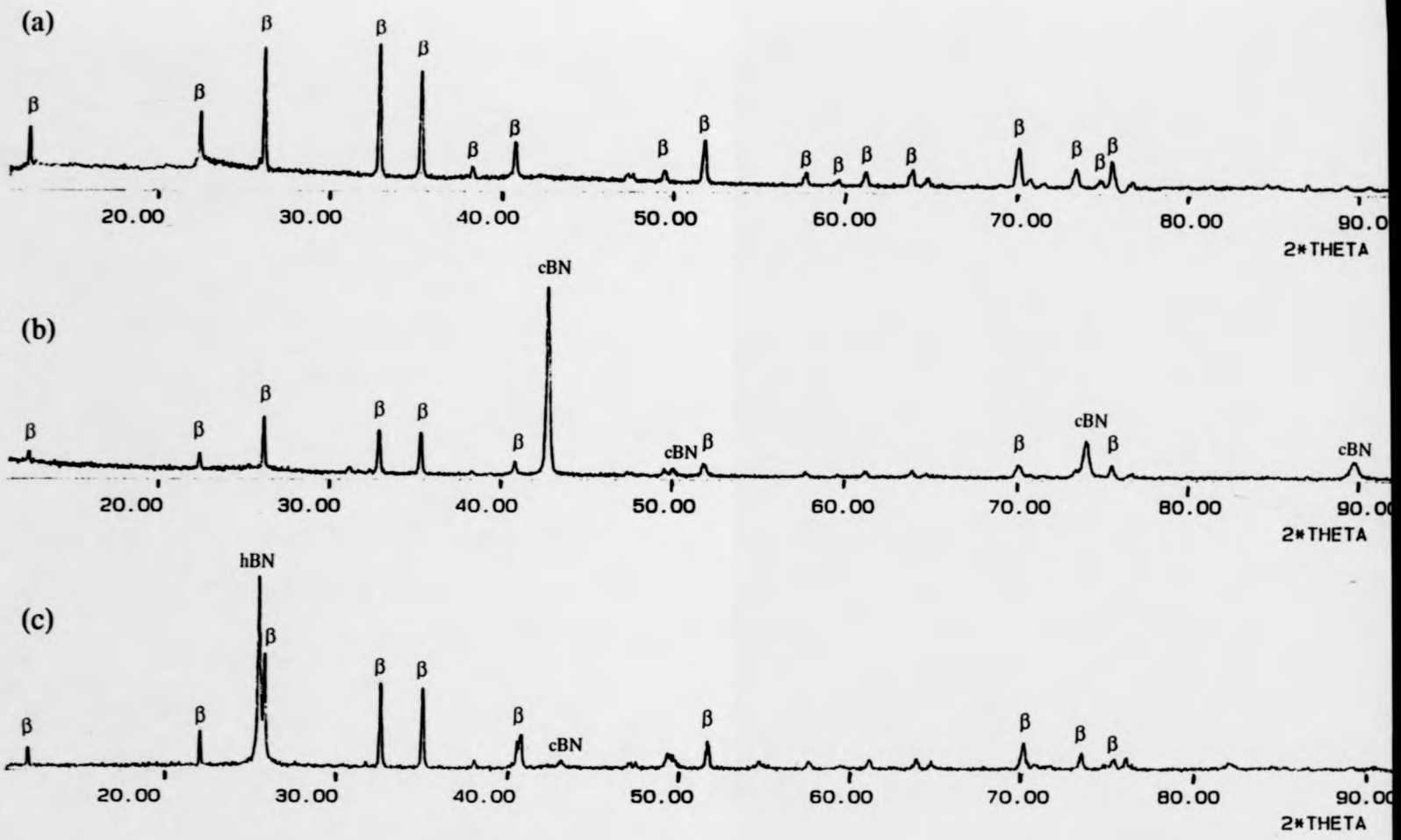

Figure 5.5: XRD spectrum fabricated at the following relatively controlled conditions in the tetrahedral anvil apparatus: (a) 4.5 GPa, 1750°C; (b) 5.0 GPa, 1700°C; (c) 5.0 GPa, 1650°C.

was ten minutes, after which the specimens were effectively quenched during the rapid cooling to about 70°C, which was achieved within one minute. As can be seen from figures 5.5 (a), (b) and (c), a complete α to β-Si_3N_4 transformation was accomplished after sintering for only ten minutes†, suggesting enhancement of the sintering rate by the extreme fabrication pressures. No traces of any residual α-Si_3N_4 are apparent from these XRD spectra, neither is there any evidence for the yttrium silicate phase (for which the most intense peaks would lie between 25° and 35°) that might have crystallised from the sintering additive liquid had the specimens cooled at a slower rate.

Comparison of figures (b) and (c) indicate that the cubic BN phase stability could not reliably be maintained during sintering at these fabrication conditions, which evidently lie close to those for cBN-hBN phase equillibrium (see section 2.3.2). The difficulty in identifying small quantities of the hBN phase is also illustrated in figure (c). Hence, the precise conditions at which the cBN stability could be maintained were unclear. The discrepancies observed between the different recorded conditions at which the cBN had reverted to hBN are believed to arise from variations in the position of the thermocouple and from uneven pressure and temperature distributions.

5.6.2 *XRD Results for Ceramics Fabricated at Pressures Above 8 GPa*

The XRD results from section 5.6.1 indicated a need for much higher fabrication pressures to be applied in order to maintain the stability of the cBN during high-temperature sintering. This led to further fabrication experiments being carried out using pressures above 8 GPa and with a sintering time of 12-15 minutes at the full pressure and temperature conditions. Figure 5.6 identifies the phases present in three cBN-Si_3N_4 composites (with different cBN content) that were fabricated at as near as possible identical conditions. The presence of the cubic BN phase is clearly indicated by the strong peak at 43.4°. However, there are considerable differences between the specimens in terms of the α and β-Si_3N_4 phase content, suggesting large differences in the actual fabrication temperatures. As far as could be ascertained from these XRD results, no reversion of the cBN to hBN phase transformation had occurred at these conditions and promisingly, the desired cBN-Si_3N_4 final phase combination was

† A similar observation has also been recorded in section 4.7.

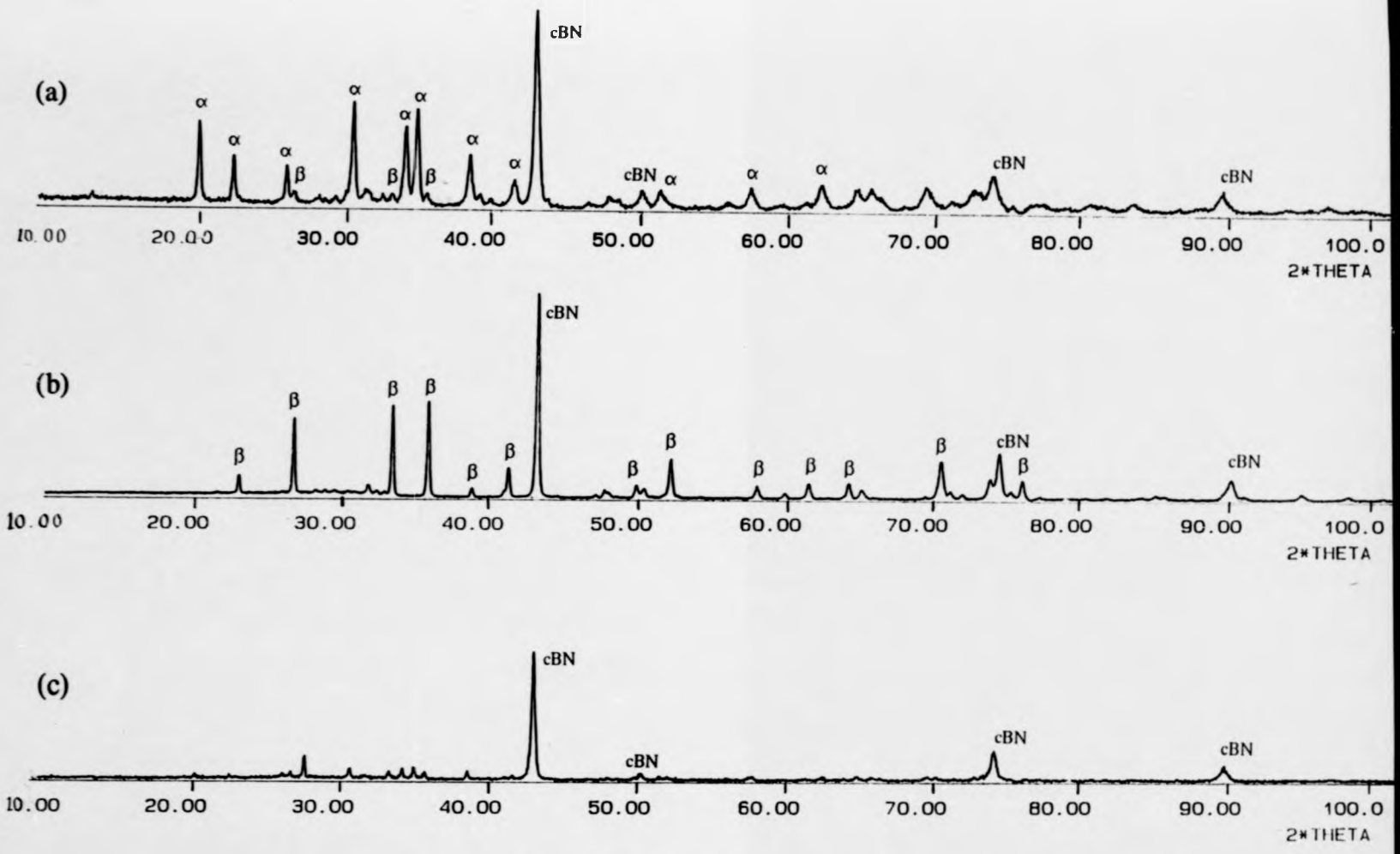

Figure 5.6: XRD spectra for cBN-Si_3N_4 composites with different cBN concentration, fabricated at 8 GPa: (a) 40 wt% cBN; (b) 60 wt% cBN; (c) 80 wt% cBN.

obtained (figure 5.6 (b)).

Finally, it was of interest to investigate whether the presence of Si_3N_4 would inhibit the high pressure synthesis of cBN from hBN, as has been suggested by Yoshihara *et al.* [117] or conversely, might act as a catalyst for this synthesis, as described in an earlier patent [113]. Some attempts were made to fabricate a cBN-Si_3N_4 composite at the same conditions as for the sintering experiments conducted at 8 GPa. Figure 5.7 shows the phases formed from such an experiment. No α to β-Si_3N_4 phase transformation is detectable in this XRD pattern, indicating that the sintering temperature was too low to promote any liquid phase sintering. Therefore, the lack of evidence for any cBN formation provides inconclusive evidence about the action of the Si_3N_4 since it is most probable that the synthesis experiments were performed at too low a temperature for any BN phase change to be expected.

5.7 GENERAL MICROSTRUCTURAL OBSERVATIONS

The distribution of the cBN and Si_3N_4-based matrix can be seen in figure 5.8 for a cBN (60 wt%)-β-Si_3N_4 ceramic (see fig. 5.6 (b)) which shows a microstructure typical of that obtained after UHP sintering at 8 GPa. This shows a network of fairly evenly dispersed cBN grains in the matrix phase which is broken up by agglomerated regions of the matrix phase, some as large as 70 μm across. The agglomerates arise from the difficulties in overcoming the strong, electrostatic forces between the fine-grained powders during the powder preparation (slip casting). This would suggest a need for improved methods of initial powder dispersion, further supported by the observation of the brighter 'specks' on this image arising from sintering additive residue that has not been distributed finely into the matrix phase.

Where cBN grains were forced into direct contact during the UHP processing, the high stresses developed between them often resulted in severe grain fragmentation. The evidence for this was particularly apparent in ceramics with the larger cBN grain size (about 8-10 μm across) in which there were many smaller cBN fragments derived from the fragmented grains (seen in figure 5.9). Extensive cracking and chipping can also be observed in several of the larger cBN grains.

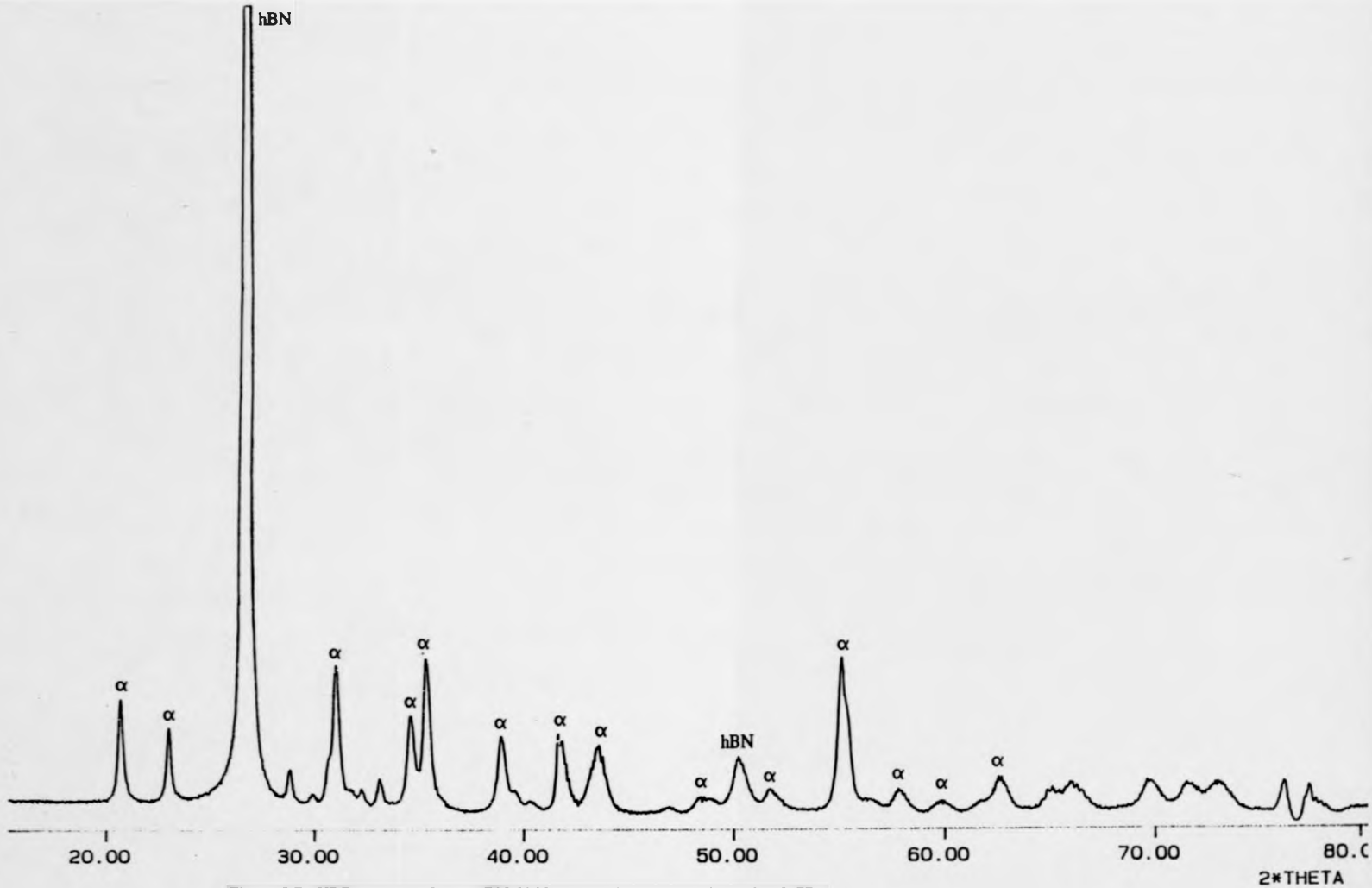

Figure 5.7: XRD spectrum for an hBN-Si_3N_4 composite that was sintered at 8 GPa.

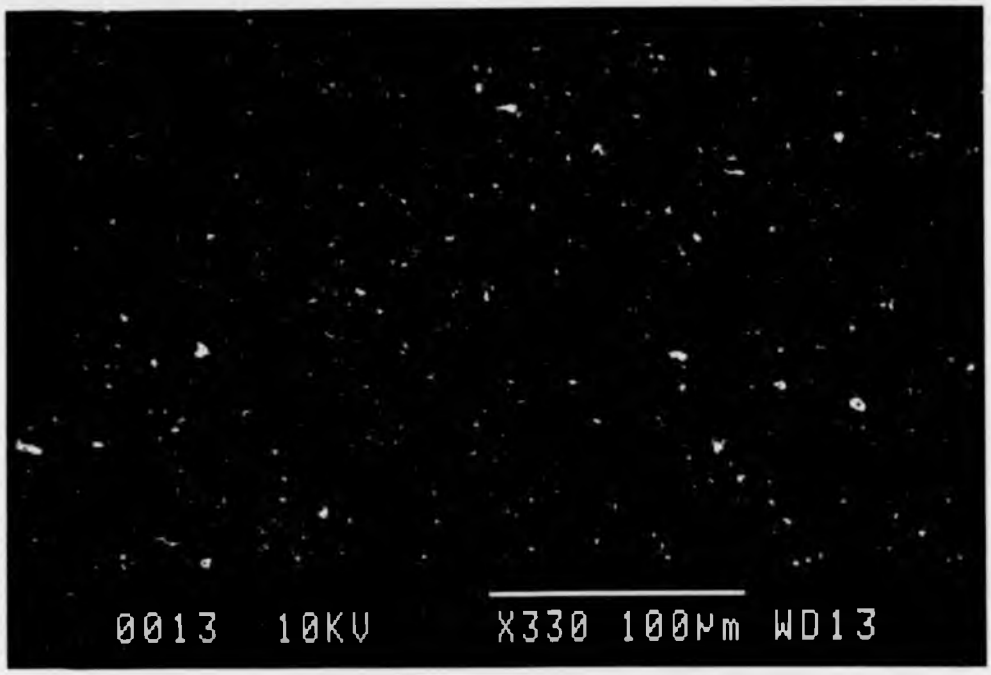

Figure 5.8: Back-scattered SEM image of the polished surface of a cBN (60 wt%)-Si_3N_4 ceramic showing the distribution of cBN grains (black) in the Si_3N_4 (grey)-based matrix. The white 'specks' represent regions with relatively high quantities of sintering additive (yttrium-containing) residue.

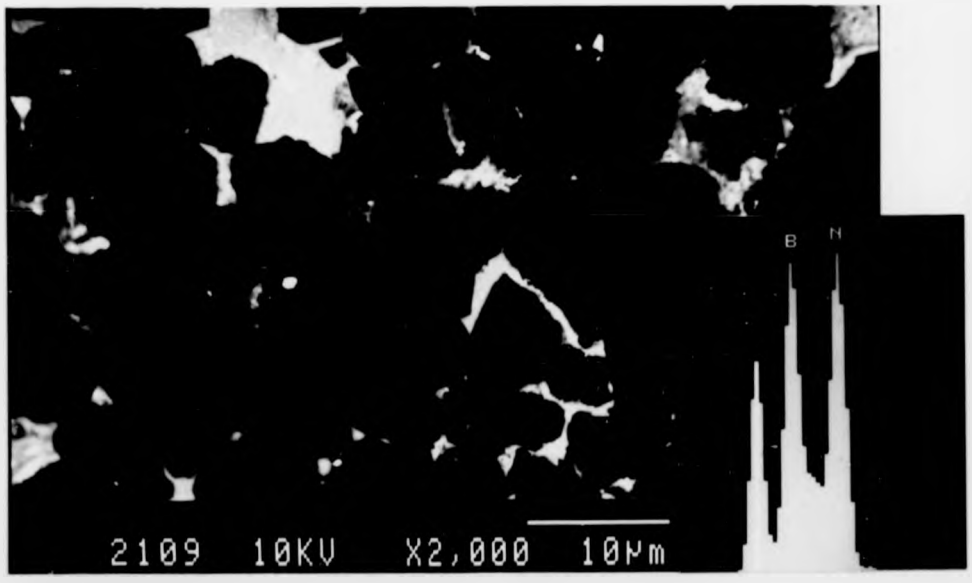

Figure 5.9: Back-scattered SEM image showing a region with considerable fragmentation of the cBN grains where they have been forced into direct contact. Inset: EDAX spectrum taken from a cBN grain.

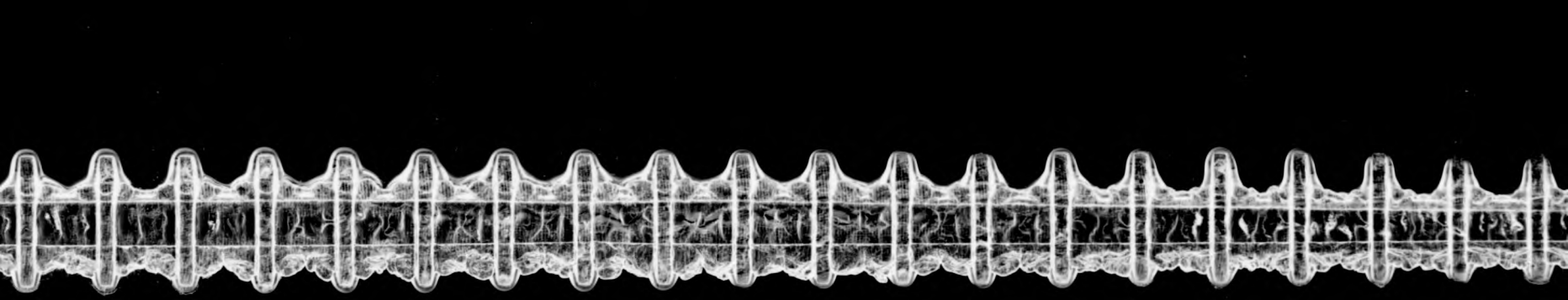

Figure 5.10 is taken from a composite with a smaller cBN grain size (about 3 μm across) and which was not removed from the sintering encapsulant materials. The irregularly shaped cBN grains ranged in size from 2 to 6 μm with many smaller fragments, as was also seen in figure 5.9. A remarkably sharp boundary is apparent at the ceramic-encapsulant interface at which the tantalum appears to have become molded around the cBN grains with no suggestion of any metallic infiltration into the bulk ceramic. The X-ray mapping in figure 5.11 identifies the presence of silicon, tantalum and iron (from an outer steel capsule around the tantalum) across the ceramic-capsule interface. The silicon map indicates the Si_3N_4 regions in the ceramic, but it should be noted that X-ray signals from the Ta Mα line (at 1.709 keV) are close in energy to those from the Si Kα line (1.739 keV) and so this X-ray map illustrates areas containing both silicon and tantalum, as is clearly seen from comparison with the tantalum map. The X-ray maps show very clearly defined interfaces between the sintered ceramic and the encapsulant materials, revealing no evidence for any metallic contamination arising during the UHP processing.

5.7.1 *Tape-cast, Laminated Ceramic*

The hybrid, laminated composite was fabricated from tape cast laminae which had been structurally arranged with an increasing cBN concentration from one face through to the opposite face. The XRD spectra taken from the opposing ceramic faces (figure 5.12) suggest that the overall structure was preserved during sintering. However, the composite appeared to be more poorly consolidated than those fabricated with a homogeneous composition and also, revealed a tendency to delaminate (along laminar interfaces) during mechanical polishing. Figure 5.13 illustrates a well-retained boundary between two neighbouring laminae of different composition. Some porosity can be observed in the region of relatively low cBN concentration, emphasised by bright flaring (seen in the image) around the holes.

The structural arrangement of the laminate is viewed over a wider scale in figure 5.14. Although there would appear to be good homogeneity within individual laminae, as there is no evidence for any agglomerated regions of the ceramic matrix, the

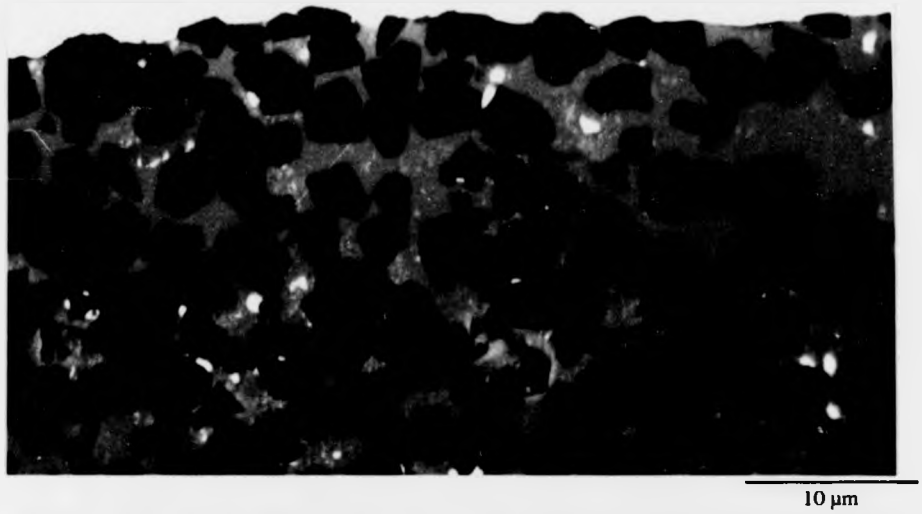

Figure 5.10: Back-scattered SEM image taken from a polished surface of a cBN (60 wt%)-Si_3N_4 composite and from which the sintering encapsulant (tantalum) had not been removed.

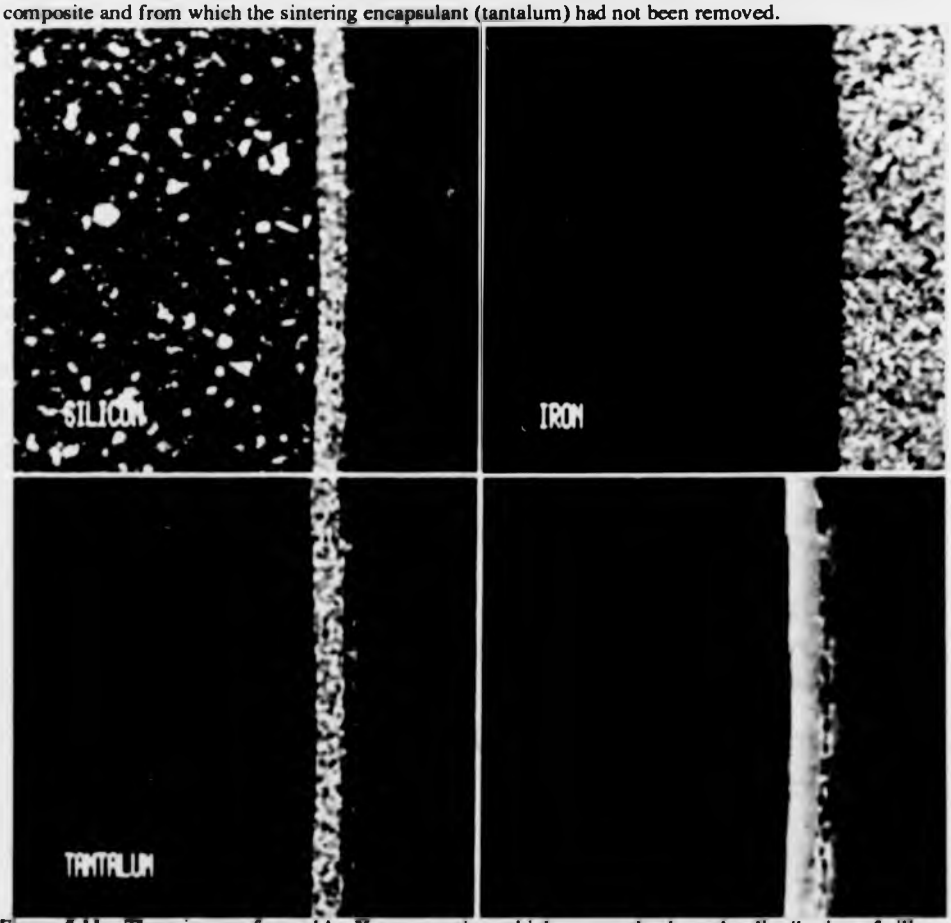

Figure 5.11: Three images formed by X-ray mapping which separately show the distribution of silicon, iron and tantalum across the ceramic-capsule interface. The secondary electron SEM image of this region is given in the bottom right hand corner.

PAGE(S) MISSING
NOT AVAILABLE

FIG 5.12

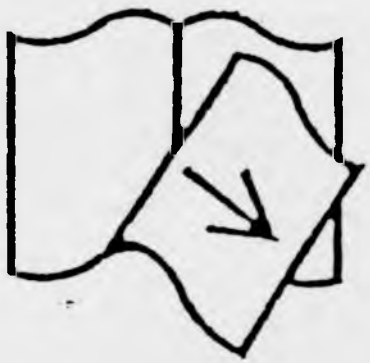

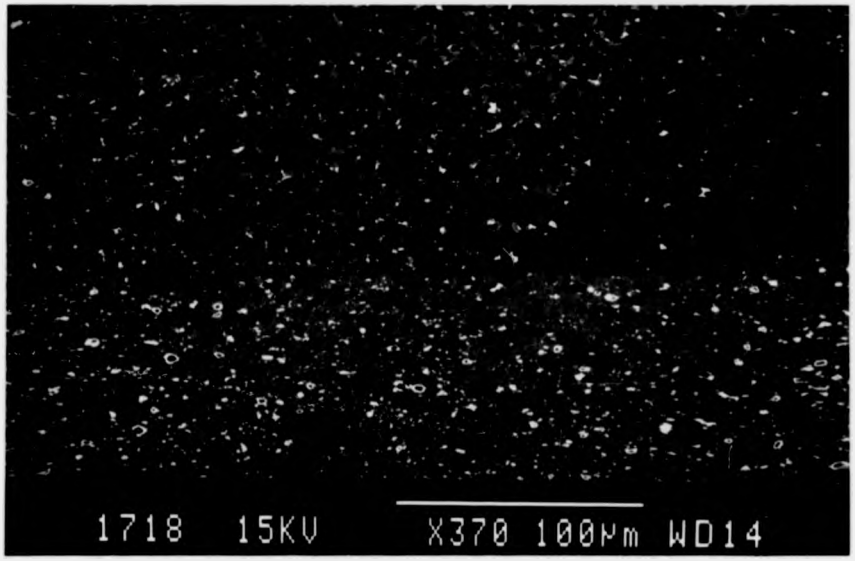

Figure 5.13: Polished cross-section of the hybrid cBN-Si_3N_4 composite. The boundary between laminae of different compositions is clearly defined.

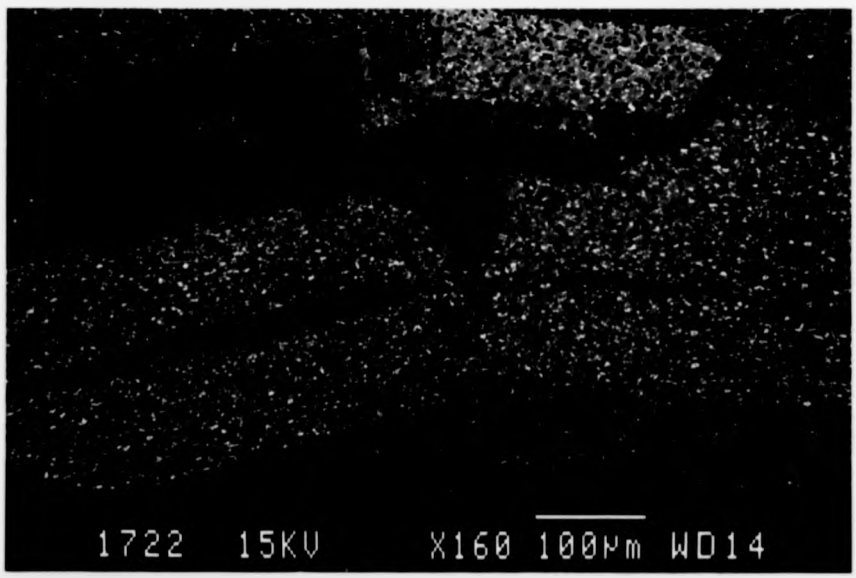

Figure 5.14: Cross-section of the hybrid cBN-Si_3N_4 composite showing the macrostructural disorder after the disruption of sequentially stacked laminae during the UHP sintering process.

laminae themselves have become fragmented and intermixed. It would seem most likely that the disruption of the laminae was caused by uneven pressure application during the sintering.

The poor consolidation of this ceramic was attributed to the enhancement of residual stresses by large differences in thermal expansion between the local regions with different compositions. To minimise such stresses it would have been necessary to preserve a compositional gradient through the ceramic.

5.8 TRANSMISSION ELECTRON MICROSCOPE OBSERVATIONS

The Si_3N_4 phase was more rapidly eroded than cBN during ion beam bombardment and so it was difficult to obtain a uniformly thin area clearly showing the relationship between cBN grains and their supporting matrix of fine Si_3N_4 crystals. Figure 5.15 shows a section through a ceramic fabricated at 4 - 5 GPa which allows a clear comparison of the relative sizes of the cBN and Si_3N_4 grains. In this example, regions of the Si_3N_4 phase separate the cBN grains typically by a few μm. The variable contrast in this image arises from overlapping and diffraction of the randomly orientated Si_3N_4 grains and to extensive plastic deformation on the cBN grains. Twin lamellae are visible on the largest cBN grain in this image whilst networks of dislocations are apparent on other cBN grains.

The structure of the Si_3N_4 matrix phase can be examined in more detail from figure 5.16. The specimen was prepared from a monolithic ceramic, sintered at 1750°C and 4.5 GPa, for which the associated XRD pattern (figure 5.5 (a)) identified complete α to β-Si_3N_4 transformation. The elongated morphology which is characteristic of β-Si_3N_4 grains can clearly be seen, but the grain size of 0.3 - 0.6 μm remains as fine as that in the initial starting powder (see table 3.1). The sintering additive residue was identified as having formed glassy pockets of an yttrium-silicate phase, finely dispersed at the Si_3N_4 grain boundaries.

A region of the Si_3N_4 matrix phase in a cBN-Si_3N_4 composite is shown in figure 5.17. The matrix phase occupies a gap between plastically deformed (and relatively thick) cBN grains. It is most likely that the slight separation that is seen

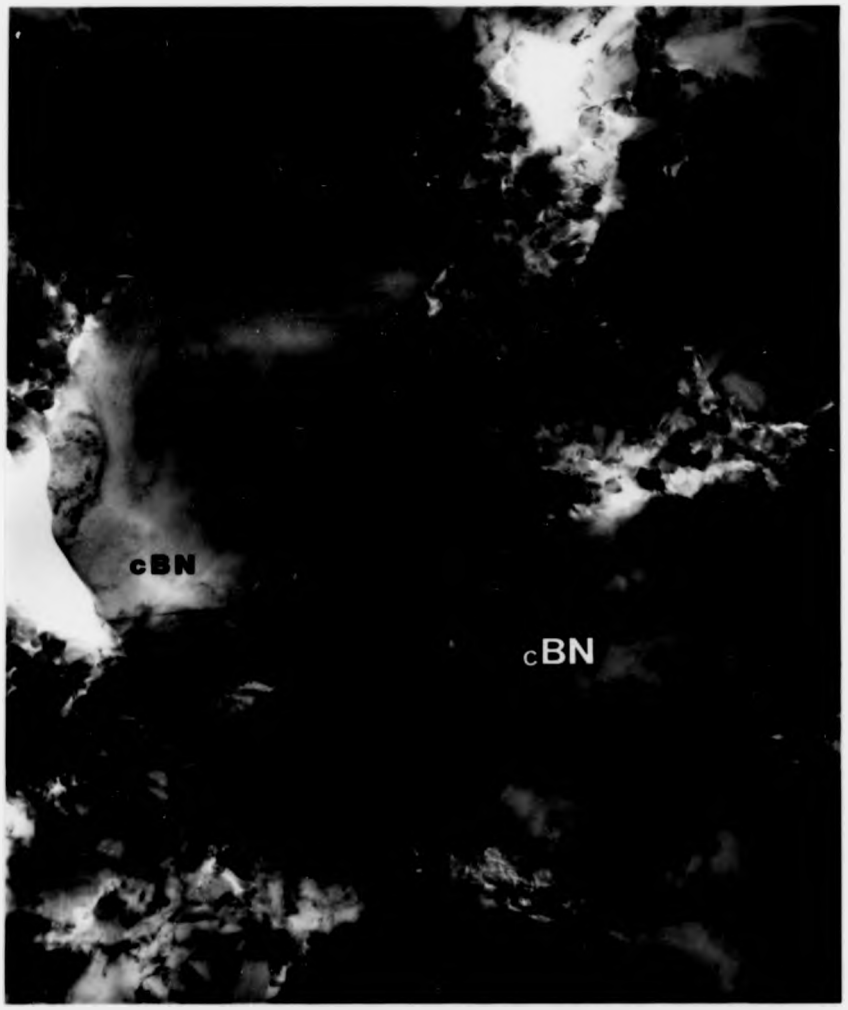

1 μm

Figure 5.15: Bright field TEM image illustrating the relative sizes of the (large) cBN grains and the much finer Si_3N_4 grains. Extensive plastic deformation is responsible for the contrast variations seen on the cBN grains. Additionally, some mechanical twinning is visible on the largest cBN grain.

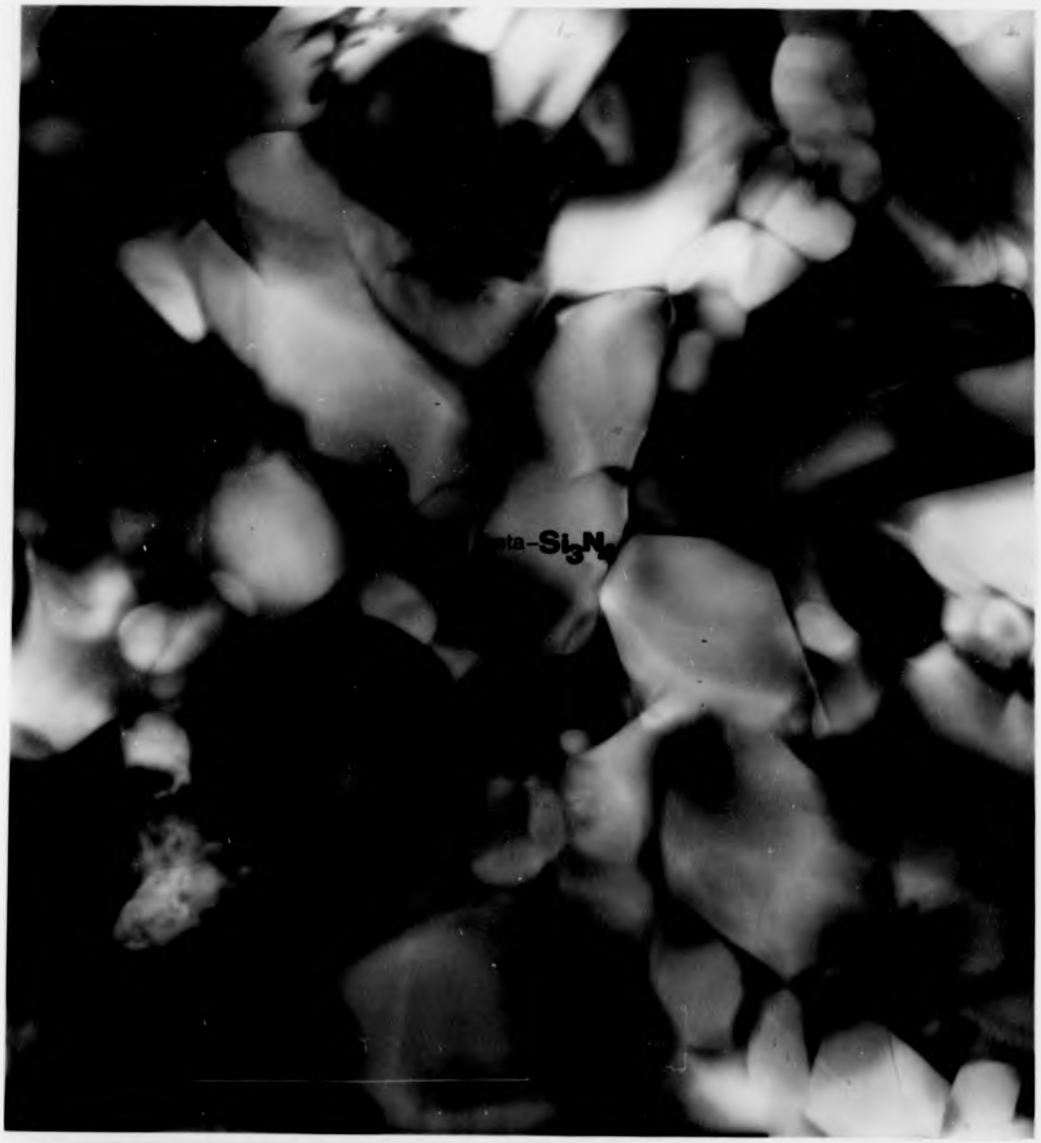

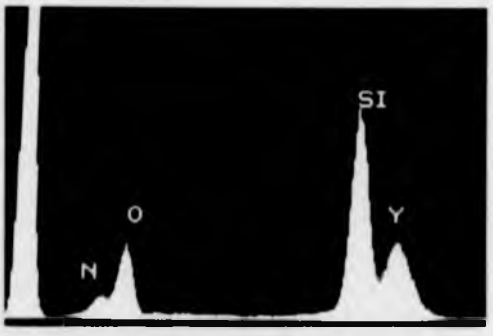

0.1 μm

Figure 5.16: Bright field TEM image, showing a section through the Si_3N_4-based matrix phase (taken from a monolithic ceramic fabricated at 4.5 GPa and 1750°C, in the tetrahedral apparatus). Inset: EDAX analysis of the glassy phase between the Si_3N_4 grains. The presence of the Si and N peaks is partly due to some overlap of the probe electron beam with the Si_3N_4 grains.

0.2 µm

Figure 5.17: Bright field TEM image, showing a region of the Si_3N_4 matrix phase between the much larger, plastically deformed cBN grains.

between the cBN and Si_3N_4 regions arose during ion bombardment of the specimen. The additional crack running to the top right of this image most likely represents a line of direct cBN-cBN grain contact during the sintering process.

The cBN grains were analysed using EELS spectroscopy, producing unambiguous spectra typical of cBN (figure 5.18) and additionally, EDAX was used to identify the elements present at the grain boundaries. Interestingly, the presence of calcium was consistently detected in the EDAX spectra obtained from intergranular glassy regions. It was most easy to determine the glass composition from regions at the thinner specimen edges (figure 5.19) for which the results would suggest that a calcium impurity, present from the initial cBN synthesis (see table 3.1), interacted with the liquid phase formed from the Y_2O_3 and SiO_2 sintering additives.

The most prominent features to be observed on the cubic BN grains themselves were deformation twins, in common with many other superabrasive compacts [112, 120, 121]. Dark field images of intersecting microtwins (figure 5.20) were formed from the $(1\bar{1}1)$ and $(1\bar{1}\bar{1})$ reflections in the diffraction pattern, revealing the associated deformation microtwins. The faint streaking visible in the diffraction pattern arises from the fine spacing of the microtwins. The corresponding bright field image also reveals a complex dislocation network, although individual dislocations can not be distinguished.

5.9 SUMMARY AND CONCLUSIONS

Cubic BN/Si_3N_4 ceramic composites have been fabricated under UHP conditions which proceed with liquid phase sintering of the Si_3N_4 matrix phase and produce a fine-grained β-Si_3N_4 microstructure comparable with that obtained by more conventional ceramic sintering methods. No evidence for the deformation of the Si_3N_4 grains was seen, which is consistent with the precipitation of the β-phase from the sintering additive liquid at UHP. However, it has been found that at the high temperatures required to promote this sintering, the stability of the cubic BN phase can not be maintained at pressures in the range 4.5-5.0 GPa. In order to prevent a rapid BN phase transformation to the hexagonal phase, it was necessary to increase significantly

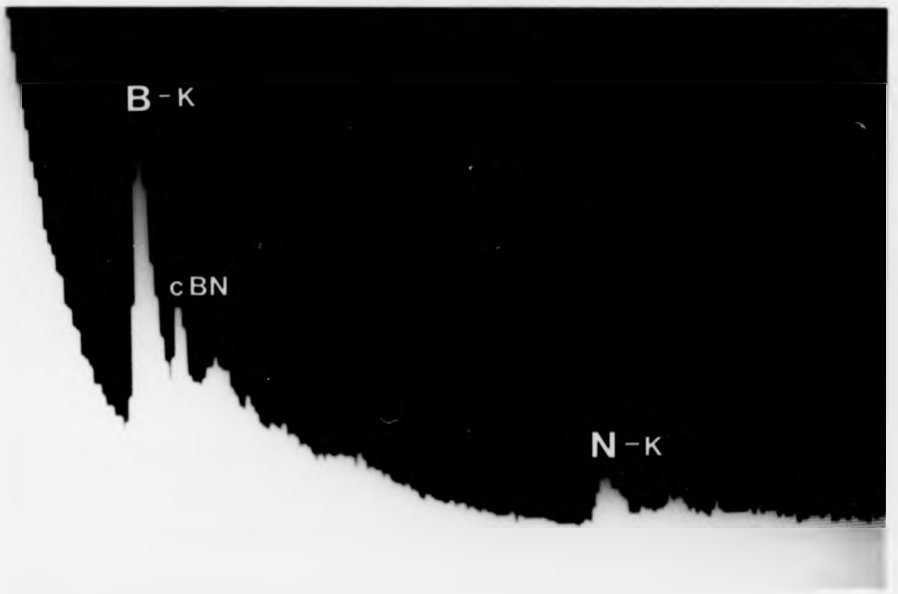

Figure 5.18: EELS spectrum, taken from a cBN grain, for which the fine structure has been identified with reference to [164].

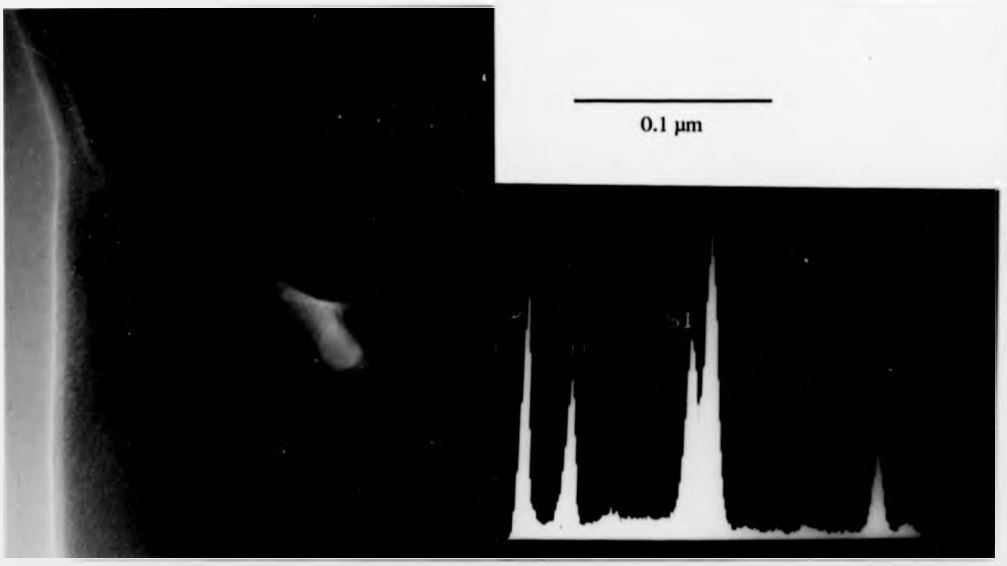

Figure 5.19: Bright field TEM image, showing a region of the glassy phase found at Si_3N_4 grain boundaries and the EDAX analysis giving the elemental composition of the glassy phase.

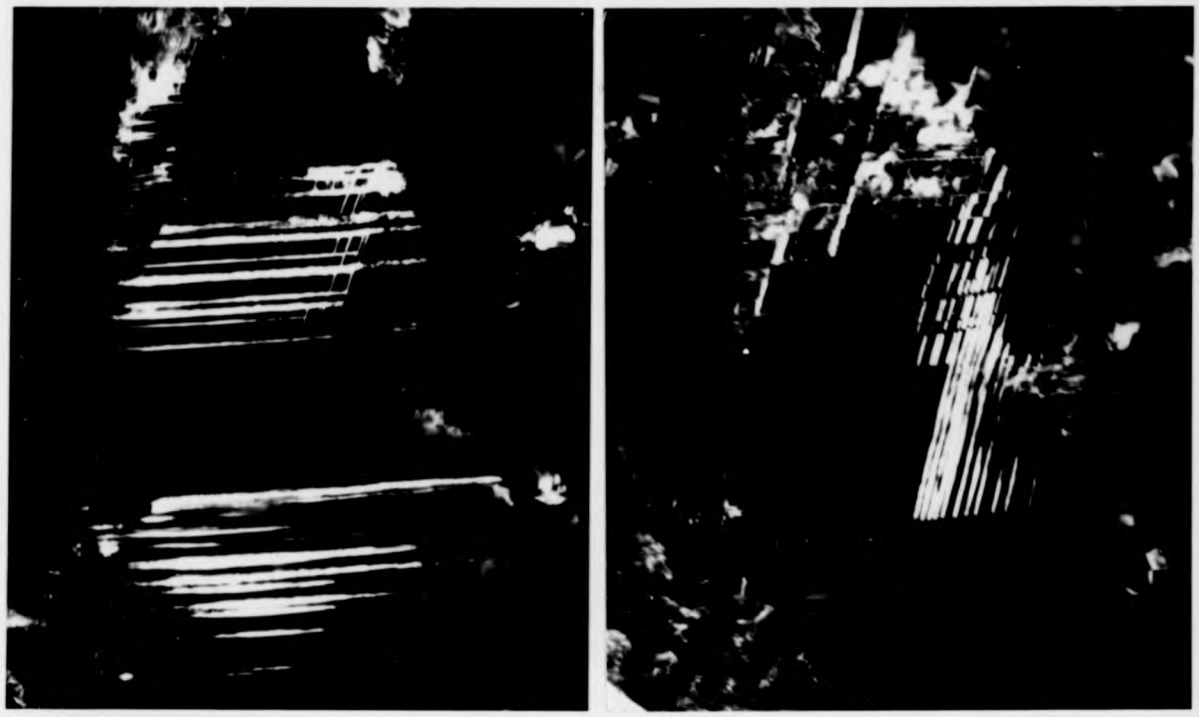

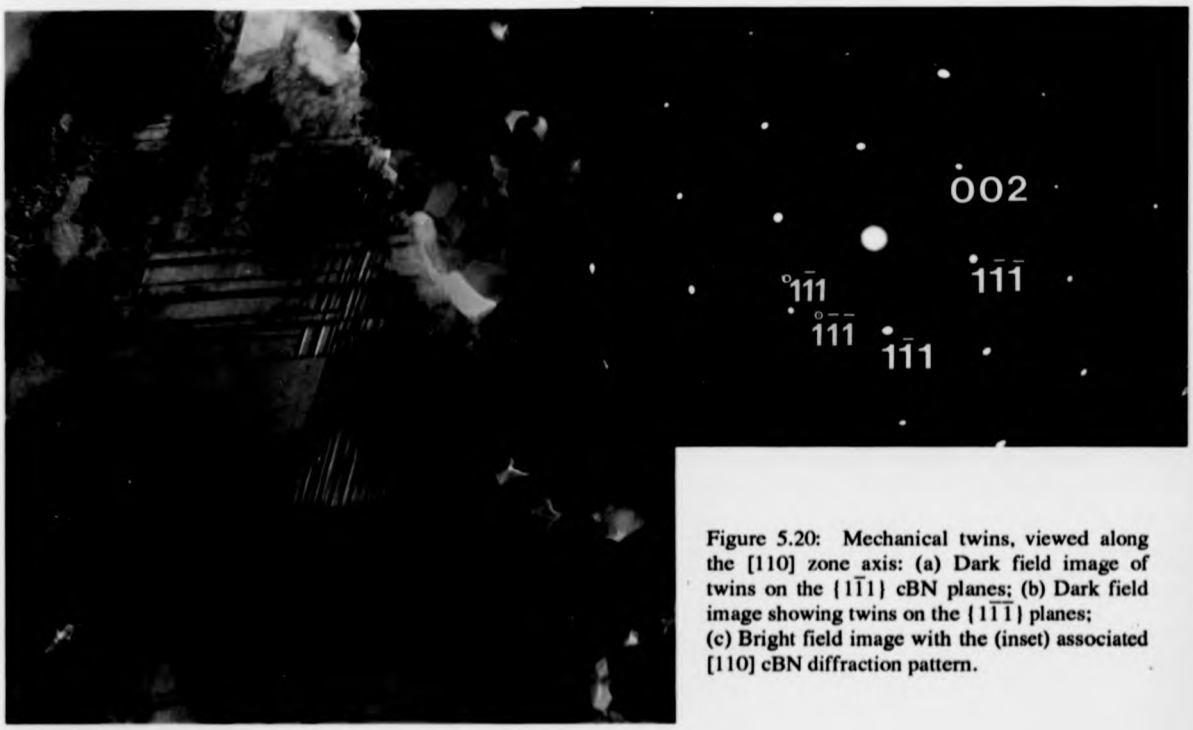

Figure 5.20: Mechanical twins, viewed along the [110] zone axis: (a) Dark field image of twins on the $\{1\bar{1}1\}$ cBN planes; (b) Dark field image showing twins on the $\{1\bar{1}\bar{1}\}$ planes; (c) Bright field image with the (inset) associated [110] cBN diffraction pattern.

the applied pressures during sintering. The additional fabrication difficulties experienced in reaching a sufficiently high sintering temperature resulted in many of the composites containing a mixture of the α and β-Si_3N_4 phases.

Homogeneous phase dispersions were best achieved in a tape-cast laminate. However, the sequential stacking of laminae with different compositions was not preserved during the UHP consolidation. The microstructural observations made on all the composites revealed many features which are typically associated with the sintering of cBN grains: grain fragmentation and high levels of plastic deformation manifest as complex dislocation networks and mechanical twinning (from the movement of partial dislocations). The cBN grains were separated by a Si_3N_4-based phase which consisted of submicron Si_3N_4 crystals with a glassy yttrium-calcium silicate phase (from sintering additive and impurity residue) at the grain boundaries. No evidence was found for any direct reaction between the cBN and Si_3N_4 phases.

Chapter Six

PHYSICAL PROPERTIES OF SILICON CARBIDE / SILICON NITRIDE AND CUBIC BORON NITRIDE / SILICON NITRIDE COMPOSITES

6.0 INTRODUCTION

This chapter presents a survey of some of the room temperature mechanical properties and also, preliminary thermal expansion data for the composites discussed in chapters four and five. Of most importance to this research were hardness, fracture toughness and strength. To evaluate these characteristics fully, the microstructural responses to crack propagation were also examined in terms of the toughening behaviour of the dispersed phases (SiC_p, cBN) and the influence due to different fabrication methods was also investigated. This enabled inferences to be made about the potential of these composites for use as new hard and impact-resistant ceramics.

The experimental procedures used to obtain the results in this chapter are discussed in chapter three. Ceramic hardness measurements were made on both the Vickers and Knoop scales. However, the large range of SiC-Si_3N_4 and cBN-Si_3N_4 compositions produced and difficulties in repeating fabrication experiments inevitably led to some variation (chiefly with regard to the available size and quantity) in the suitability of different composites for further mechanical tests. Where there was sufficient material to allow the machining of bend test bars, the strength and (SENB) fracture toughness were determined using four point bend testing. Some fracture toughness values were also estimated from the lengths of the radial cracks extending from indentations. Whilst the results obtained from these two techniques can not be accurately compared (on account of the different natures of the induced stress fields arising from bending and indentation) this provided a means of determining the relative fracture toughnesses of composites for which there was insufficient material to apply the SENB technique.

Finally, the thermal expansion behaviour was examined for a SiC-Si_3N_4 laminate and the cBN-Si_3N_4 composites, over a temperature range from 20° to 1000°C.

6.1 INDENTATION HARDNESS

Many of the composites appeared to be of higher hardness than the monolithic, Si_3N_4-based ceramics, as was indicated by their tendency to exhibit greater resistance to diamond machining and surface polishing. This was investigated for the ceramics fabricated at ultra-high pressures, using both Vickers and Knoop indenters; making a minimum of six indentations for each test. The results of these experiments are considered separately.

6.1.1 *Vickers Indentation Hardness*

The mean values obtained for the Vickers hardness are plotted in figure 6.1, to illustrate the relative hardnesses of the SiC-Si_3N_4 and the cBN-Si_3N_4 composites.

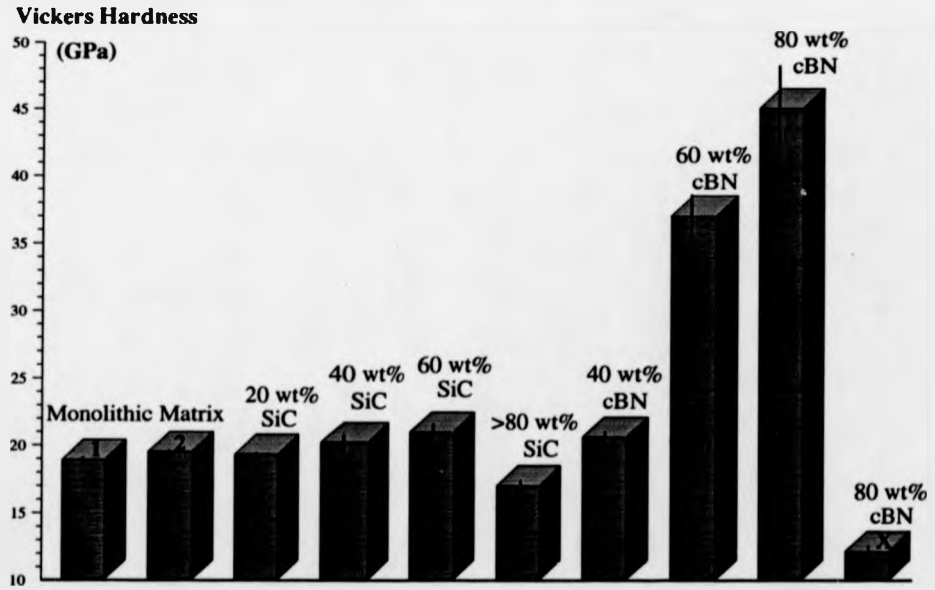

Figure 6.1: Bar chart illustrating the mean values (by the height of the front face) of Vickers indentation hardness, obtained using a 2 kg load. The error bars represent the standard error in the mean. The specimen marked '1' was hot-pressed whereas specimen '2' was UHP-sintered. Specimen 'X' was fabricated using a larger cBN grain size (average particle size 9 μm).

Consistent values were obtained for the monolithic, Si_3N_4-based matrix and these were in reasonable agreement with the typical values quoted in chapter one. The UHP-sintered (matrix, no. '2' in figure 6.1) specimen was of slightly higher hardness

than the hot pressed ceramic. This was attributed to a greater degree of densification resulting from the higher consolidation pressures. The addition of SiC (a harder phase than Si_3N_4) platelets to the Si_3N_4 matrix was expected to have produced composites of greater hardness, but instead of this, the results show unexpectedly small increments in hardness for the higher SiC_p concentrations, with overlapping error limits. In particular, the predominantly SiC composite (>80 wt% SiC) was found to be of even lower hardness than the monolithic Si_3N_4. The most likely explanation for these results is the clearly visible macrocracking, believed to arise during the post-sintering relaxation of residual stresses. This was observed in all the UHP-fabricated ceramics and appeared to be most severe in those compositions with higher dispersed phase concentrations.

The cBN-Si_3N_4 composites gave a significant increase in Vickers hardness for the compositions above 50 wt% cBN. Surprisingly, the 40 wt% cBN composite was only 6 % harder than the matrix phase, being closely comparable with the 40 wt% SiC composite. This may have been due to the presence of agglomerated regions of the Si_3N_4 matrix phase in this composite (see section 5.7). However, the hardnessess of the 60 wt% and 80 wt% cBN compositions compare closely with the ceramics discussed in section 2.3 and with commercial cBN ceramics [165]. The considerable difference found in the hardnesses of the two 80 wt% cBN composites with different grain size may be explained by their difference in density (see section 5.5). The lower hardness of the larger-grained cBN specimen and the (relatively large grained) SiC platelets would seem to support suggestions of densification difficulties associated with the sintering of relatively coarse powders.

The impressions formed using a 2 kg indentation load were clearly defined in the Si_3N_4 monoliths and the SiC-Si_3N_4 composites. However, in the composites with cBN concentrations above 50 wt%, the edges of the impressions were indistinct, as can be seen in figure 6.2. As the indentations were typically about 32 μm across, accurate measurement was more difficult for these composites and this may have contributed to the scatter in the measurements obtained. The random orientation of the cBN crystals (known to exhibit hardness anisotropy [166]) was not believed to contribute as greatly to the measurement scatter as the microstructural inhomogeneities, since the average grain size was an order of magnitude less than the average indentation size.

(a) (b)

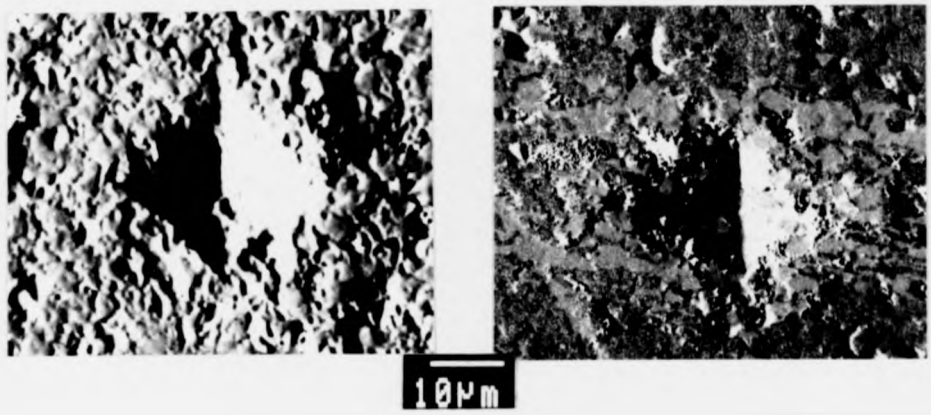

(c)

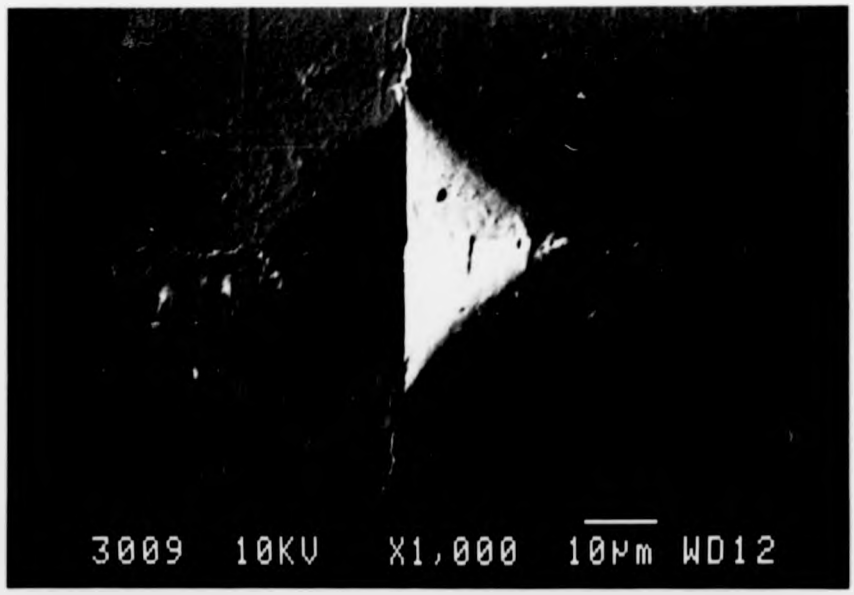

Figure 6.2 Back-scattered SEM images of Vickers indentations (made using a 2 kg load) on polished surfaces of a (a) 60 wt% cBN composite; (b) 80 wt% cBN composite; (c) Si_3N_4 monolithic ceramic. All the images are shown at the same magnification.

6.1.2 *Knoop Indentation Hardness*

Knoop indentation is well suited to the investigation of particularly hard materials. The impressions formed are longer and generally more easy to measure than those from Vickers tests and have minimal associated cracking. It was expected that the Knoop indentations might provide some clearer identification of the expected trends in the composite hardnesses. The same polished surfaces were used for these experiments as for the Vickers experiments, together with some additional cBN-Si_3N_4 specimens that had been fabricated in different batches. The results of the Knoop experiments are summarised in figure 6.3.

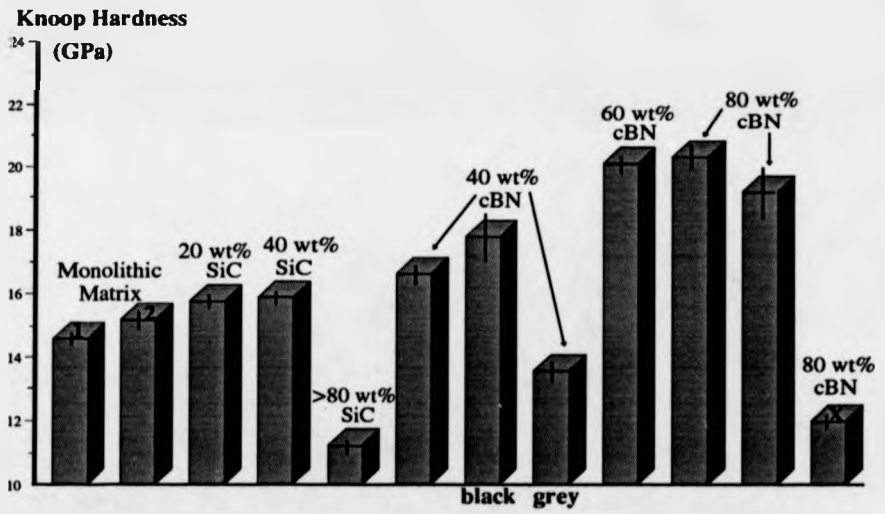

Figure 6.3: Bar chart illustrating the mean values of the Knoop hardness, obtained using a 2 kg load, for a selection of ceramic specimens. The error bars represent the standard error in the mean.

As found from the Vickers experiments, the SiC-Si_3N_4 composites showed only a slight increase in hardness over the monolithic matrix phase and the >80 wt% SiC composite was of a much lower hardness than the other compositions. Also, the 80 wt% cBN composite of larger grain size (marked 'X') was found to have a significantly lower hardness than the finer grained specimens of the same composition. The Knoop values obtained for the Si_3N_4-based monolithic materials were about 4 GPa below those obtained on the Vickers scale and little difference in hardness was found between the specimens that had been hot pressed (marked '1') and UHP-processed

(marked '2'). However, the different indentation experiments gave contradictory indications of hardness for the cBN-Si_3N_4 ceramics. While the composites with 60 wt% and 80 wt% cBN were of extreme Vickers hardness (above 35 GPa), the corresponding Knoop hardnesses for both these ceramics were close to 20 GPa, which is much lower than the Knoop hardness of 28 GPa quoted for a typical commercially-produced cBN ceramic [167]. This would suggest that other factors in addition to phase composition were contributing to the Knoop results. It is believed that the larger size of the Knoop indentations made these results more susceptible to the influence of larger scale microstructural effects, such as residual cracking in the UHP-fabricated ceramics and the inhomogeneity arising from agglomerated Si_3N_4. Particularly severe cracking attributed to residual stresses was evident in the 80 wt% cBN composites, increasing the likelihood of the cracks extending from the Knoop indentations due to residual stresses within the ceramics.

The Knoop results also indicate that there exists a larger hardness variation between specimens of the same composition than between specimens of different compositions. Composites from two separate batches were tested for the 40 wt% cBN and 80 wt% cBN compositions and the bars marked 'black' and 'grey' in figure 6.3 illustrate the hardness variation within different coloured regions of the same specimen. The lower hardness of the grey region is consistent with its lower density (section 5.5). However, it is unclear why the softer and less dense area should be found in the centre of the specimen, where the fabrication pressures and temperatures would have been greatest. One possible explanation for this is the partial reversion of cBN to the softer and less dense hexagonal phase. Although the presence of hBN in the grey regions was not identified by XRD, other research has shown [168] that only a small percentage phase reversion to hBN would be required to influence dramatically the mechanical characteristics of the material and, as has been discussed in section 5.6, the presence of hBN cannot be detected with certainty below a few wt%.

6.2 RESULTS OF CERAMIC STRENGTH MEASUREMENT

It was possible to test the strengths of one batch of the laminated SiC-Si_3N_4 composites, in which layers of increasing SiC content were stacked upon a monolithic, Si_3N_4 base (see figure 4.1b) and a selection of cBN-Si_3N_4 composites fabricated at 8 GPa. The number of tests made for each specimen ranged from four to eight, according to the number of bend test bars that were successfully prepared. Although the bars were machined as accurately as possible, there was found to be some slight non-uniformity in the widths and thicknesses. These variations should be considered as a source of error in the results obtained. The mean strength values are given in figure 6.4.

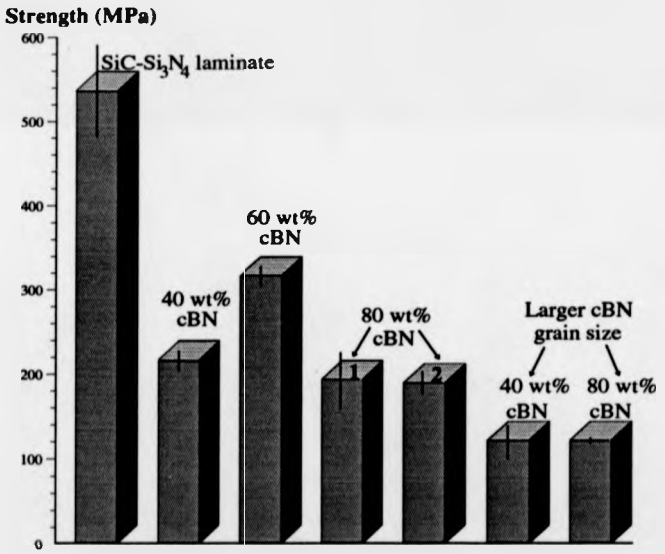

Figure 6.4: Bar chart comparing the mean strengths of the different composites, as determined from four point bend testing. Two sets of data were obtained from different batches ('1' and '2') of the 80 wt% cBN composition. The error bars represent the standard error in the mean. (The results obtained from the SiC-Si_3N_4 laminate were obtained using the monolithic face as the tensile surface.)

The SiC-Si_3N_4 laminate bars were broken such that both the monolithic surface and also, the opposing SiC-reinforced surface were tested as tensile surfaces. A wide scatter in results was obtained from both these orientations, but the strength values from the SiC surface, with average value 309 ± 60 MPa were consistently lower than from the monolithic surface, with average value 537 ± 56 MPa (the standard error in the

mean is quoted). The lower strength implied for the SiC laminae can be explained by the high residual porosity observed in these layers following incomplete densification by hot pressing at 20 MPa (section 4.4). Little evidence of composite behaviour was apparent during these tests apart from two incidents resulting in obvious delamination and from which relatively high strengths of 770 and 615 MPa were recorded. Whilst it would appear that the residual porosity in the poorly densified laminae dominated the failure mechanisms, the limited observations of delamination behaviour provided some suggestion of there being present the additional composite toughening mechanism (delamination) that had been predicted for the hybrid composite structures. To enable a more complete evaluation of toughening mechanisms in these materials to be carried out, it would be necessary to fabricate laminates which have more uniform degrees of densification in the neighbouring laminae. This might be achieved using increased fabrication pressures.

The cBN-Si_3N_4 composites were of much lower strength than the SiC-Si_3N_4 laminate, which was nearly twice as strong as the cBN-Si_3N_4 composite exhibiting the highest strength. The low strength of the cBN-Si_3N_4 composites might be explained by residual stresses arising from the UHP fabrication, the existence of which was suggested by the results of hardness testing (section 6.1). No obvious relationship was found between the strength and composition of the cBN-Si_3N_4 composites, since the 'intermediate' 60 wt% cBN composition exhibited the highest strength (316 ± 12 MPa). This may be a result of inconsistency in the fabrication process, as the 60 wt% cBN composite was alone in showing evidence for a complete transformation of the starting α-Si_3N_4 to the β-Si_3N_4 phase (section 5.6.2). (This was most likely due to the sintering taking place at a higher temperature than for the other compositions.) As the β-Si_3N_4 grains were observed to have a characteristic elongated morphology (section 5.8), the tortuous routes of cracks following intergranular fracture would lead to increased strength and fracture toughness, in the same way as for hot-pressed and HIPed Si_3N_4 ceramics [24-28,31]. The two composites exhibiting the highest strengths (60 wt% and 40 wt% cBN compositions) were also those found to have the highest percentage theoretical densities, which suggests that the remaining composites might be weakened by their greater degrees of residual porosity. The severe macrocracking exhibited by

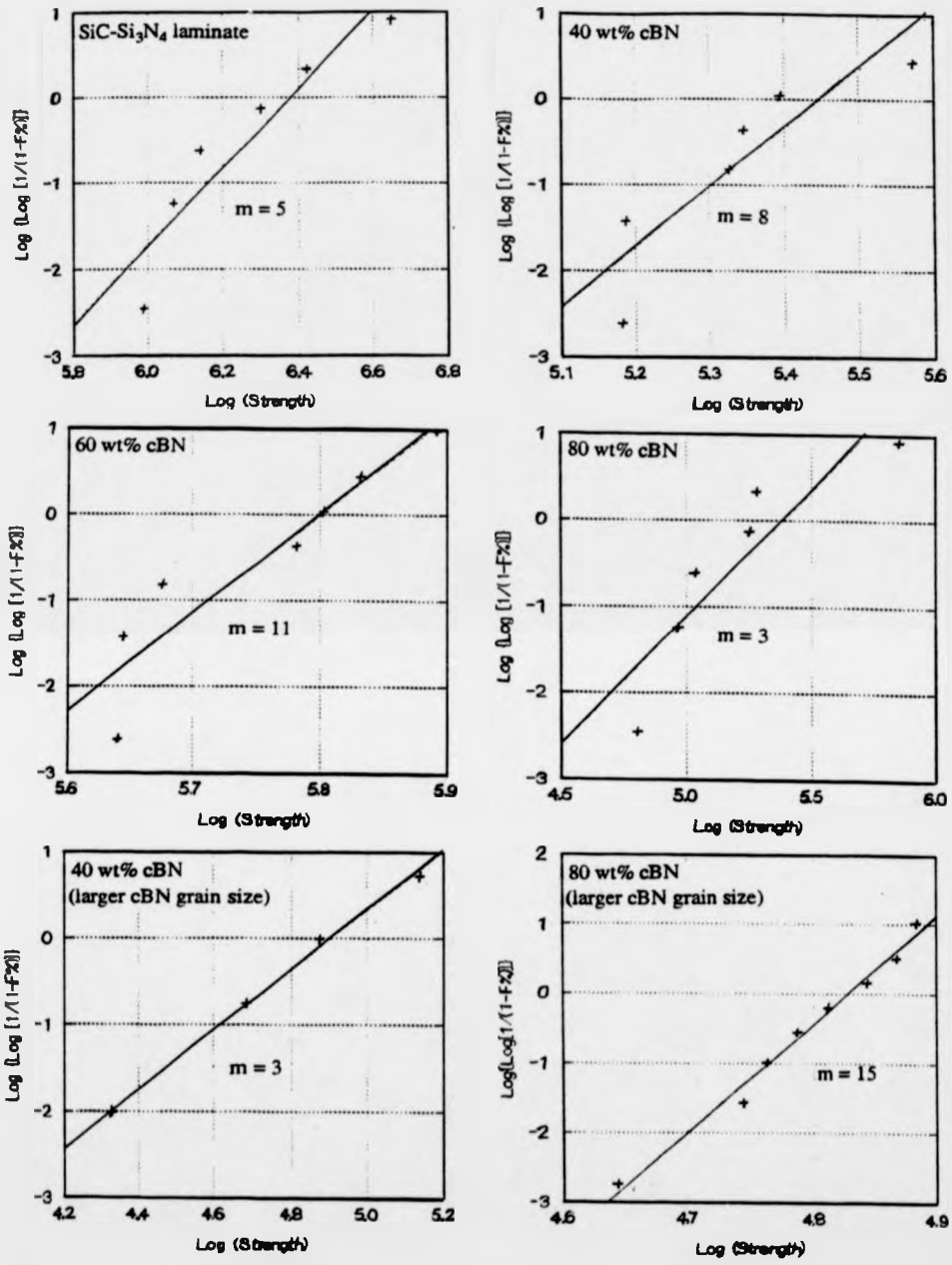

Figure 6.5: Weibull plots of the strength measurements made on different ceramic composites (labelled) to illustrate the proportion of specimens that 'fail' below a given strength value. 'F%' (on the y-axes) is the cumulative percentage of the sample population that has 'failed', 'm' is the Weibull modulus and 'log' is the natural logarithm. Lines of the 'least squares fit' have been drawn through the points.

the two 80 wt% cBN composites (attributed to residual stresses) and relatively low percentage theoretical densities provide a probable explanation for the particularly low strength obtained for this composition.

Despite the limited quantities of data, the strength distributions were also examined for each composite. The data sets which best fitted the Weibull distribution are plotted in figure 6.5 and the Weibull moduli have been determined. The low values of the Weibull modulus (m = 3, m = 5) correspond to a broad exponential probability density function, which suggests that the load at failure may be determined by a random distribution of flaws (such as porosity) or residual stresses. (Where the results do not fit the Weibull distribution very closely, the fit might be improved by the addition of a constant to the strength data, but this is not shown here.)

As the data points for the second, third and fourth plots do not really fit the Weibull distribution very well, little notice should be taken of the Weibull modulus values. The larger-grained 80 wt% cBN composite was consistently weak, with little scatter in the results (figure 6.5) and a relatively high Weibull modulus of 15 (corresponding to a much narrower exponential probability density function). It is believed that the porosity in this material (about 4%, see table 5.2) and the residual stresses (responsible for macrocracking) provided a particularly predictable failure mechanism which can also explain the low values of hardness obtained for these composites (section 6.1). In contrast, the relatively high Weibull modulus value found for the 60 wt% cBN composite (m = 11) may be attributed to the predominance of the β-Si_3N_4 phase. The less random occurrence of failure in this composite is consistent with the failure being influenced by the characteristic microstructure of the β-Si_3N_4 phase, suggesting that β-Si_3N_4 forms a 'good' matrix for particulates of cBN.

6.3 CERAMIC FRACTURE TOUGHNESS

As there was insufficient material to determine the fracture toughness of the hot-pressed laminates (using the SENB technique), results are presented only for the UHP-fabricated SiC-Si_3N_4 and cBN-Si_3N_4 composites. Four-point bending was used to determine the fracture toughnesses of the cBN-Si_3N_4 ceramics, which contrasts with the

more usual indentation methods used to examine the toughness of superabrasive ceramics. However, comparison of these results with those obtained from indentation was possible only for the 40 wt% cBN composite due to the difficulties in identifying surface cracking around the Vickers impressions (see figure 6.2). However, limited material was available to investigate the toughening behaviour in the SiC-Si_3N_4 ceramics and so indentation techniques were used for these experiments.

6.3.1 *SENB Fracture Toughness of cBN-Si_3N_4 Composites*

Initially, attempts were made to determine fracture toughness using four point bending with fracture initiation from indentation. However, the large flaw populations in the composites impeded fracture from indents made under loads as high as 5 kg. Loads greater than 5 kg were not used to promote fracture on account of uncertainties in the extent of the plastic zone that this would have introduced in the ceramic. Instead, fracture was initiated from notches cut in the bend test bars, using the SENB technique.

It is interesting to note that the fracture toughness results that were obtained closely mirror those from the strength experiments as the composites of highest strength also exhibited the highest fracture toughness (see figure 6.6).

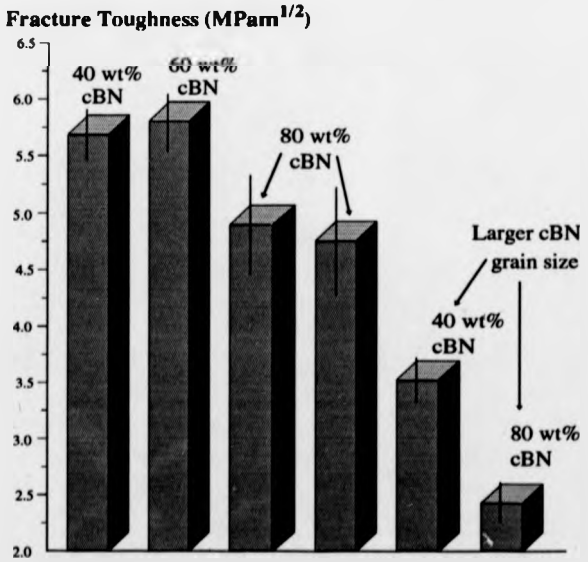

Figure 6.6: Bar chart comparing the fracture toughnesses of the cBN-Si_3N_4 composites, as determined using the SENB technique. The error bars represent the standard error in the mean.

PAGE(S) MISSING
NOT AVAILABLE

Fig 6.7

The superior fracture toughness of the 60 wt% and 40 wt% cBN composites may be attributed to their greater relative densities whilst the composites with the larger cBN grains (and lowest densities) exhibited much lower fracture toughness. In addition, the fracture toughness of the 60 wt% cBN composite might also be enhanced by the fibrous morphology of the β-Si_3N_4 phase [24-28]. The 80 wt% cBN composites were found to have a significantly lower fracture toughness than the other compositions, irrespective of the cBN grain size and most likely to be due to the greater difficulties in consolidating composites containing high cBN concentrations.

The 40 wt% and 60 wt% cBN composites both exhibited toughnesses similar to those reported for the cBN-Si_3N_4 composites (above 5.5 $MPam^{1/2}$) reviewed in chapter two [117]. The lower toughness values of the 80 wt% cBN composites were attributed to the extensive macrocracking and the particularly low toughnesses of the larger-grained composites is consistent with their lower densities, lower strengths and lower hardnesses; all indicative of poor densification.

6.3.2 *Indentation Fracture Toughness*

The fracture toughnesses of the SiC-Si_3N_4 composites fabricated at UHP and the 40 wt% cBN composite (the only cBN ceramic in which cracks were visible) were calculated from the mean of at least 16 measurements of crack length made on Vickers indentations formed using a 2 kg load. The average crack lengths, which are linearly related to the fracture toughnesses of the composites [169], are given in figure 6.8.

As can be seen from the graph, the average crack lengths in the 40 wt% cBN composite were significantly shorter than in all the SiC-Si_3N_4 composites and only in the 20 wt% SiC composite were the crack lengths shorter than those in the Si_3N_4 matrix phase, indicative of toughening behaviour associated with the SiC platelets. The average crack lengths were considerably greater in the >80 wt% SiC composite, in which the evidence of residual stresses was manifest as surface macrocracks running

parallel with the platelet plane (normal to the crystallographic c-axis) and also, perpendicular to the direction of anvil movement during UHP fabrication. Indentation induced cracks were observed to travel along these planes with greater ease than in directions normal to these planes, giving rise to anisotropic fracture toughness behaviour. This is illustrated in figure 6.8 by the two values of the average crack length which are given for the >80 wt% SiC composite (the dispersed phase concentration is not accurately represented on the graph), labelled according to their alignment with the macroscopic surface cracking.

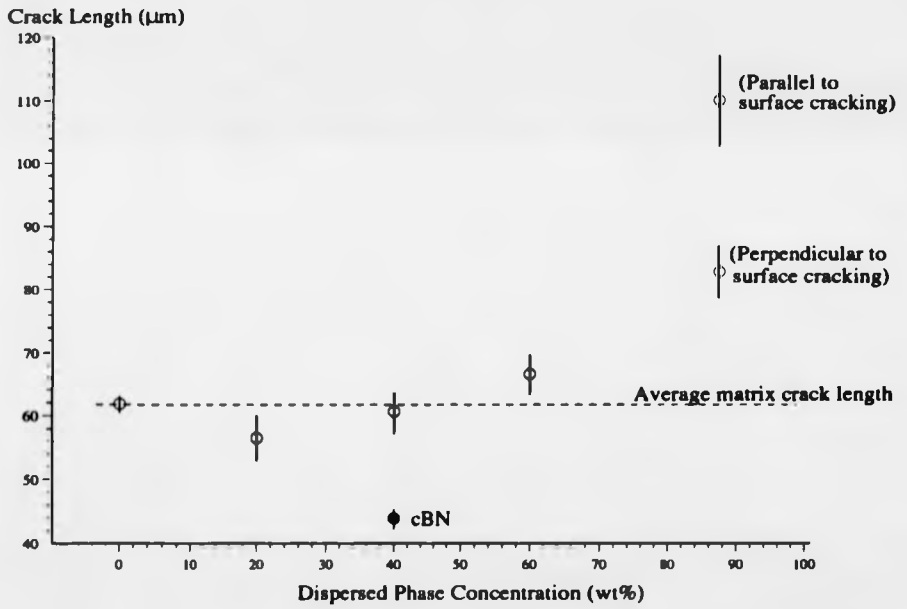

Figure 6.8: The mean crack lengths emanating from a 2 kg Vickers indentation, plotted for the SiC-Si_3N_4 composites fabricated at UHP (open circles on the graph) and the cBN (40 wt%)-Si_3N_4 composite (labelled). The error bars represent the standard error in the mean.

The fracture toughnesses have been calculated using equation 3.7 [2, 141], in which values of Young's modulus are not required and the calculated values are presented in table 6.1.

Table 6.1: Fracture Toughness of ceramic composites fabricated at ultra-high pressures. (The standard error in the mean is given with the SENB results.)

Specimen	Composition	Fracture Toughness ($MPam^{1/2}$)	
		(SENB Method)	(Indentation Method)
1	Si_3N_4-based Matrix	–	3.0
2	20 wt% SiC	–	3.4
3	40 wt% SiC	–	3.1
4	60 wt% SiC	–	2.7
5 perp†	>80 wt% SiC	–	2.0
5 para†	>80 wt% SiC	–	1.3
6	40 wt% cBN	5.69 ± 0.23	5.0
7	60 wt% cBN	5.81 ± 0.25	–
8	80 wt% cBN	4.90 ± 0.43	–
9	80 wt% cBN	4.76 ± 0.47	–
10	40 wt% cBN‡	3.53 ± 0.23	–
11	80 wt% cBN‡	2.43 ± 0.17	–

† Values calculated for directions parallel and perpendicular to the plane of severe macrocracking.
‡ Larger cBN grain size (average size 9 μm)

It is recognised that more accurate results could be obtained from indentation by making use of an equation which takes account of the relationship between the indent size and the residual stresses (between the plastically deformed zone and the surrounding elastic material), which is represented in the ratio of Young's modulus to hardness. However, Young's moduli have not been determined during this research and as it is known that Young's modulus varies non-linearly with dispersed phase concentration (or porosity), estimates were not made for the different ceramic compositions. On account of the uncertainty arising from the selected equation for fracture toughness, no errors have been estimated from the scatter in measurements of crack lengths and indent sizes.

Although the two fracture toughness values obtained for the 40 wt% cBN composite are in fairly good agreement, further comparative data would be required to identify any consistent relationship between the SENB and indentation fracture toughness. However, the results do suggest that the cBN particles (with 3 μm average grain size) are a more effective reinforcing phase than the SiC platelets. The trend of

decreasing fracture toughness with increasing SiC_p concentrations (above 20 wt%) is very similar to that reviewed in chapter two [66-69] which was explained as arising from densification difficulties associated with high proportions of SiC_p. Despite the much more extreme fabrication pressures used in this research, it would appear that comparable densification difficulties remain and the post-fabrication stresses are considerable in composites with minimal fine-grained 'matrix' phase.

The actual fracture toughnesses obtained for the SiC composites and the monolithic, (β-)Si_3N_4 phase were all found to be much lower than those reported for hot-pressed SiC_p-Si_3N_4 composites [66, 68] (discussed in chapter two) and the large differences between the results (as much as 10 $MPam^{1/2}$ [68]) are unlikely to arise from the different techniques used to determine the toughness. However, the existence of residual stresses in the UHP-fabricated ceramics (as has been suggested in sections 6.1 and 6.2) would be expected to reduce the fracture resistance by adding to applied stress levels. Although it has been suggested that the fibrous morphology of the β-Si_3N_4 phase led to a greater strength and toughness, the effect of this behaviour may be less pronounced in the UHP-fabricated composites on account of residual stresses arising from the fabrication process.

The following section describes observations made on the propagation of 'controlled' cracks in the composites, introduced by indentation, as this provided a more certain means of detecting the presence of any residual stresses.

6.3.3 *Crack Propagation*

The microstructural resistance to crack propagation was examined from indentation-induced surface cracking (using a 2 kg indenter load). Figures 6.9 and 6.10 show typical examples observed for crack propagation in the SiC-Si_3N_4 composites. The back-scattered electron contrast also reveals the inhomogeneous distribution of the bright, yttrium-containing phase (sintering additive residue) in the Si_3N_4-based matrix. The platelets are viewed 'edge on' (perpendicular to the platelet plane) as the surfaces prepared for indentation were cut along a plane parallel to the anvil movement during the UHP processing. Crack deflection along the SiC_p-matrix interfaces was commonly

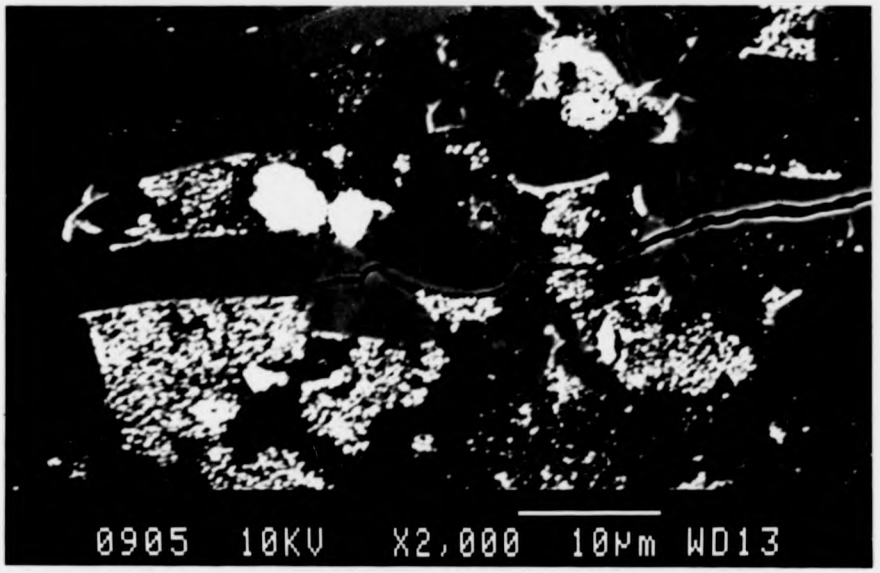

Figure 6.9: Back-scattered SEM image of crack propagation in a 20 wt% SiC composite fabricated at 4-5 GPa.

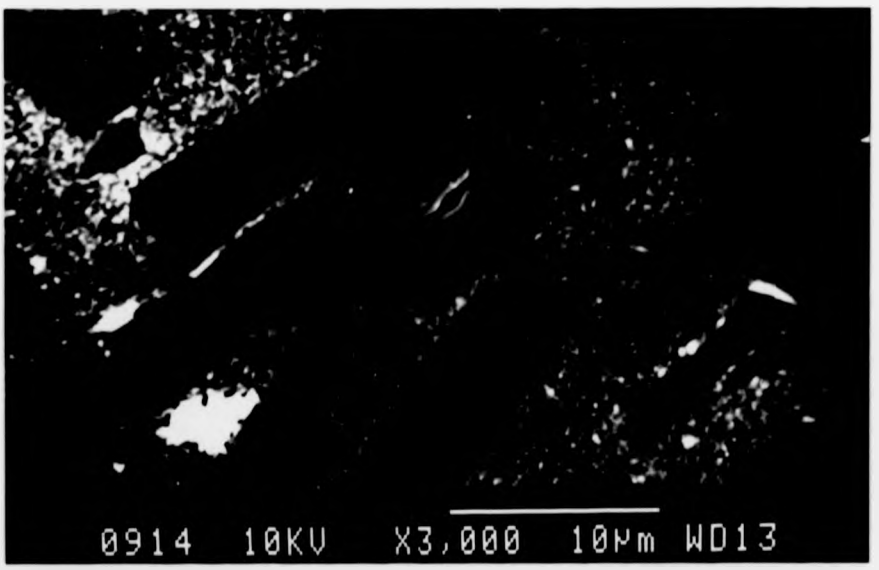

Figure 6.10: Back-scattered SEM image of crack deflection along the SiC_p-matrix interface in a 20 wt% SiC composite fabricated at 4-5 GPa.

observed, with some interfacial bonding (as can be seen in figures 6.9 and 6.10) which resulted in the absorption of the fracture energy, leading to crack termination. However, propagating cracks were also observed to have travelled straight through platelets (figure 6.9) without deviation, most often when the approaching cracks were incident normal to surfaces on the platelet (basal) plane. Some porosity or matrix microcracking is also visible in figure 6.9 at SiC_p-matrix interfaces in the vicinity of the propagating crack, possibly arising from residual stresses due to thermal expansion mismatch. Platelet rupture was also apparent (figure 6.10) as a means of absorbing fracture energy, even when SiC_p-matrix debonding occurred.

Similar observations on crack propagation were made in the composites with much higher SiC_p concentrations and which had exhibited significantly lower fracture toughness behaviour. In figure 6.11 (from the >80 wt% SiC composite), extensive cracking is visible around the indentation as is severe platelet fragmentation in the compressively stressed region of the indentation. An effect of the extreme elastic strain, introduced in the platelets during the UHP sintering, is also evident from the apparently warped appearance of some of the platelets (e.g. centre left of fig. 6.11). In many cases, the cracks have propagated via transgranular fracture of the platelets (e.g. bottom left), but there is also evidence of crack deflection along SiC_p-matrix interfaces and crack branching (e.g. top left).

It was not clear from fracture surfaces of the ceramics whether 'pullout' of the SiC platelets also contributed to the toughening behaviour. Figure 6.12 shows a rough fracture surface, from a hot-pressed SiC-Si_3N_4 laminate, in which it is possible that the debris-covered particles of about 10 μm (bottom of the image) are SiC_p that have been 'pulled out' of the surrounding matrix material. This might be established more clearly by future investigation.

The effect of cBN particles was also investigated from indentation-induced cracks. In figure 6.13, the cracks emanating from the left and right corners of the indentation follow a path between the cBN grains whilst the crack beginning at the bottom of the impression travels undeflected through a region of the matrix phase. Further evidence for crack deflection by the cBN particles is given in figure 6.14. The crack travelling down the centre of the image circumvents three of the cBN grains in its

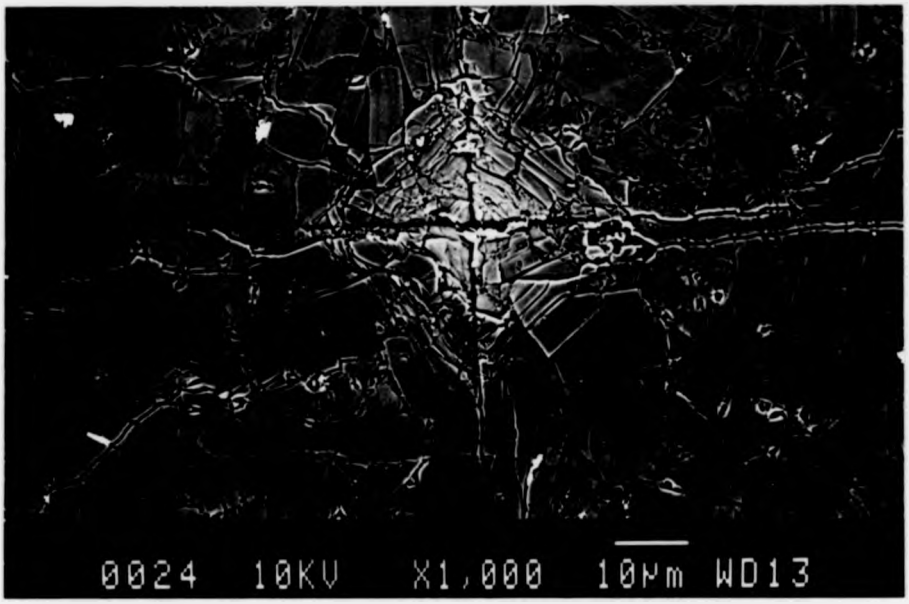

Figure 6.11: Back-scattered SEM image of a Vickers indentation (formed using a 2 kg indenter load) in the >80 wt% SiC composite.

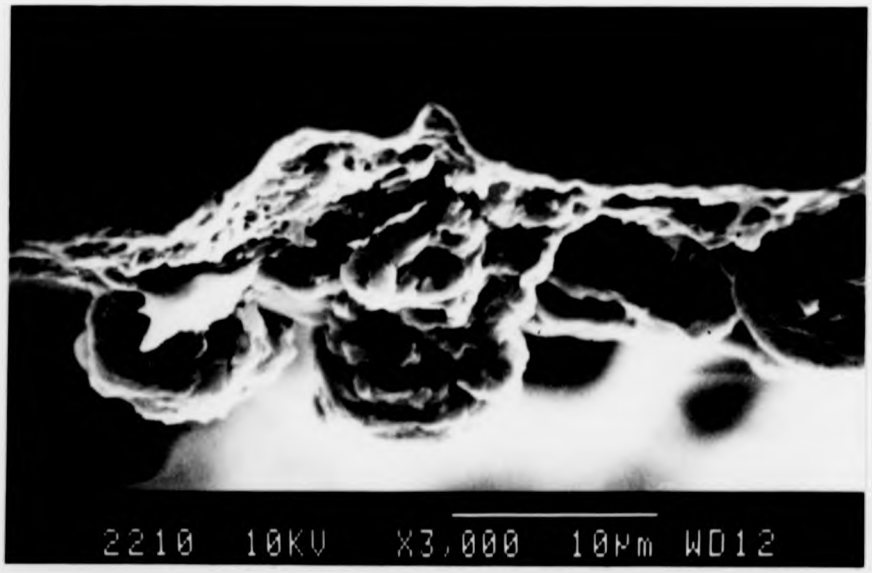

Figure 6.12: Secondary electron SEM image of the rough fracture surface of a SiC-Si_3N_4 laminate, viewed perpendicular to the plane of fracture.

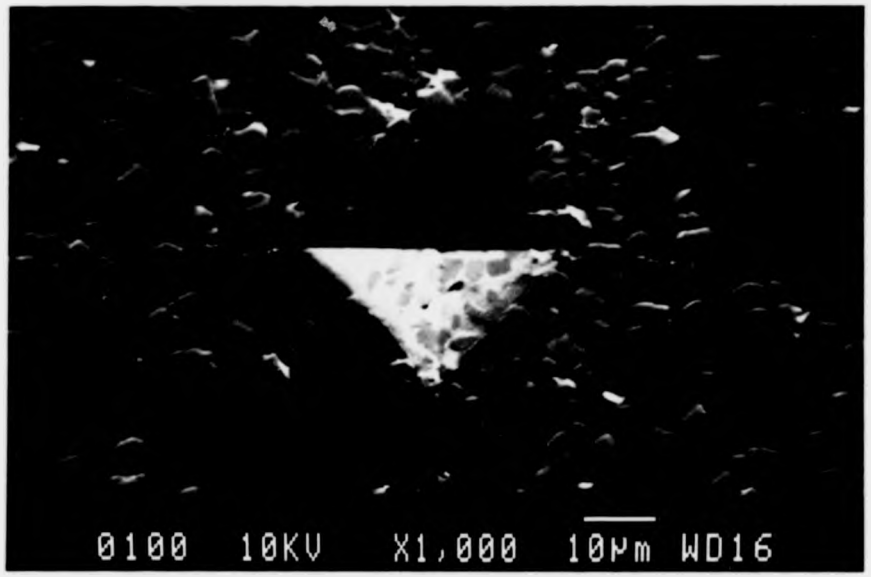

Figure 6.13: Back-scattered SEM image of a Vickers indentation (formed using a 2 kg indenter load) in a 40 wt% cBN composite.

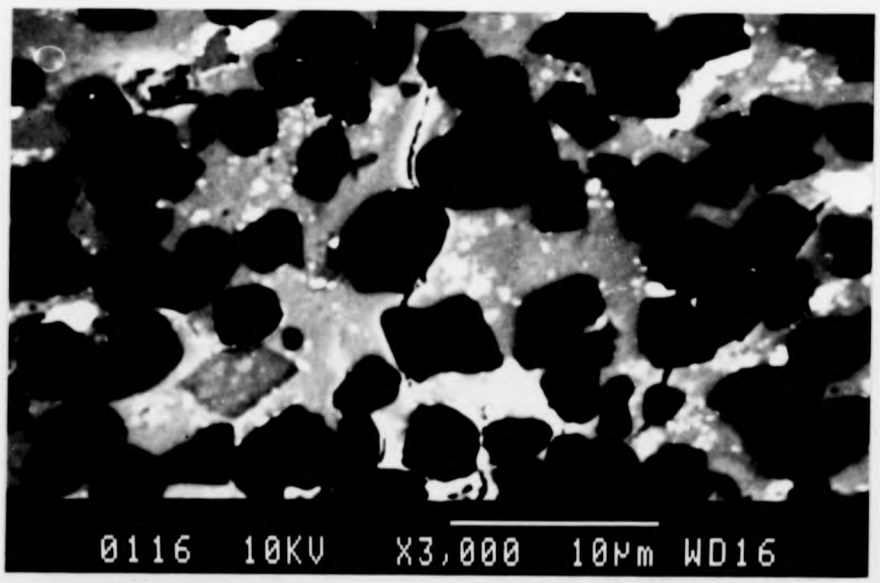

Figure 6.14: Back-scattered SEM image of a crack (centre) propagating in a 40 wt% cBN composite.

path. There is also some suggestion of microcracking in figure 6.14, visible at cBN-matrix interfaces in the right hand side of the image.

6.4 DISCUSSION OF COMPOSITE TOUGHENING MECHANISMS

In the SiC-Si_3N_4 laminate, delamination between neighbouring laminae was observed in those bend test bars which had not exhibited brittle behaviour during fracture. The delamination was attributed to weak interlaminar bonding between regions of different composition as a result of residual stresses set up by the differing thermal expansions of the neighbouring laminae. As the incidence of delamination was rare in the composites fabricated at 20 MPa, it is suggested that this potentially effective toughening mechanism might become more dominant in laminates with lower degrees of residual porosity, which is believed to be responsible for the large scatter in strength measurements (section 6.2). Although the fracture of the laminates was dominated by the prevalent porosity, the potential for a combination of microstructural toughening and delamination between neighbouring laminae has been identified.

The fracture toughness results for the SiC-Si_3N_4 composites fabricated at UHP are significantly lower than those for the SiC-Si_3N_4 composites reviewed in chapter two. However, the addition of SiC platelets to the Si_3N_4-based matrix has been observed to alter the course of propagating cracks in a similar way to that identified in other research [66-69]. Crack deflection by the platelets was most frequently observed when an advancing crack was incident on a platelet at an oblique angle, indicating that the platelet-matrix interfacial bonding was sufficiently weak to allow absorption of the fracture energy by debonding. The occurrence of debonding, rather than platelet fracture, is determined by the ratio of the fracture energies of the interface and SiC platelet, which in turn depends on the orientation of the platelet to the advancing crack and the difference in elastic moduli between the matrix and the SiC platelet [49]. The condition satisfied to allow the debonding is that the strain energy release rate of the crack advancing in the interface was at least equal to the interface fracture energy (at the relevant angle of incidence). This would suggest the existence of a weak platelet-matrix interface, providing a preferential fracture path in a similar way as for fibre-reinforced

composites [48]. There was also considerable evidence for transgranular platelet fracture, but some crack deflection also took place as the cracks traversed the platelets themselves, possibly as the propagating cracks encountered the boundaries between different structural polytypes within the platelets. The branching of propagating cracks was another contributing factor in the absorption of fracture energy. Limited evidence was observed for microcrack formation in these composites, arising from thermal expansion mismatch (during post-sintering cooling) between the Si_3N_4 and SiC and additionally, from the release of microstresses introduced by the nonuniform pressure and temperature gradients during UHP sintering. The effect on fracture of the severe deformation and polytypic phase transformation induced in the SiC platelets (section 4.9) was small compared with the observations made in conventionally sintered SiC_p composites. However, the microstructural toughening mechanisms which have been identified had little effect in preventing crack extension, unlike the behaviour found in ceramics sintered more conventionally. It would seem that the residual post-UHP fabrication stresses predisposed the composites to release the stored strain energy by crack extension.

Crack deflection was also exhibited by cBN particles (of a few μm in diameter) in the Si_3N_4 ceramic matrix, indicating the weak nature of the cBN-matrix bonding. Observations of matrix microcracking at cBN-Si_3N_4 boundaries were also made and are most likely attributed to the thermal expansion differences between these two phases and to residual microstresses caused by the nonuniformities in the UHP processing. It would seem that either the fracture toughness of the (submicron) Si_3N_4-based phase was more effectively increased by the addition of cBN (3 μm average grain size) particles than by the disc-shaped SiC platelets (17 μm average grain size), or that higher post-sintering stresses existed in the SiC composites. It was also noted that the incidence of cBN grain fracture (in response to a propagating crack) was much lower than for the SiC platelets. Whilst the SiC composites were fabricated under less extreme pressures (4 GPa) than the cBN composites (8 GPa), the possible existence of more extreme residual stresses in the SiC_p composites might be explained by the greater ease of densification afforded by the finer cBN particles. However, as the difference between the thermal expansion of the cBN and SiC phases is relatively small [4, 91], it is also

suggested that microcrack toughening was less effective in the SiC composites, on account of the SiC_p exceeding the critical size required for stress relief without weakening the material (see section 2.2.1).

Whilst the 60 wt% cBN composite exhibited a higher fracture toughness than the 40 wt% cBN composite, it is not clear whether or not this was due to the toughening mechanisms identified with the cBN particles or to additional toughening mechanisms associated with the presence of the β-Si_3N_4 phase in the 60 wt% cBN composite. The fall in fracture toughness observed for the 80 wt% cBN composites was attributed to the severity of the post-fabrication stresses, which were manifest as surface cracking.

6.5 LINEAR THERMAL EXPANSION EXPERIMENTS

Thermal expansion experiments were carried out as preliminary investigations of the linear thermal expansion behaviour of the SiC-Si_3N_4 laminates. This enabled estimates to be made of the residual stresses arising from thermal expansion mismatch between neighbouring laminae. Measurements of thermal expansion were also made on the cBN-Si_3N_4 composites that had been fabricated at 8 GPa.

6.5.1 *Thermal Expansion of SiC-Si_3N_4 Laminates*

The specimen selected for these experiments was one that had been fabricated with a gradual compositional variation through the bulk, from monolithic Si_3N_4 laminae to those with a composition of 60 wt% SiC. The measurements of expansion were carried out in a direction parallel to the laminar interfaces. Three experiments were carried out and from these, consistent results were obtained for the linear thermal expansion coefficient (within the experimental errors associated with the apparatus). At 500°C and 1000°C the expansion coefficients were determined to be $(3.9 \pm 0.1) \times 10^{-6}$ and $(4.1 \pm 0.2) \times 10^{-6}$ respectively (where the standard error in the mean is given).

The residual tensile stress in the monolithic, Si_3N_4 layer was estimated using the thermal expansion data for the composite and that for unconstrained Si_3N_4 at 1000°C (see Appendix D). Hence, it was found that a residual stress of 270 MPa

existed in the monolithic laminae, which was equal to about half of the fracture stress (see section 6.3) for these composites. An estimate was also made of the shear stress existing between a monolithic, Si_3N_4 layer and a directly adjacent layer containing a high proportion of SiC (which was assumed to have a thermal expansion close to that of monolithic SiC). Using the thermal expansion data obtained for the composite, the interlamina shear stress was estimated to be approximately 1.7 GPa. This could be severe enough to induce spontaneous delamination during the post-fabrication cooling and may explain why attempts to fabricate a composite with alternating laminae of monolithic Si_3N_4 and 60 wt% SiC (of equal thicknesses) were unsuccessful (section 4.5).

6.5.2 *Thermal Expansion of cBN-Si_3N_4 Composites*

The thermal expansion coefficients were obtained from a minimum of three experiments for the cBN-Si_3N_4 composites and the results are presented in table 6.2. The small differences in expansion found for the different compositions lie mostly within the experiments errors; although the 80 wt% cBN composites did show a greater increase in thermal expansion at the higher temperatures.

Table 6.2: Linear thermal expansion of cBN-Si_3N_4 composites

Composition	Linear Thermal Expansion Coefficient ($\times 10^{-6} K^{-1}$)	
	at 500°C	at 1000°C
40 wt% cBN	4.04 ± 0.08	4.2 ± 0.1
60 wt% cBN	4.1 ± 0.2	4.2 ± 0.2
80 wt% cBN	4.4 ± 0.2	4.8 ± 0.1

Additional observations made on the specimens after the (thermal expansion) experiments revealed that the specimen densities had decreased by a few percent. The specimens were apparently softer and they also appeared uniformly lighter in colour throughout the specimen bulk. The composites with larger cBN grain size (average grain size 9 μm) behaved in the same way as the finer-grained composites, but only after an initial experiment was carried out, in which the expansion at 1000°C was about

four times greater than in any successive experiment. The results from the first two experiments that were performed on a 40 wt% cBN composite are given in figure 6.15.

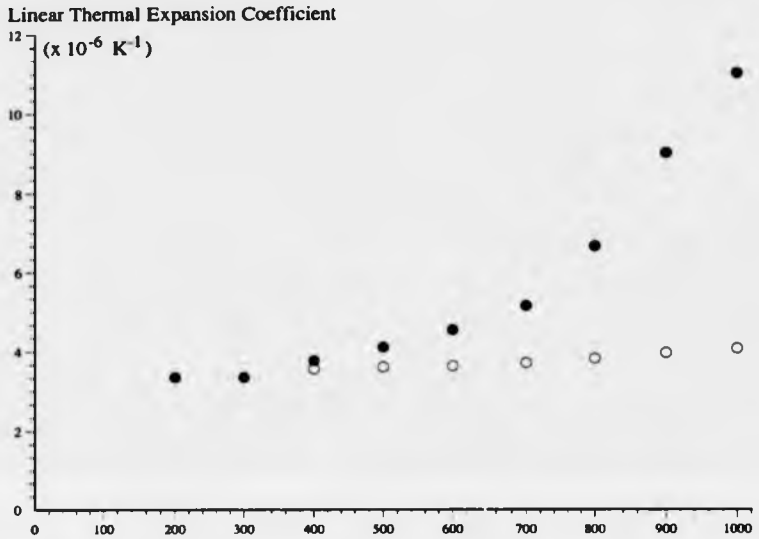

Figure 6.15: Thermal expansion behaviour of a 40 wt% cBN (larger grain size) composite during the initial (coloured circles on graph) and second (open circles) experiments performed on the specimen selected.

The changes in specimen colour, density and apparent hardness are consistent with there being some cBN phase reversion to hBN. It is expected that this phase transformation would be accompanied by an increase in thermal expansion. The thermal expansion at 1000°C (in the first experiment) is close to that reported for hot-pressed hBN, 13.3 x 10^{-6} K^{-1} [7], which suggests a considerable degree of phase transformation. However, the presence of hBN could not be identified by X-ray diffraction and the results of the subsequent experiments are inconsistent with the expected degree of expansion arising from the hexagonal BN phase. It is probable that some formation of hBN (a few wt%) did occur during the first experiment and that the X-ray diffraction evidence was masked by peaks from the Si_3N_4 phase, but this alone does not account for the considerable discrepancies found between the first and second experiments carried out on each of four separate specimens.

These results agree more closely with those of Shipilo *et al.* [170] who similarly identified a change in the thermal expansion behaviour after thermal cycling

(and annealing) and recorded a linear thermal expansion coefficient as high as 8.4 x 10^{-6} K^{-1} for investigations over a temperature range of 300-1100 K. In addition, Shipilo *et al.* reported an increase in microhardness following the heat treatment, but the converse was observed in this research. The mechanism of crystal lattice relaxation that was suggested [170] provides an explanation for the initially large expansion of the specimens; namely, releasing the stored elastic energy from the cBN lattice, which had become strained on account of the plastic deformation introduced during the UHP sintering.

6.6 SUMMARY AND CONCLUSIONS

The room temperature mechanical properties have been compared for the hybrid SiC-Si_3N_4 laminates, UHP-fabricated SiC-Si_3N_4 composites and the cBN-Si_3N_4 composites. In each case, lower than expected values (compared to other published research) of hardness, strength and fracture toughness were obtained, for reasons attributed to difficulties experienced in the fabrication processes. Whilst the strength of the hybrid laminates (570 MPa) was impaired by the residual porosity, believed to arise from inadequate pressure-assisted densification, promising evidence was found for interlaminar delamination, a mechanism that might lead to enhanced fracture toughness in laminated composites. Lower values of strength were obtained for the UHP-fabricated cBN-Si_3N_4 composites which 'mirrored' the fracture toughness results, which is most likely to be on account of the severe residual stresses believed to arise from the UHP fabrication. A similar explanation is suggested for the discrepancy between the high Vickers hardness measurements (above 35 GPa) and relatively low Knoop hardness values.

The microstructural toughening mechanisms identifed in the SiC-Si_3N_4 composites were crack deflection, microcracking, SiC platelet rupture and crack branching. The cBN grains were also observed to cause crack deflection in the Si_3N_4 matrix and some evidence for microcracking was also observed in these composites.

The thermal expansion of the hybrid laminates was used to determine the residual stress in the composites (270 MPa) and to estimate the interlaminar shear stress

(1.7 GPa). From the values obtained, it was concluded that the high stresses could be expected to promote interlaminar delamination and possibly lead to spontaneous delamination between monolithic Si_3N_4 laminae and those with a particularly high SiC content.

The cBN-Si_3N_4 composites exhibited considerable thermal expansion during the initial experiment carried out for each specimen, which might have suggested some phase transformation to hexagonal BN. However, following this, the coefficients of expansion obtained from subsequent experiments were in closer agreement with typical values associated with the dominant ceramic phases [4, 91]. Therefore, it is believed that the hysteresis shown in the thermal expansion experiments arises from the relaxation of residual stresses in the composites, as found in cubic BN by Shipilo *et al.* [170].

Chapter Seven

CONCLUSIONS AND SUGGESTIONS FOR FUTURE WORK

The original objectives, to fabricate a series of SiC-Si_3N_4 and cBN-Si_3N_4 composites and investigate the possible benefits of unconventional fabrication methods, have largely been achieved, allowing the following conclusions to be drawn.

7.1 THE SILICON NITRIDE MATRIX PHASE

A comparison of the sintering behaviour of the Si_3N_4-based ceramic matrix was made between the composites fabricated by hot-pressing and at UHP, from which it was concluded that the rate of the α to β-Si_3N_4 phase transformation was significantly enhanced by the more extreme pressures, enabling the phase transformation to be completed in only ten minutes. However, the importance of also reaching a high enough sintering temperature to promote liquid phase sintering, was indicated by incomplete α to β transformation at pressures as high as 8 GPa, where it is believed that insufficiently high temperatures were attained inside the pressure chamber.

The elongated grain growth associated with the β-Si_3N_4 phase was observed in all the composites that were fabricated. Also, the microstructure of the Si_3N_4-based matrix was very fine-grained and the Si_3N_4 crystallites were found to be of a size very similar to that of the submicron crystals of the original starting powders. Evidence for the residual sintering additives was manifest as a glassy phase at the grain boundaries in all the composites that were fabricated. The composition of this phase was identified as being an yttrium silicate. Somewhat surprisingly, in the case of the cBN-Si_3N_4 composites, additional calcium impurities in the starting cBN powder were also found to have migrated to the grain boundaries, reacting with the intergranular phase.

7.2 LAMINATED SiC-Si_3N_4 COMPOSITES

The successful fabrication of hybrid, laminated composites has revealed the potential in tailoring the ceramic macrostructure that is possible using tape casting. The tape casting method was also found to align the SiC platelets such that the plane of the

platelets lay within that of the tape. Additionally, by developing the tape slurry from the ball milling components, the possibility of agglomerates (of the fine Si_3N_4 powder) reforming at any intermediate stage could be minimised. However, to do this, it was essential to use organic tape components for which the final addition of the binder led to an increase in the slurry viscosity. The composites prepared by tape casting also showed improved homogeneity over those fabricated by slip casting.

The particle sizes of the SiC platelets and cBN particles (average sizes 17 and 3 μm, respectively) were sufficiently large to allow surface coating by the organic components to produce a well bonded and flexible tape. However, the significantly larger surface area of the submicron particles required higher organic binder concentrations (of at least 20 wt%) and also higher solvent concentrations to promote effective ball milling. This reduced the powder component of monolithic, Si_3N_4 tapes to 38 wt% and a low green density was achieved in the tapes resulting in considerable shrinkage during sintering which increased the likelihood of defects being introduced by uneven sintering rates.

Despite the overall improved homogeneity, it was not entirely possible to eliminate compositional gradients within those tapes with widely differing particle sizes, as the heavier particles, such as the SiC platelets, tended to settle out at the bottom of the tapes during the drying stage. This could only be partly offset by reducing the tape thicknesses and increasing the viscosity. Hence, areas in which the tape fabrication might be improved are in the control of ceramic phase separation during the tape drying, possibly through increased viscosity by variation of the organic tape components and possibly by accelerating this process with heating. In addition, reduction in the organic concentrations, without compromising the tape properties, would be expected to improve the final green density and reduce the possiblity of contamination arising from inadequate binder removal.

The microstructure of the hot-pressed laminates revealed distinct interlamina boundaries, indicating limited diffusion of the particles during sintering at temperatures above 1700°C and the independent sintering behaviour found for neighbouring laminae were considered to cause regular density gradients within the hybrid composites. The observations also indicated that it was not possible to densify laminae with particularly

high dispersed phase volume fractions between monolithic laminae.

The maximum fracture stress of the laminates with a gradual compositional gradient was exhibited by test bars broken from the unreinforced Si_3N_4 surface which might suggest that the expected microstructural toughening mechanisms associated with SiC platelets were inoperative. However, as some evidence for delamination and platelet 'pullout' were observed in the composites, it is believed that porosity arising from the inadequate densification (as was inferred from other microstructural observations) adversely affected their performance in the mechanical tests, limiting the fracture stress of these materials to about 540 MPa.

The laminated structure of hybrid composites sintered at UHP conditions was not well preserved during sintering at UHP conditions. Although distinct boundaries between the laminae were apparent over localised regions, it would seem that the non-uniform stress gradients during sintering were responsible for fracturing the laminae and disrupting the structural arrangement.

7.3 SiC-Si_3N_4 COMPOSITES FABRICATED AT EXTREME PRESSURES

The SiC-Si_3N_4 composites fabricated at ultra-high pressures were found to have particularly low fracture toughnesses (as determined using indentation techniques), ranging from 2.0 to 3.4 $MPam^{1/2}$ for the different ceramic compositions which were close to the value of 3.0 $MPam^{1/2}$ for the monolithic ceramic. Contrary to the indications of these results, evidence for the occurrence of microstructural toughening mechanisms was found from the analysis of crack propagation in these composites. The mechanisms identified included crack deflection, microcracking, SiC platelet rupture and crack branching, all of which are mechanisms associated with significant toughness increases in SiC-Si_3N_4 composites that have been fabricated more conventionally. It is believed that this evidence lends support to there being toughening behaviour of the SiC platelets in the matrix of Si_3N_4, but the toughening mechanisms described are ineffective on account of the much higher post-fabrication stresses in the composites thought to arise from the varying pressure and temperature gradients within the high pressure chamber. For similar reasons, it is believed that the hardness values obtained were also much lower than expected, the highest Vickers hardness of 21 GPa (obtained

for the composition with 60 wt% SiC) being only slightly greater than that of 19.5 GPa obtained for the monolithic Si_3N_4 phase.

Severe plastic deformation was induced in the SiC platelets as a result of the extreme conditions used for the composite fabrication. The microstructural observations made on the platelets revealed similarities with the extensive deformation observed on grains of the superabrasive phases after having been subjected to UHP-sintering, to form ceramic composites. A predisposition to stacking fault formation in response to applied stress has been indicated by other research [131] and so the extensive stacking fault deformation resulting from the extreme applied pressures might hardly be regarded as surprising. However, the results of the MAS-NMR and TEM investigations revealed that in addition to an increase in the crystalline disorder (indicated by the broadened XRD and MAS-NMR spectra) the deformation had proceeded by a systematic mechanism which resulted in a diffusionless polytypic phase transformation to the cubic SiC phase. It was found, using MAS-NMR studies, that such a transformation was unique to the UHP ceramic fabrication conditions and could not be induced by the less severe pressures applied during HIPing and hot-pressing at comparable sintering temperatures. However, the importance of the high temperatures was demonstrated when no evidence for any phase transition was detected from any UHP experiment carried out at ambient temperature.

The chemical shift data obtained from MAS-NMR experiments was used to identify the characteristic lattice sites of different SiC phases, using the published results of single crystal studies. The interpretation of this data was supported by the identification of the same SiC phases in an electron diffraction survey. Significant growth of a spectral peak (MAS-NMR) corresponding to a chemical shift of -16 ppm was observed following UHP sintering. This was attributed to the formation of the cubic SiC phase, achieved after only ten minutes. The results of the MAS-NMR experiments also indicated that the phase transformation was time-dependent, revealing an increase in the proportion of the cubic SiC phase after a longer sintering time.

In more detailed TEM investigations, examples of 6H platelets which had partially transformed into the 3C phase were identified and the orientation relationship at the phase boundaries suggested that the transformation had proceeded via alterations

in the stacking sequence along the crystallographic c-axis. Such a transformation mechanism has been proposed by Pirouz [139] and the evidence presented here is consistent with this: the sequential change in stacking being attributed to the co-operative motion of glide dislocations on the basal {0001} planes.

7.4 cBN-Si_3N_4 CERAMIC COMPOSITES

The cBN-Si_3N_4 composites were most successfully fabricated using high temperatures and extreme pressures close to 8GPa. The stability of the cubic BN phase was identified as being a critical factor in these experiments. At the high sintering temperatures necessary for α to β-Si_3N_4 transformation in the matrix phase and ultra-high pressures above 4 GPa, the sintering conditions were close to that for the cubic-hexagonal BN phase equilibrium and so, unsurprisingly, a significant phase reversion was found to occur during the ten minute sintering experiments. Therefore, it was necessary to sinter the cBN and Si_3N_4 powders at higher pressures, very similar to those conditions used in research where the cBN phase was also synthesised (from a lower-pressure phase) during experiments to form composites with Si_3N_4 [115, 117].

The composites which contained a large cBN volume fraction (60 and 80 wt%) exhibited the extreme Vickers hardness values (with averages of 37 and 45 GPa) which might be expected from their composition. However, using identical indentation loads, considerable discrepancies were found between the Vickers and Knoop hardness values associated with the same cBN specimens. This indicated that although small, localised regions were of the expected extreme hardness, the composites were susceptible to indentation extension, suggestive of brittle behaviour. The fracture toughnesses of the cBN-composites (determined using the SENB technique) ranged from 2.4 $MPam^{1/2}$ to 5.7 $MPam^{1/2}$. The composites with the lowest fracture toughness were those with the highest cBN concentration and the larger average cBN grain sizes of 9 μm. The composites with the finer-grained cBN particles (about 3 μm across) exhibited the highest hardnesses, fracture toughnesses and densities and this may be attributed to improved particle packing being achieved in the composite powders, allowing more uniform densification during sintering. The absence of a significant quantity of a liquid binder phase, to infiltrate any pores enclosed between the cBN

grains (as in commercial cBN compact fabrication), is believed to have led to the formation of porosity networks, possibly accompanied by some phase reversion to hBN within the voids. This was found to be particularly prevalent in larger-grained composites. This would explain the limited dependence of fracture stress on the applied load, as was found from the strength tests made on the larger-grained cBN composites, described in chapter six. The most promising mechanical properties were exhibited by a composite with a 60 wt% cBN composition, found to have a fracture stress of 316 ± 12 MPa MPa and fracture toughness of 5.81 ± 0.25 $MPam^{1/2}$. No clear relationship between the proportion of the cBN phase and the mechanical properties was identified, but it is believed that the reason for this stemmed from the many variable factors involved in the different composite fabrication histories.

Evidence for microstructural toughening mechanisms was observed in these composites, suggesting that cBN particles are suitable as a reinforcing phase in the Si_3N_4 matrix. The mechanisms which were identified (by investigating indentation-induced crack propagation) were crack deflection and microcracking.

In all the composites that were fabricated at ultra-high pressures, a strong brittle character was revealed by the results of mechanical tests. It is believed that this was caused by residual stresses arising from differential sintering behaviour which in turn may be attributed to the uneven pressure and temperature gradients and further enhanced by stresses associated with the sintering of inclusions (cBN, SiC) in the fine-grained Si_3N_4-based matrix. Further evidence for the presence of high residual stresses was suggested by the initial thermal expansion behaviour of the cBN-Si_3N_4 composites (discussed in chapter six), where an initially large thermal expansion was attributed to the relaxation of residual stresses.

A dependence of the magnitude of the stresses on the size of the inclusions might explain why composites with relatively large SiC platelet concentrations exhibited inferior fracture toughness to those with equivalent concentrations of finer-grained cBN particles. In general, the inherent stresses in these composites have been found to negate any effects of composite toughening associated with the ceramic microstructure, suggesting that current ultra-high pressure processing techniques are unsuitable for the fabrication of ceramic composites.

7.5 SUGGESTIONS FOR FUTURE WORK

In the fabrication of hybrid, laminated composites, it was found that hot-pressing was ineffective in bringing about the densification of laminae containing high volume fractions of the dispersed phase. However, as promising evidence was found for delamination in addition to microstructural composite toughening, it is believed that the mechanical potential of the hybrid composites might be achieved if improvements could be made in their densification. Some improvements may be made to reduce density gradients in ceramic tapes through more refined control of the slurry viscosity and tape drying procedure.

HIPing is suggested as an appropriate sintering technique, since significantly greater pressures could be applied during the ceramic sintering, with none of the disadvantages identified with UHP processing. Additional experiments might then be carried out to sinter the hybrid composites in an atmosphere conducive to the formation of a thin, compressive Si_3N_4 layer on predominantly SiC surfaces, further improving the fracture toughness as was found for the experiments discussed recently by Dongliang *et al.* [78].

Following more complete densification of the hybrid arrangements described in this research, the importance of the relative thicknesses of different laminae on the interlaminar shear stresses and the mechanical properties might well be established.

To enable composite fabrication at ultra-high pressures to become more feasible, technical improvements are required to reduce the pressure and temperature gradients within the high pressure chamber. However, even with the current constraints, it is believed that further progress could be made in the development of cBN-Si_3N_4 ceramics. As no advantage was found in the use of the expensive cubic BN phase as a starting material, it is recommended that this is replaced by hexagonal BN, as was used in other research [115, 117]. At the extreme pressures eventually used for the composite fabrication, it would be expected that phase transformation to cBN would occur if sufficiently high sintering temperatures could be achieved. An additional advantage would be that the formation of entrapped pores, as is believed to have occurred during compaction of the hard, cBN particles, would be less likely.

APPENDIX A

COMPOSITION OF THE CERAMIC MATRIX PHASE

The exact proportions of the Si_3N_4 and sintering additive powders (Y_2O_3, SiO_2) were determined so that the final phases formed on the crystallisation of all the residual phases would be Si_3N_4, Si_2N_2O and $Y_2Si_2O_7$, the end points of the shaded triangle in figure 2.3 [39]. Some SiO_2 was already present as an oxidation layer on the Si_3N_4 grain surfaces and the amount was calculated from the measurement of 1.2 wt% oxygen content in the powder, as supplied by the manufacturer [147]. The equivalent percentage of SiO_2 can be found from the number of moles of oxygen present, as

$$(1 \text{ mole}) SiO_2 \rightarrow (1 \text{ mole}) Si + (2 \text{ moles}) O \qquad (A1)$$

and the number of moles of oxygen in 100 g of powder is

$$\frac{1.55 \text{ g}}{15.994 \text{ g}} = 0.0969 \text{ moles} \qquad (A2)$$

where 15.994 g is the molecular weight of oxygen, giving the equivalent number of moles of SiO_2 (in 100 g) as 0.0484 moles and hence, the percentage of SiO_2 present is

$$0.0484 \times 60.085 \text{ g} = 2.910 \ \% \qquad (A3)$$

where 60.085 g is the molecular weight of SiO_2.

The position of the matrix composition on the Si-Y-O-N phase diagram (shown in figure 3.1) was calculated for a mixture of 5 g Y_2O_3 and 1 g SiO_2 powders added to 95 g (UBE) Si_3N_4 powder. Assuming that each of the elements present have only one fixed valency, the co-ordinates on the 'Equivalent % Nitrogen' axis are found from

$$\text{Eq\% N} = \frac{\text{Total charge from N ions}}{\text{Total charge from the anions (N and O)}} \qquad (A4)$$

and similarly, the co-ordinates on the 'Equivalent % Yttrium' axis are found from

$$\text{Eq\% Y} = \frac{\text{Total charge from the Y ions}}{\text{Total charge from the cations (Y and Si)}} \qquad (A5)$$

Taking into account the SiO_2 content in the (UBE) Si_3N_4 powder, the overall composition of the matrix powder is 91.26 g Si_3N_4, 3.74 g SiO_2 and 5.0 g Y_2O_3 (molecular weight, 225.82 g), giving an overall oxygen content of 3.05 %. The number of moles of each phase in 100 g of powder is 0.651 moles Si_3N_4, 0.062 moles SiO_2.

In one mole of Si_3N_4, the total negative charge is 4 x N^{-3} = -12 and therefore, the negative charge contributed by the N ions in the matrix composition is

$$0.651 \text{ moles} \times (-12) = -7.81 \qquad \text{(A6)}$$

The positive charge contributed by the Si ions in the matrix composition is

$$0.651 \text{ moles} \times (3 \times Si^{+4}) = +7.81 \qquad \text{(A7)}$$

Following the same reasoning, the charge contributed by the Si ions in the SiO_2 is +0.249 and the charge contributed by the Y ions in the Y_2O_3 is +0.133. Therefore, the position of the matrix composition on the 'Eq% Y' axis is

$$\frac{0.133}{0.133 + (7.810 + 0.249)} = 1.62 \text{ eq\% Y} \qquad \text{(A8)}$$

From very similar calculations, the negative charge contributed by the O ions in the SiO_2 is -0.249, the charge contributed from the O ions in the Y_2O_3 is -0.133 and the position of the matrix composition on the 'Eq% N' axis is 95.34 eq% N.

As can be seen from figure 3.1, this composition lies within the shaded area of the shaded traingle in figure 2.3. Hence, the eutectic formed from the residual phases after sintering would most likely crystallise into the Si_3N_4, Si_2N_2O and $Y_2Si_2O_7$ phases.

APPENDIX B

THEORETICAL DENSITIES CALCULATED FROM THE LAW OF MIXTURES

The composition of the Si_3N_4-based matrix phase assuming the complete reaction of the sintering additives with the Si_3N_4 phase. From consideration of equation (3.2), 0.022 moles of Y_2O_3 (as are present in 100 g of the starting powder) leads to the formation of 0.022 moles of $Y_2Si_2O_7$, which is equivalent to

$$0.022 \times 345.99 \text{ g} = 7.66 \text{ g } Y_2Si_2O_7 \qquad \text{(B1)}$$

where 345.99 g is the molecular weight of $Y_2Si_2O_7$ and as

$$\text{(2 moles) Y + (2 moles) Si + (7 moles) O} \rightarrow Y_2Si_2O_7 \qquad \text{(B2)}$$

the oxygen content associated with this is

$$0.022 \times (15.994 \text{ g}) \times (7 \text{ moles}) = 2.48\% \text{ O}$$

which leaves a remainder of (3.05 - 2.48 = 0.57) % O, or 0.036 moles, for the formation

of the Si_2N_2O phase (in 100 g of powder). Assuming complete reaction of the remaining oxygen, the quantity of Si_2N_2O formed was

$$116.18\,g \times 0.036 \text{ moles} = 4.14\,g\ Si_2N_2O \qquad (B3)$$

Therefore, the phase composition of the final matrix phase is 7.66 wt% $Y_2Si_2O_7$, 4.14 wt% Si_2N_2O and 88.20 wt% Si_3N_4. The theoretical density of the matrix phase was calculated as 3.235 g/cm^3 using the law of mixtures and the density values given in table B1 [171, 172].

Table B1: Densities of the phases consituting the ceramic matrix.

	Density (g/cm^3)
Si_3N_4	3.19
(α) $Y_2Si_2O_7$	3.98
Si_2N_2O	2.82

Theoretical densities were calculated similarly for all the ceramic compositions that were fabricated and are given in table B2. The density of the SiC platelets was given as 3.20 g/cm^3 by the manufacturers and the density of cBN was taken as 3.48 g/cm^3 [89].

Table B2: Theoretical densities of the Si_3N_4-based composites.

Ceramic Composition	Theoretical Density (g/cm^3)
100 wt% Matrix	3.235
20 wt% SiC	3.228
40 wt% SiC	3.221
60 wt% SiC	3.214
80 wt% SiC	3.207
40 wt% cBN	3.333
60 wt% cBN	3.382
80 wt% cBN	3.431

APPENDIX C

CHEMICAL SHIFT DATA FOR THE SiC POLYTYPES

The chemical shift data that has been reported for the 3C, 6H, 4H and 15R polytypes of SiC by other researchers is summarised in table C1. In references 158-160, the experiments were performed on single crystals.

Table C1: ^{29}Si chemical shifts for different polytypes of SiC

SiC Polytype	^{29}Si Chemical Shift Data for SiC Polytypes (in ppm)			
	Hartman *et al.* [151]	Guth *et al.* [152]	Dando *et al.* [153]	Leach [154]
3C	-18.3	-16.1 -18.4	-16	—
6H	-13.9 -20.2 -24.5	-14.3 -20.4 -24.9	-14.4 -20.5 (? 15R) -25	—
15R	-14.9 -20.8 -24.4	-14.6 -20.5 -24.1	-15.2 -20.2 (? 6H) -24	—
4H	—	—	—	-19.7 -22.5

Although there is only one distinctive type of Si lattice site in 3C SiC, it is interesting to note that two different chemical shifts have been identified with this phase. Guth *et al.* suggested that this could be explained by the different thermal histories of the 3C crystals affecting the interplanar lattice spacings. The specimen which gave rise to the chemical shift of -16.1 ppm had been prepared by chemical vapour deposition whereas the specimen giving a chemical shift of -18.4 ppm was prepared by 'siliconising' porous carbon particles. The specimen on which Dando *et al.* carried out experiments, for which the shift of -16 ppm was also obtained, had been plasma produced.

APPENDIX D

CALCULATION OF RESIDUAL THERMAL STRESS IN HYBRID COMPOSITES

The residual strain in Si_3N_4 monolithic laminae sintered to SiC-Si_3N_4 composite laminae arises on account of the difference between the expansion of the composite and the expansion that would occur in unconstrained Si_3N_4. In the thermal expansion experiments, the composite thermal expansion, α, at 1000°C was found to be 4.1 x 10^{-6} K^{-1} and the thermal expansion of unconstrained Si_3N_4 at 1000°C was taken to be 3.2 x 10^{-6} K^{-1} [4]. The strain, ε, is given by (see equation 3.11)

$$\varepsilon = \left(\frac{\Delta l}{l}\right)_{comp} - \left(\frac{\Delta l}{l}\right)_{Si_3N_4} = \Delta T\,(\alpha_{comp} - \alpha_{Si_3N_4}) \qquad \text{(D1)}$$

where Δl = the change in length on expansion, l = the length at ambient temperature and ΔT = 1000°C. The residual stress can be found using the equation for Young's modulus,

$$\sigma = E\ \Delta T\,(\alpha_{comp} - \alpha_{Si_3N_4}) \qquad \text{(D2)}$$

where E = Young's modulus, taken to be 300 GPa for Si_3N_4 [3]. Therefore, the residual stress was calculated as

$$\sigma = 300\ GPa \times 1000° \{(4.1 - 3.2) \times 10^{-6}\ K^{-1}\} = 270\ MPa \qquad \text{(D3)}$$

To evaluate the interlaminar shear stress on expansion, it was assumed that the compressive force induced in layer '1', of relatively high thermal expansion,

$$F_1 = E_1\varepsilon_1 \times A \qquad \text{(D4)}$$

where A = the cross-sectional area, was equal to the tensile stress induced in layer '2' of relatively low thermal expansion. Substituting for ε in equation D4,

$$F_1 = E_1 \times \left(\frac{l_{comp} - l_1}{l}\right) \times A \qquad \text{(D5)}$$

where F_1 is the compressive force, E_1 is the Young's modulus for layer '1', l is the length of the composite at ambient temperature, l_{comp} is the expanded length of the composite and l_1 is length to which layer '1' would expand if unconstrained. A similar expression is obtained for the tensile force induced in layer '2' and the shear force is found from the sum of these two expressions.

Therefore, the shear force is given by

$$F = A\left[E_1\left(\frac{l_{comp} - l_1}{l}\right) + E_2\left(\frac{l_{comp} - l_2}{l}\right)\right] \qquad (D6)$$

and the interlaminar shear stress, σ can be found from (F / A) and, using equation 3.10, is written as

$$\sigma = \alpha_{comp}\Delta T(E_1 - E_2) + \Delta T(E_1\alpha_1 - E_2\alpha_2) \qquad (D7)$$

If layer '1' is taken to be Si_3N_4 and layer '2' is taken to be SiC, then E_1 = 300 GPa [3], E_2 = 436 GPa [3], $\alpha_1 = 3.2 \times 10^{-6}\ K^{-1}$ and $\alpha_2 = 4.8 \times 10^{-6}\ K^{-1}$, then for ΔT = 1000°C, the interlaminar shear stress is 1.7 GPa.

REFERENCES

1. E. F. Smart and E. M. Trent, Int. J. Prod. Res. 13 [3] (1975) 265-280, *Temperature distribution in tools used for cutting iron, titanium and nickel*

2. A. G. Evans and E. A. Charles, J. Am. Ceram. Soc. 59 [7-8] (1976) 371-372, *Fracture Toughness Determination by Indentation*

3. G. R. Anstis, P. Chantikul, B. R. Lawn and D. B. Marshall, J. Am. Ceram. Soc. 64 [9] (1981) 533-538, *A Critical Evaluation of Indentation Techniaues for Measuring Fracture Toughness: I, Direct Crack Measurements*

4. R. N. Katz, Science 208 (1980) 841-847, *High Temperature Structural Ceramics*

5. Lucas Cookson Syalon Ltd. Publication no. 4191 (1984)

6. R. J. Lumby, Private communication

7. P. T. Shaffer (Ed.), Plenum Press Handbooks of *High Temperature Materials*, No. 1, Materials Index (1964) Plenum Press, NY.

8. A. Y. Liu and M. L. Cohen, Science 245 (1989) 841-842, *Prediction of new compressibility solids*

9. A. R. Badzian, Appl. Phys. Lett. 53 [25] (1989) 2495-2497, *Superhard material comparable in hardness to diamond*

10. E. V. Kocherovskii and E. A. Neginskii, Soviet Eng. Res. 8 [5] (1988) 111-114, *Cutting forces in the finish turning of iron parts with cBN and ceramic tools*

11. Y. S. Konyaev, proc. 6th AIRAPT Conf. July 1977, Colorado, ed. K. D. Timmerhaus and M. S. Barber, Plenum Press, *Use of new synthetic polycrystalline materials, carbonado-type diamond and cubic boron nitride*

12. J. Liu and P. D. Ownby, J. Am. Ceram. Soc. 74 [10] (1991) 2666-2668, *Normal-pressure hot-pressing of α-alumina-diamond composites*

13. C. E. Inglis, Trans. Inst. Naval Architects, 55 (1912) 219-230, *Stresses in a plate due to the presence of cracks and sharp corners*

14. A. A. Griffith, Philos. Trans. R. Soc. London A221, (1920) 163-198, *The phenomena of rupture and flow in solids*

15. J. F. Knott (University of Birmingham), *The Science and Engineering of Fracture*, to be presented at the ICF8, Kiev, Ukraine, June 1993

16. G. R. Irwin, J. Appl. Mech. 24, (1957) 361-364 *Analysis of Stresses and Stains near the end of a Crack Traversing a Plate*

17. A. G. Evans and A. H. Heuer, J. Am. Ceram. Soc. 63 [5-6] (1980) 241-248, *REVIEW-Transformation Toughening in ceramics: martensitic transformations in crack-tip stress fields*

18. D. Hardie and K. H. Jack, Nature, 180 (1957) 332-3, *Crystal Structures of Silicon Nitride*

19. W. P. Clancy, Microscope 22 (1974) 279-315, *A Limited Crystallographic and Optical Characterisation of Alpha and Beta Silicon Nitride*

20. H. M. Jennings, B. J. Dalgleish, P. L. Pratt, J. Mater. Sci. 23 (1988) 2573-2583, *Reactions between silicon and nitrogen, Part 2 Microstructure*

21. C. Greskovich and S. Prochazka, Comm. Am. Ceram. Soc. 64 (1981) C-96-97, *Stability of Si_3N_4 and Liquid Phase(s) During Sintering*

22. W. D. Kingery, J. Appl. Phys. 30 [3] (1959) 301-310, *Densification during Sintering in the Presence of a Liquid Phase*

23. C. M. Hwang and T. Y. Tien, Proc. Inter. Inst. for Sci. of Sintering (IISS) Symp., held in Tokyo, Nov. 1987, Vol. II, 1028-1033, *Densification and Phase Transformation During Sintering of Silicon Nitride Ceramics*

24. G. R. Terwilliger and F. F. Lange, J. Am. Ceram. Soc. 57 (1974) 25-29, *Hot-Pressing Behaviour of Silicon Nitride*

25. L. J. Bowen, R. T. Weston, T. G. Carruthers and R. J. Brook, J. Mater. Sci. 13 (1978) 341-350, *Hot-pressing and the α-β phase transformation in silicon nitride*

26. P. Drew, M. H. Lewis, J. Mater. Sci. 9 (1974) 261-269, *The Microstructure of Silicon Nitride Ceramics During Hot-Pressing Transformations*

27. F. F. Lange, J. Am. Ceram. Soc. 62 [7-8] (1979) 428-430, *Fracture Toughness of Si_3N_4 as a function of the initial α-phase content*

28. L. J. Bowen and T. G. Carruthers, J. Mater. Sci. Lett. 13 (1978) 684-687, *Development of Mechanical Strength in Hot-Pressed Silicon Nitride*

29. F. Lange, J. Am. Ceram. Soc. 56 [10] (1973) 518-522, *Relation Between Strength, Fracture Energy and Microstructure of Hot-Pressed Si_3N_4*

30. G. Ziegler, L. D. Bentsen and D. P. H. Hasselman, Comm. Am. Ceram. Soc. 64 (1981) C-35, *Orientation Effects on the Thermal Diffusivity of Hot-Pressed Silicon Nitride*

31. Hun C. Yeh and Paul F. Sikora, Am. Ceram. Soc. Bull. 58 [4] (1979) 444-447, *Consolidation of Si_3N_4 by Hot Isostatic Pressing*

32. K. H. Jack and W. I Wilson, Nature 238 (1972) 28-29, *Ceramics based on the Si-Al-O-N and Related Systems*

33. Y. Oyama and O. Kamagaito, Jap. J. Appl. Phys. 10 (1971) 1637, *Solid Solubility of Some Oxides in Si_3N_4*

34. K. H. Jack, J. Mat. Sci. 11 (1976) 1135-1158, *Review: Sialons and Related Nitrogen Ceramics*

35. G. G. Deeley, J. M. Herbert and N. C. Moore, Powd. Met. 8 (1961) 145-151, *Dense Silicon Nitride*

36. G. E. Gazza, J. Am. Ceram. Soc. 56 [12] (1973) 662, *Hot-Pressed Si_3N_4*

37. R. R. Wills, S. Holmquist, J. M. Wimmer and J. A. Cunningham, J. Mat. Sci. 11 (1976) 1305-1309, *Phase Relationships in the System Si_3N_4-Y_2O_3-SiO_2*

38. F. F. Lange, S. C. Singhal and R. C. Kuznicki, J. Am. Ceram. Soc. 60 [5-6] (1977) 249-252, *Phase Relations and Stability Studies in the Si_3N_4-SiO_2-Y_2O_3 Pseudoternary System*

39. L. J. Gauckler, H. Hohnke and T. Y. Tien, J. Am. Ceram. Soc. 63 [1-2] (1980) 35-37, *The System Si_3N_4-SiO_2-Y_2O_3*

40. T. Hayashi, H. Munakata, H. Suzuki and H. Saito, J. Mat. Sci. 21 (1986) 3501-3508, *Pressureless sintering of Si_3N_4 with Y_2O_3 and Al_2O_3*

41. A. Giachello, P. C. Matrinengo, G. Tommasini and P. Popper, Am. Ceram. Soc. Bull. 59 (1980) 1212-1215, *Sintering and Properties of Silicon Nitride Containing Y_2O_3 and MgO*

42. N. Hirosaki, A. Okada and K. Matoba, J. Am. Ceram. Soc. 71 (1988) C144-147, *Sintering of Si_3N_4 with the Addition of Rare-Earth Oxides*

43. N. Hirosaki, A. Okada and M. Mitomo, J. Mat. Sci. 25 (1990) 1872-1876, *Effect of oxide addition on the sintering and high-temperature strength of Si_3N_4 containing Y_2O_3*

44. J. Cornie, Y. M. Chiang, D. R. Uhlman, A. Mortensen and J. M. Collins, Am. Ceram. Soc. Bull. 65 [2] (1985) 293-304, *Processing of Metal and Ceramic Matrix Composites*

45. F. F. Lange, J. Am. Ceram. Soc. 56 [9] (1973) 445-450, *Effect of Microstructure on Strength of Si_3N_4-SiC Composite System*

46. P. D. Shalek, J. J. Petrovic, G. F. Hurley and F. D. Gac, Am. Ceram. Soc. Bull. 65 [2] (1986) 351-356, *Hot-Pressed SiC Whisker/Si_3N_4 Matrix Composites*

47. S. T. Buljan, J. G. Baldoni and M. L. Huckabee, Am. Ceram. Soc. Bull. 66 [2] (1987) 347-352, *Si_3N_4-SiC Composites*

48. D. B. Marshall and A. G. Evans, J. Am. Ceram. Soc. 68 [5] (1985) 225-31, *Failure Mechanisms in Ceramic-Fiber/Ceramic-Matrix Composites*

49. M. Y. He and J. W. Hutchinson, J. Appl. Mech. (Trans. ASME) 56 (1989) 270-278, *Kinking of a Crack Out of an Interface*

50. F. F. Lange, Phil. Mag. 22 (1970) 983-992, *The Interaction of a Crack Front with a Second-phase Dispersion*

51. K. T. Faber and A. G. Evans, Acta. Metall. 31 [4] (1983) 565-576, *Crack Deflection Processes-I. Theory*

52. H. Liu, K. Weisskopf and G. Petzow, J. Am. Ceram. Soc. 72 [4] (1989) 559-563, *Crack Deflection Process for Hot-Pressed Whisker-Reinforced Ceramic Composites*

53. G. Pezzotti, I. Tanaka and T. Okamoto, J. Am. Ceram. Soc. 74 [2] (1991) 326-332, *Si_3N_4/SiC-Whisker Composites without Sintering Aids: III, High-Temperature Behaviour*

54. M. Ruhle, B. J. Dalgleish and A. G. Evans, Scripta. Met.21 (1987) 681-686, *On the Toughening of Ceramics by Whiskers*

55. P. L. Swanson, C. J. Fairbanks, B. R. Lawn, Y. Mai and B. J. Hockey, J. Am. Ceram. Soc. 70 [4] (1987) 279-289, *Crack-Interface Grain Bridging as a Fracture Resistance Mechanism in Ceramics: I, Experimental Study on Alumina*

56. Y. Mai and B. R. Lawn, J. Am. Ceram. Soc. 70 [4] (1987) 289-294, *II, Theoretical Fracture Mechanics Model*

57. P. F. Becher, C. Hsueh, P. Angelini and T. N. Tiegs, J. Am. Ceram. Soc. 71 [12] (1988) 1050-61, *Toughening Behaviour in Whisker-Reinforced Ceramic Matrix Composites*

58. N. Claussen, J. Am. Ceram. Soc. 59 [1] (1976) 49-51, *Fracture Toughness of Al_2O_3 with an Unsatbilized ZrO_2 Dispersed Phase*

59. M. Ruhle, A. G. Evans, R. M. McMeeking and P. G. Charalambides, Acta. Metall. 35 [11] (1987) 2701-2710, *Microcrack Toughening in Alumina/Zirconia*

60. A. G. Evans, Acta. Metall. 26 (1978) 1845-1853, *Microfracture from Thermal Expansion Anisotropy-I. Single Phase Systems*

61. R. W. Davidge and T. J. Green, J. Mat. Sci. 3 (1968) 629-634, *The Strength of Two-Phase Ceramic/Glass Materials*

62. G. C. Wei and P. F. Becher, Am. Ceram. Soc. Bull. 64 [2] (1985) 298-304, *Development of SiC-Whisker-Reinforced Ceramics*

63. M. F. Stanton, M. Layard, A. Tegeris, E. Miller, M. May, E. Morgan and A. Smith, JNCI 67 [5] (1981) 965-975, *Relation of Particle Dimension to Carcinogenicity in Amphibole Asbestoses and Other Fibrous Minerals*

64. J. D. Birchall, D. R. Stanley, M. J. Mockford, G. H. Pigott and P. J. Pinto, J. Mat. Sci. Lett. 7 (1988) 350-352, *Toxicity of silicon carbide whiskers*

65. S. G. Malghan, M. Vaudin, J. P. Cline, P. S. Wang, L. -S. H. Lum and M. K. Jain, Proc. 2nd Int. Ceram. Sci. & Technol. Congress, Orlando, Florida, 12-15 Nov. (1990), *Characterisation of Phase and Surface Composition of Silicon Carbide Platelets*

66. X. Y. Zheng, F. P. Zeng, M. J. Pomeroy and S. Hampshire, Br. Ceram. Proc. 45 (1985) 187-198, *Reinforcement of Silicon Nitride Ceramics with Whiskers and Platelets*

67. D. Baril and M. K. Jain, Ceram. Eng. Sci. Proc. 12 [7-8] (1991) 1175-1192, *Evaluation of SiC Platelets as a Reinforcement for Oxide Matrix Composites*

68. H. Sakai, K. Matsuhiro and Y. Furuse, Proc. 2nd Int. Ceram. Sci. and Technol. Congress, 12-15 Nov. 1990, *Mechanical Properties of SiC Platelet Reinforced Ceramic Composites*

69. I. Wadsworth and R. Stevens, J. Mat. Sci. 26 (1991) 6800-6808, *Strengthening and toughening of cordierite by the addition of silicon carbide whiskers, platelets and particles*

70. N. Street, J. Colloid Sci. 12 (1957) 1-9, *Effect of a Polyanion on the Rheology of a Kaolinite Suspension*

71. L. C. DeJonghe and M. N. Rahaman, Mat. Res. Symp. Proc. Vol. 155 (1989) (Mat. Res. Soc.) 353-361, *Densification of Particulate Ceramic Composites: The Role of Heterogeneities*

72. M. W. Weiser and L. J. DeJonghe, J. Am. Ceram. Soc. 71 [3] (1988) C-125-127, *Inclusion Size and Sintering of Composite Powders*

73. M. J. Hoffman, A. Nagel and G. Petzow, Mat. Res. Symp. Proc. 155 (1989) (Mat. Res. Soc.), *Processing of SiC-Whisker Reinforced Si_3N_4*

74. H. Takebe and K. Morinaga, J. Ceram. Soc. Jpn. Inter. Ed. 96 (1988) 1122-1128, *Fabrication and Mechanical Properties of Lamellar Al_2O_3 Ceramics*

75. W. J. Clegg, K. Kendall, N. McN. Alford, T. W. Button and J. D. Birchall, Nature, 347 (1990) 455-457, *A simple way to make tough ceramics*

76. W. J. Clegg and L. R. Seddon, Proc. 4th Int. Symp. on Ceramic Materials & Components for Engines, Gothenburg, Sweden, 10-12 June 1991, Pub. Elsevier (1992), Ed. R. Carlsson, T. Johansson and L. Kahlman, *Toughening Ceramics by Laminating Composite Elements*

77. E. D. Kragness, M. F. Amateau and G. L. Messing, J. Composite Materials 25 (1991) 416-432, *Processing and Characterisation of Laminated SiC Whisker Reinforced Al_2O_3*

78. J. Dongliang, S. Jihong, T. Shouhong, G. Jingkun and P. Greil, Proc. 4th Int. Symp. on Ceramic Materials & Components for Engines, Gothenburg, Sweden, 10-12 June 1991, Pub. Elsevier (1992), Ed. R. Carlsson, T. Johansson and L. Kahlman, *SiC-Si_3N_4 Gradient Composite Ceramics by Special HIP Processing*

79. H. M. Strong, U. S. Patent 3 030 662 (1962) *Pressure distribution in reaction vessels*

80. D. L. Decker, J. Appl. Phys. 36 [1] (1965) 157-161, *Equation of State of NaCl and its Use as a Pressure Gauge in High-Pressure Research*

81. R. N. Jeffery, J. D. Barnett, H. B. Vanfleet and H. T. Hall, J. Appl. Phys. 37 [8] (1966) 3172-3180, *Pressure Calibration to 100 kbar Based on the Compression of NaCl*

82. J. E. Tydings and A. A. Giardini, Proc. Symp. of High Pressure Measurements, New York, Nov. 1962, Pub. in '*High Pressure Measurements*' ed. A. A. Giardini and E. C. Lloyd, Butterworths, Washington (1963), *A Study of Stress Homogeneity in Cylindrical Cavities at High Pressures*

83. W. F. Sherman and A. A. Stadtmuller, '*Experimental Techniques in High Pressure Research*', Wiley, Chichester (1987)

84. R. E. Hanneman, H. M. Strong and F. P. Bundy, *A Critical Review of the Effect of Pressure on Thermocouple emf's*, in the National Bureau of Standards Special Publication no. 326, Accurate Characterisation of the High-Pressure Environment, ed. E. C. Lloyd, issued March 1971

85. P. N. La Mori, *The Use of Solid-Solid Transitions at High Temperatures for High-Pressure Calibration*, in NBS pub. no. 326 (see previous ref.)

86. R. H. Wentorf, Jr., J. Chem. Phys. 26 [4] (1957) 956, *Cubic form of Boron Nitride*

87. F. P. Bundy and R. H. Wentorf, Jr., J. Chem. Phys. 38 [5] (1963) 1144-1149, *Direct Transformation of Hexagonal Boron Nitride to Denser Forms*

88. R. E. Hanneman, H. M. Strong and F. P. Bundy, Science (1967) 995-997, *Hexagonal Diamonds in Meteorites*

89. T. Soma, A. Sawaoka and S. Saito, Mat. Res. Bull. 9 (1974) 755-762, *Characterisation of Wurtzite Type Boron Nitride Synthesised by Shock Compression*

90. K. Ichinose, M. Wakatsuki, T. Aoki and Y. Maeda, Proc. 4th Int. Conf. on High Press., Kyoto, Japan (1974) 436-440, *Synthesis of Polycrystalline Cubic BN*

91. G. A. Slack, S. F. Bartram, J. Appl. Phys. 46 [1] (1975) 89-98, *Thermal Expansion of some Diamondlike Crystals*

92. G. A. Slack, J. Phys. Chem. Solids, 34 (1973) 321-335, *Nonmetallic Crystals with High Thermal Conductivity*

93. Corrigan, U.S. Patent 4 188 194 (1980), *Direct Conversion Process for making Cubic Boron Nitride from Pyrolytic Boron Nitride*

94. F. R. Corrigan, *Thermal Conductivity of Polycrystalline Cubic Boron Nitride* in Proc. High Pressure & Technology Sixth AIRAPT Conf. July 1977, Vol. I, Pysical Properties and Material Synthesis, ed. K. D. Timmerhaus and M. S. Barber, Plenum Press (1979)

95. R. H. Wentorf, R. C. De Vries and F. P. Bundy, Science, 208 (1980) 873-880, *Sintered Superhard Materials*

96. M. Wakatsuki, K. Ichinose and T. Aoki, Mat. Res. Bull. 7 (1972) 999-1004, *Synthesis of Polycrystalline Cubic BN*

97. A. P. Garshin and V. E. Shvaiko-Shvaikovskii, Sverhtverdye Materialy, Vol. 8 [1] (1986) 19-23 (trans. pub. by Allerton Press Inc. 1986), *Investigation of the Interaction of Cubic Boron Nitride with Oxygen and Nitrogen*

98. N. N. Sirota and A. M. Mazurenko, G.B. Patent no. 1317716 (24 March, 1971) *Method of Producing Cubic Boron Nitride*

99. F. R. Corrigan and F. P. Bundy, J. Chem. Phys. 63 [9] (1975) 3812-3819, *Direct Transitions Among the Allotropic Forms of Boron Nitride at High Pressures and Temperatures*

100. V. L. Solozhenko, Doklady Akademii Nauk USSR 301 [1] (1988) 147-149, *Phase Diagram of Boron Nitride*

101. V. L. Solozhenko, Proc. 28th Europ. High Press. Res. Group (1990), *The Thermodynamic Aspect of Boron Nitride Polymorphism and the BN Phase Diagram*

102. E. Tani, T. Soma, A. Sawaoka and S. Saito, Jap. J. Appl. Phys. 14 [10] (1975) 1605-1606, *A Stability of Wurtzite Type Boron Nitride Under High Pressure*

103. R. H. Wentorf, Jr., J. Chem. Phys. 34 [3] (1961) 809-812, *Synthesis of the Cubic Form of Boron Nitride*

104. R. C. DeVries and J. F. Fleisher, J. Cryst. Growth 13/14 (1972) 88-92, *Phase Equilibria Pertinent to the Growth of Cubic Boron Nitride*

105. T. Kobayashi, K. Susa and S. Taniguchi, Mat. Res. Bull. 10 [11] (1975) 1231-1236, *New Catalysts for the High Pressure Synthesis of Cubic BN*

106. T. Kobayashi, J. Chem. Phys. 70 [12] (1979) 5898-5905, *High Pressure Syntheses of cubic BN using water, urea and boric acid catalysts*

107. T. Endo, T. Sato and O. Fukunaga, U. S. Patent 4 562 163 (31 Dec. 1985), *Boron Nitride Complex and Processes for Preparing a Light-Transmitting Dense Body of Cubic System Boron Nitride*

108. S. Hitoshi, E. P. Patent 0 407 946 A1 (1990), *Cubic Boron Nitride Sintered Compact and Method of Preparing the Same*

109. S. Hirano, T. Yamaguchi and S. Naka, J. Am. Ceram. Soc. 64 [12] (1981) 734-736, *Effects of AlN Additions and Atmosphere on the Synthesis of Cubic Boron Nitride*

110. H. Itoh, T. Matsudaira, K. Inoue and S. Naka, J. Mater. Sci. 25 [1] (1990) 203-206, *Effects of Added c-BN Seed Crystals on the Reaction Sintering of c-BN Accompanied by a Conversion from h-BN to c-BN*

111. O. Fukunaga, T. Endoh, M. Akaishi, T. Oosawa and S. Yamaoka, Proc. of the International Symposium of Factors in Densification and Sintering of Oxide and Non-oxide ceramics, 1978 Japan, 328-338, *High Pressure Sintering of Cubic Boron Nitride Based Composite*

112. J. C. Walmsley and A. R. Lang, J. Mat. Sci. 22 [11] (1987) 4093-4102, *A Transmission Electron Microscope Study of a Cubic Boron Nitride-Based Compact with AlN and AlB_2 Binder Phases*

113. T. Kabayama, U. S. Patent 3 959 443 (25 May, 1976), *Method of Synthesising Cubic Crystal Structure Boron Nitride*

114. F. R. Bell, U. S. Patent 3 944 398 (16 March, 1976), *Method of forming an Abrasive Compact of Cubic Boron Nitride*

115. H. Tan and T. J. Ahrens, J. Mater. Res. 3 [5] (1988) 1010-1020, *Dynamic Consolidation of cBN and its admixtures*

116. S. N. Gromyko, V. B. Zelyavskii, A. V. Kurdyumov and A. N. Pilyankevich, Sov. Phys. Dokl. 34 (1989) 1095-1096, *Solubility of Silicon Nitride in Cubic Boron Nitride*

117. H. Yoshihara, A. Onodera, K. Suito, H. Nakae, Y. Matsunami and T. Hirai, J. Mat. Sci. 25 (1990) 4595-4603, *Behaviour of B-N-Si Under High Pressure and High Temperature*

118. V. G. Gargin, Sverkht. Mater. 8 [3] (1986) 7-11 (trans. pub. by Allerton Press 1986), *The Effect of Sintering Temperature on the Properties of Cubic Boron Nitride Polycrystals*

119. V. B. Shipilo, N. G. Anichenko, L. A. Makovetskaya and G. P. Popel'nyuk, Soviet Powder Metallurgy and Metal Ceramics (1986) 61-64 (trans. from Poroshk.Metall. 277 [1], 1986), *Influence of Sintering Conditions on the Properties of Polycrystalline Cubic Boron Nitride*

120. B. F. Britun and A. N. Pilyankevich, Soviet Powd. Metall. and Metal Ceramics, 28 [10] (1989) 772-776, *Electron Microscopic Examination of Cubic Boron Nitride*

121. O. J. Pullum and M. H. Lewis, Mater. Lett. 9 [2-3] (1990), *Microstructural Analysis of a Cubic Boron Nitride Ceramic*

122. O. Yeheskel and Y. Gefen, Mater. Sci. & Eng. 78 (1986) 209-216, *Properties and Microstructure of Hot Isistatically Pressed Si_3N_4*

123. L. Pejryd, Mat. Sci. & Engin. A105/106 (1986) 169-174, *The Effect of Temperature and Yttria Content on the Properties of Hot Isostatically Pressed Si_3N_4*

124. M. Shimada, A. Tanaka, T. Yamada and M. Koizumi, 'Ceramic Powders' ed. P. Vincenzini, Elsevier Sci. Pub. Comp., Amsterdam (1983) 871-879, *Densification and Phase Transformation of Si_3N_4 by High Pressure Sintering*

125. M. Shimada, A. Tanaka, T. Yamada and M. Koizumi, 'Fracture Mechanics of Ceramics', Vol. 6, ed. R. C. Bradt, A. G. Evans, D. P. H. Hasselman and F. F. Lange, Plenum Pub. Corp. (1983) 181-188, *Fracture Toughness of High Pressure Sintered Si_3N_4 Without Additives*

126. A. R. Verma and P. Krishna, *Polymorphism and polytypism in crystals*, Wiley, NY, (1966)

127. J. P. Hirth and J. Lothe, *Theory of Dislocations*, John Wiley & Sons Inc., New York (1982)

128. H. N. Baumann, Jr., J. Electrochem. Soc. 99 (1952) 109-114, *The Relationship of Alpha and Beta Silicon Carbide*

129. M. I. Sokhor, V. G. Kondakov and L. I. Fel'dgun, Soviet Physics-Doklady 12 [8] (1968) 749-751, *Transition of Silicon Carbide from the Hexagonal to the Cubic Phase Under the Influence of High Pressures and High Temperatures*

130. J. C. Walmsley, PhD Thesis, University of Bristol (1986), *The Microstructure of Superhard Material Compacts*

131. K. Maeda, K. Suzuki, S. Fujita, M. Ichihara and S. Hyodo, Phil. Mag. A, 57 [4] (1988) 573-592, *Defects in plastically deformed 6H SiC single crystals studied by transmission electron microscopy*

132. K. B. Alexander, P. F. Becher and S. B. Waters, Proc. 12th Int. Congress for Electron Microscopy, 1032-1033, Pub. San Francisco Press., Inc. (1990), *Characterization of Silicon Carbide Platelet-Reinforced Alumina*

133. H. Suematsu, T. Suzuki and T. Iseki, J. Am. Ceram. Soc. 74 [1] (1991) 173-8, *Kinking and Cracking Caused by Slip in Single Crystals of Silicon Carbide*

134. M. Mitomo, N. Yang, Y. Kishi and Y. Bando, J. Mat. Sci. 23 (1988) 3413-3419, *Influence of powder characteristics on gas pressure sintering of Si_3N_4*

135. H. R. Usala and M. J. Darmon, Proc. of the Annual Meeting of the American Ceramic Society Electronics Division in Illinois, April 1986, *Solvent-based MLC Binder Studies*

136. J. Bohnlein-Mauss, W. Sigmund, G. Wegner, W. H. Meyer, F. Hessel, K. Seitz and A. Roosen, Adv. Mater. 4 [2] (1992) 73-81, *The Function of Polymers in the Tape Casting of Alumina*

137. ICI (Imperial Chemical Industries) publication 210-4E/1454.2Ed.SC.DH/ Sept. 1988, Ed. N. Van Der Avort, *Hypermer polymeric dispersants for advanced ceramic applications*

138. W. Johnson, A. G. Mamalis, M. C. de Malherbe and H. K. Tonshoff, Forschritt-Berichte der Zeitschriften, 2 [37] (1979) 35-40, VDI-Verlag, Dusseldorf, *Ultra-high pressure equipment and techniques mainly for synthesising diamond and cubic boron nitride*

139. J. Lees, Advances in High Pressure Research, Ch. 1, Ed. R. S. Bradley, Academic Press (1966), *The design and performance of U. H. P. equipment. An interim report on the tetrahedral apparatus*

140. E. R. Andrew, Phil. Trans. R. Soc. Lond. A 299 (1981) 505-520, *Magic angle spinning in solid state n.m.r. spectroscopy*

141. I. J. McColm, *Ceramic Hardness*, Plenum Press (1990)

142. K. E. Amin, in *Engineered Materials Handbook*, Volume 4, *Ceramics and Glasses*, ASM International (1991), 599-609, *Toughness, Hardness, and Wear*

143. L. A. Simpson, J. Am. Ceram. Soc. 57 [4] (1974) 151-154, *Use of the Notched-Beam Test for Evaluation of Fracture Energies of Ceramics*

144. B. Gross, J. E. Srawley, NASA Technical Note D-2603 (1965), *Stress Intensity Factor for SENB Specimens in Bending and Tension by Boundary Collocation of a Stress Function*

145. R. E. Mistler, Am. Ceram. Soc. Bull. 69 [6] (1990) 1022-1026, *Tape Casting: The Basic Process for Meeting the Needs of the Electronics Industry*

146. L. Braun, J. R. Morris, Jr. and W. R. Cannon, Am. Ceram. Soc. Bull. 64 [5] (1985) 727-729, *Viscosity of Tape-Casting Slips*

147. UBE Industries, Ltd. (Tokyo) data sheet 3.500.S (1990)

148. D. S. Wilkinson, K. P. Plucknett, to be pub. in Proc. Mater. Res. Soc. Symp. 249 (1992), *Tape Casting Using Fine Ceramic Powders*

149. Du Pont MLC Materials Systems data sheet E-53568(7/83) (1983) (E. I. Du Pont De Nemours & Co. Inc.)

150. G. R. Finlay, J. S. Hartman, M. F. Richardson and B. L. Williams, J. Chem. Soc. Chem. Commun. 3 (1985) 159-161, *^{29}Si and ^{13}C Magic Angle Spinning N. M. R. Spectra of Silicon Carbide Polymorphs*

151. J. S. Hartman, M. F. Richardson, B. L. Sheriff and B. G. Winsborrow, J. Am. Chem. Soc. 109 (1987) 6059-6067, *Magic Angle Spinning NMR Studies of Silicon Carbide: Polytypes, Impurities and Highly Inefficient Spin-Lattice Relaxation*

152. J. R. Guth and W. T. Petuskey, J. Phys. Chem. 91 [20] (1987) 5361-5364, *Silicon-29 Magic Angle Sample Spinning Nuclear Magnetic Resonance Characterization of SiC Polytypes*

153. N. R. Dando and M. A. Tadayyoni, J. Am. Ceram. Soc. 73 [8] (1990) 2242-2246, *Characterization of Polyphasic Silicon Carbide Using Surface-Enhanced Raman and Nuclear Magnetic Resonance Spectroscopy*

154. M. J. Leach, PhD Thesis (1990), University of Durham, *Synthesis and multinuclear magnetic resonance studies of some nitrogen-containing ceramic phases*

155. K. R. Carduner, R. O. Carter III, M. E. Milberg and G. M. Crosbie, Anal. Chem. 59 (1987) 2794-2797, *Determination of Phase Composition of Silicon Nitride Powders by Silicon-29 Magic Angle Spinning Nuclear Magnetic Resonance Spectroscopy*

156. J. W. Yang, T. Suzuki, P. Pirouz, J. A. Powell and T. Iseki, Mat. Res. Soc. Symp. Proc. 242 (1992) 531-536, *Stress-Induced Polytypic Transformation in SiC*

157. J. W. Yang and P. Pirouz, J. Mater. Res. (1993) (in press), *The α->β Polytypic Transformation in High-Temperature Indented SiC*

158. P. Pirouz and J. W. Yang, Ultramicroscopy (1992), *Polytypic Transformations in SiC: The Role of TEM*

159. H. Blank, P. Delavignette, R. Gevers and S. Amelinckx, Phys. Stat. Sol. 7 (1964) 747-764, *Fault Structures in Wurtzite*

160. P. Pirouz, R. Chaim, U. Dahmen and K. H. Westmacott, Acta. Metall. Mater. 38 [2] (1990) 313-322, *The Martensitic Transformation in Silicon-I. Experimental Observations*

161. P. Pirouz, Inst. Phys. Conf. Ser. No. 104, Ch. 1, Proc. Int. Symp. on Struct. Prop. Disloc. Semicond. Oxford (1989), *Dislocation mechanisms for twinning and polytypic transformations in semiconductors*

162. P. Pirouz, J. W. Yang, J. A. Powell and F. Ernst, Inst. Phys. Conf. Ser. (1991) No. 117, section 3 (Pres. at the Microsc. Semicond. Mater. Conf., Oxford, 25-28 March 1991, *The role of dislocations in the 3C <-> 6H SiC polytypic transformation*

163. T. Evans, S. T. Davey and S. H. Robertson, J. Mat. Sci. 19 (1984) 2405-2414, *Photoluminescence studies of sintered diamond compacts*

164. J. Hosoi, T. Oikawa and M. Inoue, J. Electr. Spectros. & Related Phenom. 27 (1982) 243-254, *Study of Boron Nitride by Electron Energy-Loss Spectroscopy*

165. M. -O. Guillou, J. L. Henshall and R. M. Hooper, J. Hard Mater. 1 [4] (1990) 289-296, *Time-dependent Effects in the Room Temperature Indentation Hardness and Fracture of Cubic Boron Nitride Aggregates*

166. C. A. Brookes, R. M. Hooper and W. A. Lambert, Phil. Mag. A, 47 [5] (1983) L9-L12, *Identification of Slip Systems in cubic boron nitride*

167. P. J. Heath, Indust. Diamond Rev. 3 (1986) 120-127, *Properties and Uses of Amborite*

168. A. V. Bochko, O. N. Grigor'ev, T. M. Svazkina and A. M. Shatokhin, Soviet Powder Metallurgy and Metal Ceramics, 25 [4] (1986) 339-342, *Effect of Heat Treatment Conditions on the Mechanical Properties of Boron Nitride Polycrystals*

169. C. B. Ponton and R. D. Rawlings, Br. Ceram. Trans. J. 88 (1989) 83-90, *Dependence of the Vickers Indentation Fracture Toughness on Surface Crack Length*

170. V. B. Shipilo, I. M. Bel'skii, L. A. Makovetskaya and G. P. Yaroshevich, Vestsi Akademii Navuk BSSR, Ser-Fiz-Mat., No. 5 (1984) 79-82, *Study of the Thermal Expansion of Cubic Boron Nitride*

171. M. H. Lewis, C. J. Reed and N. D. Butler, Mater. Sci. & Engin. 71 (1985) 87-94, *Pressureless-sintered Ceramics Based on the Compound Si_2N_2O*

172. Landolt-Börstein Handbook, Ed. K. -H. Hellwege, volume III d1, Springer-Verlag (1985)

PUBLISHED PAPERS NOT FILMED FOR COPYRIGHT REASONS

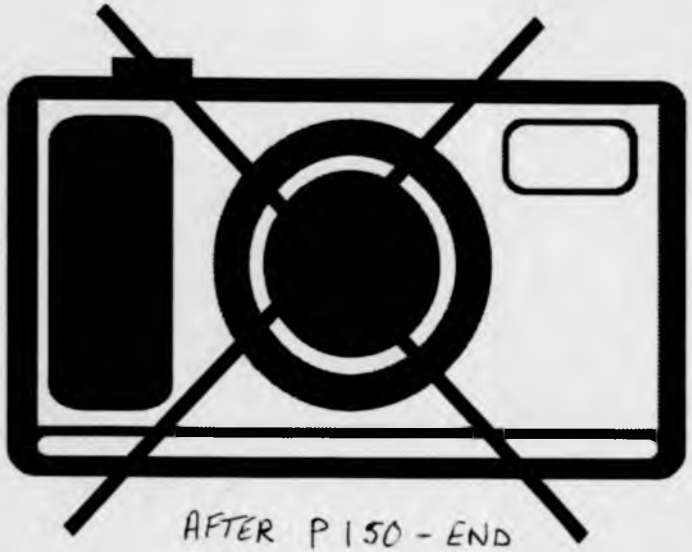

AFTER P 150 - END

TITLE THE FABRICATION AND ANALYSIS OF HARD Si3N4-BASED, DISPERSED PHASE COMPOSITES

AUTHOR Olwen J PULLUM

DEGREE Ph.D

AWARDING BODY Warwick University

DATE 1993

THESIS NUMBER DX177946

C 7K